[FOR POSTER PRESENTATION] SIRONA-1: A SELENOCENTRIC PLATFORM HOSTING INTERNATIONAL PAYLOADS G. Bailet[1] and C. O. Laux[1], [1]Laboratoire EM2C, CNRS, CentraleSupélec, Université Paris-Saclay, 3, rue Joliot Curie, 91192 Gif-sur-Yvette cedex, France (gilles.bailet@centralesupelec.fr).

Introduction: Over the millennia of recorded human history, the Moon has been the focus of great fascination and a goal to reach. Lunar exploration started with the Luna-1 flyby (1959), culminated during the Apollo era.

The Lunar and Planetary Institute established a list of major questions still not answered since 1959. On that impulse, space agencies are projecting new missions to the Moon. Although these have great potential of scientific return, their costs do not fall within the allocated budgets. For the sake of illustration, since 2000, only 4 US, 3 Chinese, 1 Indian, 1 European and 1 Japanese have flown to the Moon.

We present in this paper a new platform based on the CubeSat standard, named SIRONA (20 kg), dedicated to bringing in lunar orbit a suite of payloads developed by universities around the world. Led by the student Space Center of CentraleSupélec (CS^3), the collaborative effort to conduct this mission will provide innovative and exploratory science return with a low budget, and will foster new impetus for Lunar exploration.

On the way to the Moon: To reduce launch costs, improve mission flexibility and demonstrate CubeSats capabilities, an off-the-shelf ion thruster will be used. From a polar orbit at low altitude around Earth to a polar orbit around the Moon (200 km), SIRONA will transit during 12 months toward the it scientific orbit.

Payloads: a scientific board will be formed with a panel of Lunar science experts and representatives of space agencies. The universities and research laboratories worldwide will be invited to respond to a call for proposal to embark payloads onto the SIRONA platform. The call will emphasize a priority on the scientific and technology demonstration objectives such as study of the Moon's water ice, development of a deployable high gain antenna, characterization of the far side of the Moon…

The scientific board will review the proposals taking in account the scientific merit of the expected return, the expected mass/volume/energy consumption of the experiment, as well as the educational impact. The board will select payload packages and backups to ensure a wide diversity of science objectives.

Conclusion: SIRONA is a unique low cost opportunity to fly multiple university-developed payloads to the Moon. The mission will investigate several critical Lunar exploration questions, allowing the scientific community to test different approaches for more in-depth studies in future flagship missions.

IN-SITU STUDIES OF THE LUNAR WATER CYCLE BY ION TRAP MASS SPECTROMETRY

S. J. Barber[1], S. Sheridan[1], I. P. Wright[1], B. A. Cohen[2] and W. M. Farrell[2]. [1]School of Physical Sciences, The Open University, Milton Keynes, MK7 6AA, UK, [2] NASA Goddard Space Flight Center, Greenbelt, MD 20771, USA. (simeon.barber@open.ac.uk)

Introduction: Whereas the Moon might have previously been considered 'a completely waterless planet' [1], multiple recent discoveries in sample analysis [2] and remote sensing [3] are changing that paradigm. The numerous missions that are in preparation by agencies and commercial entities present an opportunity to obtain multiple in-situ measurements of volatiles at the lunar surface that could provide ground truth for remote sensing and may reveal the dynamic water and volatiles cycles potentially occurring on the Moon today. It is furthermore important that these studies are performed before the fragile lunar atmosphere is perturbed by further human activity [4]. This paper describes mass spectrometers being developed for these upcoming missions, to study the present-day occurrence and processing of water and volatiles at the Moon. It focusses on plans for new instruments to study the lunar exosphere in-situ.

Mass spectrometers for volatiles analysis: A particularly compact and versatile mass spectrometer was developed for the Ptolemy instrument [5] on the Philae lander of the Rosetta mission to comet 67P. This was an ion trap mass spectrometer (ITMS) with an approximate volume of 1 litre and mass 1 kg including electronics. Analyte molecules are subjected to a flow of electrons emitted by a cold cathode (field effect) or heated wire filament (thermionic emission) source. The resulting analyte ions may become bound or 'trapped' within stable orbits within a cavity defined by a ring electrode and two end cap electrodes all of hyperbolic profile. The quadrupolar trapping field is created by the application of suitable radiofrequency potentials to these electrodes. Subsequent manipulation of that field enables the ejection of the ions into an external secondary electron multiplier detector in order of increasing mass-to-charge (m/z) ratio. The output of that detector thus constitutes a mass spectrum, representing nature of the analyte (m/z ratio of fragment ions) and its concentration (peak area). The process of ionization, mass sorting and detection of ions is rapid such that a full mass spectrum in the range up to m/z ~150 (appropriate for most volatiles) takes around 10-20 milliseconds.

Instrument Implementation: Drawing upon heritage from the Ptolemy instrument, an ITMS is being developed for use in ESA's PROSPECT package as part of the Roscosmos Luna-27 lander (Figure 1) planned to visit the south polar region of the Moon in 2023-4 [6]. The ITMS forms part of the 'ProSPA' analytical laboratory [7]. It accepts regolith from the 'ProSEED' drill, which samples at depths up to ~1.2 m, comparable to those probed by remote sensing from orbiters and sufficient to sample beneath the uppermost layers potentially contaminated by exhaust emissions during landing. The drill can translate laterally enabling multiple boreholes across an arc ~0.5 m.

Although highly capable, the mass of PROSPECT (some 30+ kg) means that other, simpler systems may be beneficial to utilise the ITMS on smaller landed platforms. Examples in development include:

i-Drill [8] is an instrumented ~1.2 m drill which utilizes the heat generated during descent to release and transport volatiles to an integral ITMS for evolved gas analysis all for <15-20 kg.

LUVMI is a lightweight rover affording increased lateral coverage to the ITMS [9] integrated within a '**Lunar Volatiles Scout**' [10] instrument of <2 kg and accessing depths of 15-20 cm. Future developments may incorporate the ITMS within probes to be deployed in areas otherwise inaccessible to the rover.

L-DART [11] - named for 'Direct Analysis of Resource Traps' - is a more extreme example in which probes or 'darts' are released from low lunar orbit and self-deploy at a speed of ~300 metres/sec into targeted regions of the Moon including PSRs such as Cabeus crater. The probes penetrate to a depth of several metres, and on-board instruments measure regolith geotechnical, thermal and volatile properties before, during and/or after impact. A rugged, impact-hardened ITMS provides the first true in-situ measurements of PSR volatiles, which are released during the high-energy landing and subsequent thermal soak.

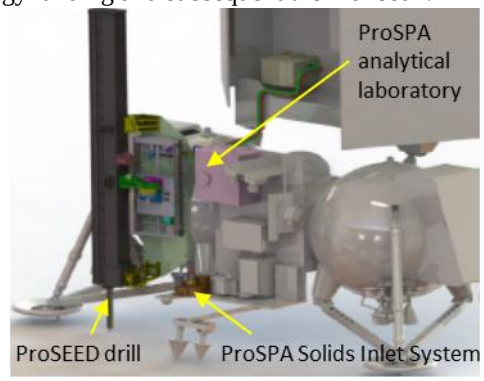

Fig 1: PROSPECT elements ProSPA & ProSEED on Luna-27 lander (IKI/Roscosmos/Leonardo)

ITMS for lunar exosphere studies: The nature and dynamics of the lunar exosphere are still poorly understood. The Moon has a very tenuous atmosphere (exosphere) made up primarily of neon, helium, and argon, [12], molecular hydrogen [13], with smaller abundances of methane [14], sodium, and potassium [15]. To date, water and OH have only been reported in the exosphere during meteor stream events by the LADEE NMS and UVS [16]. Because of the rate at which atoms escape from the lunar atmosphere, there must be a continuous source of particles to maintain even a tenuous atmosphere. Work in the last decade has pointed to a lunar "water" cycle with three principal components: primordial (interior) water, surficial water (linked to solar wind and meteorites), and polar (sequestered) water. Identifying and characterizing the lunar volatile reservoirs and evaluating their interrelations is a high priority for both lunar science and for exploration purposes, as surficial water could represent a key resource for human utilisation.

With the foregoing motivation, proposals have recently been submitted to both ESA and NASA for an ITMS on landed missions to provide the first in-situ quantification of OH/H_2O on the lunar surface. The ITMS would provide this measurement, along with vastly improved quantitation of exospheric species of interest to both science and human exploration as outlined above. In addition to measuring the abundance of these species, the investigation would link the surface to upper exosphere via the LADEE measurements, constraining models for the global evolution of these species. Monitoring the diurnal variability of the species would provide insights into the surface chemistry that creates, maintains, and/or sequesters such molecules. This landed investigation would be useful anywhere on the Moon: equatorial siting would be particularly useful to compare with LADEE, but polar would be particularly useful in monitoring migration of water molecules toward PSRs. At the time of writing the ITMS has been selected by NASA in the frame of its Commercial Lunar Payload Services program and is under review at ESA.

The proposed instrument is based on Ptolemy heritage as updated within the PROSPECT/ProSPA program. In the CLPS implementation, the ITMS will be supplied by The Open University and housed in a mechanical and thermal interface adapter provided by NASA Goddard Spaceflight Center. This adapter consists of four parts: a custom interface plate to attach ITMS to the lander, a deployable door over the MS inlet valve for landing, a baffle to shield the instrument from lander-derived species; and a passive thermal control solution for the specific lander selected by NASA (Figure 2).

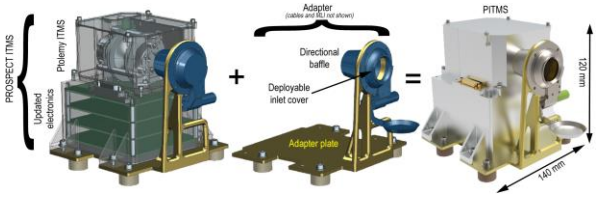

Figure 2: ITMS derived from European heritage packed within NASA GSFC adapter for NASA CLPS

The goal is to monitor the tenuous near-surface lunar exosphere up to m/z 150 throughout the mission, in response to natural (*e.g.*, diurnal temperature cycle) and artificial (*e.g.*, landing event, lander activities) stimuli. The measurement would characterise the lunar exosphere after descent and landing, and throughout the lunar day to understand the release and movement of volatile species. The investigation would provide measurements of the exosphere that would significantly improve our knowledge of the abundance and behavior of volatiles on the Moon, linking the lunar surface to LADEE measurements, and inform robotic and human mission design by characterising the interaction between surface assets and the lunar environment. Deployment of similar packages on multiple landers would assist in building a global picture of the lunar volatiles cycle.

Acknowledgement: ProSPA is being developed by a consortium led by The Open University, UK, under contract to the PROSPECT prime contractor Leonardo S.p.A., Italy, within a programme of and funded by the European Space Agency.

References:

[1] Heiken et al. *Lunar Sourcebook* p.634 [2] Hauri et al. (2017) *Ann. Rev, Earth Plan. Sci.* 45:89–111 [3] Various (2018) *PSS* LRO Special Issue, 162 [4] National Academy of Science (2007) *Scientific Context for the Exploration of the Moon* [5] Wright, I.P. et al. (2015) *Science* Vol.349 (6247), pp.aab0673 [6] Trautner et al. (2018) IAC paper 42773 [7] Barber et al. (2018) LPSC [8] Timoney et al. (2019) ELS [9] Biswas et al. (2019) ELS [10] Sheridan et al. (2019) ELS [11] Barber et al. (2018) LPSC [12] Benna et al., (2015) Geophys. Res. Lett., 42(10), 3723-3729 [13] Hurley et al. (2017) Icarus, 283, 31-37 [14] Hodges (2016) Geophys. Res. Lett., 43(13) [15] Colaprete et al. (2016) Science, 351(6270), 249 [16] Colaprete et al. (2015) NASA Exploration Forum

CRYSTAL SIZE DISTRIBUTION ANALYSIS OF APOLLO 15 MARE BASALTS: NEW METHODS AND SOME RECOMMENDATIONS. S. K. Bell[1], M. E. Hartley[1], K. H. Joy[1] and J. F. Pernet-Fisher[1], School of Earth and Environmental Sciences, University of Manchester, Oxford Road, Manchester, M19 3PL, UK (samantha.bell@manchester.ac.uk).

Introduction: Crystal size distribution (CSD) analysis is a non-destructive, quantitative method of understanding the crystallization history of a magma [1,2,3]; from which, signatures of magma mixing, accumulation, fractionation and multi-stage cooling histories can be identified and crystal residence times can be calculated [2]. As a result, CSD analysis enables examination of the magmatic and thermal history of planetary-scale processes.

Traditional CSD data collection is often time-intensive, requiring the manual tracing of crystals within a sample from a digital image e.g., [4,5]. QEMSCAN is an automated quantitative petrology system that combines scanning electron microscopy with energy-dispersive spectrometry to produce high-resolution mineral maps.

Here, we have used Apollo 15 mare basalt samples to investigate the feasibility of using QEMSCAN for semi-automated crystal size distribution analysis. This work is part of a wider project to understand the petrogenetic relationship between the Apollo 15 quartz-normative and olivine-normative suites [6]. We present plagioclase, pyroxene and olivine CSD data for five Apollo 15 mare basalt thin sections (15597,12, 15597,18, 15125,6, 15475,15 and 15555,209), gathered using both manual and QEMSCAN methods. To fully assess the potential of QEMSCAN analysis, samples were selected to incorporate as many potential CSD trends as possible and reflect the range of crystal shapes and sizes within the Apollo 15 mare basalt collection.

Manual data collection: Backscattered electron (BSE) maps were collected using an FEI QUANTA 650 field emission gun (FEG) scanning electron microscope (SEM) at the University of Manchester. Data were collected at a resolution of 0.98 µ/pixel. The crystal edges of the mineral(s) plagioclase, pyroxene and olivine were manually traced from the BSE maps in CorelDraw X6. Crystal shapes were then analysed using ImageJ version 1.51 [7] to attain properties such as major and minor axis length. The 2D crystal data were processed using CSD*slice* [8] to estimate true 3D crystal shape, before stereologically converting into 3D crystal lengths using CSD*corrections* [4]. The natural logarithm of the crystal population density was then plotted against corrected crystal length to produce a CSD graph.

QEMSCAN data collection: The FEI QEMSCAN at the University of Manchester operates using a QUANTA 650 FEG SEM, equipped with a single Bruker XFlash energy dispersive X-ray spectrometer (EDS). The QEMSCAN software, iExplorer, uses a combination of EDS spectra and BSE brightness to assign a mineral to each pixel using a Species Identification Protocol (SIP) list. The SIP list is a series of pre-defined mineral definitions that can be entered by the user. Samples were classified using a SIP list specifically especially set up for lunar samples. Mineral phase maps of each sample were acquired using step sizes (i.e. pixel sizes) of 5, 10 and 20 µm to understand the effect of resolution on the final CSD analysis. All mineral phase maps were analyzed using processors found in iExplorer. The granulator processor was used to extract crystals of a specified mineral from the mineral map. The touching particles processor was used to separate touching crystals. When used in combination, these two processors allow crystals of a particular mineral to be separated and displayed. Crystals from each sample were than analyzed using ImageJ, CSD*slice* and CSD*corrections* in the same way as the manually collected data (Fig.1).

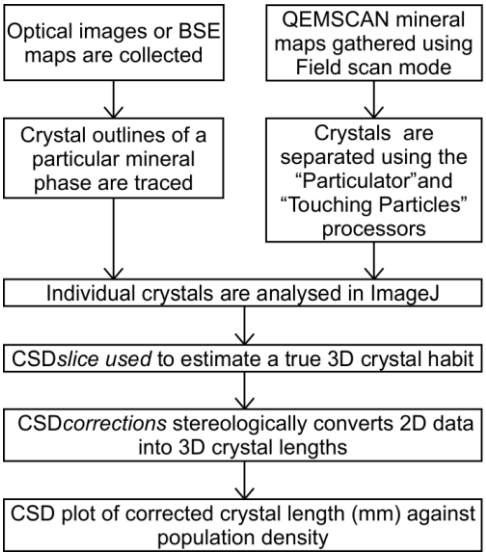

Figure 1. Flow diagram summarising the steps involved to produce CSD plots using manual and QEMSCAN methods.

Results: CSD plots of population density against crystal length were produced for pyroxene crystals in 15597,12, 15597,18, 15125,6 and 15555,209; plagioclase crystals in 15475,15; and olivine crystals in 15555,209. In all samples except 15555,209, we observe differences between the CSD trends produced from manual and QEMSCAN-derived data (Fig.2).

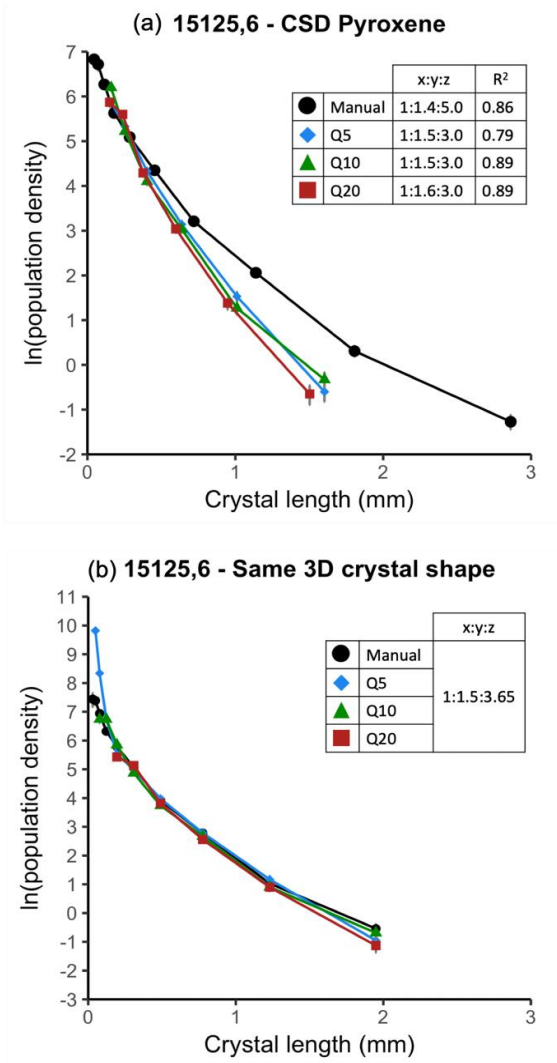

Figure 2. CSD plots for sample 15125,6. (a) CSD plots where Q5, Q10 and Q20 correspond to QEMSCAN step sizes of 5, 10 and 20 µm, respectively. The short-, intermediate- and long-axis ratios (x, y, z) and R^2 value for the 3D crystal shape estimates are also shown for each plot. (b) Reprocessing of the data sets in (a) using the same 3D crystal shape.

In most cases, the manual data result in CSD trends with shallower gradients that extend to larger crystal lengths than the QEMSCAN CSD data. The 3D crystal shape estimates from CSD*slice* are near-identical for QEMSCAN data collected at different step sizes; however, the 3D crystal shape estimates for manually derived CSD data often have larger long-axis values compared to QEMSCAN data. Discrepancies in the CSD plots between manual and QEMSCAN-derived data can be resolved by reprocessing all data sets with the same 3D crystal shape estimate (Fig. 2a). The 3D crystal shape estimate, in this case, was calculated by taking a weighted average (based on R^2 values) of 3D crystal shape estimate from the QEMSCAN data at 5, 10 and 20 µm step-sizes. However, whilst such processing masks an underlying segmentation issue that most strongly affects the longest crystals in the sample. We find that the iExplorer touching particles processor often fails to identify and separate elongate crystals that are in contact with other crystals. This inefficient segmentation causes long crystals to be split into multiple smaller-length crystals, and therefore artificially reduces the long (z) axis portion of the 3D crystal shape estimate calculated in CSD*slice*. The underestimation of the number of long crystals, combined with the underestimation of crystal aspect ratio, results in QEMSCAN-derived CSD plots with artificially steepened gradients that extend to shorter crystal lengths (Fig. 2a). Not only does this effect the ability to recognizes signatures of certain magmatic processes, but calculations of crystal residence times can also differ by up to a factor of ~8. In the case of 15555,209, the two methods produced CSD plots which fell within error of each other at step-sizes of 5 and 10 µm. This is due to 15555,209 consisting of coarser, rounded crystals touching only in a few places, which are more easily separated by the touching particles processor.

Conclusion: Differences between data collected by manual and QEMSCAN methods were seen in four out of five of the Apollo 15 mare basalt samples in this study. Such differences have the potential to influence petrologically important signatures of crystal accumulation and/or fractionation and calculations of crystal residence times. The texture and crystal habit of the sample plays and important role as to how well the touching particles processor performs, affecting the overall reliability of the QEMSCAN data. QEMSCAN should only be used for CSD analysis after careful consideration of the suitability of the samples texture and average crystal habit.

References: [1] Cashman, K.V. and Marsh, B.D. (1988) *Contributions to Mineralogy and Petrology*, *99*(3), 292-305. [2] Marsh, B.D. (1988) *Contrib Mineral Petrol*, 99, 277-291. [3] Marsh, B.D. (1998) *Journal of Petrology*, 39, 553-599. [4] Higgins, M.D. (2000) *American Mineralogist*, *85*, 1105-1116. [5] Neal, C.R. et al. (2015) *Geochimica et Cosmochimica Acta*, 148, 62-80. [6] Chappell, B.W. and Green, D.H. (1973) *EPSL*, *18*, 237–246. [7] Abramoff, M.D. et al. (2004) *Biophotonics International*, 11, 36-42. [8] Morgan D. J. and Jerram, D.A. (2006) *Journal of Volcanology and Geothermal Research*, 154, 1-7.

FUTURE LOW-COST LUNAR AND PLANETARY MISSIONS ENABLED BY COMMERCIAL SPACE COMPANIES. Alain Berinstain[1] and Robert D. Richards[2], [1]Moon Express Inc., alainberinstain@moonexpress.com, 100 Spaceport Way, Cape Canaveral, Florida 32920, [2]Moon Express Inc. bob@moonexpress.com.

Introduction: Science missions to the Moon need no longer be seen as rare and expensive opportunities. Affordable, repeated access to lunar orbit and/or the lunar surface is being made possible by innovations by commercial space companies.

Moon Express has been selected as a vendor for NASA's Commercial Lunar Payload Services (CLPS) initiative. This is a 10-year contract under which NASA-funded payloads will ride along with other customers on our missions to the Moon.

Moon Express' vision is to open the lunar frontier with turn-key payload, data and services for missions to the Moon for a wide range of customers globally, including governments, NGO's, commercial enterprises, universities, and consumers.

Like the Earth, the Moon has been enriched with vast resources through billions of years of bombardment by asteroids and comets. Unlike the Earth, these resources are largely on or near the lunar surface, and therefore relatively accessible. Moon Express is blazing a trail to the Moon to seek and harvest these resources to support a new space renaissance, where economic trade between countries will eventually become trade between worlds. All Moon Express expeditions will prospect for materials on the Moon as candidates for economic development and in-situ resource utilization.

One of the greatest practical space discoveries of our generation is the presence of vast quantities of water on the Moon. Water not only supports life but its constituents, hydrogen and oxygen, are energetic and clean rocket fuel. The discovery of water on the Moon is a game changer, not just for the economic viability of lunar resources, but for the economics of humans reaching Mars and other deep space destinations. Water is the oil of the solar system, and the Moon can become a gas station in the sky to fuel human space exploration, development and settlement of the solar system. Moon Express will begin prospecting for water resources on the Moon with its very first expedition.

The MX family of spacecraft: Moon Express has developed a family of flexible, scalable robotic explorers that can reach the Moon and other solar system destinations from Earth orbit. The MX spacecraft architecture supports multiple applications, including delivery of scientific and commercial payloads to the Moon at low cost using a rideshare model, or charter science or commercial expeditions to distant worlds.

The MX robotic explorer spacecraft are optimized for launch on existing and emergent rocket systems. The payload masses quoted below assume no launcher constraints.

MX-1: A single stage spacecraft capable of delivering up to 30kg to the lunar surface.

MX-2: A dual-stage spacecraft that doubles the capability of the MX-1 and can reach the moons of Mars.

MX-5: A cis-lunar workhorse spacecraft that can deliver up to 150kg to lunar orbit or 50kg to the surface.

MX-9: A lunar prospector/harvester that can deliver up to 500kg to the lunar surface, including an embedded MX-1R spacecraft that can launch from the lunar surface and return lunar samples to Earth.

The MX spacecraft architecture supports multiple applications, including delivery of scientific and commercial payloads to the Moon at low cost using a rideshare model, or charter science expeditions to distant worlds.

Designed for Scout Class exploration capabilities starting from low Earth orbit, MX-1 delivers flexibility and performance to revolutionize access to the Moon and cis-lunar space.

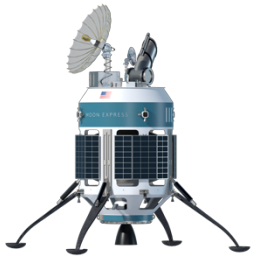

MX-1 Spacecraft

Dual stage flexibility drives more payload to the lunar surface or extends the reach to deep space. Compatible with existing and emergent launch vehicles, the MX-2 delivers Scout Class possibilities for exploration and commerce at low cost.

MX-2 Spacecraft

Characterization of the Lunar Volatiles Scout for In-Situ Volatiles Extraction and Analysis. J. Biswas[1], P. Reiss[1], S. Sheridan[2], S. Barber[2,], C. Pitcher[2], M. Reganaz[3], L. Richter[3] [1]Institute of Astronautics, Technical University of Munich, Boltzmannstr. 15, 85748 Garching, Germany, (j.biswas@tum.de), [2]The Open University, Milton Keynes, MK7 6AA, UK, [3]OHB System AG, Manfred-Fuchs-Str. 1, 82234 Weßling, Germany,

Introduction: Multiple remote sensing missions have confirmed the existence of volatiles on the lunar surface and have provided data on the global distribiution, possibly indicating significant deposits near the lunar poles. However, ambiguities remain in the interpretation of this data and local distribution, chemical composition, physical state, and extractability of this potential resource remain unkown [1]. Future surface investigations need mobility to address expected heterogenous volatiles distribution and be affordable enough to justify exposure to hazards inherent to polar permanently shadowed regions.

The Lunar Volatiles Scout (LVS) is a small and compact instrument for the in-situ extraction and analysis of volatiles that can be accommodated on small lunar rovers [2]. Recent thermal-vacuum testing of an integrated prototype of the LVS successfully demonstrated the extraction of volatiles from icy regolith simulants, the determination of their abundance, and the analysis of chemical species.

Instrument Description: The instrument consists of core drill of 15 – 20 cm length that allows sampling of the shallow lunar subsurface. The regolith sample is heated in-situ inside the drill shell to extract enclosed volatiles. The pressure inside of the drill shell is monitored by two Pirani sensors to determine the abundance of released volatiles. A small orifice connects the sample volume to a miniature ion trap mass spectrometer, which allows to determine the released chemical species and their relative concentrations. The m/z range is 10 to 150, which allows the detection of all species that were present in the LCROSS ecejta plume [3]. The total instrument mass is 1.9 kg.

Thermal Vacuum Analogue Testing: A thermal vacuum test setup was established at Technical University of Munich to allow testing of the instrument under simulated lunar conditions. In this setup, the LVS is suspended on a vertical actuator above a lunar regolith simulant sample. For the experiments, the simulant JSC-1A was hydrated by mixing with water and subsequent freezing to -50 °C. A total of 20 experiments were performed with water contents between 0.1 wt% and 5.3 wt%. After drilling into the sample, the heating rod of the LVS prototype was activated for 90 min at 15 W constant power. After heating, the drill was retracted and residual soil in the drill shell was measured to assess cross-contamination.

Results:

Volatiles Abundance: To assess the ability of the LVS to determine the volatiles abundance in a sample, a test series was conducted with frozen moisturized samples of variying water content. Figure 1 shows the development of the pressure inside the drill shell for different water contents. Expectedly, higher water content lead to higher pressures inside the sample volume. Although the sample volume is only sealed by the regolith, the pressures rise to at least 10 mbar, above which the Pirani sensors become insensitive.

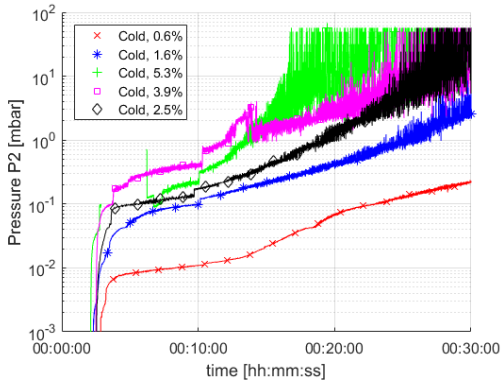

Figure 1: Pressure in LVS drill shell for different water contents of the sample

Volatiles Analysis: A sample with 0.2 wt% water was prepared for the combined gas extraction and analysis test. The mass spectrometer was able to continuously scan for the 90 min heating duration. An image of the mass spectra after 600 s is shown in Figure 2. A clear peak at m/z 18 is visible, along with a small signal at m/z 16 and 17, proving the release of water. A maximum pressure of $2 \cdot 10^{-3}$ mbar was measured inside the volume of the mass spectrometer.

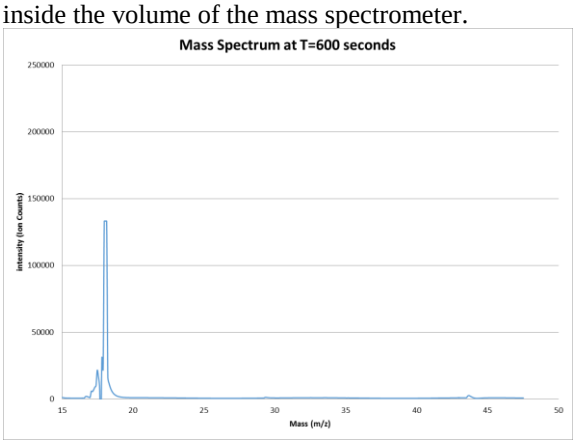

Figure 2: Mass spectra of a moisturized sample after 600 s of heating

Conclusion & Future Work: The presented results demonstrate the ability of the LVS to extract and analyse volatiles in a representative scenario under Moon-like conditions. With the LVS it is possible to distinguish measurements of different vola-

tile contents. For a more conclusive determination of the volatiles abundance, further characterization measurements are planned that take into account the effect of soil bulk density and temperature. In addition, the LVS prove to identify the released chemical species during heating. In an next step it will be investigated to what extent the LVS can also determine relative concentrations of chemical species to increase the scientific output. Further thermal-vacuum experiments are planned to achieve a full characterization of the instrument and to further increase its maturity. The LVS currently currently has a technology readiness level of 5-6 and will be available for near-future flight opportunities.

Acknowledgements:
The LVS development has been funded since 2012 through the German LUISE activity under a DLR grant and the more recent LUVMI project funded by the European Commission as part of the Horizon 2020 framework.

References: [1] L. Theodoro, V. Eke, R. Elphic, W. Feldman, D. Lawrence (2014) JGR 119, , 574-593. [2] Biswas et al. (2018), *ELS VI.*. [3] Colaprete A. et al (2010) *Science, 330,* 463–468.

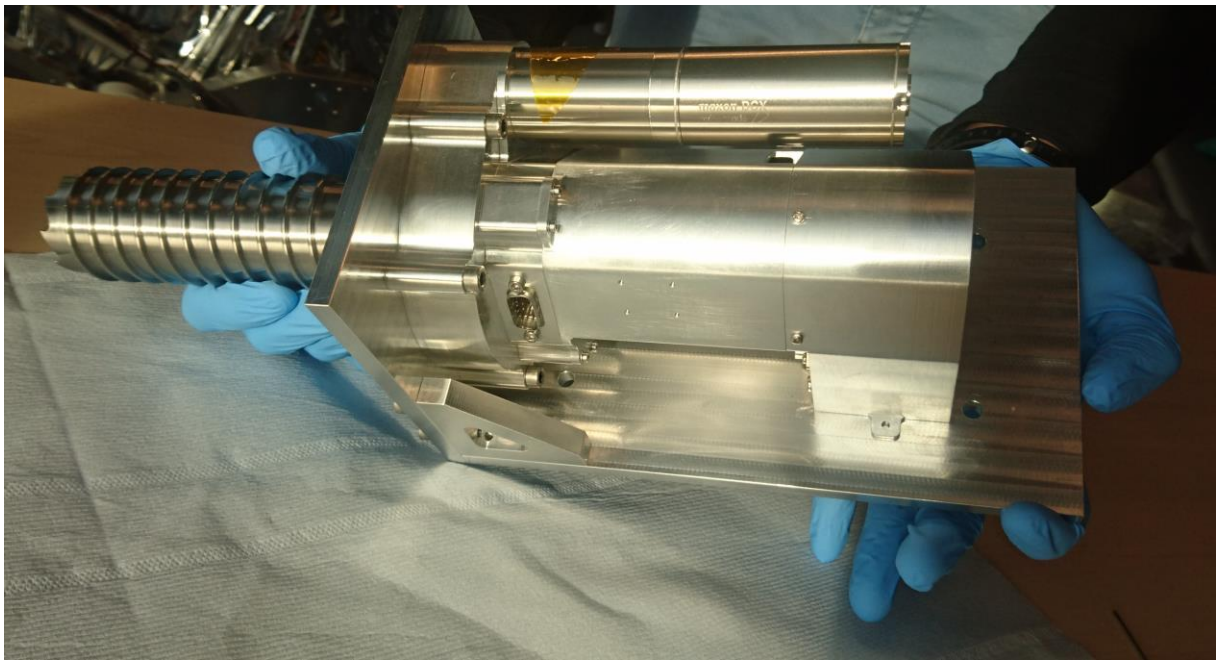

Figure 3: Image of the Lunar Volatiles Scout (LVS) prototype

REVISED CRATER SIZE-FREQUENCY DISTRIBUTION MEASUREMENTS AT THE APOLLO 14 LANDING SITE. D. Borisov[1], H. Hiesinger[1], W. Iqbal[1], and C. H. van der Bogert[1], [1]Institut für Planetologie, Westfälische Wilhelms-Universität Münster, Wilhelm-Klemm-Str. 10, D-48149 Münster, Germany (contact: d.borisov@uni-muenster.de).

Introduction: In [1], crater size-frequency distribution (CSFD) measurements of the Apollo 14 landing site were reported in conjunction with a well-constrained crystallization age of impact melt rock 14310 using Pb-Pb, Rb-Sr, Lu-Hf, and Sm-Nd isotopic systems, in an attempt to constrain the 'A14/Fra Mauro Formation (FMF)' calibration point on the lunar cratering chronology function [2-5]. Here, we investigate the CSFDs in more detail based on additional measurements on Lunar Reconnaissance Orbiter (LRO) Narrow Angle Camera (NAC) and Wide Angle Camera (WAC) images. Using the data presented here and in [1], our study aims to constrain the cumulative crater-frequency $N(1)$ and the absolute age of the Fra Mauro Formation, i.e. the Imbrium basin, using both laboratory and remote-sensing techniques.

Apollo 14 Landing Site: The Apollo 14 landing site is situated about 600-800 km south of the Imbrium basin within the Fra Mauro Formation (FMF), which is interpreted to represent megabreccia formed during the Imbrium basin formation event (e.g., [6]). The landing site was originally chosen to sample ejecta blocks that were excavated by the very young Cone crater and interpreted to unambiguously represent the FMF [6]. The original CSFD measurements yielded an $N(1) = 3.7 \pm 0.7 \times 10^{-2}$ km^{-2} [2], while the currently accepted isotopic age range for the Imbrium basin is 3.91-3.94 Ga based on Secondary Ion Mass Spectrometry (SIMS) Pb-Pb dating on accessory minerals of impact melt rocks, recently summarized in [7].

Geological Mapping and CSFDs: A geological map (1:1,500,000) of the FMF was prepared and is shown in Fig. 1. CSFDs were measured on the LRO WAC mosaic using the same count area as [2] (Fig. 1, red area), as well as a new count area, defined to cover the largest area with homogenous geology and topography within the newly remapped FMF (Fig. 1, yellow area). The results yielded a mean cumulative crater frequency of $N(1) = 4.40 \pm 0.09 \times 10^{-2}$ km^{-2} (Fig. 2), using the production and chronology functions of [3], and are concordant with the original study [2]. An inferred absolute model age (AMA) of 3.94 Ga agrees with the most recent isotopic age estimate of the Imbrium basin [7].

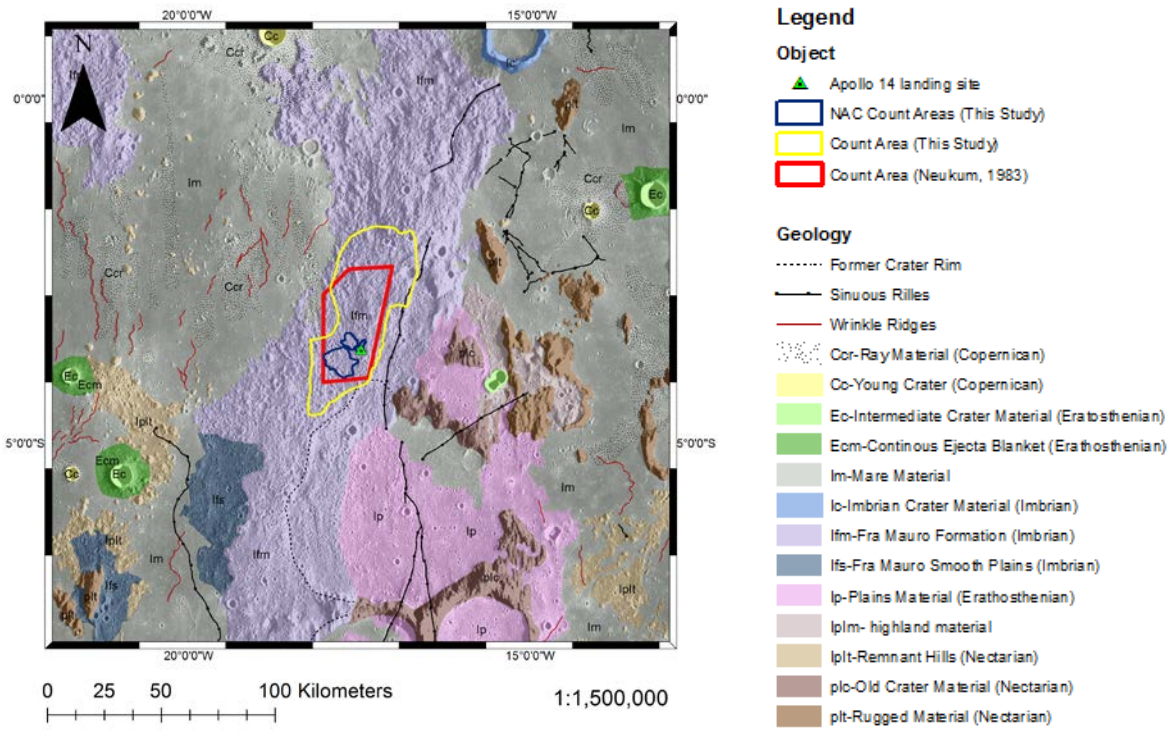

Fig. 1: *New geological map of the area around the Apollo 14 landing site (1:1,500,000).*

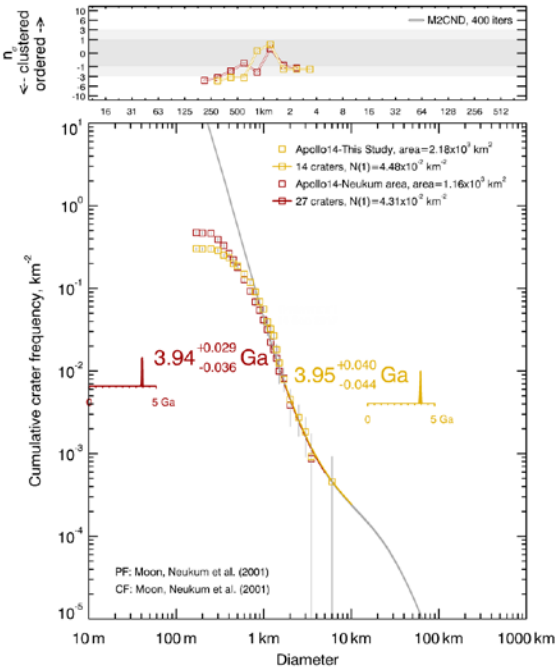

Fig. 2: *CSFD measurements based on the LRO WAC mosaic for the original count area by [2] (black), compared with a newly defined count area on the Fra Mauro Formation on the basis of our new geological map (red).*

To investigate the distribution of small craters on the FMF, LRO NAC and Kaguya images with a pixel size of ~1 m/pixel and ~10 m/pixel were analyzed. Currently, only one Digital Terrain Model (DTM) exists at this scale for the FMF and, thus, only one detailed NAC CSFD measurement can be performed for the FMF using topographical data to more precisely identify old degraded crater rims (Fig. 3; black). The count area was selected to avoid steep slopes, which might affect the CSFD measurements [8, 9]. A cumulative crater frequency of $N(1) = 2.27 \times 10^{-2}$ km^{-2} was determined. To test and validate this observation, two further NAC count areas were focused on measuring craters with diameters of >200 m, because craters below that size are in equilibrium. The results show that all NAC count areas combined yield a total $N(1) = 4.43 \times 10^{-2}$ km^{-2} (Fig. 3; blue).

Discussion: The variations of the CSFDs based on NAC data are most likely because many old and small craters in this area are heavily degraded and often do not have well-defined crater rims, which makes crater diameter determinations difficult. Additionally, target property effects, such as the relatively high porosity of the FMF [10, 11], which particularly affect small craters, might be partially responsible for the measured deviations. Thus, it is reasonable to assume that a better approximation of the $N(1)$ for the FMF is given by the WAC count areas, which encompass craters larger than those affected by strength-scaling effects and generally have higher statistical significance. Based on these data and the various isotopic data collected in the last 10 years [7], we conclude that the FMF has an $N(1) = 4.40 \pm 0.09 \times 10^{-2}$ km^{-2}, which is correlated to an absolute age of 3.91-3.94 Ga. Overall, these data are more precise, but still concordant with the pioneering studies [2, 3], which supports the current position of the A14 calibration point on the lunar chronology function.

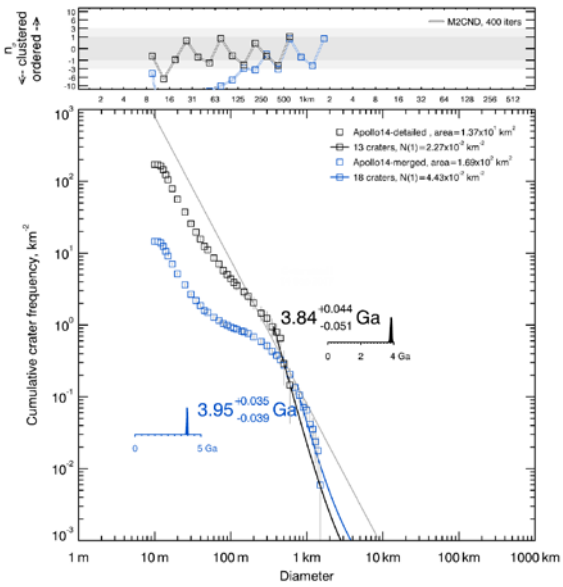

Fig. 3: *CSFD measurments based on LRO NAC and Kaguya images, and a NAC DTM for a count area directly at the Apollo 14 landing site (black), and for a merge of three NAC count areas on the FMF focusing on craters >200 m (blue).*

Acknowledgements: CvdB was supported by EU H2020 project #776276, PLANMAP.

References: [1] Borisov et al. (2018) *LPS XLVIV*, Abstract #1933. [2] Neukum (1983) Habilitation thesis, University of Munich. [3] Neukum et al. (2001) *"Chron. and evol. of Mars.", Springer Netherlands, 2001*, 55-86. [4] Hartmann and Neukum (2001) *"Chron. and evol. of Mars.", Springer Netherlands, 2001*, 165-194. [5] Stöffler et al. (2006) *Rev. in Min. and Geochem.*, 60, 519-596. [6] Swann et al. (1977) *"Geology of the Apollo 14 landing site in the Fra Mauro highlands.", Washington: US Govt. Print. Off.* [7] Bottke and Norman (2017) *Annu. Rev. Earth Planet. Sci.*, *45*, 619-647. [8] Basilevsky (1976) *Proc. Lunar Sci. Conf. VII*, 1005-1020. [9] Meyer et al. (2016) *DPS XLVIII*, Abstract #223.04. [10] Kiefer et al. (2012) *Geophys. Res. Lett.*, *39*. [11] van der Bogert et al. (2017) *Icarus*, *298*, 49-63.

A NEW MAP OF THERMAL VARIATIONS WITH DEPTH WITHIN COPERNICUS CRATER USING CHANG'E-2 (CE-2) MICROWAVE RADIOMETERS (MRMS) DATA. R. Bugiolacchi[1], G-P Hu[1], K. L. Chan[1], Y-C Zheng[2], K. T. Tsang[3]. [1]Space Science Laboratory, M.U.S.T., Avenida Wai Long, Taipa, Macau - rbugiolacchi@must.edu.mo, [2]NAO, CAS, Beijing 100012, China, [3]United International College, Zhuhai, China.

Introduction: By its longer wavelength in comparison to UV-VIS-IR, microwave radiation carries information from deeper into the surface and can extend to several times the observation wavelength. Moreover, passive microwave measurements can be carried out during night time and in shadowed regions. Most observations of the lunar surface in these frequencies were Earth-based but they helped develop theoretical models to obtain the brightness temperature (TB) of the lunar surface and derive several of physical parameters including heat flow [1]. Here, we preview the results from a new investigative approach that takes advantage of global lunar microwave data obtained from the Chang'E-2 mission (CE-2) focusing on crater Copernicus. The multi-channel radiometers worked at four different frequencies (about 37, 19, 8, and 3 GHz), probing increasingly deeper into the surface.

Data and method: The Level 2C Chang'E-2 (CE-2) Microwave RadioMeter (MRMs) data [2-3] was used in this study, following system calibration and geometric correction with Planetary Data System [4]. The MRM underwent onboard adjustments to ensure its reliability and accuracy using a two-point calibration method (for details see [2-5-6]). We used spherical harmonic fits for the Brightness Temperature (TB) variations with local time [6] to suppress the lunar phase effect. Normalized TBs at midnight were chosen to minimise the topographic effects on the emission [7].

We selected the widest range possible of data from the four frequencies available (3 GHz, T1, and 37 GHz, T4) to compare the average thermal emission at different depths within the lunar regolith at midnight (centimetres range for T4, 0.81 cm wavelength, to several meters T1, 10 cm wavelength). The penetration depth mainly depends on wavelength but also on the bulk density and loss tangent of the lunar regolith.

We subtracted T4 from T1 to focus on the subsurface temperature variations with a surface resolution of around 6 km/px (TB_{diff}, Fig. 1A). One of the advantages of using a subtractive technique is the sharpening of boundary definition by a bucking effect: the subtraction minimizes the absolute value error caused by the calibration issues in some degree since the errors are found to be systematic at each channel [7].

Results. Copernicus crater has been the subject of many dedicated studies, even a proposed Apollo landing site. The diverse morphology of its rim (slumped southern terraces and ejecta apron, see Fig. 1-B in [8]). has been mostly attributed to a low-angle impact from the south-east.

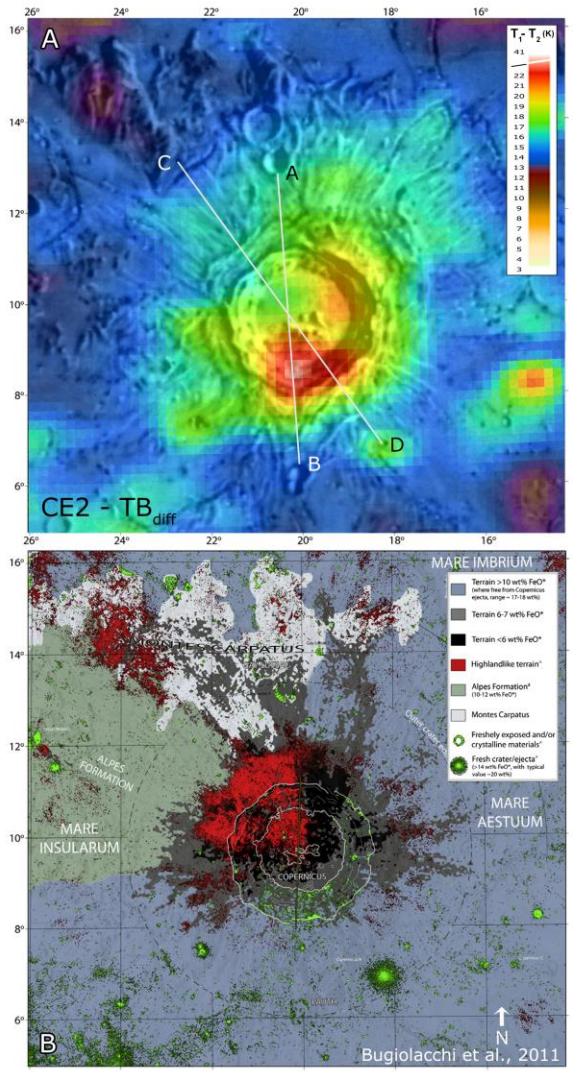

Figure 1. **A**] TB_{diff} in the Copernicus crater region superimposed on a shaded relief map [13]; **B**] Geological map highlighting FeO (wt%) variations and fresh materials (strong NIR absorption features) [8].

The interior of large Copernican craters appears as microwave "hot spots" during daytime and "cold spots" during night time [9]. [10] proposed that the abundance of rocks in the interior would influence the diurnal change of MW and IR thermal emissions; these

could be correlated with the age of the impact and used as a diagnostic tool.

The TB_{diff} map reveals that unlike other large young crates in the region (e.g., Aristarchus), Copernicus' MW emissions are anisothermal along its rim and interior (Fig. 1-A). The distribution is highly asymmetrical with very low values across the location of the "A wedge" [11] and high values (~40 K) around the southern rim.

The highest brightness temperatures differences within the crater floor (Fig. 2) match the surface roughness morphology, described as 'hummocky' (Ccfh) in geological maps [12] and in contrast with the 'smooth' wedge (Ccfs). Thus, as a preliminary conclusion, it appears that the surface's physical properties such as roughness and rockiness to be the leading factors influencing the microwave signature from the subsurface.

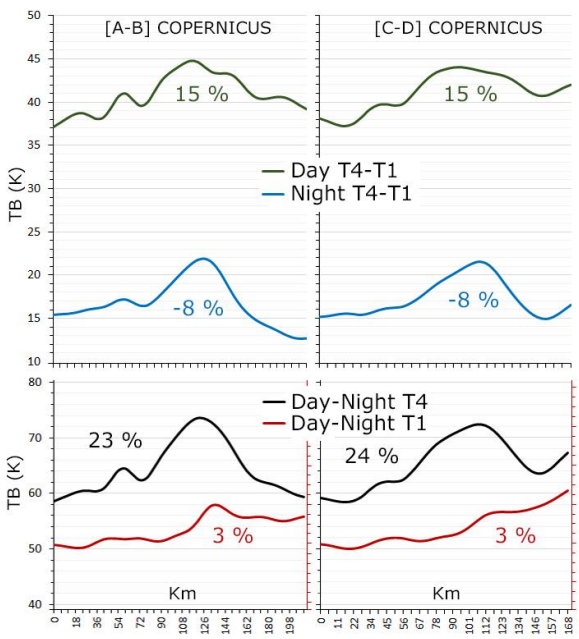

Figure 2. Alternative TB comparisons for the cross-sections A-B and C-D as from Fig. 1. Top graphs represent the differences in temperature between the two channels T1 and T4 at daytime (green) and midnight (blue). Average differences values are expressed as percentages. Lower graphs show TB differences between the same channels during daytime and night.

Fig. 2 shows how daytime and night time temperatures derivations vary according to the chosen frequency channel. The surface layer is on average ~15% hotter than the immediate subsurface, an indication of the low thermal conductivity of the regolith materials. During the night this gap halves (~8%). Day and night differences between the same channels again show much larger swings in temperatures between channel T4 (~24%) than T1, which remains relatively constant in temperature (~3%).

Discussion: [11] propose that the north-western segment ("red spot") be due to the higher silicic content of the ejecta. [8] had also noted FeO (wt%) variances in the Copernicus quadrant with values ranging from very low values (<6%, 'red and black') in the northern half of the edifice and nearby ejecta to 'mare background' levels in the south (>10%), Fig. 1-B.

Further, the spectral data reveal a local presence in the southern rim of materials exhibiting a strong 1 µm absorption feature, usually diagnostic of less weathered or even fresh mafic materials. This could originate from an enhanced fragmentation of the wall materials due to mechanical properties of the local rocks and steeper slopes and/or their relative higher mafic content. The TB_{diff} data, therefore, support the hypothesis that the impactor might have hit a heterogeneous target region, exhuming different ejecta materials.

Thus, the reason for the anisothermal TB_{diff} values around the crater rim might be due to both *morphological* differences brought about by an enhanced gravitationally-led slumping rate in the southern part of the rim, creating a larger population of fractured rocks, and *compositional*, due to its relatively higher mafic content against the silicic north-western 'wedge'.

Conclusions: This work represents just a preliminary look at the high-quality microwave data produced by the MRM instruments. Together with a qualitative analysis of spatial distribution of TB differences, progress is being made to extract quantitative data relating to several physical parameters, including ilmenite content, rocks distribution, and craters age estimation.

References:

[1] Keihm S. J. and Langseth M. G. (1975) *Science*, 187, 64-66.
[2] Zheng Y. C. et al. (2012) *Icarus*, 219, 194-210.
[3] *NAO, CAS*, accessed Feb 29, 2016. //moon.bao.ac.cn/ceweb/datasrv/dmsce1.jsp.
[4] McMahon S. K. (1996) *P& SS*, 44, 3-12.
[5] Chan K. L. et al. (2010) *Earth and Planet. Sci. Lett.*, 295, 1-2, 287-291.
[6] Wang Z. Z. et al. (2010) *Science China: Earth sciences*. 53, 1392-1406.
[7] Hu G. et al. (2017) *Icarus*, 294, 72-80.
[8] Bugiolacchi et al., (2011) *Icarus*, 213, 43-63.
[9] Zheng Y-C et al., (2018) *Icarus*, 319, 627-644.
[10] Gong, X, Y-Q Jin (2013) *Acta Astr.*, 86, 237-246
[11] Shkuratov Y. et al. (2016) *Icarus*, 272, 125-139.
[12] Schmitt H.H. et al. (1967) US Geol. Surv. Misc. I-515 (LAC-58).
[13] U.S. Geol. Survey, I-2769.

DISK-INTEGRATED LUNAR BRIGHTNESS TEMPERATURES AT INFRARED (6 - 12 µm) AND MM-WAVELENGTHS (1.6 - 3.4 mm). M. J. Burgdorf[1] and T. G. Müller[2]
[1]Universität Hamburg, Meteorological Institute, Bundesstraße 55, 20146 Hamburg, Germany (martin.burgdorf@uni-hamburg.de)
[2]Max-Planck-Institut für extraterrestrische Physik, 85748 Garching, Germany (tmueller@mpe.mpg.de)

Measurements of the disk-integrated brightness temperature T_B of the Moon at 89, 157, 183, and 190 GHz are presented for phase angles between -80° and 50° relative to full Moon. They were obtained with the Microwave Humidity Sounder (MHS) on NOAA-18, a meteorological satellite on a polar orbit. 39 instances of the Moon appearing in the deep space view of this instrument were identified and analyzed. The main uncertainty in the calculation of the lunar T_B is the beam size of the different channels. We determined it from the width of the "light" curves of the Moon intrusions and achieved this way a higher accuracy than the tests on ground. Polynomials were then fitted to the measured T_B as a function of phase angle and the maximum temperature in each channel and the phase angle of its occurrence were determined. A comparison of these results with the predictions from three different models or parametrical expressions, [1–3], revealed significantly larger phase lags for the lower frequencies in the data from MHS (see Figure 1). This result is very robust given the fact that it requires MHS only to identify the largest flux in a series of measurements. As the Moon has appeared hundreds of times in the field of view of MHS and other microwave sounders, this investigation demonstrates the potential of weather satellites for identifying even small flaws in models of the radiance of the Moon.

A similar investigation, but using less Moon intrusions in the deep space view, was carried out with data from HIRS/4 (High-resolution InfraRed Sounder), which is aboard the same satellites as MHS. The fluxes in various thermal infrared channels were measured for several phase angles and compared to a thermophysical model of the Moon based on [4–9] (see Figure 2). Again, a photometric accuracy of a few percent could be achieved for most channels.

This work was supported by FIDUCEO, which has received funding from the European Union's Horizon 2020 Programme for Research and Innovation under Grant Agreement no. 638822.

The research leading to these results has received funding from the European Union's Horizon 2020 Research and Innovation Programme, under Grant Agreement no 687378, as part of the project "Small Bodies Near and Far" (SBNAF).

References: [1] Keihm S. J. (1984) *Icarus, 60,* 568-589. [2] Mo T. & Kigawa S. (2007) *JGR Atmospheres, 112,* D20. [3] Yang H. et al. (2018) *TGRS, 56,* 6723-6733. [4] Müller T. & Lagerros J. (1998) *A&A*, *338*, 340-356. [5] Rozitis B. & Green S. (2011) *MNRAS*, *415*, 2042-2062. [6] Hayne P. et al. (2017) *JGRE*, *122*, 2371-2400. [7] Racca G. (1995) *P&SS, 43,* 835-842. [8] Muninonen K. et al. (2010) *Icarus*, *209*, 542-555. [9] Grant M. (2008) *Applied Optics, 47*, 4981-4993.

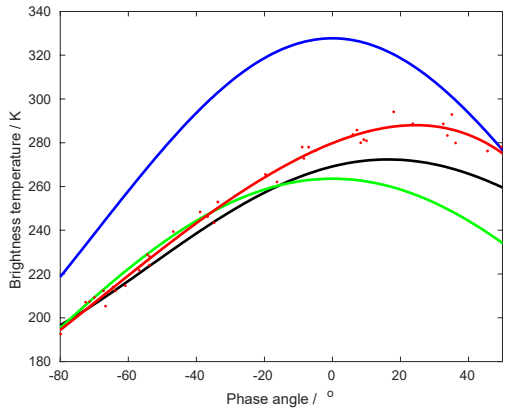

Figure 1: Disk-integrated brightness temperature of the Moon for different phase angles relative to full Moon at 89 GHz. The measurements with MHS on NOAA-18 are shown as red dots and were fitted with the red line. The other lines represent different models: [1] is black, [2] is blue, and [3] is green. None of the models reproduces the measured difference in brightness temperature between waxing and waning Moon exactly.

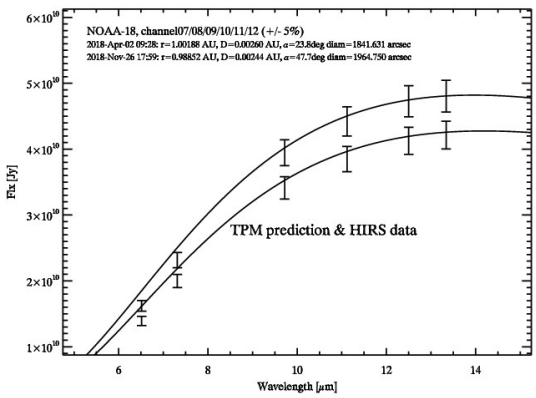

Figure 2: Disk-integrated flux of the Moon in six channels of HIRS/4 on NOAA-18 for two different phase angles α. The predictions of the thermophysical model are given as solid lines.

PRECISION COUNTING OF VERY SMALL CRATERS AT LUNAR LANDING SITES.

P. H Cadogan, Elville House, 126 The Park, Cheltenham Glos UK GL50 2RQ. peter.cadogan@zen.co.uk

Introduction: Automated processing of LROC NAC images of the lunar maria can yield precise measurements of craters down to 3 metres in diameter. Matching craters across multiple images and the use of templates improves precision and enables false positives and false negatives to be identified. The results for a number of lunar landing and impact sites reveal significant and unexpected differences across the lunar near side. At many sites, crater distributions are best explained by a combination of a steady state population up to about 45m plus much old craters larger than 45m. In Oceanus Procellarum (Apollo 12) there are four times as many such larger craters than there are in Mare Tranquillitatis (Apollo 11 and Ranger 8). Other sites are more complex, some indicating the presence of secondaries.

Crater fitting: The methods employed for this work have previously been briefly described [1], [2]. For each site, the largest area that is common in four favourably illuminated images is selected and only those craters that are matched in at least two images are counted. This enables false negatives to be included. Automatically generated templates are used to optimise fits and only the highest resolution (ie 0.5m/pixel) images are normally used. Calibrated and projected images are required to ensure optimal pixel values and perfect alignment.

Low contrast limit. Craters are assigned to one of 5 freshness classes, based on the contrast between its highlight and shadow. Total crater counts can be very sensitive to the specified low limit for the vaguest craters, which is based on the distribution of grey levels in the image. The low albedo Apollo 17 site is an extreme case in this respect. However, SFD slopes are barely affected by the limit used, but setting it too low can result in false positives.

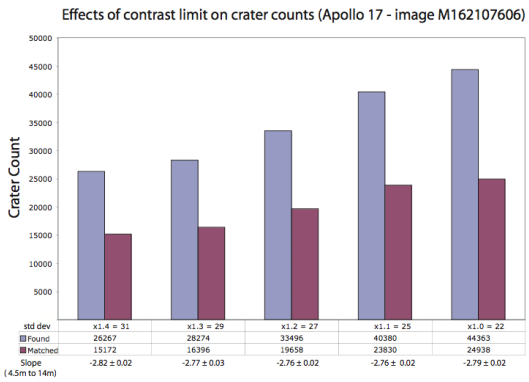

Fit quality. After fitting a rim, crater centre and diameter are adjusted to minimise the deviation from the appropriate template. Very few diameters need to be adjusted by more than 2 pixels. After matching craters in other images, deviations from the mean diameter are less than 3 pixels for 95% of craters.

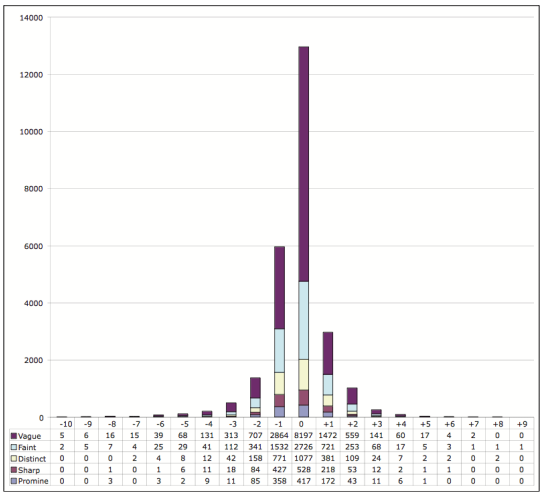

Diameter changes after template adjustment

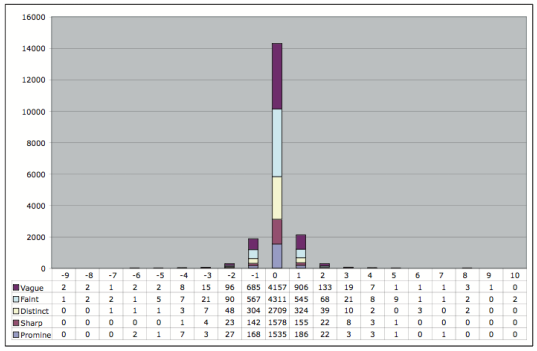

Diameter vs mean diameter

Matching quality. In practice, >90% of craters are matched in at least two images. Of the 856 craters larger than 18m in an Apollo 15 benchmark test [3], 848 (ie 99%) were matched in this work.

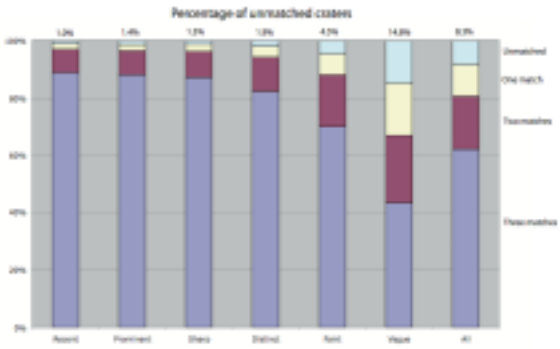

Plot showing % matched craters by freshness class

Size Frequency Distributions: The SFD plot is the most appropriate format to present the high crater

counts at very small diameters. Counts between 4.5m and 13m at the Apollo 11 site define a steep fit line with a slope of –4.34 ± 0.09. When this plot is extrapolated to 40m, there are few points above it.

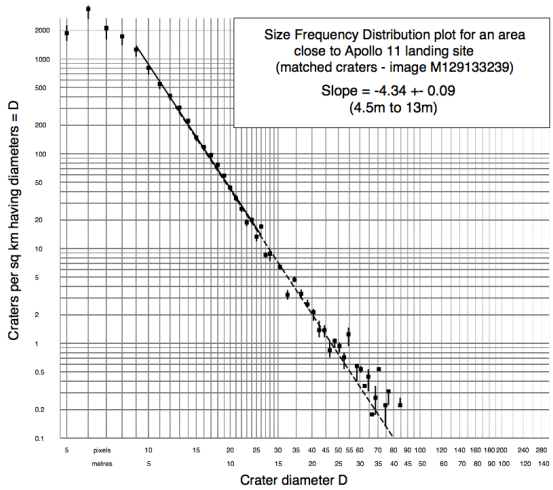

By contrast, the SFD for the Lunokhod 1 site is shallower, with a slope of –3.73 ± 0.08 betweem 3m and 13m, and a significant excess of larger craters.

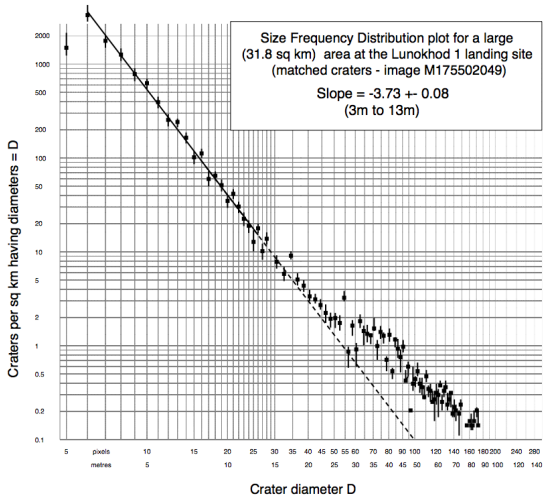

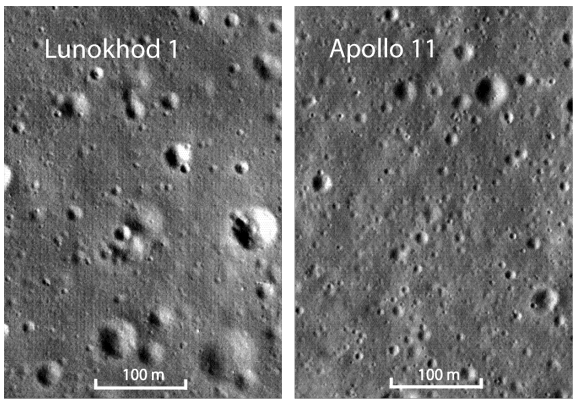

Below 13m diameter, crater counts are considered to be in a steady state, so some explanation is needed to account for the different slopes. A visual comparison of small areas at each site at the same image scale is sufficient to visualise the differences. Steep initial slopes are also found at the Ranger 6, Ranger 8 and Surveyor 5 sites in Mare Tranquillitatis.

Cumulative Size Frequency Distributions: At larger diameters, when crater counts are low, it is more appropriate to use cumulative size frequency distribution (CSFD) plots, enabling the diameter range to be extended up to 150m.

The CSFD for the Lunokhod 2 landing site at Le Monnier crater, on the borders of Mare Serenitatis, reveals that below 13m diameter, the plot is linear, but with a shallower slope than in the SFD (in this case –2.95 ± 0.04). Above 65m the curve steepens, reaching –3.0 at about 95m (solid red line), as would be expected for a mare of medium age [4].

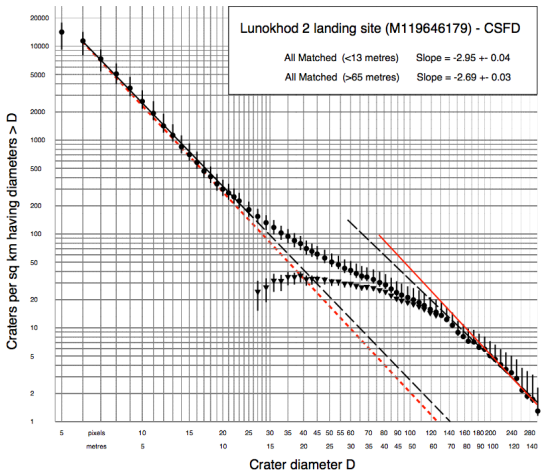

If the 3m-15m range is in a steady state, the extrapolated equilibrium count above 15m can be subtracted from the measured values to yield an excess cumulative value. The resulting excess counts (shown by inverted triangles) are essentially constant up to about 45m (at about 30 craters per sq km), implying that ALL craters smaller than this must belong to the equilibrium population. In fact, because cumulative counts below 15m include counts for sizes > 45m, the equilibrium line must be slightly shallower (red dotted line), which explains why the excess dips down towards 15m.

Not all sites conform to this model and SFDs indicate that there are some craters smaller than 45m that are NOT in equilibrium. At the Apollo 13 S-IV-B impact site, for example, there is good evidence for the presence, in the intermediate size range, of secondary craters from the nearby young crater Landsberg B. The deficiency of craters > 45m in Mare Tranquillitatis, and the almost total lack of such excess craters at the Luna 16 site in Mare Fecunditatis remain to be explained.

References: Cadogan P. H. (2017) *Abstract ELS5* [2] Cadogan P. H. (2018) *Abstract* ELS6 [3] Robbins S. J et al. (2014) *Icarus* 234 109-131 Moore H. J et al. (1980) *Moon & Planets* 23, 231-252

THE UNUSUAL ATLAS/HERCULES REGION OF THE MOON. J.T.S. Cahill[1], P. Hayne[2], S. Liu[3], G.W. Patterson[1], and B. Greenhagen[2], [1]Johns Hopkins University Applied Physics Laboratory, Laurel, MD (Joshua.Cahill@jhuapl.edu), [2]University of Colorado, Boulder, CO, and the [3]Lunar and Planetary Institute.

Introduction: Additional enigmatic deposits have emerged since the Lunar Reconnaissance Orbiter (LRO) entered orbit that contrast with the lunar regolith at large. Unlike optical anomalies, such as swirls, this new class of deposits are unusual for their thermophysical characteristics. One ubiquitous class consists of lunar cold-spot craters, so named because they are characterized with extensive regions, relative to their cavity diameter and depth, of anomalously cold temperatures in nighttime Diviner data [2]. These extensive cold regions are not easily explained by conventional impact mechanics. Hayne et al., [1] further characterized these ejecta features with high H-parameter values suggesting their thermophysical properties are consistent with a 'fluffed up' regolith in the upper 10 to 30 cm created by some aspect of the impact process.

However, also reported by Hayne et al., [1] were cold spots associated with pyroclastics as well as the thermophysically unique Atlas crater region (~45N, ~45E). With thermophysical similarities to cold-spot regoliths initially it seems to fit the definition of a cold-spot. But, the Atlas region is without similar geomorphological characteristics and bears dramatic differences in spatial scale. The 'Atlas thermophysical anomaly' also consists of high H-parameter values relative to its surroundings, similar to lunar cold-spots, and suggests it consists of finer regolith materials, with higher porosities, and with lower thermal inertias than typical regolith. But, unlike typical cold-spots, the mechanism for formation is even less clear.

Objectives: The Atlas region may provide a unique insight into how the lunar regolith is being mechanically and chemically weathered that contrasts with cold-spots in general. For example, unlike Atlas, cold-spots are not typically observed in radar wavelengths. Here we focus our investigation on the physical properties of the Atlas region and how they may or may not be synergistic with its thermophysical properties with increasing depth. And we do this with a combination of monostatic and bistatic observations at multiple wavelengths of the region. We also begin to postulate potential formation mechanisms of this region relative to lunar cold-spots and radar-dark halo craters (e.g., new craters, pyroclastic deposits, etc.). Questions we aim to answer include: How does this mechanism that formed the Atlas thermophysical anomaly contrast with that of typical cold spots and radar dark halo craters? Does its signature manifest Why don't all radar dark halo craters form thermal anomalies similar to the Atlas region?

Methods: Most of the initial study of this region starts with the analysis of LRO Mini-RF monostatic S-band (12.6 cm) and Earth-based Arecibo Observatory-Greenbank Observatory (AO/GO) bistatic P-band (70.3 cm) observations. The contrast in physical sensitivity between circular polarization ratio of these two data sets is very informative regarding surface and subsurface scatterer sizes and depth.

We are also utilizing Arecibo-Mini-RF bistatic observations which are more targeted towards boundaries of the thermophysical region. Collecting bistatic radar data involves AO and/or DSS-13 illuminating the lunar surface at S-band (12.6 cm) or X-band (4.2 cm) wavelength, respectively, with a circularly polarized, chirped signal and tracking the Mini-RF antenna boresight intercept on the surface of the Moon. Transmitted pulses from AO and/or DSS-13 are 100 to 400 μs in length and the Mini-RF receiver operates continuously, separately receiving the horizontal and vertical polarization components of the signal backscattered from the lunar surface. The resolution of the data is ~100 m in range and ~2.5 m in azimuth but can vary from observation to observation, as a function of the viewing geometry. For analysis, the data are averaged in azimuth to provide a spatial resolution of 100 m.

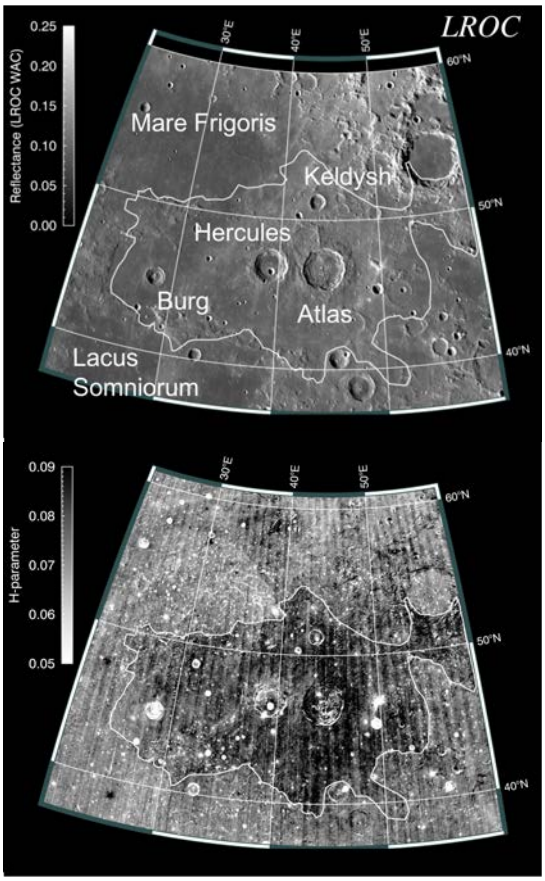

***Figure 1**: The Atlas crater region in LROC WAC monochrome and Diviner derived H-parameter maps (color bar inverted) of Hayne et al., [1].*

This yields an ~40-look average for each sampled location in an observation and an average $1/N^{1/2}$ uncertainty in the backscattered signal of ±16%. In theory, this should also enable a modest improvement in along track resolution, but processing for that effort has not yet been attempted.

Discussion of Other Observations: In radar wavelengths, 12.6 and 70 cm, the Atlas region shows distinctive low backscatter characteristics far more consistent with radar-dark halo craters than lunar cold-spots (Figure 2) [1, 3]. In fact, multiple radar-dark halo craters are apparent including Burg, Atlas, and Hercules. These backscatter properties are consistent with lunar regolith devoid of scatterers (boulders, fractures, and other corner reflectors) to at least ~10 meter depths, significantly greater depths than suggested by Diviner. The peculiar aspect of this region is its thermophysical properties relative to other radar-dark halo craters. Unlike Atlas, most other radar-dark halo craters show no significant contrast in the Diviner H-parameter relative to their surroundings. This suggests something about this region is unique or differential to other radar-dark halo craters. However, there are a few exceptions which we will examine in further detail during this study. Hayne et al., [1] also noticed some interesting similarities with certain cold-spots associated with pyroclastic deposits, particularly Aristarchus, which we will also examine further.

References: [1] Hayne P.O. et al. (2017) Journal of Geophysical Research-Planets, 122, 2371-2400. [2] Bandfield J.L. et al. (2014) Icarus, 231, 221-231. [3] Ghent R.R. et al. (2005) Journal of Geophysical Research-Planets, 110, doi:10.1029/2004JE002366.

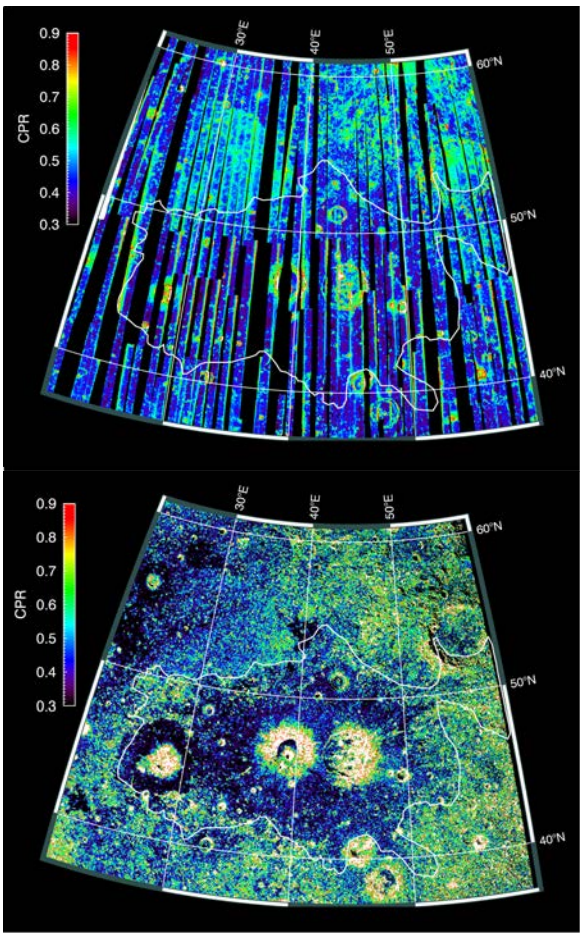

***Figure 2**: Circular polarization ratio observations of the Atlas crater region in (Left) Mini-RF 12.6 cm monostatic and (Right) P-band 70.3 cm bistatic configurations.*

SCRUTINIZING THE PRESENCE OF LAMP IDENTIFIED LUNAR SWIRLS RELATIVE TO MODELED MAGNETIC SOURCES. J.T.S. Cahill[1], A.A. Wirth[1,2], A.R. Hendrix[3], K.D. Retherford[4], B.W. Denevi[1], A.M. Stickle[1], D.M. Hurley[1], K.E. Mandt[1], Y. Liu[5], T.K. Greathouse[4], F. Vilas[3], and D.T. Blewett[1]. [1]JHU/APL (Joshua.Cahill@jhuapl.edu), [2]Case Western Reserve University, [3]Planetary Science Institute, [4]Southwestern Research Institute-San Antonio, and the [5]Lunar and Planetary Institute/USRA.

Introduction: The sinuous lunar surficial markings known as 'swirls' are amongst the most intriguing features on the surface of the Moon [1-3]. Several hypotheses for their formation exist and include 1) magnetic shielding from solar wind [6], 2) cometary or meteorite swarm scouring of the shallow regolith [7-9], or 3) electromagnetic charge induced levitation and sorting of lunar dust [10, 11].

Three initial examinations of swirls have been performed in the ultraviolet (UV) [1, 12, 13], each one examined progressively shorter wavelengths ranges. Denevi et al. [1] mapped swirls in the Lunar Reconnaissance Orbiter Camera (LROC) Wide Angle Camera (WAC) near-UV (NUV) images, observing that the most distinguishing characteristic of swirls in this wavelength region is a low 321/415 nm ratio coupled with moderate to high 415 nm reflectance. This methodology appears effective for differentiating swirls even within areas of high albedo. Denevi et al. [1] further note that some swirls cannot be discerned in the optical maturity index (OMAT) or band-depth images. Hendrix et al. [12] detailed examinations of the Reiner Gamma and Gerasimovich swirls using Lyman Alpha Mapping Project (LAMP) wavelengths >130 nm, noting swirls to be characterized by reddened FUV spectra. They also demonstrate that immature regolith becomes brighter (i.e., bluer) with exposure to space weathering. Finally, in a precursor to the work presented here, Cahill et al. [13], examined LAMP global Lyman-α (Ly-α) albedo (121.6 nm) maps and noted FUV evidence consisting of low albedo for swirls coincident with regions noted by Denevi et al. [1] as well as in previously undocumented areas.

In a previous report, Cahill et al. [14] leveraged the unique viewing geometry and wavelength range offered by LAMP nighttime observations to comprehensively map lunar swirls in the FUV (Fig. 1). Secondly, Cahill et al. [14] compared their observations with previous work in order to detail what can and cannot be observed in the FUV relative to the NUV, and vice versa. Here, we build upon this work comparing the results of Cahill et al. [14] with the recent modeling results of Wieczorek [4] mapping the proximity to the surface of plausible subsurface magnetic sources (Fig. 2). This is done in an effort to further scrutinize findings of plausible swirls only observed in the FUV by Cahill et al. [14].

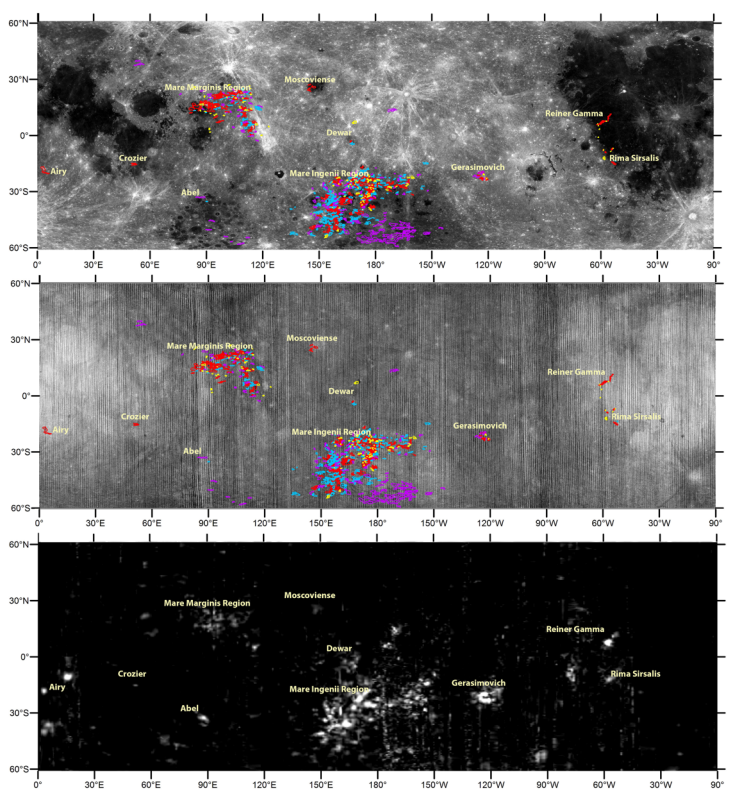

***Fig. 1**: (Top) WAC 415 nm, (middle) nighttime Ly-α , and (bottom) LP |B| (2-10 nT) [5]. (Red) Swirls observable independently by both FUV and NUV. (Light Blue) Swirls observed by FUV only. (Yellow) NUV identified [1] and confirmed in FUV. (Purple) Plausible LAMP-identified swirls near weak magnetic anomalies.*

Data Sets: LAMP continues to provide insights into the upper ~100 nm of the regolith. LAMP is a FUV (57-196 nm) push-broom photon-counting imaging spectrograph [15]. LAMP has also routinely collected both day and nighttime data of both polar and equatorial regions of the Moon. Here, global nighttime Lyman-α (Ly-α; 121.6 nm) normal albedo data are examined for low-albedo features as they relate to the detection and mapping of lunar swirls (**Fig. 1**). This data set is unique in comparison to all other LRO data sets in that it collects reflected light from surfaces that are diffusely lit by solar Ly-α scattered off of interplanetary H atoms from all directions. The Ly-α skyglow intensity varies with respect to the motion of the solar system. Furthermore, point sources from

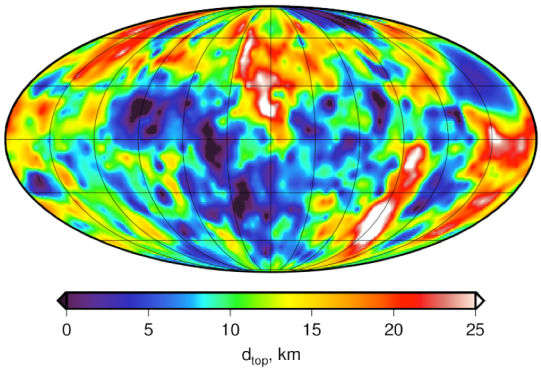

***Fig. 2**: Inversion results for ensembles of magnetized sills; depth to the top of the magnetized region [4].*

UV-bright stars are more plentiful in the southern hemisphere owing to the Galactic plane [15, 16]. As a result, the signal-to-noise ratio of the LAMP nighttime data varies with latitude, with longer wavelength star light signals increasing from north to south. Other instrument-derived maps analyzed include the LROC WAC color [17, 18] and Lunar Prospector (LP) fluxgate magnetometer [5] data. Finally, data products derived by Wieczorek [4] of the depth to the top and bottom of plausible magnetic sources (**Fig. 2**) are also examined.

Swirls… Low-Albedo?: Unlike the NUV and visible where lunar swirls are known to show high reflectance relative to their surroundings, in Ly-α they have low albedo due to changes in material optical properties below ~180 nm.

Mapping Methodology: LAMP global Ly-α albedo maps were surveyed by Cahill et al. [14] for low-albedo features with sinuous 'swirl-like' characteristics. During this process a WAC 415 nm reflectance mosaic was used for regional context. To maintain an initial independent LAMP assessment, this initial step was taken without referring to swirl boundary maps detailed by *Denevi et al.* [1] or LP magnetic anomaly maps [5]. Once low-albedo regions were identified in Ly-α, they were compared to LP magnetic anomaly maps as well as WAC color composite maps. This resulted in four classes of low-albedo features, shown in **Fig. 1**: 1) Independently verified, (in red; i.e., regions identified independently by both FUV and NUV surveys, respectively), 2) Ly-α identified (in light blue; i.e., only observed in the 121.6 nm band), 3) NUV identified/FUV confirmed (in yellow; i.e., swirls not initially noticed in the initial FUV survey, but documented by Denevi et al. [1] and subsequently confirmed in Ly-α), and 4) Plausible swirls (in purple; i.e., low-albedo features with an ambiguous morphology or setting and associated with weaker magnetic strength anomalies).

Discussion: Consistent with Denevi et al. [1], swirls are detected in LAMP Ly-α in the regions of Reiner Gamma, Mare Marginis, Rima Sirsalis, Crozier, Airy, Gerasimovich, Dewar, and South Pole-Aitken basin (**Fig. 1**). Swirls have previously been identified in all of these regions, however Ly-α often shows boundaries encompassing NUV and visible boundaries and often also show additional nearby sinuous low-albedo regions, swirls, not previously identified. That said, there are numerous areas with swirls that go initially unseen in Ly-α. Some of these (shown in yellow) are subsequently identified with additional NUV or magnetic data context, others are not. An analysis of these regions shows they have lower Ly-α albedo and higher magnetism values on average relative to their surroundings (**Fig. 2**). Swirl regions denoted by Denevi et al. [1] are consistent with these characteristics. Interestingly, low-albedo regions denoted as 'Plausible swirls' while showing similar average Ly-α values as swirls identified with high certainty, have lower values of total magnetic field strength (but higher magnetic field strength than 'off swirl' regional analyses).

References: [1] Denevi et al. (2016) Icarus, 10.1016/j.icarus.2016.01.017. [2] Blewett et al. (2011) JGR, 116, 1. [3] Kramer et al. (2011) JGR, 116, doi:10.1029/2010JE003729. [4] Wieczorek (2018) JGR, 10.1002/2017JE005418. [5] Purucker and Nicholas (2010) JGR, 115. [6] Hood and Schubert (1980) Science, 208, 49. [7] Starukhina and Shkuratov (2004) Icarus, 167, 136. [8] Schultz and Srnka (1980) Nature, 284, 22. [9] Syal and Schultz (2015) Icarus, 257, 194. [10] Pieters et al. (2014) LPSC, 45, 1408. [11] Garrick-Bethell et al. (2011) Icarus, 167, 136. [12] Hendrix et al. (2016) Icarus, 273, 68. [13] Cahill et al. (2016) LPSC, XXXXII. [14] Cahill et al. (2017) LPSC, 48, 2947. [15] Gladstone et al. (2012) JGR, 117, doi:10.1029/2011JE003913. [16] Pryor et al. (1992) AJ 394, 363. [17] Sato et al. (2014) JGR, 119, 1775. [18] Boyd et al. (2012), 43, 2795.

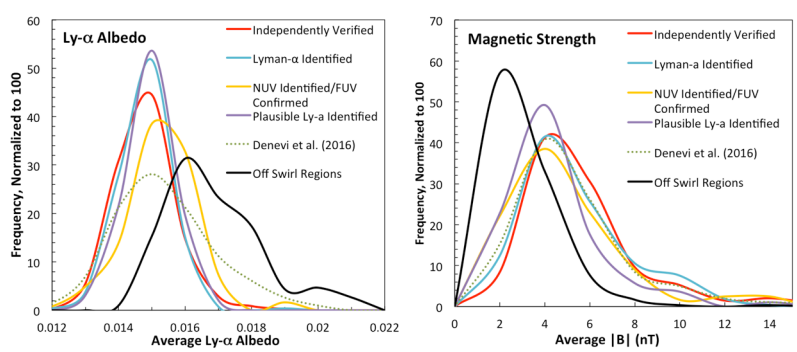

***Fig. 3**: Histograms of swirl characteristics detailing (Left) Ly-α, and (Right) total magnetism |B|. (Dotted) Study of Denevi et al. [1] mapped swirl regions. (Black) Regions nearby, but off swirl regions.*

LUNAR EXPLORATION IN ESA'S EUROPEAN EXPLORATION ENVELOPE PROGRAMME

J.D. Carpenter on behalf of the ESA team. ESA ESTEC, Keplerlaan 1, 2201 AG, Noordwijk, The Netherlands. (James.carpenter@esa.int)

The European Exploration Envelope Programme E3P is the European Space Agency's (ESA's) space exploration programme. The programme was initiated (Period 1) at ESA's Council at Ministerial Level in 2016 and includes activities in Low Earth Orbit, Moon and Mars. Lunar Activities in E3P Period 1 focussed on:

- Development of the European Service Module (ESM) for NASA's Orion vehicle [1],
- Contributions to the Russian Luna-27 mission
    - PROSPECT [2], to investigate the science and utilisation potential of lunar volatiles,
    - PILOT to provide soft precision landing and hazard avoidance capabilities
- Preparatory activities for the future including for the Lunar Gateway [3], future surface missions with international partners (e.g. HERACLES) [4], and missions to demonstrate the use of lunar resources [5].

In addition ESA has prepared a strategy for science at the Moon, a strategy for space resource utilisation and is preparing a strategy for technology. These startegies should be implemented through the future periods of the E3P programme.

Period 2 of E3P is now in preparation for decision at the next ESA Council at Ministerial Level (Space19+) in November of 2019. E3P Period 2 consists of four cornerstones. Low Earth Orbit, robotic exploration of Mars, obotic missions to the Moon and human missions beyond Low Earth Orbit.

The proposed activities at the Moon in Period 2 include:

- Commitment to deliver future ESMs,
- Development to flight of PROSPECT and PILOT
- Development of European contributions to the Gateway, a human tended outpost in lunar vicinity, and preparation of the first European science payloads for the platform.
- Delivery of the first ESA science and technology payloads to the lunar surface on Missions of Opportunity and preparation of payloads for future missions [6]
- Preparatory activities for the future utilisation of lunar resources including ground based research and the advancement of payloads for flight
- The advancement of new commercial partnerships and support for European commercial interests at the Moon
- Advancement of future ESA mission activities for implementation in coordination with international and commercial partners [7].

In the coming year ESA will be enaged in lunar exploration and preparing its future programme at the Moon, working with international partners, with industry and with the science community. The future scope of ESA's activites at the Moon will be decided by ESA's member states at the end of 2019.

References:

[1] https://www.esa.int/Our_Activities/Human_and_Robotic_Exploration/Orion/European_Service_Module

[2] http://exploration.esa.int/moon/59102-about-prospect/

[3] http://exploration.esa.int/moon/59374-overview/

[4] https://www.esa.int/Our_Activities/Human_and_Robotic_Exploration/Exploration/Landing_on_the_Moon_and_returning_home_Heracles

[5] http://exploration.esa.int/moon/60127-in-situ-resource-utilisation-demonstration-mission/

[6] http://exploration.esa.int/moon/60922-lunar-mission-campaign/

[7] http://www.esa.int/About_Us/Business_with_ESA/Business_Opportunities/Partners_for_Space_Exploration

LARGE IMPACT CRATERS: LINKING SPECTRAL COMPOSITION (M3) AND MORPHOLOGICAL FEATURES AT HIGH RESOLUTION (LRO). S. D. Chevrel[1,2], P. C. Pinet[1,2], Y. Daydou[1,2] , M. Loche[1,2], [1]Université de Toulouse; UPS-OMP; IRAP; Toulouse, France, [2]CNRS; IRAP; 14, avenue Edouard Belin, F-31400 Toulouse, France (serge.chevrel@irap.omp.eu).

Interest of impact craters: Impact craters are complex formations showing a great diversity of morphological features and compositions for their materials. In large impact craters deep-seated materials excavated and deposited during the cratering processes give information on the structure, formation and evolution of the lunar crust. However understanding the nature and the origin of the excavated materials is not easy because large volumes of the target have been melted throughout the cratering processes. During this process, melting occurs at different degrees and significant lithic fragments can be entrained by the impact melts. To add to the complexity, impact melts cool at different rates, resulting in materials within and around the crater presenting a range of textures from glassy ("pure melt") to coarse-grained crystalline (recrystallized melt). Therefore for crater materials spectral mineralogical features are more or less preserved, and, as a result, lunar impact melt spectra can show a complex behavior, being a function of both the composition of the target material and the conditions of melting and/or cooling history.

Objectives and data: In order to better interpret multispectral data and to understand cratering processes our objective is to link the compositional information to small scale morphological observations obtained at very high spatial resolution. Given the freshness of their morphological units and materials, the well-preserved Aristarchus and Copernicus craters are good candidates to link composition and morphological features. In addition these two craters give information on the composition of the lunar crust [e.g., 1, 2] which is not well exposed in the Procellarum KREEP Terranes (PKT). In this work spectral data are from the M3 instrument (Chandrayaan 1; 140 m/pixel; 540-3000 nm; 85 bands) and morphological images (up to 5 m/pixel) are from LROC (Lunar Reconnaissance Orbiter). Spectra of the Aristarchus and Copernicus M3 images have been fitted using Modified Gaussian Model (MGM) [3,4] based on model parameters (position, strength, and width of absorption bands) established for laboratory spectra of terrestrial pyroxenes and olivines and their combinations [5,6]. We point out: -i) that the MGM modeling currently used needs further adaptation to M3 lunar spectra and, -ii) that the spectral signature of the Fe-bearing glass is not presently considered.

Olivine bearing materials in Aristarchus and Copernicus: In previous works [5,6] units of large impact melt deposits of low albedo were found on the north-eastern terraced walls of Aristarchus, showing spectral anorthositic signatures mixed with pyroxenes (red and orange in figure 1). Within these units, LROC very high resolution images (0.5 m/pixel) show large ejected boulders (up to 100 m in size for some), most of them being embedded and mantled with dark melt deposits (see figure 4) [7]. Spectral signature may arise from these boulders and/or from partially crystallized melts [6].

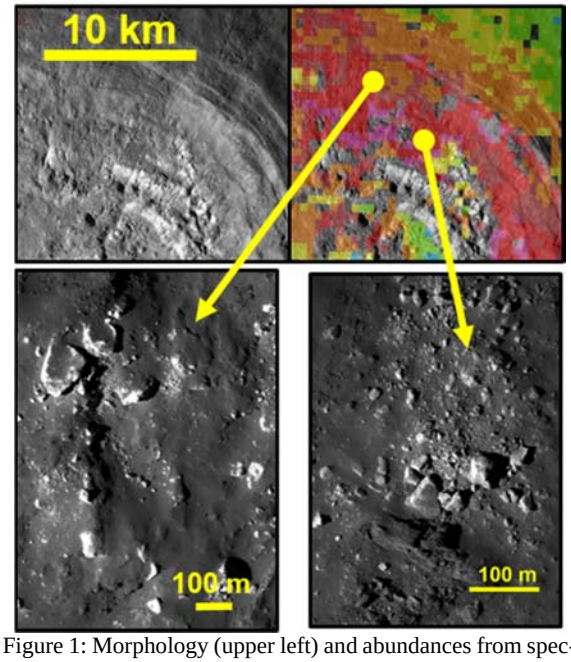

Figure 1: Morphology (upper left) and abundances from spectral data (upper right) of anorthositic rich material with pyroxenes (orange and red meaning high abundances) on the north-eastern rim of Aristarchus (see [4,5]). Detailed images (lower left and right) show ejected boulders and melt deposits (images from LROC NAC M120161915LE).

Olivine-rich bearing materials were found in previous studies in the southeastern part of Aristarchus (e.g. [1,2,8]. Through the MGM model we identified [10]. the most olivine-rich bearing materials forming a radial pattern, associated with low albedo impact melt in the ejecta on the walls (area A in fig. 2) in and outside the crater, in its southeast quadrangle (e.g., area A in fig. 2), and some places on the southern wall. From morphology the spectral signature of the olivine might predominantly be the result of the presence of significant lithic

fragments embedded in the melt [6]. It must be noted that due to scaling effects the proportion of clasts in the impact melt is expected to be higher on the Moon than on the Earth [10].

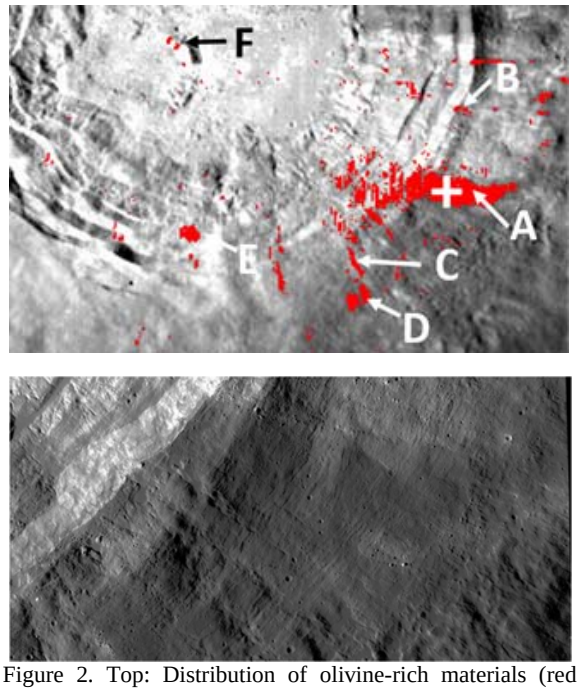

Figure 2. Top: Distribution of olivine-rich materials (red patches) in Aristarchus. Bottom: area correspond to patch noted A.

We also found olivine-rich bearing materials in the Copernicus crater within the central peaks and on the floor north-east of the peaks [11]. On the floor, some olivine-rich patches are clearly associated to mounds of impact melt showing boulders at the summit and/or at the bottom (figure 3).

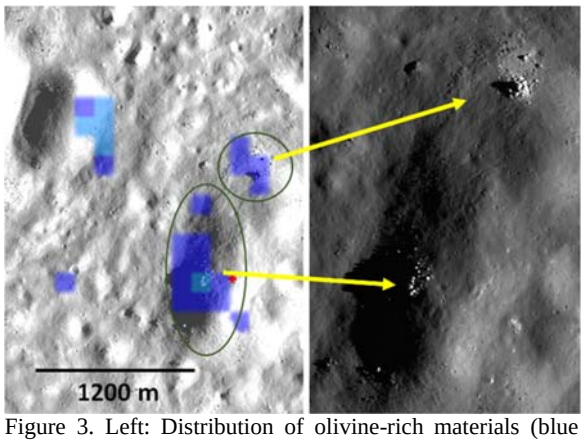

Figure 3. Left: Distribution of olivine-rich materials (blue patches) on the floor of Copernicus. Right: LRO image showing boulders about 10-20m in size.

However some olivine patches do not correspond to blocky areas, but to typical smooth impact melt material areas instead. Therefore the occurrence of olivine-rich materials in Aristarchus and Copernicus are associated with different types of morphologies, either areas of melt materials presenting boulders or melt materials only (or presenting rock fragments). This demonstrates the complexity of craters materials and the difficulty in establishing spectral and morphological links.

At some point it will be required to conduct in situ detailed investigations (analysis and sampling) of large craters to better understand the nature, the texture, the morphology at small scale and the distribution of the materials having undergone various degrees of melting , transport and deposition. However the future in situ investigations of crater interior and ejecta by automated and/or humans mean appear to be very challenging because the accessibility and the navigation across the impact structures present major difficulties [5,6,12]. Linking spectral composition and morphology is also important to prepare traverses of automated rovers for rock analysis and samples return (e.g. Heracles ESA mission).

References:
[1] Mustard J. F. et al. (2011), *J. Geophys. Res., 116*, E00G12; [2] Chevrel S. D. et al. (2009) *Icarus, 199*, 9-24; [3] Clénet et al (2011), *Icarus, 213*, 404-422; [4] Sunshine J.M. et al. (1990) *J. Geophys. Res., 95, B5*, 6955-6966; [5] Chevrel S. D. et al (2015), abstract, Moon 2020-2030, ESA; [6] Chevrel S. D. et al. (2016), abstract, European Lunar Symposium 4th; [7] Zanetti M. et al. (2011), *LPSC 42nd*, Abstract#2262.; [8] Le Mouélic, S. et al., (1999), *Geophys. Res. Lett., 26*, 1195-1198 ; [9] Chevrel S.D. et al. (2017), abstract #1907, LPSC 48th; [10] Cintala M.J. and Grieve R.A.F. (1994) *Geol. Soc. of Amer. In Large meteorite impacts and planetary evolution, ed. Dressler B ;* [11] Pinet P.C. et al. (2018), abstract #1899, LPSC 49th. [12] Chevrel S.D. et al. (2019), abstract #2393, LPSC 50th.

FAULT SLIP MOVEMENT ALONG WRINKLE RIDGE-LOBATE SCARP TRANSITIONS IN THE LAST 100 MA. J. D. Clark[1], C. H. van der Bogert[2], H. Hiesinger[2], T. R. Watters[3], and M. S. Robinson[1], [1] School of Earth and Space Exploration, Arizona State University, Tempe, AZ, USA, [2] Institut für Planetologie, Westfälische Wilhelms-Universität, Münster, Germany, [3]Center for Earth and Planetary Studies, National Air and Space Museum, Smithsonian Institution, Washington, DC, USA, (jclark@ser.asu.edu)

Introduction: The lunar surface is covered with tectonic landforms (e.g., graben, lobate scarps, wrinkle ridges) without the presence of Earth-like plate tectonics. Both lobate scarps and wrinkle ridges are the result of compressional stresses, however, their appearance and formation mechanisms are different [1-5]. Typically, lobate scarps are only a few kilometers in length and have few large superposed craters [1, 6-9]. Found mainly in the anorthositic highlands, the faults that created the scarps are thought to offset only the upper kilometer of the lunar crust [9-11]. Derived model ages place the lobate scarps at <700 Ma with many less than 100 Ma, making them some of the youngest endogenic landforms on the Moon [6-10]. Wrinkle ridges on the other hand are interpreted to be blind thrust faults, where horizontal shortening is accommodated by a fault that does not reach the surface. Wrinkle ridges formed in the maria 0.1-0.65 Ga after basalt emplacement due to basin subsidence [12-16]. The faults that created the wrinkle ridges are suggested to extend to depths between 100's of meters to several kilometers [12,13,17].

Typically, lobate scarps and wrinkle ridges are not thought of as being colocated. However, after global mapping of wrinkle ridges [18] and lobate scarps [10], it was revealed that there are at least nine cases where a lobate scarp transitions into a wrinkle ridge at a highland-mare boundary [5,19-21]. The scarp-ridge transition on the western edge of Mare Serenitatis [20] was the first to be examined using crater size-frequency distribution (CSFD) measurements to derive absolute model ages (AMAs) in determing the timing of potential seismically-induced resurfacing [22]. After applying both traditional CSFD and Buffered Crater Counting (BCC) methods [23, 24], it was estimated that the lobate scarp and wrinkle ridge were active in the last ~50 Ma [22]. In this study, we investigated relatively young fault activity using multiple CSFD methods along a ridge-scarp transition on the eastern rim of Mare Serenitatis (Fig. 1).

Data and Methods: NAC (Narrow Angle Camera) image data from the Lunar Reconnaissance Orbiter Camera (LROC) were processed using the Integrated Software for Imagers and Spectrometers (ISIS) [25,26]. In ArcGIS, count areas and CSFD measurements were generated using CraterTools [27]. The CSFDs were plotted and fitted in Craterstats [28], using techniques described in [23]. The derived AMAs use the production and chronology functions [29], valid for craters >10 m and <100 km in diameter.

Similar to [22], we implemented two methods to determine AMAs for each of the tectonic landforms. First, a count area was defined on relatively flat (<10º) portions of the lobate scarp and wrinkle ridge. Because the lobate scarp traverses a steep portion of the highlands, the scarp face itself is horizontal and thus optimal for CSFD measurements [e.g., 7]. Second, the BCC technique was implimented since both landforms have craters (>10 m in diameter) that superpose their fault traces. The BCC technique allows for the determination of ages of linear features independently from the surrounding geologic units [24]. Conventional crater counting includes all craters whose centers are inside the measurement areas, whereas the BCC technique only includes craters that superpose the linear feature. A buffer is calculated from the diameter from each included crater [30].

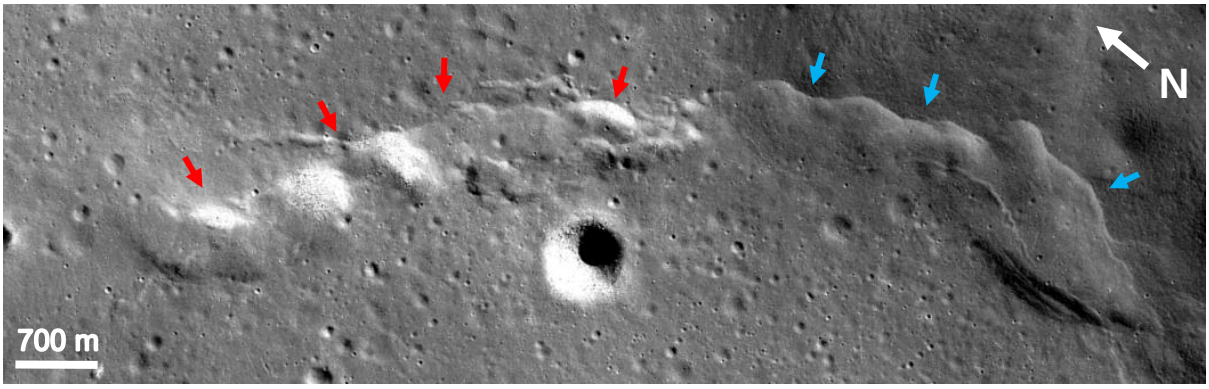

Figure 1: *LROC NAC (M192768045) showing the wrinkle ridge-lobate scarp transition (21.7°N, 28.9°E) on the eastern side of Mare Serenitatis. The wrinkle ridge (red arrows) exhibits high albedo boulders along the ridge highs and scarp faces similar to what was observed on the ridge-scarp transition on the western side of Mare Serenitatis [20,22]. The uphill-facing lobate scarp is marked with blue arrows.*

A comparision study between traditional CSFD measurements and the BCC technique on lobate scarps found that both methods produced similar results in most cases [7]. Using both age dating methods can help validate the derived AMAs for the tectonic landforms if similar ages are determined between the two methods.

Results and Discussion: The CSFD measurements determined AMAs of ~26 Ma for the lobate scarp and ~65 Ma for the wrinkle ridge (Fig. 2). The BCC method yielded ages of <25 Ma for both the scarp and ridge, an age which may represent the last measurable movement of slip on the faults [e.g.,7]. However, it should be noted that the steep slopes flanking the scarp and ridge could be affected by gravity-driven mass wasting processes that erase small impact craters postdating fault movement, leading to underestimated ages with the BCC method [7].

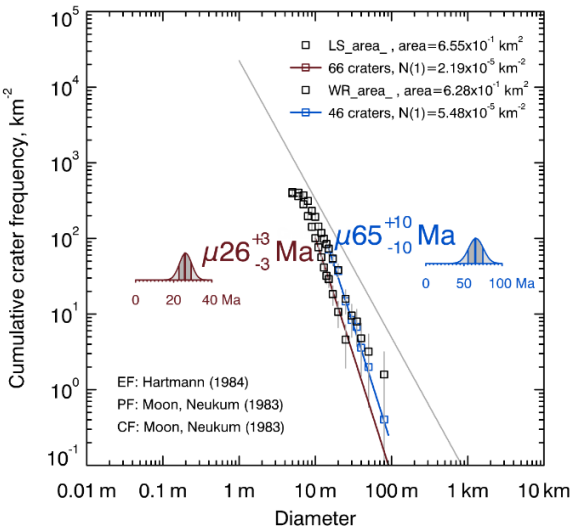

Figure 2: *AMAs determined for the lobate scarp (LS) and wrinkle ridge (WR) of the east Mare Serenitatis transition.*

The young AMAs suggest seismic slip on both the wrinkle ridge and lobate scarp thrust faults within the last 65 Ma. Although wrinkle ridges are generally thought to have formed 3.5 -2.4 Ga age [16], continued crustal strain generated by late-stage global contraction seems to be expressed as recent activitiy on both lobate scarps and wrinkle ridges [31-33].

Located on the highest topographic expressions of the East Serenitatis scarp-ridge transisiton are high albedo blocks (Fig. 3), which are suggested to indicate active geologic processes occurring on the wrinkle ridges [31,34, 35]. Typically, meter-sized wide blocks only survive for <1 Ga, and therefore could not have survived since the initial formation of the wrinkle ridges [36]. High albedo blocks were also discovered on the West Serenitatis wrinkle ridge previously investigated by [22] and other ridges mapped by [32].

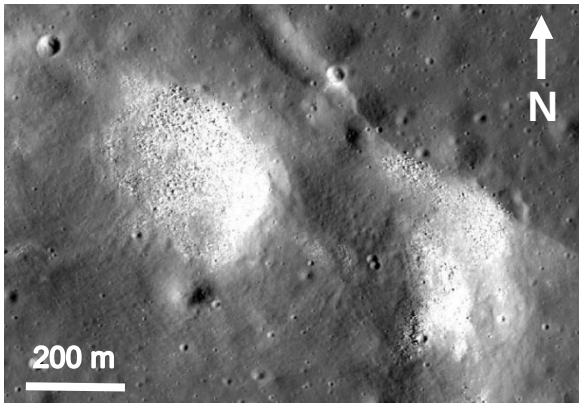

Figure 3: *Boulder outcrops on the wrinkle ridge are characterized by high albedo patches with meters to 10s of meters wide boulders (see also 31-33).*

For the other scarp-ridge transistion cases on the Moon, we find that most include blocky material at the summits of the wrinkle ridges.

Conclusions: Recent lunar tectonic activity can be documented not only at lobate scarps, but also along wrinkle ridges, indicating that late-stage global contraction is not limited to the lunar highlands.

References: [1] Watters and Schultz (2010) Planetary Tectonics, Cambridge Univ. Press. [2] Schultz (1976) Moon Morphology, University of Texas Press, Austin, TX. [3] Binder (1982) Earth, Moon, and Planets, 26, 117-133. [4] Watters and Johnson (2010) Planetary Tectonics, Cambridge Univ. Press. [5] Watters et al. (2010) Science, 329, 936-940. [6] Binder and Gunga (1985) Icarus 63, 421. [7] van der Bogert et al. (2018) Icarus 306, 225-242. [8] Clark et al. (2015) LPSC XLVI, 1730. [9] Clark et al. (2016) LPSC XLVII, 1380. [10] Watters et al. (2015) Geol-ogy 43, 10. [11] Williams et al. (2013) JGR-Planets, 118. [12] Schultz (2000) JGR, 105, E5. [13] Solomon and Head (1979) JGR, 84. [14] Solomon and Head (1980) Rev. Geophys. Space Phys., 18, 1. [15] Plescia and Golombek (1986) GSA Bull., 97. [16] Yue et al. (2017) LPSC XLVIII, 1926. [17] Watters (1993) JGR-Planets, 98. [18] Thompson et al. (2017) LPSC XLVIII, Abstract #2665. [19] Howard and Muehlberger (1973) Apollo PSR SP-330, NASA SP-330. [20] Lucchitta (1976) LPS 7, 2761-2782. [21] Watters (1988) JGR 93, 10236. [22] Clark et al. (2017) LPSC XLVIII, 1001. [23] Neukum (1983) Meteoritenbombardement und Datierung planetarer Oberflächen, Habil. Thesis, Univ. Munich. [24] Fassett and Head (2008) Icarus, 195, 61-89. [25] Robinson et al. (2010) Space Sci. Rev. 150, 55. [26] Anderson et al. (2004) LPSC XXXV, 2039. [27] Kneissl et al. (2011) PSS 59, 1243-1254. [28] Michael and Neukum (2010) EPSL 294, 223. [29] Neukum et al. (2001) Space Sci. Rev. 96, 55. [30] Kneissl et al. (2015) Icarus, 250, 384-394. [31] Valentinas and Kinch (2017) LPSC XLVIII, 2190. [32] Valentinas and Schultz (2018) LPSC XLIX, 2385. [33] Williams et al. (2013) LPSC XLIV, 2949. [34] French et al. (2014) LPSC XLV, 2489. [35] Williams et al. (2019) New Views of Tectonism in Mare Frigoris, submitted to Icarus, 2019. [36] Basilevsky et al. (2013) PSS 89, 118-125.

NASA'S LUNAR DISCOIVERY AND EXPLORARTION PROGRAM. S. W. Clarke[1], D. B. J. Bussey[1], J. E. Jenkins[1], [1]NASA Science Mission Directorate, NASA HQ, 300 E St SW Washington D.C. 20546 (steven.w.clarke@nasa.gov)

Introduction: The Lunar Discovery and Exploration Program, within NASA's Science Mission Directorate, is responsible for several lunar-related activities. These include

- Commercial Lunar Payload Services (CLPS)
- Instruments to fly on CLPS missions
- Instrument Development
- Lunar Reconnaissance Orbiter
- Lunar SmallSats
- Future medium-class landers and rovers

Commercial Lunar Payload Services (CLPS): NASA is looking to jumpstart the U.S. commercial lunar lander services industry. In November 2018, NASA selected nine providers for the CLPS catalogue. These companies all have plans to launch small landers to the lunar surface, selling available payload space. NASA will be one of the early customers for these companies. The nine CLPS providers are:

- Astrobotic Technology Inc.
- Deep Space Systems
- Draper
- Firefly Aeronautics Inc.
- Intuitive Machines, LLC
- Lockheed Martin Space
- Masten Space Systems Inc.
- Moon Express
- Orbit Beyond

NASA is intending to release the first delivery Task Orders in 2019, with the goal of flying as soon as the landing service providers are ready.'

Instruments to fly on CLPS Landers: NASA recently put out two calls for ready (or near-ready) to fly instruments to fly on early CLPS missions.

NASA Provided Lunar Payloads (NPLP). The NASA Provided Lunar Payload call supports ready-to-fly and the completion of near ready-to-fly science and technology payloads. In February 2019 NASA announced the first 12 NPLP selections. The selected payloads include a wide selection of scientific instruments. The Linear Energy Transfer Spectrometer will measure the lunar surface radiation environment. There are three resource prospecting instruments that have been selected to fly. The Near-Infrared Volatile Spectrometer System is an imaging spectrometer that can measure surface composition. The Neutron Spectrometer System and Advanced Neutron Measurements at the Lunar Surface are neutron spectrometers that will measure hydrogen abundance. The Prospecting for Exploration, Commercial Exploitation, and Transportation instrument is an ion-trap mass spectrometer that will measure volatile contents in the surface and exosphere. A magnetometer will measure the surface magnetic field. NASA has also selected the Low-frequency Radio Observations from the Near Side Lunar Surface instrument, a radio science instrument that will measure the photoelectron sheath density near the surface.

Three instruments will acquire critical information during entry, descent, and landing on the lunar surface which will inform the design of the next human lunar lander. The Stereo Cameras for Lunar Plume-Surface Studies will image the interaction between the lander engine plume as it hits the lunar surface. The Surface and Exosphere Alterations by Landers payload will monitor how the landing affects the lunar exosphere, and the Navigation Doppler Lidar for Precise Velocity and Range Sensing payload will make precise velocity and ranging information during the descent.

There are two exciting technology demonstrations that are selected to fly. The Solar Cell Demonstration Platform for Enabling Long-Term Lunar Surface Power will demonstrate advanced solar arrays for longer mission duration, and the Lunar Node 1 Navigation Demonstrator will demonstrate a navigational beacon to assist with geolocation for lunar orbiting spacecraft and future landers.

Lunar Surface Instrument and Technology Payloads (LSITP): LSITP was a call to the external (non-NASA) science, technology and exploration communities for potential payloads to fly on early CLPS missions. The final proposals were received on February 27 2019, with selections expected by the summer of 2019.

Instrument Development. It is the goal of LDEP to have a healthy supply of instruments ready to fly with the CLPS providers. Whilst the initial NPLP and LSITP calls focused on near ready-to-fly payloads, the goal is to have a mechanism to take ideas with low Technical Readiness Levels (TRL) and provide a pathway to propose these ideas for flight. Instrument development programs include The Development and Advancement of Lunar Instrumentation (DALI) call is a lunar instrument development program with the purpose of maturing the instrument development to TRL-6.

Lunar Reconnaissance Orbiter (LRO): LRO has been in orbit around the Moon for almost a decade, and continues to acquire key new data sets. In

addition to conducting scientific discovery, LRO will be used, where possible, to help the CLPS providers with landing site reconnaissance.

Small Satellites: The Small Innovative Missions for Planetary Exploration (SIMPLEX) is a call for small innovative planetary exploration missions. Any lunar missions that are selected will be managed under LDEP.

Medium Class Landers and Rovers: It is also in the LDEP portfolio to study the options for flying medium class (~500 Kg payload) landers and potential accompanying rovers. An example for such a mission could be a polar prospecting mission.

CONSTRAINING SOLAR SYSTEM BOMBARDMENT USING SAMPLES AND IN SITU RADIOMETRIC DATING. B. A. Cohen, NASA Goddard Space Flight Center, 8800 Greenbelt Rd. Greenbelt MD 20771 USA (barbara.a.cohen@nasa.gov)

Introduction: Our knowledge of absolute surface ages on other bodies, including Mars, Mercury, asteroids, and outer planet satellites, relies primarily on the crater calibration record for the Moon. Surface ages record two fundamental planetary processes: differentiation and volcanism via internal heating, and impact cratering. Despite the ubiquity of these processes, little headway has been made in creating a common framework of absolute ages for these events across the Solar System, including the Late Heavy Bombardment, planetary volcanism, and windows of habitable environments on the Earth, Mars, and beyond.

The leading, but contentious, model for Solar System impact history includes a pronounced increase in large impact events between 4.1 and 3.9 Ga [1-4]. This cataclysm would have bombarded an Earth and Mars that had atmospheres, oceans, and continents, and may have influenced the course of biologic evolution. Dynamical models to explain such a phenomenon rearrange the architecture of our very Solar System and are invoked to explain the arrangement of exoplanets around other stars. Evidence for a cataclysm, and constraints on the rest of the solar system impact flux, come largely from geochronology of samples derived from multiple samples from the Moon and asteroids.

Constraints from Apollo and Luna samples: The older end of the flux curve is bounded by the large, nearside lunar basins. However, the relationships between samples collected by the Apollo missions and the Imbrium, Serenitatis, and Nectaris basins have been called into question by new research using samples and orbital data. Imbrium appears to be 3.92 ± 0.01 Ga, based on Apollo 12 and 14 KREEP-rich melt rocks [5-7]. At Apollo 17, where the mission objective was to sample and date the Serenitatis basin, new work has reinterpreted the Sculptured Hills deposits as having an Imbrium origin [8-10]. The aluminous Descartes breccias from Apollo 16, originally interpreted as Nectaris ejecta, are coeval with KREEP-rich melt rocks interpreted elsewhere as Imbrium ejecta [11]. These updated interpretations reopen the pre-Imbrian impact history to debate, which will only be solved by absolute chronology of samples definitively reset in lunar basins (e.g., SPA, Crisium, Nectaris, Orientale, Schrodinger).

Younger chronology is constrained by mare basalt flows and younger benchmark craters such as Copernicus, Tycho, Autolycus, and Aristillus [12]. Model ages of these craters generally agree with radiometric ages of the Apollo landing sites, but in some places can differ by a factor of 2-3, causing uncertainties in absolute age by up to 1 Gyr [13-15]. Newly-acquired U-Pb ages of samples from Aristillus are ~200 Myr younger than previously proposed ages and new Autolycus crater size-frequency distributions do not correspond to radiometric ages [16, 17]. Crater-density relationships imply that significantly older and younger basalts exist, expanding the active period of the Moon [13, 18]. Older basaltic clasts appear in lunar meteorites [19], but these lack known provenance. Volcanism may have continued much longer than previously thought in the form of Irregular Mare Patches (IMPs), which exhibit a paucity of superposed impact craters suggesting they are younger than 100 Ma, or have physical properties that don't support craters, and are instead billions of years old [20, 21]. Constraining the chronology of the post-basin era will require measuring radiometric ages of samples with well-established provenance, including young mare basalts and key stratigraphic craters.

Other Constraints: Lunar meteorites provide another source of information about impact history from locations potentially far removed from Imbrium. Although relatively few crystallization ages have been determined for impact melt rock clasts, their distribution is broadly similar to that inferred from the Apollo samples and crater density studies of the lunar surface, with the oldest apparent ages around ~4.2 Ga, a peak at ~3.7 Ga, and a declining number of ages to ~2.5 Ga [22-24]. As many of the feldspathic lunar meteorites are regolith breccias, the longer tail to younger ages in the meteorite clasts compared to the Apollo melt rocks may reflect smaller or more localized impact events than the basins sampled by the Apollo sites.

Impact ages are also derived from asteroidal meteorites [25-27]. H-chondrites show a prominent group of reported 40Ar-39Ar ages between ~3.5 and 4.0 Ga [26, 28]. Eucrites and howardites from the asteroid 4 Vesta have numerous impact-caused Ar ages between 3.4 and 4.1 Ga, with groups of reliable ages at ~3.5 and 3.8–4.0 Ga, and few such ages between 4.1 and 4.5 Ga, but which may not be readily related to the crater density history revealed by missions like Dawn [25, 29-31]. Mesosiderites commonly yield Ar ages of 3.8 to 4.1 Ga [25], although the very slow cooling experienced by these meteorites following disruption and re-accretion of their parent body complicates the interpretation of these data.

Absolute ages of Martian surface units are uncertain by as much as a factor of two on older surfaces [32] and disagreements can be an order of magnitude or more on younger, lightly-cratered

surfaces, limiting our ability to understand the timing or Martian evolutionary milestones [33, 34]. For example, we do not know whether the crucial Noachian-Hesperian boundary, where a warm, wet Mars became arid [35], occurred before, after or concurrent with the late heavy bombardment on the Moon and the oldest intact rocks on Earth, so Martian climate change cannot yet be put into the context of Solar System history.

Future work - In Situ Dating: Absolute ages are the primary driver for the largest flagship mission in the US Planetary Science Decadal Survey, Mars Sample Return, and for the highest-priority lunar mission, sample return from the South Pole-Aitken Basin. However, these missions are acknowledged to be large and costly. NASA documents specifically recommend developing in situ dating capabilities, specifically recommending maturing age dating to TRL 6 by 2020 and noting its potential use in Discovery, New Frontiers, and future Mars missions.

Multiple groups are developing dedicated in situ dating instruments [36-40]. These instruments are on track to demonstrate TRL 6 readiness by 2020 and will need to be selected in the 2020's and 2030's for competed and directed flight missions to relevant destinations where in situ precision (±100 Myr) can provide meaningful constraints on geologic history. The capability for in situ geochronology on the Moon will open up the ability for this crucial measurement to be accomplished at multiple locations aboard stationary landers or mobile rovers. Discovery mission concepts and directed mission payloads that would take advantage of in situ dating for the Moon and Mars have been considered, developed, and proposed [41-44].

Multiple landing sites on the Moon, Mars, and asteroids such as Ceres and Vesta exist where these questions may be answered, whereas returning samples from all these places would be a daunting order. Though some questions will require the precision of laboratory measurements, many more are addressable with an accurate, though perhaps less precise, in situ age. For example, even a single mission to a key basin, such as Crisium or Nectaris, would add an enormous amount of clarity to understanding the cataclysm. A single mission to an IMP would resolve the wide disparity in interpretations of their origin. But countless missions could benefit from in situ dating capabilities, because geochronology is a fundamental measurement for the Moon and other planets. To develop a common framework for absolute ages across the solar system, in situ geochronology instruments should become a common tool, along with our imaging and compositional tools, for landers and rovers on the Moon, Mars, asteroids, and beyond.

References: [1] Bottke, W.F. and M.D. Norman (2017) Annual Review of Earth and Planetary Sciences 45, 619-647. [2] Ryder, G. (1990) EOS 71, 313, 322-323. [3] Turner, G. and P.H. Cadogan (1975) Proc. Lunar Sci. Conf. 6th, 1509-1538. [4] Tera, F., et al. (1974) Earth Planet. Sci. Lett. 22, 1-21. [5] Liu, D., et al. (2012) Earth Planet. Sci. Lett. 319-320, 277-286. [6] Merle, R.E., et al. (2017) Met. Planet. Sci. 52, 842-858. [7] Snape, J.F., et al. (2016) Geochim. Cosmochim. Acta 174, 13-29. [8] Fassett, C.I., et al. (2012) J. Geophys. Res. 117. [9] Spudis, P.D., et al. (2011) J. Geophys. Res. 116. [10] Thiessen, F., et al. (2017) Met. Planet. Sci. 52, 584-611. [11] Norman, M.D., et al. (2010) Geochim. Cosmochim. Acta 74, 763-783. [12] Stöffler, D. and G. Ryder (2001) Space Sci. Rev. 96, 9-54. [13] Hiesinger, H., et al. (2012) J. Geophys. Res. Planets 117. [14] Robbins, S.J. (2014) Earth Planet. Sci. Lett. 403, 188-198. [15] Williams, J.-P., et al. (2014) Icarus 235, 23-36. [16] Grange, M.L., et al. (2013) J. Geophys. Res. Planets 118, 2180-2197. [17] Hiesinger, H., et al. (2016) Lunar Planet. Sci. Conf., 1879. [18] Morota, T., et al. (2011) Earth Planet. Sci. Lett. 302, 255-266. [19] Terada, K., et al. (2007) Nature 450, 849-52. [20] Qiao, L., et al. (2017) Met Planet Sci 53, 778-812. [21] Braden, S.E., et al. (2014) Nature Geoscience 7, 787. [22] Cohen, B.A., et al. (2005) Met. Planet. Sci. 40, 755-777. [23] Cohen, B.A., et al. (2000) Science 290, 1754-1756. [24] Joy, K.H. and T. Arai (2013) Astronomy & Geophysics 54, 4.28-4.32. [25] Bogard, D.D. (2011) Chemie der Erde 71, 207-226. [26] Swindle, T.D., et al. (2014) Geological Society, London, Special Publications 378, 333-347. [27] Jourdan, F. (2012) Australian Journal of Earth Sciences 59, 199-224. [28] Swindle, T.D., et al. (2009) Met. Planet. Sci. 44, 747-762. [29] Kennedy, T., et al. (2013) Geochim. Cosmochim. Acta 115, 162-182. [30] Cohen, B.A. (2013) Met Planet Sci 48, 771-785. [31] Marchi, S., et al. (2013) Nature Geoscience 6, 303-307. [32] Hartmann, W.K. and G. Neukum (2001) Space Sci. Rev. 96, 165-194. [33] Swindle, T.D., et al. (2004) Met. Planet Sci. 39, 5149. [34] Doran, P.T., et al. (2004) Earth Sci Rev 67, 313–337. [35] Bibring, J.P., et al. (2006) Science 312, 400-4. [36] Anderson, F.S., et al. (2015) Rapic Comm Mass Spect 29, 191-204. [37] Cohen, B.A., et al. (2014) Geost Geoanal Res 38, 421-439. [38] Devismes, D., et al. (2016) Geost Geoanal Res. DOI: 10.1111/ggr.12118. [39] Cho, Y., et al. (2016) Planet Space Sci 128, 14-29. [40] Cho, Y. and B.A. Cohen (2018) Lunar Planet. Sci. Conf., [41] Anderson, F.S., et al. (2015) Lunar Exploration Analysis Group, 2034. [42] Cohen, B.A., et al. (2018) Lunar Planet. Sci. Conf., [43] Plescia, J.B. (2012) Concepts and Approaches for Mars Exploration, 4159. [44] Ostrach, L.R., et al. (2015) Lunar Exploration Analysis Group.

Spaceship EAC – Progress on Current Activities for Lunar Construction and Oxygen Production ISRU

A. Cowley[1], L. Offermann[1], L. Turk[1], L. Thiebaut[1], M. Fateri[2], M. Sperl[2], [1] European Astronaut Centre EAC, European Space Agency, 51170 Köln, Germany, [2] Institut für Materialphysik im Weltraum, Deutsches Zentrum für Luft- und Raumfahrt, 51170 Köln, Germany.

Introduction:

Spaceship EAC is a multidisciplinary innovation-driven team based within the European Astronaut Centre which aims to develop and validate operational concepts and low-TRL-level technologies in support of lunar human exploration scenarios, as part of the ESA E3P/EXPERT (European Exploration Envelope Programme/Exploration Preparation, Research and Technology). In the past the team has focused on planetary fabrication approaches with ISRU, focusing on utilizing both direct microwave heating and indirect susceptor driven heating of regolith simulant in order to enable an additive manufacturing methodology using this material (following from the ESA General Studies Programme project concept proposed in 2013 [1]).

In the past year, the initiative has begun to investigate novel O_2 production, extraction and capture methodologies. Herein we present our progress and results on a range of these ongoing activities:

Direct and Hybrid Microwave Processing of Regolith – Development of a test setup (2.4 GHz, 300 – 900 W incident power) to demonstrate a methodology for rastering a microwave focal point in a cavity across a regolith simulant, as a precursor for realizing an additive manufacturing methodology. In addition, a similar technique can be used to realise a local hotspot for heating (fig. 2) with applications for volatile extraction and construction [2]. Hybrid heating using SiC susceptors are also under investigation.

Novel Oxygen Production Techniques – we are investigating distinct novel approaches to Oxygen production via processing of regolith simulant. It is known that Fluorine is a powerful extracting agent, whereby aqueous HF and F_2 can readily reduce many of the compounds present in regolith. Heretofore uninvestigated, we report on initial work on developing a PFC/SF_6 low-pressure plasma activated process for extracting O_2 from regolith. In addition, two electrolysis processes are being compared and evaluated for ISRU: one is performed in molten Calcium Chloride and the other is done in an aequeous NaOH solution. Both processes used industrially for the production of titanium and pure iron respectively.

Flexible Toolkit for Lunar Regolith Processing & Offgasing (FLOP) - All ISRU oxygen extraction processes have one thing in common: They produce a gas that contains O_2, H_2O, CO_2 or other oxygen-bearing compounds. But the purification and the gas treatment to yield in pure oxygen or water requires further steps. Therefore, a modular gas treatment toolkit is developed by matching gas separation and purification technologies with the output compositions from oxygen extraction processes and the input requirements of user technologies such as life support systems and liquid fuel engines.

In all our activities, concept/technology development and demonstration projects are coordinated with ESA centres and exploit synergies with EAC facilities as well as with the surrounding DLR campus, commercial partners and European research groups.

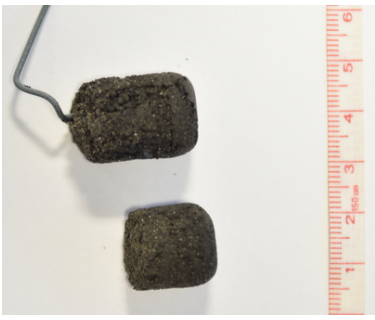

Fig. 1 *– Thermally sintered EAC-1 regolith simulant, produced under vacuum (10^{-3} mbar) at 1100 °C, 1 hour.*

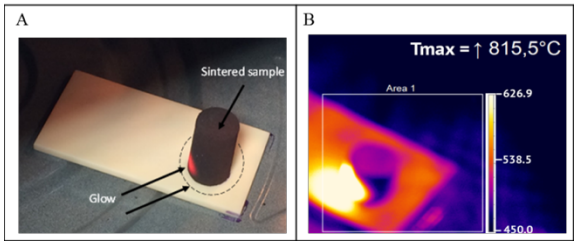

Fig. 2 *– Glow appearance at the sample's surface due to the microwave irradiation (A), thermal imagery of the sample exterior during heating (B) [2].*

References:

[1] ESA GSP study on Lunar Base 3D printing: http://www.esa.int/Our_Activities/Space_Engineering_Technology/Building_a_lunar_base_with_3D_printing

[2] *'Localised microwave thermal post-treatment of sintered samples of lunar simulant'* M. Fateri, A. Cowley, M. Kolbe, O. Garcia M. Sperl, S. Cristoforetti, Journal of Aerospace Engineering (forthcoming)

IMPLICATIONS OF AN EARLY LUNAR ATMOSPHERE. I.A. Crawford[1], D. Schulze-Makuch[2], M. Patel[3], J. Schirmack[2], L. Jentzsch[2] and M. Sylvest[3]. [1]Department of Earth and Planetary Sciences, Birkbeck College, University of London, UK (i.crawford@bbk.ac.uk), [2]Zentrum für Astronomie und Astrophysik, Technische Universität, Berlin, Germany, [3]School of Physical Sciences, Open University, Milton Keynes, UK.

Introduction: In an important paper, Needham and Kring [1] have argued that at the peak of lunar mare volcanism (~3.5 Ga ago) outgassing would have resulted in a transient (~70 Ma duration) atmosphere with a peak pressure of ~9 mbar. This is higher than the current atmospheric pressure on Mars (~6 mbar) and would have had a significant impact on lunar surface processes at that time.

Implications of a lunar atmosphere:

Stability of liquid water. A pressure of 9 mbar exceeds the triple-point pressure of water (6.1 mbar) so during this time pure water would have been stable at the lunar surface, albeit over a very restricted temperature range of ~6°C. Brines would have been stable over a wider temperature range, just as on Mars today. The extent to which water would have been outgassed by mare volcanism depends on the, still controversial water content of the mare basalt source regions. However, based on their survey of literature estimates, Needham and Kring [1] estimated a mass of ~10^{14} kg of outgassed water at the peak of mare volcanism, sufficient to cover the lunar surface to an average depth of ~3 mm. Even allowing for the small temperature range over which liquid water would have been stable, it seems likely that this would have facilitated the interaction of liquid water with igneous minerals in near-surface regolith leading to the formation of hydrated minerals. There is currently only very limited and controversial evidence for hydration in the existing sample collection (e.g. [2,3]), but additional searches appear worthwhile. The best places to look for evidence of liquid water interactions at the time of mare volcanism would probably be palaeoregoliths dating from that time, but now protected by burial under later lava flows or crater ejecta (for a discussion of lunar palaeoregolith deposits see [4]). Obtaining such samples will require renewed, targeted, sampling of the lunar surface, but ultimately may be the best way of testing Needham and Kring's hypothesis.

Attenuation of solar wind and galactic cosmic rays. The presence of an ~9 mbar atmosphere would prevent solar wind particles from impacting the lunar surface, and would attenuate the primary cosmic ray flux. Quantifying the magnitude of these effects will require further investigation, but it is possible that they might be identified in palaeoregoliths that were exposed at the lunar surface during this time.

Effect on micrometeorite flux. A significant lunar atmosphere would cause incoming micrometeorites to burn up before reaching the surface. This would presumably reduce the rate of regolith formation during this time and merits further study. Moreover, small meteorites that didn't burn up might be expected to develop fusion crusts. Joy et al. [5] have drawn attention to the lunar surface as an archive of meteoritic materials, and it would be worth searching this archive for meteoritic debris retaining evidence of atmospheric interactions.

Potential habitability. As discussed by Schulze-Makuch and Crawford [6], the possibility that liquid water was once stable on the lunar surface raises the intriguing question of a habitability window for the Moon ~3.5 Ga ago. Even if abiogenesis never occurred on the Moon, the possibility of inoculation by meteorites from the Earth [7] must be considered given the abundant evidence that Earth was inhabited by microorganisms at that time. Although at the extreme end of the spectrum of possibilities, finding evidence that life ever existed on the Moon would have multiple implications for astrobiology by (i) significantly expanding the known range of habitable environments; (ii) demonsting either that abiogenesis can occur in an environment similar to the lunar surface 3.5 Ga ago, or alternatively that life can be successfully transferred through space on meteorites; and (iii) informing planetary protection protocols. Given the importance of determining whether or not life could have persisted on the lunar surface 3.5 Ga ago, we are currently performing experiments in an environmental chamber to determine if microorganisms can grow and reproduce under the inferred conditions. Preliminary results will be presented. Experiments have shown that the lunar regolith is in principle able to preserve a range of organic materials [8] and palaeoregolith layers would again be the most likely locations for the preservation of possible biomarkers.

Conclusions: The suggestion that the early Moon may have had a transient atmosphere comparable to that of present-day Mars has far reaching implications for multiple aspects of lunar science and, more speculatively, for astrobiology. Proving this hypothesis, and assessing its implications, will likely require returning to the Moon to sample palaeoregolith deposits dating from that time.

References: [1] Needham, D.H. and Kring, D.A. (2017) *EPSL*, 478, 175–178. [2] Shearer, C.K. et al. (2014) *Geochim. Cosmochim. Acta*, 139, 411–433. [3] Joy, K.H. et al. (2015) *MAPS*, 50, 1157–1172. [4] Crawford, I.A. and Joy, K.H. (2014) *Phil. Trans. Roy. Soc.*, 372, 20130315. [5] Joy et al. (2016) *Earth, Moon & Planets*, 118, 133-158. [6] Schulze-Makuch, D. and Crawford, I.A. (2018) *Astrobiology*, 18, 985-988. [7] Armstrong, J. et al. (2002) *Icarus* 160, 183–196. [8] Matthewman, R. et al. (2015) *Astrobiology*, 15, 154–168.

IMPACT-MELT SAMPLE POPULATIONS IN APOLLO DRIVE-TUBE 68001/68002. N. M. Curran[1,2,3] (natalie.m.curran@nasa.gov) and B. A. Cohen[1], [1]NASA Goddard Space Flight Center; [2]NASA Postdoctoral Program, [3]Universities Space Research Association.

Introduction: The age and composition of lunar impact-melt samples, both returned to (Apollo and Luna, [1-3]) and found here on Earth (lunar meteorites [4-5]), have been used to address questions relating to the impact history of the Moon. Understanding the impact bombardment history of the Moon is a key scientific goal of the planetary science community [6] for determining the modification of the lunar crust, as well as understanding the evolution of the inner Solar System. However, the gardening process that occurs at the lunar surface plays a major role in distributing impact-melt samples throughout the regolith. Gardening of the regolith has resulted in many episodes of burial, exhumation and overall transportation of individual particles. For example, many older (e.g., >3.9 Ga) impact-melt rocks have experienced much longer periods of bombardment and gardening process, potentially making them volumetrically rare at the surface. The opposite may be true for the younger impact-melt rocks, particularly if the samples were collected near small, young craters. In some cases, the role of gardening is likely to have affected the preservation of impact-melt samples possibly biasing those collected at the surface. One way to test this theory and the role of gardening is to investigate the age and composition of impact-melt sample populations with depth.

Samples and techniques: The Apollo 16 double-drive tube 68001/68002 (Fig 1) provides an opportunity to evaluate individual impact-melt particles at various depths in the lunar regolith. The double-drive tube has been determined to have five distinct units based on composition and the soil maturity parameter I_s/FeO, as well as a small horizon which may be related to the South Ray impact crater [7]. The compositional differences between the five horizons suggest that each may potentially host different populations of impact-melts. We have separated 50-70 particles (250+ μm size fraction) from 6 sub-samples of 68001/2, one from each of the distinct units plus one from the near surface (0.5 g bulk soil each). Particles from each sub-sample were then classified based on texture using a Phenom desktop scanning electron microscope (SEM) at NASA Goddard Space Flight Center. Further classification to determine parent lithology was performed on minerals using electron microscope analysis (EMPA) at the Carnegie Institute of Science.

Although the EMPA data were useful, the mineral chemistry that makes up the analyzed impact-melts are extremely similar [8]. Groups of samples may have indistinguishable major- and minor-element compositions, but an improved recognition of compositional groups, to relate particles to parent lithologies, is better achieved using trace elements, such as Sc and Th [e.g., 9]. To achieve a more robust grouping of impact-melts we have taken several particles from various textural groups and sub-samples, and analyzed them for trace-element compositions.

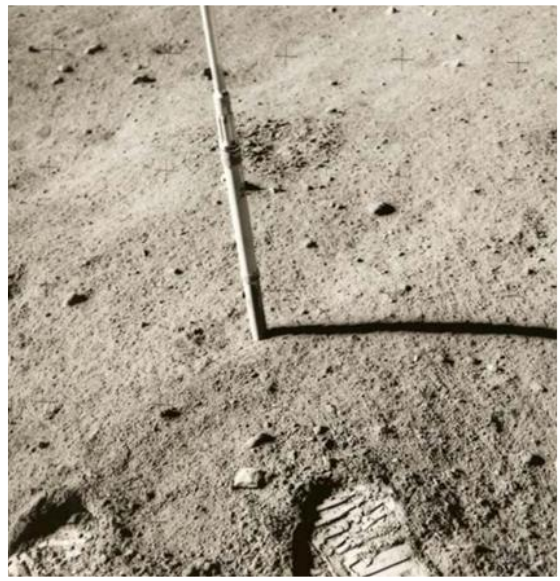

Fig 1: Surface photo for double drive tube 68001/68002 (NASA: AS16-108-17684).

Results and Discussion: 68001/2 contains a wide variation of texturally diverse impact-melt particles [e.g., 8] including both clast-rich and clast-poor, crystalline and devitrified glass. A number of regolith breccias and granulites were also found in addition to impact-melts.

Group 1 impact-melts are texturally heterogeneous including various types of clast-bearing and granulititc types, as well as minor poikilitic particles. Impact-melts show low Sm/Sc ratios, low incompatible trace-elements (ITEs) (Fig 2) and low Th content (Fig 3). Apollo 16 impact-melts have roughly been defined to lie on two trend lines, the 'eastern' and 'western' trends [9]. Particles from Group 1 tend to follow the eastern trend, although most of the particles fall out of the groupings made by [9] (Fig 2). It is possible that group 1 impact-melts have sampled the older feldspathic, KREEP-poor material of the Descartes Formation.

Group 2 impact-melts have a poikilitic texture and have been grouped based on concentration of Sm exceeding 15 ppm (similar to Group 1 of [9], Fig 2). Group 2 shows the highest Sm/Sc ratios of the particles analyzed in this study, which are KREEP-bearing (Fig 3) and have the highest ITEs. Group 2 follows the western trend of [9] and is thought that the impact-melts are formed from the younger KREEP-bearing material of the Cayley Plains.

Group 3 impact-melt are characterized by their lower Sm/Sc ratios and ITEs compared to Group 2. Group 3 is compositionally similar to the Apollo 16 regolith and are intermediate to Group 1 and Group 2 (Fig 2 and 3).

Conclusion and future work: The trace-element concentration are an effective tool for grouping particles to parent lithologies and potentially linking together material formed in the same impact event. Further samples will be analyzed to build up more information on each sub-sample of 68001/2 and the different impact-melt population contained within them. Our aim is to continue grouping particles according to parent lithology and conduct Ar-Ar dating on representative particles to determine the material that has been contributed to each horizon. Deciphering the chemical distinctions and determining the ages of these particles will provide an understanding of the effect that gardening has had on the regolith at the Apollo 16 landing site.

References: [1] Norman et al., (2006). GCA 70, 24: 6032-6049. [2] Norman and Nemchin. (2014). EPSL 388, 15: 387-398. [3] Fernandes et al., (2013). MAPS 48, 2: 241-269. [4] Cohen et al., (2000). Science 290, 1754. [5] Cohen et al., (2005). MAPS 40, 5: 755-777. [6] ational Research Council (2007). The Scientific Context for Exploration of the Moon, Final Report. [7] Korotev et al. (1997). GCA 61, 2989-3002. [3] Cohen et al. (2005). Met Planet Sci 40, 755-777. [8] Curran et al., (2018). 49th LPSC, abstract 2083. [9] Korotev, R.L. (1994). GCA 58, 3931. [10] Korotev et al., (2011). GCA 75, 1540-1573.

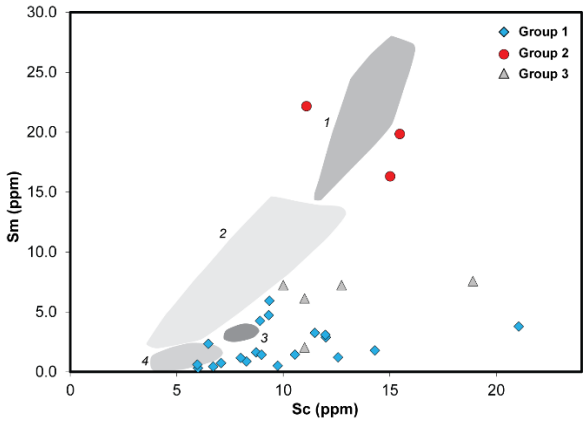

Fig 2: Sm verses Sc concentrations for impact-melts in Apollo 16 double drive-tube 68001/2. Fields represent impact-melt groups (1, 2, 3, and 4) from [9].

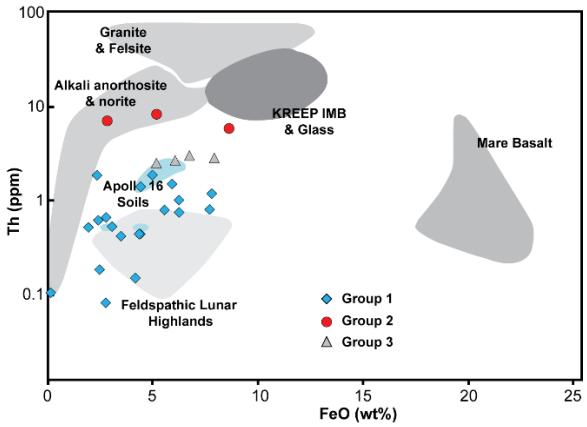

Fig 3: FeO verses Th content for impact-melts particles in 68001/2. Fields for different lithologies are taken from [10].

Towards Understanding the Role of Scattering in Thermal Transfer on the Moon using the Oxford Space Environment Goniometer. R. J. Curtis, T. J. Warren, K. L. Donaldson Hanna, N. E. Bowles[1], [1]Atmospheric, Oceanic and Planetary Physics, Parks Road, University of Oxford, OX1 3PU (rowan.curtis@trinity.ox.ac.uk).

Introduction: By comparing a thermal model of lunar surface temperatures to those measured by remote sensing (e.g. with the Diviner Lunar Radiometer Experiment), it is possible to constrain surface composition, roughness, emissivity, density, albedo, as well as subsurface (several meters deep) temperatures [1]. To validate such models, we are performing laboratory goniometry measurements using Apollo lunar regolith samples and regolith simulants. At the European Lunar Symposium, I will present the latest reflectance measurements from the Oxford Space Environment Goniometer (OSEG) and will show how these measurements can be used to improve the accuracy of both 1D and 3D thermal models.

Diviner: Diviner is an 8-channel thermal infrared (TIR) radiometer onboard NASA's Lunar Reconnaisance Orbiter (LRO). It has been in orbit since 2009 and now has global coverage of the lunar surface at multiple times of day (which is important for comparing the lunar data to 3D thermal models). Of the 8 channels, 2 are broadband solar, 3 are compositional and 4 are broadband thermal channels used for measuring the surface bolometric temperatures [2].

1D Thermophysical Modeling: To accurately model the lunar surface temperature, a thermal model must include an accurate scattering function. A 1D thermal model requires an accurate scatter function at the surface layer describing how visible albedo changes with incidence angle [1].

In the 1D Hayne thermal model the surface albedo is assumed to be non-Lambertian with incidence angle [3]. Equation 1 and Figure 1 show the typically used parameterization of the albedo scattering function in the Hayne and Vasavada models [3],[4]. The scattering function values 'a' and 'b' refer to the prefactors in Equation 1 [3]. The 'a' and 'b' values were tuned in the Hayne model as to best match the Diviner measurements and were not based on any laboratory scattering measurements, since at the time no albedo scattering measurements were available.

$$A = A_0 + a\left(\frac{\theta}{\pi/4}\right)^3 + b\left(\frac{\theta}{\pi/4}\right)^8 \qquad (1)$$

Where A is albedo, A_0 is the albedo at normal solar incidence, θ is solar incidence angle and 'a' and 'b' are scattering function inputs – typically assumed to be a = 0.06 and b = 0.25 in the Hayne model (but assumed to other values in different models [3], [4]). Figure 1 shows how varying 'a' and 'b' values affects albedo.

Figures 2 and 3 show how using accurate scattering functions are critical in modeling surface temperature profiles of high latitude areas on the lunar surface.

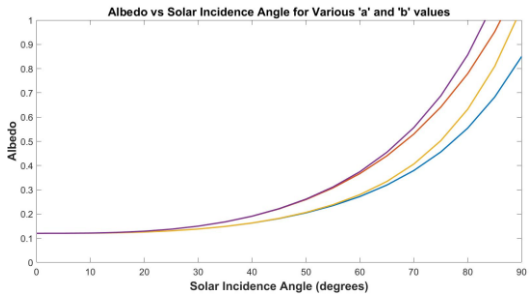

Figure 1: Showing how varying the scattering functions within the 1D Hayne model affects Albedo. Where the blue line is for a = 0.06, b = 0.25, yellow is for a = 0.1, b = 0.25, red is for a = 0.06, b = 0.45 and purple is for a = 0.1, b = 0.45.

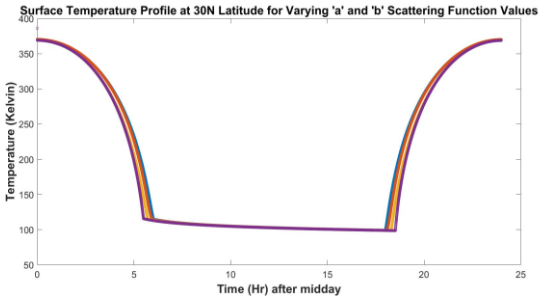

Figure 2: Showing how varying the scattering functions within the 1D Hayne model affects surface temperature profile at 30^0N latitude. Where the blue line is for a = 0.06, b = 0.25, yellow is for a = 0.1, b = 0.25, red is for a = 0.06, b = 0.45 and purple is for a = 0.1, b = 0.45.

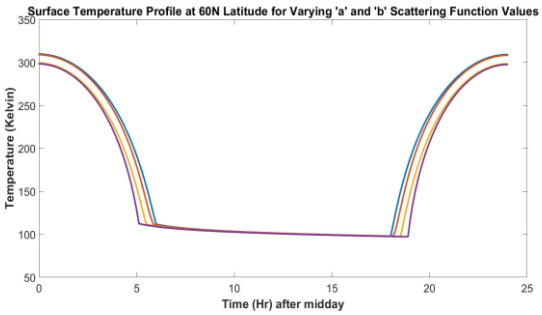

Figure 3: Showing how varying the scattering functions within the 1D Hayne model affects surface temperature profile at 60^0N latitude. Where the blue line is for a = 0.06, b = 0.25, yellow is for a = 0.1, b = 0.25, red is for a = 0.06, b = 0.45 and purple is for a = 0.1, b = 0.45.

3D Thermophysical Modeling: In equatorial regions (<70° lat), a 1D model is generally sufficient to model the surface temperature [5]. However, due to the Moon's relatively low obliquity ~1.53°, the illumination of the surface in the polar regions is permanently at low incidence angles (<70°) causing large shadows to be cast, and inside these shadows, the surface temperature is driven by scattered radiation from illuminated regions. A 3D thermal model (3DTM) with full ray tracing and a complete, accurate scattering function is therefore required to model these shadowed regions. Knowledge of how the surface of the Moon scatters visible and thermal radia-

tion for all viewing angles (i.e. incidence, emission and azimuth) is then required for 3DTMs [4].

For example, using a non-Lambertian TIR scattering function within a 3DTM for the Moon gives modelled temperature profiles which change by up to 15 Kelvin when compared with Lambertian temperature profiles and preliminary work shows a similar change in surface temperatures when including non-Lambertian visible scattering [4]. Understanding how scattering affects temperature puts constraints on the areas for which volatiles such as water ice can be identified in cold traps in the polar regions of the Moon [1].

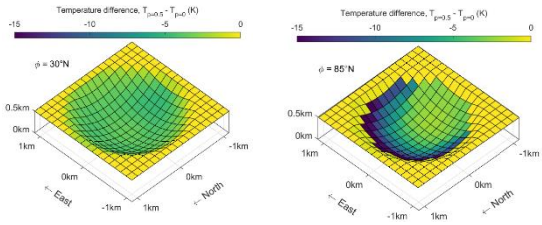

Figure 4: The surface temperature profile for a crater at (Left) 30^0N latitude and (Right) 85^0N latitude. This shows the difference in the surface temperature distribution when assuming Lambertian TIR scattering (i.e. cos(emission angle)) compared to $cos^{1.5}$(emission angle). The largest effect occurs at high latitudes where the illumination is more extreme due to topography. Errors of up to 15K are observed with a Lambertian assumption.

Goniometer measurements can further our understanding of such scattering effects and hence, we require new experimental data to validate thermophysical models [6].

Goniometer: The Oxford Space Environment Goniometer (OSEG) is a novel goniometer system inside a vacuum chamber specifically designed to measure how visible and infrared radiation is scattered from a particulate surface [7]. OSEG can take Bidirectional Reflectance Distribution Function (BRDF) and Directional Emissivity (DE) measurements for lunar regolith samples and regolith simulants across visible (0.4 - 0.7 µm) and thermal to far infrared wavelengths (5 – 400 µm) [7]. The BRDF is the function (often modeled by the Hapke BRDF model) which describes how visible and near infrared light is scattered from a surface [8]. It only defines how visible and near infrared light is scattered and does not describe how infrared is emitted from a surface. However, the DE describes how infrared light is emitted from a surface for all viewing angles [7]. OSEG is currently setup in visible BRDF measurement mode to measure Apollo lunar regolith and lunar regolith simulant samples across 0–70^0 reflection, 0–70^0 incidence, 0–360^0 azimuthal and down to 6^0 phase angles**.**

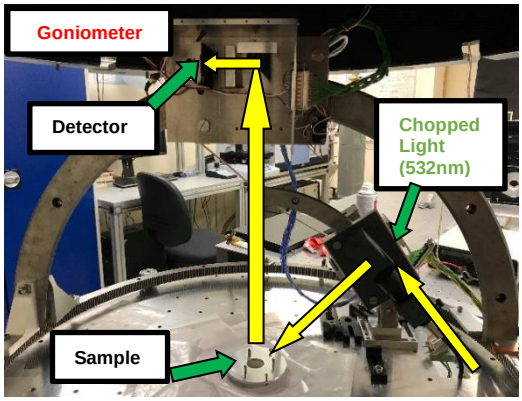

Figure 5: The Oxford Space Envirionment Goniometer (OSEG).

References: [1] Bandfield, J. L. et al. (2015) *Icarus*, vol. 248, pp. 357–372. [2] Warren, T. (2016) *LPSC XXXXVII.* [3] Paige, D. A. et al. (2010) *Science* (80-). [4] Vasavada, A. R. et al. (2012) *J. Geophys. Res. E Planets.* [5] Rozitis, B. and Green, S. F. (2011) *Mon. Not. R. Astron. Soc.* [6] Foote, E. et al. (2010) *AGU Fall Meet. Abstr.*, p. 1499-. [7] Warren, T. (2015) DPhil Thesis. [8] Hapke, B. (2011) *Cambridge University Press.*

SPACE PLASMA PHYSICS SCIENCE OPPORTUNITIES FOR THE DEEP SPACE GATEWAY.

I. Dandouras[1], R. A. Bamford[2], G. Branduardi-Raymont[3], D. Constantinescu[4], J. De Keyser[5], Y. Futaana[6], H. Lammer[7], F. Leblanc[8], A. Milillo[9], R. Nakamura[7], E. Roussos[10], M. G. G. T. Taylor[11], and J. Carpenter[11], [1]Institut de Recherche en Astrophysique et Planétologie, Université de Toulouse / CNRS / CNES, Toulouse, France (Iannis.Dandouras@irap.omp.eu), [2]Rutherford Appleton Laboratory, Chilton, UK, [3]Mullard Space Science Laboratory / UCL, Holmbury St Mary, UK, [4]Institute for Space Sciences, Bucharest, Romania, [5]Royal Belgian Institute for Space Aeronomy, Brussels, Belgium, [6]Swedish Institute of Space Physics, Kiruna, Sweden, [7]Space Research Institute / OEAW, Graz, Austria, [8]Laboratoire Atmosphères, Milieux, Observations Spatiales / IPSL, Paris, France, [9]Institute for Space Astrophysics and Planetology / INAF, Rome, Italy, [10]Max Planck Institute for Solar System Research, Göttingen, Germany, [11]ESTEC / ESA, Noordwijk, The Netherlands.

The Deep Space Gateway is a crewed platform that will be assembled and operated in the vicinity of the Moon by ESA and its international partners, and will offer new opportunities for fundamental and applied scientific research.

The Moon, during most part of its orbit around the Earth is directly exposed to the solar wind. Due to the absence of a substantial intrinsic magnetic field its vicinity is the ideal environment to study galactic cosmic rays (GCRs), solar wind and solar energetic particles (SEPs), and Jovian energetic electrons. This environment is typical of deep space. During 5–6 days every orbit, however, the Moon crosses the tail of the terrestrial magnetosphere. It is then exposed not to the solar wind but to the terrestrial magnetotail plasma environment, offering the possibility to study in-situ magnetotail dynamics and its dependence on solar and geomagnetic activity. It is then also very well situated to study atmospheric escape from the Earth into space, in the form of heavy ions upwelling from the terrestrial ionosphere and then transported and lost into the deep magnetotail. When the Moon gets again outside of the magnetotail, terrestrial magnetosphere dynamics can be monitored through remote sensing, using a variety of magnetospheric imaging techniques (ENA imaging, solar wind charge exchange X-rays, plasmasphere EUV imaging, or exosphere Lyman-α imaging). The lunar environment also offers a unique opportunity to study the Moon surface-bounded exosphere, its dynamics, its coupling with the surface and with space plasmas (solar wind and the terrestrial magnetotail plasma), and its escape into space. Such interactions are ongoing on all atmosphere-less bodies in the Solar System.

Space plasma physics measurements can be performed either from the Deep Space Gateway platform, or from instrumented cubesats released from the platform and placed into low-lunar orbits, or directly from the Moon surface. The Moon surface offers also exciting possibilities for studying energetic ion implantation in the lunar regolith, solar wind implantation or neutralisation and reflection from the regolith, solar wind interaction with crustal magnetic anomalies, lunar pick-up ion generation, or lunar surface electrostatic charging and dust levitation, just to mention few examples.

In preparation of the scientific payload of the Deep Space Gateway, we have formed a topical team to prepare and to support the definition of payload studies in the field of space plasma physics.

RUSSIAN LUNAR EXPLORATION STRATEGY AND CURRENT ACTIVITIES. M. I. Danilova[1] and Dr. G. F. Karabadzhak[2], FGUP TSNIImash, Pionerskaya st.4 Korolev Moscow region 141070, Russia ([1]danilovami@tsniimash.ru, [2] gfk@tsniimash.ru).

Introduction: According to the strategic documents for space activities of Russian Federation the main direction of prospective human flights missions after 2025 is the Moon. Some elements of Russian lunar program are planned in the actual Federal space program for 2016-2025, for instance robotic spacecraft, crew vehicle, and launch vehicles.

The roadmap of lunar exploration: The roadmap of lunar exploration includes four major phases.

The first one is preparative and based mainly on the first robotic spacecrafts, that will investigate the most interesting lunar landing sites and demonstrate a number of technolohies. During this phase development of Russian space transportation system for human and cargo delivery will be realized and critical technologies will be tested.

On the second phase the initial lunar communication and navigation systems will be deployed. The first Russian human mission on the lunar orbits will be lauched. The technology of automatic lunar regolith return to Earth will be tested.

The third phase is a construction of human lunar base on the Moon in its' minimal configuration and infrastructure development for components and resources manufacturing, scientific and experimental complexes development, manufacturing foundation for the purpose of permanently manned lunar base.

The fourth phase is a lunar base enlargement and closed-loop life-support system development, that will function with the use of lunar resources; organization of propellant components production and its' usage in Russian space transportation system, oxygen, water, metals, constructional materials recovery from lunar resources.

This roadmap is presenting a wide range of opportunities for moon exploration by virtue of robotic and human spacecrafts combination.

The importance of international partnerships: The many years of human and robotic space exploration shows that the most sustainable and cost effective way to explore space and to the greatest benefits to Earth, is to establish partnerships. Based on International Space Station experience, the future Lunar orbital platform – Gateway is now under discussion. In Russian lunar exploration strategy the lunar orbital platform is not the core element but it enables the opportunity to expand the program of scientific experiments to study the deep space environment, solar wind and others. Also in prospect the Gateway could become a hub for the deep space exploration (Mars and asteroids).

Collaborative design of payload for robotic spacecraft also brings powerful capabilities for international partnership.

Key technologies development: The roadmap of lunar exploration realization is considering the key technologies development. The task of the specification the key technology areas now is solving by the International Space Exploration Coordination Group (ISECG), in which Russia also participates. The status of this work is documented in ISECG's Global Exploration Roadmap (GER) [1]. According to this investigation we can place emphasis on the next key technology areas and its' subareas that are critical for the moon exploration:

- launch propulsion systems,
- space power and energy storage,
- robotics, telerobotics, and autonomous systems,
- communications and navigation,
- entry, descent, and landing Systems,
- human health, life support, and habitation systems,
- in-situ resource utilization.

Current activities: Nowdays a number of lunar robotic missions are preparing for the first phase of Moon exploration [2].

Luna-25. This spacecraft is a lightweight robotic spacecraft for complex research on the lunar surface in the circumpolar lunar region. It is also preaping for soft-landing technology testing.

Luna-26. This orbiter is supposed for global observation and lunar resource survey, for supporting networking with two descent spacecrafts Luna-25 and Luna-27, and for supporting communication of future lunar base with Earth.

Luna-27. The project provides highly-precise and safe landing in difficult geological conditions of near-polar area. Also it provides a scientific harware complex, including lunar manipulating complex for soil sampling and investigation.

Luna-28. The main project goal is to deliver vacuum-packed lunar ice sample with undisturbed structure on Earth for further investigation in ground research centers. Also there is an option to dock it to the Gateway for on-station samples research.

References:

[1] Global Exploration Roadmap (2018), https://www.globalspaceexploration.org/wordpress/wp-content/isecg/GER_2018_small_mobile.pdf.

[2] K. Raykunov, M. Danilova, Dr. G. Karabadzhak (2017) GLEX-2017, Paper ID 37020.

THE MOON AND ASTEROIDS AT THERMAL INFRARED WAVELENGTHS. K. L. Donaldson Hanna[1,2], B. T. Greenhagen[3], and N. E. Bowles[2], [1]Department of Physics, University of Central Florida, Orlando, Florida, USA (Kerri.DonaldsonHanna@ucf.edu), [2]Atmospheric, Oceanic and Planetary Physics, University of Oxford, Oxford, UK, [3]Johns Hopkins Applied Physics Laboratory, Laurel, Maryland, USA.

Introduction: The surfaces of most Solar System airless bodies (i.e., the Moon, asteroids, Mercury, Phobos, and Deimos) are dominated by particulate regolith materials. The heat or emitted radiation that we measure using telescopes and spacecraft originates from the upper hundreds of microns of regolith of these airless bodies. Early laboratory studies and radiative transfer modeling demonstrated that the vacuum environment in the near-surface regolith of airless bodies creates a thermal gradient, which causes known spectral features to shift position and change in contrast [e.g., 1–3]. The thermal gradient and how much these spectral features shift and change in contrast are governed by key regolith properties including composition, albedo, particle size, and porosity [e.g., 4–6].

Thus, to better interpret thermal infrared (TIR) remote sensing observations of Solar System airless bodies, we need laboratory measurements of well-characterized analog materials measured under the appropriate near-surface conditions. Here we present laboratory thermal infrared emissivity spectra of lunar and primitive asteroid analogs measured under lunar- and asteroid-like near-surface conditions and discuss the implications for the interpretation of remote sensing observations to better constrain composition and physical properties.

Experimental Set-up and Analog Samples: Near-surface environments for the Moon and asteroids can be simulated using the Planetary Analogue Surface Chamber for Asteroid and Lunar Environments (PASCALE). The vacuum environment chamber is located within the Planetary Spectroscopy Facility (PSF) at the University of Oxford and is capable of simulating near-surface conditions for a range of Solar System bodies by varying the atmospheric pressure inside the chamber and the incident solar-like irradiation on the sample [7]. By varying the near-surface environment, the thermal gradient in the upper hundreds of microns of the sample is varied, which affects the position and contrast of diagnostic features in TIR spectra [e.g., 4–7]. PASCALE is attached to a Bruker VERTEX 70V Fourier Transform Infrared (FTIR) spectrometer capable of measuring thermal infrared wavelengths (~5-50 microns or 2000-200 cm^{-1}).

We simulate lunar-like conditions in PASCALE by removing atmospheric gases within the chamber (pressure < 10^{-4} mbar), heating the sample from below to 353K, and heating the sample from above until the estimated brightness temperature of the sample is ~390K. We simulate asteroid-like conditions by removing atmospheric gases within the chamber (pressure < 10^{-4} mbar), heating the sample from below to 353K, and heating the sample from above until the estimated brightness temperature of the sample is ~350K.

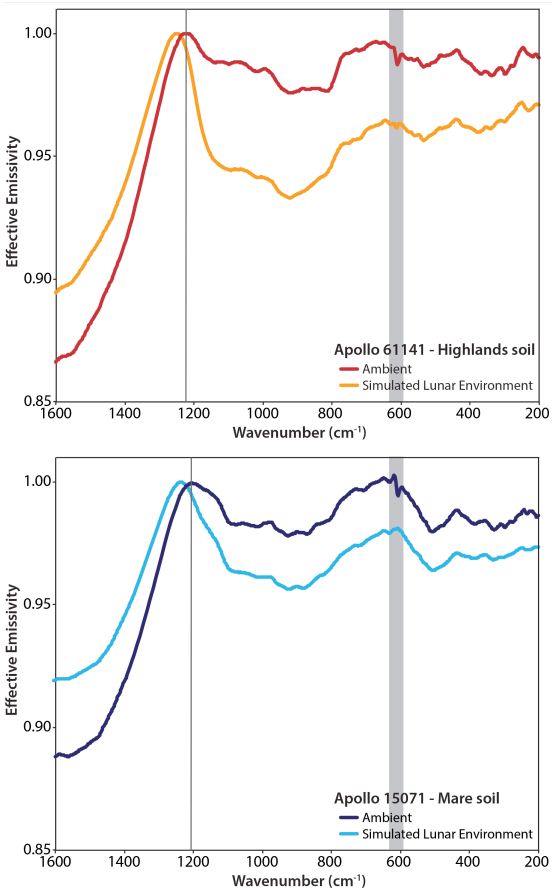

Figure 1. Ambient and SLE spectra of Apollo bulk soils 61141 (**top**) and 15071 (**bottom**). Vertical lines denote the Christiansen feature position measured under ambient conditions. Grey boxes highlight regions of low signal-to-noise ratio (SNR) due to the FTIR beamsplitter.

The analog sample suite used here includes well-characterized Apollo bulk soils [8] and chondritic meteorites. Apollo bulk soils have particle size distributions < 1 mm. The chondritic meteorites have been crushed and sieved to a range of particle size distributions (< 45, 45–75, 75–125, 125–250, 250–500 μm) and then physically mixed to represent the regolith of an impact gardened carbonaceous asteroid [7].

Results: Ambient and simulated lunar environment (SLE) spectra of Apollo bulk soils 61141 and 15071 are shown in Figure 1. Diagnostic features

observed in the spectra include the: (1) Christiansen feature (CF) – an emissivity maximum shown to be related to silicate composition [9], (2) reststrahlen bands – emissivity minima related to fundamental vibration bands of the crystal lattice [e.g., 10], and (3) transparency feature (TF) – an emissivity minimum related to silicate composition and fine particle sizes [e.g., 11]. In the highlands (61141) and mare (15071) soils, we observe the CF to shift to higher frequencies and an increase in spectral contrast between the CF and RB under SLE conditions. We also observe a greater spectral contrast increase between the CF and RB in the higher albedo, highlands soil sample (61141). These results corroborate earlier measurements [8].

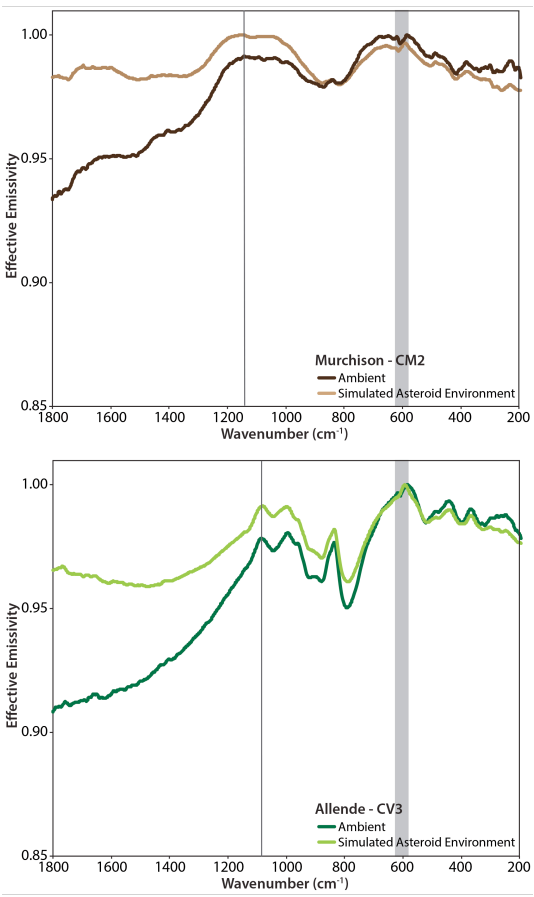

Figure 2. Ambient and SAE spectra of carbonaceous chondrites Murchison (**top**) and Allende (**bottom**). Vertical lines denote the Christiansen feature position measured under ambient conditions. Grey boxes highlight regions of low SNR due to the FTIR beamsplitter.

Ambient and simulated asteroid environment (SAE) spectra of carbonaceous chondrite meteorites Murchison and Allende are shown in Figure 2. It should be noted that the meteorites, due to their carbon-rich nature, are lower in albedo than the Apollo soils. Murchison spectra are dominated by spectral signatures indicative of hydrated mineralogy (phyllosilicates) and Allende spectra are dominated by the spectral signature of olivine. Unlike the Apollo soil spectra, we do not observe shifts in the CF position or increases in spectral contrast between the CF and RB in spectra of either meteorite. Also, in the meteorite ambient spectra we observe less spectral contrast across the entire wavelength range when compared to the Apollo ambient soil spectra. The observed differences in spectral behavior between the Apollo soils and the carbonaceous chondrite meteorites are most likely related to the differences in albedo between the samples.

Conclusions and Future Work: Laboratory measurements of lunar soils and carbonaceous chondrite meteorites presented here show the dramatic effects of albedo on thermal infrared spectra. These results suggest that the thermal gradient in the near-surface environment of carbonaceous asteroids is greatly reduced when compared to the lunar thermal gradient, which is linked to the low albedo nature of carbonaceous materials. To better understand how well physical properties can be constrained using thermal infrared spectral observations additional laboratory studies focused on particle size distributions and porosities are needed.

References: [1] Logan L. M. and Hunt G. R. (1970) *JGR, 75,* 6539–6548. [2] Salisbury J. W. and Walter L. S. (1989) *JGR, 94,* 9192–9202. [3] Henderson B. G. and Jakosky B. M. (1994) *JGR, 99,* 19063–19073. [4] Logan L. M. et al. (1973) *JGR*, 78, 4983–5003. [5] Salisbury J. W. and Wald A. (1992) *Icarus*, 96, 121–128. [6] Salisbury J. W. et al. (1991) *Icarus*, 92, 280-297. [7] Donaldson Hanna K. L. et al. (2019) *Icarus*, 319, 701–723. [8] Donaldson Hanna et al. (2017) *Icarus,* 283, 326–342. [9] Conel J. E. (1969) *JGR*, 74, 1614-1634. [10] Hamilton V. E. (2000) *JGR*, 105, 9701-9716. [11] Cooper B. L. et al. (2002) *JGR*, 107, doi:10.1029/2000JE001462.

MOON DIVER: A DISCOVERY MISSION CONCEPT FOR UNDERSTANDING SECONDARY CRUST FORMATION THROUGH THE EXPLORATION OF A LUNAR MARE PIT CROSS-SECTION. K.L. Donaldson Hanna[1], L. Kerber[2], B.W. Denevi[3], I. Nesnas[2], L. Keszthelyi[4], J.W. Head[5], C. Pieters[5], L. Wilson[6], J. Haruyama[7], R.V. Wagner[8], P.O. Hayne[9], J.W. Ashley[2], J.L. Whitten[10], A.M. Stickle[3], A. Parness[2], R.C. Anderson[2], D.M. Needham[11], P. Isaacson[12], L. Jozwiak[3], R. Klima[3], C. Jackson[10], T.C. Prissel[13,14], C.W. Hamilton[15], K. Uckert[2], C. Elder[2], [1]Univ. of Central Florida, Orlando, FL (kerri.donaldsonhanna@ucf.edu), [2]JPL, California Institute of Technology, Pasadena, CA, [3]Johns Hopkins APL, MD, [4]Astrogeology Science Center, Flagstaff, AZ, [5]Brown Univ., Providence, RI, [6]Lancaster Univ., UK, [7]ISAS, JAXA, Sagamihara, Japan, [8]Arizona State Univ., Tempe, AZ, [9]Univ. of Colorado, Boulder, CO, [10]Tulane Univ., New Orleans, LA, [11]NASA MSFC, Huntsville, AL, [12]Aerospace Corp., Chantilly, VA, [13]NASA JSC, Houston, TX, [14]Lunar & Planetary Institute, Houston, TX, [15]N. Arizona Univ., Flagstaff, AZ.

Introduction: In 2009, the Japanese spacecraft Kaguya discovered several holes in the surface of the Moon [1]. Some of these holes are more than 100 m deep, and open into large caverns extending an unknown distance beneath the lunar surface [2–3]. Hypothetical lunar lava tubes may provide beneficial locations for future habitation: the caves offer protection from radiation, a shield from micrometeorites, and, with a predicted constant temperature of ~20°C, they provide refuge from the extreme temperature swings of the lunar surface [4–5]. Scientifically, the treasure is found within the walls of the pits: the exposure of near-vertical cross-sections through the Moon's uppermost crust, extending from the top of the regolith, through the regolith/bedrock transition, and through up to 70 m of intact lunar mare bedrock layers [2–3].

The *Moon Diver* mission concept proposes to use the extreme terrain Axel rover [6] to descend into the lunar mare (**Figure 1**), using a pit in Mare Tranquillitatis as a natural drill hole with which to access an unprecedented exposure through the regolith and bedrock of the Moon's secondary crust. At the bottom of the pit wall, *Moon Diver* will peer into a lunar cavern, and become the first mission ever to venture beneath the surface of another world.

Science Goals: *Moon Diver's* science goals are to understand the formation and evolution of the Moon's secondary crust. The Moon provides an especially useful example of secondary crust formation since (unlike the Earth and Venus) it is one of the few places where resurfacing stopped before the primary crust was completely obscured—meaning that we can determine both the composition of the secondary crust as well as the composition of the original crust through which it was emplaced. The relative geological simplicity of the Moon means that the evidence of these processes can be exquisitely preserved for billions of years. *Moon Diver*'s science objectives, derived directly from community documents [7–8], are to: **(1)** Determine the extent to which the regolith is representative of the underlying bedrock. **(2)** Determine the nature of the transition from regolith to bedrock. **(3)** Determine whether the mare basalts were emplaced massively in turbulent flows, or if they were emplaced incrementally in smaller, but more numerous complex or inflated flows. **(4)** Determine the composition(s) of the parental magmas of the exposed basalts and what they tells us about the magma source regions in the lunar interior.

Figure 1. Representation of the Axel rover rappelling into a lunar pit (left) and exploring the cavity below (right) as part of the *Moon Diver* mission.

These objectives will be met by scaling the cross-section exposed in the wall of a mare pit, where both the process of regolith formation and the sequence of mare lava formation can be understood in their full contexts. Required measurements include:

(1) Elemental and mineralogical assessment of the regolith and the underlying basalts.

(2) Macro- and microscale physical characterization of the regolith up to and including the transition to the first bedrock layers.

(3) Assessment of macroscale lava flow morphology and microscale flow textures, lava layer thicknesses, and lava composition in order to determine lava flow rates.

(4) Chemical, mineralogical, and textural characterization of lava layers to constrain their petrologic origins.

Science Implementation: *Moon Diver* combines classic measurement techniques with a novel mobility system to achieve its ambitious science objectives. To make the measurements described above, the rover carries a suite of three simple instruments: (a) a trio of high-resolution cameras

(Mars 2020 EECAM heritage [9]) to capture the macroscale morphology of the regolith and near and far pit walls with 20 megapixel color stereo images, (b) an Alpha-particle X-ray Spectrometer (APXS; MSL heritage [10]) to measure the elemental composition of both regolith and lavas, and (c) a multispectral microscopic imager (MMI) that uses controlled LED lighting to characterize grain, vesicle, and crystal size as well as capturing spatially resolved mineralogy [11]. The rover also carries a surface preparation tool, which creates a fresh, flat surface for the instruments to examine when needed.

Mission Implementation: Access to the record exposed in the wall of the target pit is provided by two key technologies: pinpoint landing (allowing the delivery of the payload close to the pit) and extreme terrain mobility (allowing the delivery of the instruments to the cliff wall to make their measurements).

Pinpoint landing uses Terrain Relative Navigation, similar to Mars 2020, which allows the spacecraft to recognize landmarks on the surface and adjust its trajectory to land extremely accurately [12]. It is expected to be even more accurate on the Moon in the absence of an atmosphere.

The extreme terrain mobility is provided by the Axel rover, which descends from the lander, rolls across the surface, and rappels down into the pit [6]. The lander provides mechanical support, power, and communication with the rover through its tether. The rover houses a winch on board, which pays out the tether as Axel moves. The instruments are housed inside Axel's wheel wells, where they are protected from the environment. The wheel wells rotate independently from the rover's wheels, allowing the surface preparation tool, the MMI, and the APXS to be placed on the same target with a high degree of accuracy [6]. Axel's simple design protects its instruments and makes it robust to the challenges of navigating a steep wall of lava layers.

Field Preparations: To test the mission concept and develop procedures for operating the rover and instruments in a lunar pit environment, a prototype of the Axel rover was outfitted with a suite of representative instruments: commercial equivalents of the EECAMs and APXS and a brassboard version of the MMI. This integrated suite was deployed to a terrestrial analogue site: a steep-sided basaltic collapse pit in Arizona called "Devolites Pit". **Figure 2** shows relative sizes of the Axel rover, Devolites Pit, with a long axis of 50 m, and the Tranquillitatis Pit on the Moon (100 m diameter). The rover was driven from a remote "mission" control, navigating the flat, funnel, and wall portions of the pit and taking representative science measurements along the way.

Implications: The terrestrial planets are dominated by secondary crust. Understanding the process of secondary crust formation on the Moon, where there are fewer unknown or confounding variables, can provide a keystone for understanding crustal formation on other bodies [13]. In particular, planetary flood basalt flow rates currently have an uncertainty of many orders of magnitude, ranging from slow, laminar flows to fully turbulent flows. The measurements taken by *Moon Diver*, such as accurate flow thicknesses, could reduce this uncertainty for lunar basalts by up to seven orders of magnitude. Similarly, an examination of regolith formation and evolution from the surface to bedrock on the Moon, in concert with accumulated knowledge from *Apollo* and *Luna* samples, lunar meteorites, and remote sensing datasets, would help us interpret this process on other airless bodies where only remote datasets are available or where samples are available without contextual information.

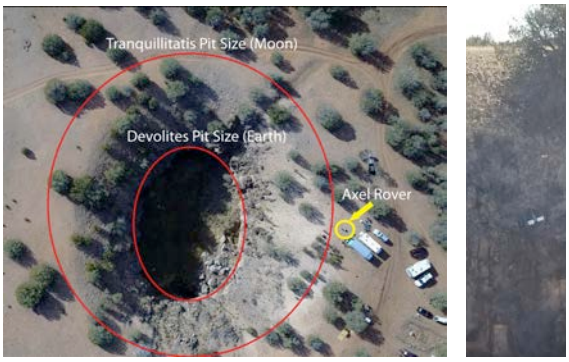

Figure 2. Left: Field test site. Red circles show size of terrestrial versus lunar pits compared to the Axel rover (yellow). Right: The Axel rover on a vertical basalt wall.

References: [1] Haruyama, J., et al. (2009) *GRL 36*, L21206 [2] Robinson, M.S. et al. (2012) *PSS 69*, 18–27. [3] Wagner, R.V., Robinson, M.S. (2014) *Icarus 237*, 52–60. [4] Hörz, F. (1985) *Lunar Bases & Space Act. of the 21st Cent.*, pp. 405–412. [5] Haruyama, J. et al. (2012) *Moon*. [6] Nesnas, I., et al. (2012) *J. of Field Robotics 29*, 663– 685. [7] Abell et al., (2016) *Lunar Expl. Roadmap*. [8] NRC (2007) *Sci. Context for Expl. of the Moon*. [9] Singh, K., et al. (2017) *47th ICES* Abs. 212 [10] Gellert, R. et al. (2015) *Elements 11*, 39–44. [11] Nunez, J. et al. (2013) *Astrobiology 14*, 132–169. [12] Johnson, A. E., & Montgomery, J. F. (2008) *IEEE Aero.* (pp. 1–10). [13] Taylor, S.R. (1989) *Tectonophysics 161*, 147–156.

Acknowledgments: This work was carried out at the Jet Propulsion Laboratory California Institute of Technology under a contract with NASA.

MAGMATIC STAGES WITHIN OLIVINE CUMULATE GABBRO OF THE NWA 773 CLAN AND VOLATILE ELEMENTS IN RESIDUAL LIQUIDS RECORDED BY APATITE. T.J. Fagan[1], Y. Egawa[1] H. Nagaoka[2,3] and R. Tartèse[4], [1]Earth Science Dept., Waseda Univ., Tokyo, Japan (fagan@waseda.jp), [2]ISAS/JAXA, Sagamihara, Japan, [3]Research Inst. Sci. Engineering, Waseda Univ., Tokyo, Japan, [4]School of Earth and Environmental Sci., Univ. Manchester, Manchester, UK.

Introduction: Northwest Africa 773 (NWA 773) and affiliated meteorites comprise a geochemically distinct clan of rocks from the Moon [1-3]. A key lithology in the NWA 773 clan is the olivine cumulate gabbro (OC), which is interpreted as a rock that crystallized at early, high-temperature stages in a magmatic system [4]. Other, more felsic and ferroan rocks that occur as clasts in the NWA 773 clan breccias apparently formed during later stages of crystallization of the same magmatic system [4,5].

In this study, we identify two sequential stages within the NWA 773 clan OC: an earlier, higher-temperature unit enriched in low-Ca pyroxene (mpx-OC) and a later unit with more abundant plagioclase feldspar (fsp-OC). Furthermore, we use apatite compositions to evaluate the roles of water and halogens during crystallization of residual OC liquids.

Methods: *Varieties within OC lithology.* Modal and compositional varieties within the NWA 773 clan OC lithology were discovered as a result of long-term characterization of this clan of lunar meteorites. The results reported here are from NWA 2977 (two polished thin sections labelled pts-A and pts-B) and NWA 6950 (one pts). Mosaics of the thin sections were prepared in plane polarized light (PPL), backscattered electrons (BSE) and elemental X-ray maps. The BSE and element maps were collected using a JEOL JXA-8900 electron probe micro-analyzer (EPMA) at Waseda University (WU).

Mineral modes were collected from the fsp-OC and mpx-OC varieties in NWA 2977 pts-B and NWA 6950. Modes were determined manually using a grid overlain on elemental and BSE maps. Compositions of olivine, pyroxene and plagioclase feldspar in fsp-OC and mpx-OC were analyzed using the WU EPMA in NWA 2977 pts-A and pts-B and in NWA 6950. Analyses were conducted by wavelength-dispersive analysis using oxide and silicate standards and the following beam conditions: 15 kV; 20 nA; ~1µm beam diameter. In order to ensure wide, even distributions of analyses in the exposed portions of fsp-OC and mpx-OC, a grid was drawn over each pts and a few analytical points were selected in each box of the grid.

ToF-SIMS images and apatite analyses. As a consequence of elemental mapping of the thin sections, intercumulus pockets with incompatible element-rich minerals, including apatite, were found. Two pockets from NWA 2977 pts-B—pocket 4E in fsp-OC and pocket 1 in mpx-OC—were selected for ToF-SIMS imaging and analyses. We used the IDLE-3 ToF-SIMS instrument at the University of Manchester [6] to image the distribution of volatile species. A ~1 nA (DC) beam of Au^+ ions focused to a spot size of ~1 µm was used to sputter clean the sample surface over areas on the order of 200 µm across. Following this, high mass resolution ($m/\Delta m \sim 3000$) secondary ion mass spectra were acquired over ~120 × 120 µm areas. Mass resolved images in positive secondary ions and negative secondary ions were acquired over areas of interest for ~10-30 min. Concentrations of F, SO_3 and Cl were calculated based on calibrations with well-established apatite reference materials [7].

Results: *Feldspar-rich vs. pyroxene-rich OC.* Feldspar-rich olivine cumulate gabbro (fsp-OC) has high modal abundances of plagioclase feldspar and olivine, and low abundances of low-Ca pyroxene compared to the pyroxene-rich OC (mpx-OC; see Table 1 and Figs. 1 and 2).

Table 1. Modes of fsp-OC vs. mpx-OC (mode%).

	NWA 2977B		NWA 6950	
	fsp-OC	mpx-OC	fsp-OC	mpx-OC
Low-Ca pyx	17.1	45.7	18.0	37.5
High-Ca pyx	12.1	16.5	10.8	25.9
Olivine	54.1	33.6	54.0	31.0
Feldspar	16.1	4.2	16.4	5.6
Other	0.5	0	0.7	0
n (# points)	(923)	(569)	(816)	(232)

In all three thin sections, mafic silicates of the fsp-OC are slightly more ferroan than in the mpx-OC. For example, in NWA 2977A fsp-OC olivine has mean $Fa_{30.7 \pm 0.7}$ and pyroxene has Fe# (molar Fe/[Fe+Mg] ×100) = 25.9 ±2.7 (uncertainties of ±1σ), compared to olivine $Fa_{29.5 \pm 0.7}$ and pyroxene Fe# = 23.3 ±1.2 in the mpx-OC. In contrast to the mafic silicates, plagioclase feldspar compositions in the fsp-OC and mpx-OC are similar (An_{89-91}).

F:Cl:OH ratios in apatite. The intercumulus pockets that host apatite are more abundant in the fsp-OC than in the mpx-OC (Fig. 1b). Apatite was identified along with merrillite, ilmenite and K-Ba-feldspar in several pockets (Figs. 2,3).

All of the apatite crystals analyzed in NWA 2977B pocket 4E in the fsp-OC and pocket 1 in the mpx-OC are water-bearing, similar to previous analyses of apatite in the NWA 773 clan (Figs. 3,4; see [8,9]). All of the analyses from pocket 1 and several from pocket 4E are Cl-poor, similar to the mare-affiliated apatite compositions compiled by [10]. However, pocket 4E apatite exhibits a range in Cl up to

0.22 atoms per formula unit (with F+Cl+OH = 1) in small apatite grains (Figs. 3 and 4). One EPMA analysis from [8] in NWA 2977 also has high Cl (Fig. 4).

Discussion: Based on textures, modes and Fe# of mafic silicates, the mpx-OC appears to be an early stage, high-temperature unit within the NWA 773 clan OC lithology. We suspect that the mpx-OC was dominated by crystal growth, whereas the fsp-OC was affected to a greater extent by crystal accumulation. In fact, clots of mpx-OC were probably accumulated in the fsp-OC.

It is difficult to calculate F:Cl:OH ratios directly from apatite because of the preferential partitioning of F into apatite [11]. However, from the apatite imaging and analyses, we infer that: (1) H_2O was present in residual, intercumulus liquids in the NWA 773 mpx-OC and fsp-OC; (2) F was fractionally removed from residual liquid by apatite crystallization in pocket 4E. These results also suggest that fine-grained Cl-rich apatite might be more common than previously recognized in NWA 773 (and other mafic rocks from the Moon) as a consequence of some bias toward analyzing coarser grains.

References: [1] Fagan T.J. et al (2003) *MaPS 38,* 529-554. [2] Jolliff B.J. et al (2003) *GCA 67,* 4587-4879. [3] Jolliff B.J. et al (2007) *LPSC 38,* #1489. [4] Fagan T.J. et al (2014) *GCA 133,* 97-127. [5] North-Valencia S.N. et al (2014) *LPSC 45*, #2858. [6] Henkel T. et al (2006) *Appl. Surf. Sci. 252*, 7117-7119. [7] McCubbin F.M. et al (2012) *Geology 40*, 683-686. [8] Zhang A.-C. et al (2011) *MaPS 45*, 1929-1947. [9] Tartèse R. et al (2014) *MaPS 49*, 2266-2289. [10] McCubbin F.M. et al (2015) *Amer. Mineral. 100,* 1668-1707. [11] Boyce J.W. et al (2014) *Science 344*, 400-402.

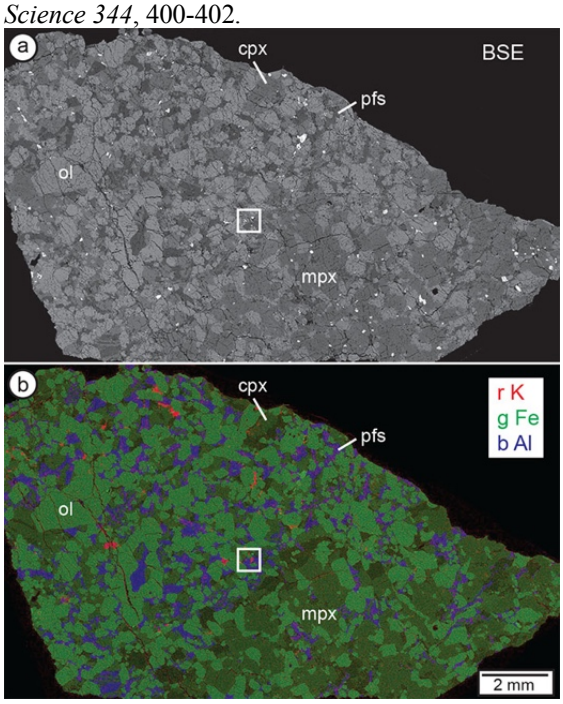

Fig. 1. NWA 2977 pts-B in BSE (a) and K:Fe:Al (Kα X-rays) in red:green:blue (b). Note contrast between mpx-rich OC at lower right and pfs-rich OC at upper left. Abbreviations: cpx = high-Ca pyroxene; mpx = low-Ca pyroxene; ol = olivine; pfs = plagioclase feldspar. Intercumulus pocket outlined by white box is shown in detail in Fig. 2.

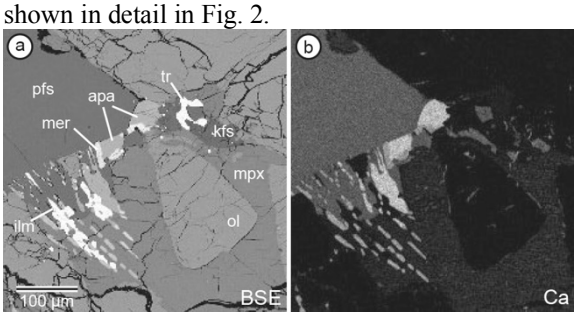

Fig. 2. Images of pocket 4E from NWA 2977 pts-B in BSE (a) and Ca Kα (b). Abbreviations as in Fig. 1 and: apa = apatite; ilm = ilmenite; kfs = K,Ba-feldspar; mer = merrillite; tr = troilite. Apatite is darker than merrillite in BSE (due to high REE in merrillite) and brighter than merrillite in Ca Kα.

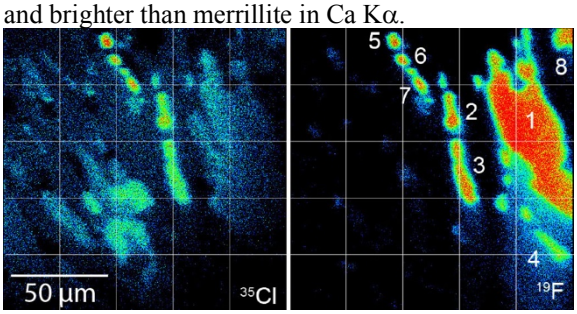

Fig. 3. ToF-SIMS images of ^{35}Cl and ^{19}F from pocket 4E (see Fig. 2). Numbers on ^{19}F image show areas where F:Cl:OH ratios were quantified.

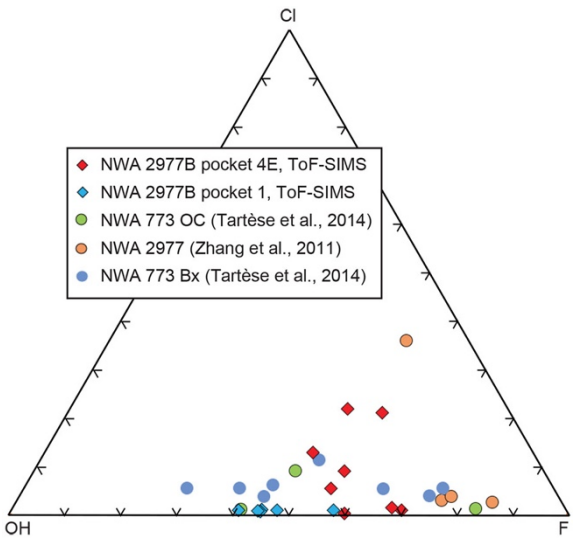

Fig. 4. NWA 773 clan apatite F:Cl:OH ratios from ToF-SIMS (this work), and electron microprobe data of [8,9]. Results from NWA 773 are shown for breccia (Bx) and olivine cumulate gabbro (OC) lithologies. NWA 2977 consists entirely of OC. Pocket 4E is located in the feldspar-rich gabbro (fsp-OC), and pocket 1 is located in the low-Ca pyroxene-rich variety (mpx-OC).

AN INVESTIGATION INTO SULFUR OXIDATION STATE WITHIN LUNAR APATITE. S. J. Faircloth[1], M. Anand[1,2], I. A. Franchi[1], S. S. Russell[2] and R. C. Greenwood[1]. [1]The Open University, School of Physical Sciences, Walton Hall, MK7 6AA, United Kingdom (sam.faircloth@open.ac.uk), [2] Department of Earth Sciences, The Natural History Museum, London, SW7 5BD, UK.

Introduction: Apatite is a late-stage crystallising igneous mineral with an idealised chemical formula of $Ca_5(PO4)_3(F,Cl,OH)$. It has the ability to hold volatiles within its crystal lattice and, as a result, apatite has been a target mineral for measuring water (OH) and other volatiles (F & Cl) in lunar samples. The proportion of the three anions (F^-, Cl^-, OH^-) held wthin the anion (X) site needs to be approximately equal to 1 [1].

It has been suggested that the volatiles OH, Cl and S exist within apatite in lunar basalts in comparable abundances to those in terrestrial samples [2]. On Earth, S can exist in multiple oxidation states (e.g. sulfate: S^{6+}, sulfite: S^{4+} and sulfide: S^{2-}) and, in terrestrial apatites, two possible S substitution reactions are known to occur ($S^{6+} + Si^{4+} \leftrightarrow 2P^{5+}$ and $S^{6+} + Na^{+} \leftrightarrow P^{5+} + Ca^{2+}$) [3] at the tetrahedral (T) cation site [4] under more oxidising conditions where SO_3 contents are relatively high [3]. For lunar apatite, it was speculated that there might be an alternative mechanism operating, whereby the X-site is capable of holding S, probably as S^{2-} [2 & 5].

Experiments on a natural terrestrial apatite and an experimentally crystallised apatite with μ-XANES spectroscopy at the S K-edge have shown that S^{6+}, S^{4+} and S^{2-} can exist together, to varying degrees, within apatite at an oxygen fugacity of FMQ+3 down to FMQ. It was concluded that a simultaneous incorporation of S^{6+} and S^{2-} at different crystallographic sites within the apatite (T-site and X-site, respectively) might be possible [6].

The results of very recent S-XANES spectroscopy [7] for apatite grains within two Apollo basalt samples (10044,33 and 12039,4) have been interpreted as evidence for the dominance of S^{2-}, where more than half of measurements had $S^{6+}/\Sigma S$ <3%. It was suggested that the presence of S^{2-}–only apatites was indicative of apatite crystallisation from a relatively low fO_2 lunar magma.

By determining the oxidation state of S within lunar apatite, a greater understanding of the history of lunar magmas can be obtained. For example, if different oxidation states of S are able to exist within lunar apatite, as is suggested for terrestrial apatite, it would be possible to use S within apatite to determine the oxidation state of the magma from which the apatite crystallised.

Samples and preliminary investigations: In order to investigate the oxidation state of S in lunar apatite, several Apollo basalts were examined. Intial characterisation of grains was performed using secondary electron microscopy (SEM), backscatter electron (BSE), secondary electron and cathodoluminescence (CL) images, providing textural context and highlighting crystal zonation. Some apatite grains do contain concentric or oscillatory zonation (~1-5 μm thickness), which may be an indication of volatile (Cl and/ or S) inhomogeneity in the grain (Fig. 1). Electron probe micro-analysis (EPMA) was used to confirm the composition of apatite grains and the abundance of S. Long exposure to the electron beam was avoided in order to prevent any reduction or oxidation of S e.g. a reduction of S^{6+} to S^{4+}.

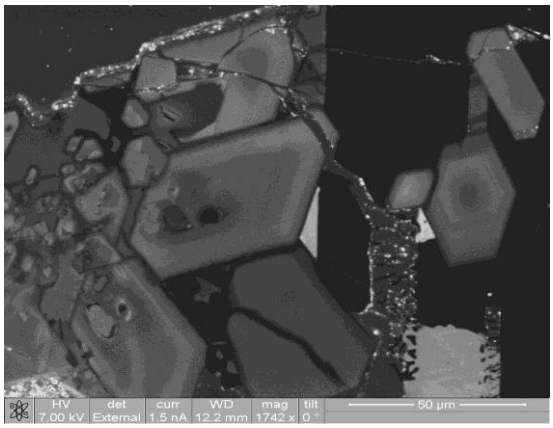

Fig. 1: Zoned apatite grains in sample 12039,45. With the use of CL imaging, both concentric and oscillatory zoning can be clearly seen within the apatite grains that fill this image.

Methods: With use of known sulfur reference materials (e.g. anhydrite and troilite) to define the peak energy positions for S^{6+}, S^{4+} and S^{2-} (with energy peaks of ~2482 eV, ~2478 eV and ~2470 eV, respectively) [8], the oxidation state(s) of S within lunar apatite is determined with X-ray absorption near edge structure (XANES) spectroscopy at the S K-edge. Given the small size of the grains and the relatively low S abundance within lunar apatite, care must be taken to prevent beam damage during S-XANES analyses by monitoring individual measurements for S oxidation or reduction [8].

References: [1] Hughes J. M. et al. (1990) *Am. Mineral*., 75, 295-304. [2] Boyce J. W. et al. (2010) *Nature*, 466, 466-469. [3] Peng G. et al. (1997) *Am. Mineral*., 82, 1210–1224. [4] Hughes J. M. and J. F. Rakovan (2015) *Elements*, 11, 165-170. [5] Boyce J. W. et al. (2012) 43rd LPSC, no. 2675. [6] Konecke B. A. et al. (2017a) Am. Mineral., 102, 548–557. [7] Brounce M. et al. (2019) *Am. Mineral*., 104, 307-312. [8] Wilke M. et al. (2008) *Am. Mineral*., 93, 235-240.

Commercial Lunar Missions Support Services (CLMSS) programme. J. Friend[1], G. Lay[1], N. Offord Harlé[1], C. Cranstoun[1], A. Mafficini[1], M. Cosby[2], C. Saunders[2], B. Hufenbach[3] [1] Surrey Satellite Technology Limited, Tycho House, 20 Stephenson Road, Surrey Research Park, Guildford, United Kingdom, GU2 7YE United Kingdom, [2] Goonhilly Earth Station, Goonhilly Downs, Helston, Cornwall, United Kingdom TR12 6LQ, [3] European Space Agency, European Space Technology Centre, Keplerlaan 1, 2201AZ, Noordwijk, Netherlands

Introduction: Surrey Satellite Technology Ltd (SSTL) and Goonhilly Earth Station Ltd (GES), in partnership with the European Space Agency (ESA) are developing the Commercial Lunar Missions Support Services (CLMSS) programme. The goal of this programme is to provide infrastructure in the form of lunar communications relay and navigations service, as well as providing opportunities for payload delivery and payload hosting. These services will significantly reduce the entry costs for teams wishing to fly lunar missions, bringing space exploration within the reach of more nations, agencies, universities and companies. These services will simplify the process of operating a mission in the lunar environment to the point where it will be similar to operating a spacecraft in Low Earth Orbit. The system will be available to play a role in supporting large lunar programmes currently being planned by NASA, ESA, CSA, JAXA and other agencies in the lunar vicinity [1][2]. CLMSS implementation is taking a phased approach with the first phase currently under way with the upgrade to the GES ground station in the UK, with the aim to expand to additional locations around the globe in the next phases. This activity will make the antenna the first node in a commercial deep space communications network and will provide interoperability with current institutional networks such as ESA's European Satellite Tracking network (ESTRACK) and NASA's Deep Space Network. Phase 2 will see the launch of the Lunar Services Pathfinder mission which will provide communications relay and initial navigation services. This mission will provide the opportunity for payloads to be aggregated for rides to lunar orbit and payload hosting opportunities. Phase 3 of the programme will see further spacecraft launched to provide enhanced coverage, navigation performance, and increased throughput as a constellation is assembled. This will build towards the long term vision of providing full lunar communications and navigation coverage enabling international cooperation. In the future the model for these services could be extended to support robotic and crewed exploration further out in the solar system.

[1] International Space Exploration Coordination Group (ISECG) (2018), *Global Exploration Roadmap*. [2] National Aeronautics and Space Administration, *National Space Exploration Campaign Report*.(2018)

The mission SELPHIE to investigate lunar water. Y. Futaana[1], M. Grande[2,*], S. Barabash[1], P. Wurz[3], D. Hurley[4], and SELPHIE proposal team, [1]Swedish Institute of Space Physics, Box 812, Kiruna SE98128, Sweden (yoshifumi.futaana@irf.se), [2]Aberystwyth University, Wales, UK, [3]University of Bern, Bern, Switzerland, [4]Johns Hopkins University Applied Physics Laboratory, Maryland, US.

Introdcution: We are approaching a new era of space exploration: **Utilization of our Moon for Human Beings**. Intensive international efforts targeting human activities on the Moon have been initiated, and developed drastically in this decade. The revolution enabling the activities was the discovery of water at the Moon. We envisage utilizing the water for Lunar surface activities, as well as for explorations to farther Deep Space destinations. Although multiple datasets have revealed the existence of Lunar water, fundamental scientific questions remain unanswered: Where has the surface and cold trap waters come from? What are the relative roles between solar wind protons and delivery from space for the Lunar surface water? What is the role of transportation of surface water to cold traps? The top-level science question of SELPHIE is formulated as **How is the lunar surface water delivered or produced, transported, and accumulated in cold traps?** The SELPHIE mission is a lunar mission, with focuesed scientific objectives derived from its precursor mission, SELMA [Futaana et al., 2018].

Science objectives: The Moon is covered with regolith. One of the most important manifestations of the space environment–regolith interactions is the formation of OH/H_2O bearing materials ("surface water") in the outermost layer of regolith. The surface water shows a variation with one Lunar day, suggesting that the water formation (and extraction) is an ongoing, dynamic process. However, the origin of the surface water either by solar wind or asteroids is still a controversial scientific problem. Furthermore, quantification of the variability is uncertain due to poorly constrained thermal correction. Thus, the first key question of the SELPHIE mission is **"What is the origin of the surface water?"** Using global measurements with properly coordinated remote-sensing and in situ instruments, the SELPHIE mission reveals **the relative roles of the solar wind and meteoroid / comet impacts as the origin of surface water**.

Another reservoir of water at the Moon is the cold traps, inside permanently-shadowed craters near the poles. A series of surveys have detected signatures of water ice in cold traps. The key open question is **"What is the origin of water in cold traps?"** Is it the solar wind origin, or cometary origin? What is the relation between the cold trap water and the surface water? What is the contribution of the endogenic water to the cold trap water? SELPHIE addresses these questions by measuring the D/H ratio directly derived from impact experiments.

Transport of water within the exosphere is the central mechanism for the lifecycle of Lunar water. The exosphere is a conduit between the surface water and cold trap water. The final key question is formulated as **"What is the role of the exosphere in transporting surface water to cold traps?"** By inevitably detecting the global distributions of water and OH using the state-of-the-art instru-ments, and by correlating coordinated measure-ments to monitor the external environment, the SELPHIE mission identifies how the exosphere and its water compositions respond against varia-tions of the external conditions, and determines the water cycle in the Lunar exosphere.

Mission profiles: The SELPHIE mission is composed of six scientific sensors (three remote sensing and three in situ sensors) together with two impact experiments. Scientific sensors are operated from an SELPHIE orbiter to reveal the comprehensive picture of the lunar water cycle; namely from space to cold traps via surface and exosphere. Two impact experiments (two identical systems, enabling two independent experiments) will be executed to reveal the source of water under cold traps. Each impact experiment contains a 6U cubesat and a small impactor (4 kg). The impactor will impact to a permanently shadowed crater to make ejecta. The cubesat will sound the plume.

The following six instruments on board the main orbiter is considered.

LuIS: The Luna Infrared Spectrometer is based on the heritage of the SIR-2 spectrometer and the experience of the M3 instrument on Chandrayaan-1. A Linear Variable Filter is used as a band-pass filter. The LVF has a range between 0.4 to 3.6 μm with 1% resolution. This wavelength performance allows to measure the water line at the lunar surface. A dual-hybrid detector (silicon and HgCdTe) is thermally insulated and is cooled and stabilized through a four-stage Peltier element. A 280 × 280 pixel detector provides imaging capabilities. The optics have a focal length of 150 mm and an f- number of 4.5 yielding an IFOV of 0.015° per pixel. The active FOV is 3.2 × 3.2°. Sampling time is 6 ms.

SPOSH: Smart Panoramic Sensor Head is a frame camera built to observe meteoroid impacts in the visible range (400–800 nm) on the farside of the Moon. It will allow detection of any meteoroid impact with a mass larger than a few grams. Modifications to the original design will allow daylight operation despite featuring a highly-sensitive CCD (1024× 1024 pixels). The highly sensitive CCD allows the

detection of impact flashes on the dark side of the Moon. Full angle is 61.7˚, with the active FOV of 60x33˚with IFOV 0.031˚.

ENAT: ENA Telescope is based on the CENA (Chandrayaan-1 Energetic Neutrals Analyzer) and ENA (Energetic Neutrals Analyzer) instruments for the Chandrayaan-1 and BepiColombo missions. ENAT features only one single viewing pixel with 5°×5° angular pixel size, which provides a factor-of-10 better angular resolution and a factor-of-10 larger geometrical factor. The energy range of 10 eV–3 keV with 50% energy resolution allows to map the solar wind proton flux at the Lunar surface.

LEMS: Lunar Exospheric Mass Spectrometer is a ToF mass spectrometer using an ion mirror (reflectron) for performance optimization. The LEMS mass range is 1–300 amu, the mass resolution is M/ΔM=1100, and the dynamic range is at least 6 decades for a 5 s integration period, allowing for the identification of species down to a partial density of about 1 cm–3 in such a measurement.

LSoW: Lunar Solar Wind sensor provides the in situ ion bulk properties (including the flux) of the solar wind protons. The sensor, providing fast 2π measurements in the energy range 1 eV-10 keV with 2s time resolution, is customized for the energy range and the dynamic range encompassing solar wind near the Moon.

LDD: Lunar Dust Detector is an in situ dust detector to map the variability of the spatial and size distribution of dust near the Moon. It is a 'build-to-print' version of the LDEX instrument that flew onboard NASA's LADEE mission from September 2013 to April 2014. LDD monitors the dust ejecta cloud generated by the continual bombardment to the lunar surface by micrometeoroids. Individual dust particle is detected by measuring the charge generated by the high- velocity (>1 km/s) impacts onto a hemispherical shaped detector. The mass of the dust particle is derived from the impact charge.

The impact experiment is equped with a cubesate and 4-kg passive impactor. The cubesat will carry a mass spectrometer, as well as a hyperspectral camera.

PHIE cubesat system: The PHIE cubesat envelope is 6U. In addition to a standard cubesat system configuration, the cubesat will host a mass spectrometer and a camera as payload. After a release of the cubesat giving its impact trajectory, an impactor will be released. The impactor (4-kg tungsten ball as a baseline) will precede the cubesat, impact to the selected cold trap, and produce a plume. The cubeat will carry out the scientific measurement by mass spectrometer and imaging at least for 5s in the plume. The cubesat shall send the telemetry to the SELPHIE orbiter in real time. Two identical systems are prepared.

IEMS: Impact Experiment Mass Spectrometer is based on MSSL CubeSat-based INMS and ChaPS instruments flown on the QB50 and TechDemoSat missions. The instrument is a cylindrical geometry, electrostatic analyser with ToF (currently under development for the EU DISCOVERER mission, scheduled to be launched in early 2020). IEMS has an energy acceptance of < 60 eV with 3% energy resolution and is optimized for separation of H1 and H2 to enable measurement of D/H ratios. The IEMS 2° narrow field-of-view is oriented in the CubeSat ram direction, picking up plume ions produced by the impactor. A set of electrostatic deflector plates permits additional angular acceptance range over 10°.

Referecne:

Futaana, et al., SELMA mission: How do airless bodies interact with space environment? the Moon as an accessible laboratory, Planet. Space Sci., 156, 23–40, doi:10.1016/j.pss.2017.11.002, 2018.

MINERALOGY OF SMALL LUNAR VOLCANOES: ERUPTION STYLES OF PYROCLASTIC DEPOSITS INFERRED FROM MOON MINERALOGY MAPPER DATA. L. Gaddis[1], B. Horgan[2], K. Bennett[1], M. McBride[2], L. Glaspie[3], J. Stopar[4], S. Lawrence[5]. [1]USGS Astrogeology Science Center, Flagstaff, AZ (lgaddis@usgs.gov); [2]Purdue University, Indianapolis, IN; [3]Northern Arizona University, Flagstaff, AZ; [4]Lunar and Planetary Institute, Houston, TX; [5]NASA Johnson Space Center, Houston, TX.

Introduction: We have mapped pyroclastic deposits across the lunar surface [1-3], including 20 "regional" deposits (>1000 km^2) and >85 "localized" deposits (<1000 km^2 [1]). Regional deposits are thought to be emplaced by more energetic and sustained Hawaiian-style fire fountaining, resulting in ballistically emplaced glass-rich deposits [4,5]. Localized pyroclastic deposits are primarily emplaced via low-effusion rate Vulcanian eruptions during which volatiles build up under a cooled magma plug, periodically releasing entrained gas in explosive eruptions [6-8] of fragmented magma and local country rock. Both types of lunar pyroclastic deposits are driven by magmatic volatiles [4,5,9], so these deposits can provide important constraints on the volatile content and composition of lunar magmas and the early lunar interior [10-12], and the presence of possible resources [13].

Previous studies have shown that glass is present within pyroclastic deposits at all sizes [2,3,14-16], although it is often mixed with orthopyroxene, clinopyroxene and possibly olivine, suggesting that eruption styles for lunar small volcanoes are not as simple as commonly believed. Using hyperspectral data from the Global Mode mapping campaign of the Moon Mineralogy Mapper (M^3) visible/near-infared (VNIR; 0.35-3.0 μm) instrument [17] at 140-280 m/pixel, we studied the mineralogies of several small pyroclastic deposits to constrain their eruption styles and volatility, assess whether single or multiple eruptions may have occurred, and to identify possible changes in composition of source materials with time and/or distance from the vent.

Improved knowledge of the composition of small lunar pyroclastic deposits permits identification and characterization of possible juvenile components, and evaluation of the distributions and relative amounts of juvenile vs. host-rock components. In addition, a compositional assessment allows us to examine whether shallow intrusions favor the formation of small pyroclastic deposits [15,18]. If deeper sources are involved, our results should indicate a greater abundance of juvenile materials (volcanic glass, olivine, clinopyroxene) and if shallower eruptions are dominant, mixing with local crust should introduce more orthopyroxene and possibly plagioclase. Further, eruptions from deeper in the crust may involve higher-energy eruptions and possibly some amount of volatiles such as CO or H_2O.

Methods: Using low-temperature M^3 hyperspectral data when possible, we characterized the position and shape of the 1 and 2 μm iron absorption bands to identify and map distributions of Fe-bearing minerals (pyroxenes, olivines, and glass) using the methods of [19]. We first smooth the data and then remove the continuum using a linear convex hull and finding local band maxima near 0.7, 1.5 and 2.6 microns. The "glass band depth" spectral parameter is calculated as the average band depth below the continuum at 1.15, 1.18, and 1.20 μm, and the "orthopyroxene (OPX) band depth" spectral parameter is calculated as the average band depth below the continuum at 0.88, 0.90, and 0.92 μm. The band analysis methods of Horgan et al. [19] are then used to parameterize the centers and depths of the 1 and 2 μm iron absorption bands. Maps of these parameters are used to distinguish between orthopyroxene (OPX; band centers between 0.9-0.94 and 1.8-1.95 μm), clinopyroxene (CPX; 0.98-1.06 and 2.05-2.4 μm), and iron-bearing glass (1.06-1.2 and 1.9-2.05 μm). Mixtures of these minerals have band centers that fall between the endmembers [19]. Other iron-bearing minerals, including olivine and plagioclase feldspars, can be identified using similar methods. Olivine has an asymmetric 1 μm band centered near 1.05-1.08 μm and plagioclase has broad, shallow bands centered between 1.25-1.35 μm (neither has a 2 μm band).

Earlier Work: Our previous analyses of 12 pyroclastic deposits at Alphonsus crater with M^3 data [20] revealed pyroclastic deposits with spectra consistent with a mixture of glass and OPX, with local concentrations of glass mixed with CPX near the vents. These observations support previous characterizations [7] and modeling of these deposits via a Vulcanian-style eruption, and near-vent CPX signatures suggest longer cooling times in thick pyroclastic deposits, thin lava flows, or fragmented basalt from within the source dike [20]. By contrast, our work on 15 deposits at Oppenheimer crater [3] indicated that the smallest floor pyroclastic deposits are dominated by glass, but medium and larger deposits had CPX and CPX-glass mixtures, with no country-rock. This mineralogy suggests that the deposits were emplaced by more continuous Strombolian-style or fire fountaining eruptions, which may have had enhanced volatile contents that contributed to sustained, higher effusion rate eruptions.

Studies of pyroclastic deposits at the volcanic complex in the Marius Hills [21,22] from mineral mapping with M^3 data [23] indicates that OPX dominates at the mafic lava domes and mafic glass dom-

inates at the cinder cone sites. At the Compton-Belcovich volcanic complex on the lunar far side are volcanic domes and plateaus around a central depression, interpreted as viscous, silicic lava flows and caldera collapse [24] with associated pyroclastic eruptions [25]. A strong hydration signature was observed over the complex [26], and our work suggested that this was associated with weak 1 and 2 μm absorption bands consistent with glass [27]. In part because Fe-poor felsic minerals are usually not detectable in the M^3 spectral range, this result is consistent with the presence of silicic lava flows and the presence of a glassy felsic ash such as one might find in an ash flow caldera on Earth.

Schrödinger basin: Recent analysis [28] of a conical edifice, associated pyroclastic deposit and nearby lava flows in the floor of Schrödinger crater near the lunar South Pole showed distinctive iron-bearing absorption bands at 1 and 2 μm in these volcanic deposits. These data suggested that the pyroclastic deposit is dominated by a mixture of glass and OPX, interpreted to be consistent with an explosively pyroclastic deposit mixed with crater floor material. Spectra of the inner peak-ring mafic units have signatures that are consistent with CPX and minor glass, suggesting emplacement as a volcanic fissure eruption with possible associated effusion.

J. Herschel crater: The pyroclastic deposits at J. Herschel crater are situated along at least 4 irregular depressions aligned along or adjacent to floor fractures [e.g., 29]. M^3 data for this area reveal a glass component that is particularly prominent along the largest fracture and dissipates in abundance as distance increases, with lesser clinopyroxene located nearest to at least two of the possible vents. Orthopyroxene is largely observed in association with small craters and fracture walls, not the pyroclastic deposits. This observed distribution of juvenile materials is typical of a Vulcanian-style eruption in which a relatively cool, localized gas-rich eruption is initially broadly spread, but the plume's extent decreases as magmatic gas is depleted, concentrating juvenile materials proximal to the vent.

Conclusions: Our mafic mineral mapping reveals the spatial distribution of glass, country rock, and crystalline igneous components in the deposits, allowing us to place more rigorous constraints on their eruption styles. Our results indicate that small lunar pyroclastic deposits are mineralogically diverse and their eruption styles are considerably more varied than previously understood. One result of our work suggests that the simplistic "regional" vs. "local" terms likely do not reflect the range and diversity of lunar explosive volcanic eruption styles. The diversity of observed mineralogies in lunar pyroclastic deposits indicates that their volcanic eruption styles are also diverse, including examples that are dominated by Vulcanian, Strombolian and Hawaiian styles, along with occasional effusive flows. This diversity is likely caused by differences in geologic context, magmatic source depth, and magma composition and volatility.

The geologic context of lunar pyroclastics described here includes those situated in volcanic provinces, inside or adjacent to mare-filled basins, and often located within floor-fractured craters. While the fractured, brecciated subsurface of impact basins can promote near-surface sill development, intra-crater dikes are more likely to reach the surface and create a localized eruption site [30]. Eruption style also is strongly influenced by volatile content; on the Moon this is thought to be higher for magmas sourced from greater depths [31]. For example, a possible volatile enrichment in fire-fountain eruptions at Oppenheimer compared to Vulcanian eruptions at Alphonsus could be caused by a greater magmatic source depth at Oppenheimer. The influence of composition on eruption style is observed in the dispersed pyroclastic deposits at Compton-Belkovich when compared to the localized cinder cones at Marius Hills; both may be consistent with late-stage explosive activity from a volatile-poor magma source, but the explosivity at Compton-Belkovich may have been increased by higher viscosity of the silicic magmas. Through modeling at sites such as Alphonus [32], we are currently working to assess the varying influence of these and other factors on lunar pyroclastic eruption styles.

References: [1] Gaddis et al (2003) Icarus 161, 262. [2] Gustafson et al (2012) JGR 117, E00H25. [3] Bennett et al (2016) Icarus 273, 296-314. [4] Heiken et al (1974) GCA 38, 1703-1718. [5] Wilson & Head (1981) JGR 86, 2971-3001. [6] Hawke et al (1989) LPSC 19, 255. [7] Head & Wilson (1979) 5th LPSC, 2861-2897. [8] Gaddis et al (2000) JGR 105, 4245-4262. [9] Delano (1986) JGR 91, D201. [10] Shearer et al (2006) RMG 60, 365. [11] McCubbin et al (2015) Am Min 100, 1668–1707. [12] Milliken & Li (2017) Nat Geosci 10, 561-565. [13] Duke et al (2006) RMG 60, 597. [14] Besse et al (2014) JGR 119, 355-372. [15] Jawin et al (2015) JGR 120, 1310-1331. [16] Trang et al (2017) Icarus 283, 232-253. [17] Pieters et al (2009) Curr Sci 96, 500-505. [18] Thomas et al (2015) Earth & Planetary Science Letters, 164–172. [19] Horgan et al (2014) Icarus 234, 132-154. [20] Gaddis et al (2016) LPSC 47, #2065. [21] Lawrence et al (2013) JGR 118, 615-634. [22] Besse et al (2011) JGR 116, E00G13. [23] McBride et al (2018) LPSC, abs. 2798. [24] Jolliff et al (2011) Nat Geosci 4, 566-571. [25] Chauhan et al (2015) Icarus 253, 115-129. [26] Bhattacharya et al (2013) Curr Sci 105, 685-694. [27] Horgan et al (2018) Eur. Lunar Symp., Toulouse, France. [28] McBride et al (2019) 50th LPSC, abs. #1985. [29] Stopar et al (2019) 50th LPSC, abs. #1937. [30] Jozwiak et al (2015) 248, 424-447. [31] Weitz et al (1999) JGR 104, 18933-18956. [32] Glaspie et al (2018) 100th AGU Ann. Mtg., abs. #P12A-08.

LUNAR "VOLATILE AND MINERALOGY MAPPING ORBITER (VMMO)" MISSION

Yang Gao[1,*], Roman V. Kruzelecky[2], Piotr Murzionak[2], Craig Underwood[1], Chris Bridges[1], Roberto Armellin[1], Andrea Luccafabris[1], Jonathan Lavoie[2], Ian Sinclair[2], Gregory Schinn[2], Edward Cloutis[3], Johan Leijtens[4], Roger Walker[5] and Johan Vennekens[5]
[1]Surrey Space Centre, University of Surrey, Guildford, GU2 7XH, UK
[2]MPB Communications Inc., 151 Hymus Blvd., Pointe Claire, Québec, H9R 1E9, Canada
[3]University of Winnipeg, 515 Portage Ave. Winnipeg, Manitoba, R3B 2E9, Canada
[4]Lens Research & Development, s'Gravendijkseweg 41B, 2201CZ Noordwijk, The Netherlands
[5]ESTEC European Space Research and Technology Centre, Noordwijk, Netherlands
[*]Corresponding author yang.gao@surrey.ac.uk

Introduction: The lunar CubeSat mission proposal called VMMO (Volatile & Mineralogy Mapping Orbiter) is among the two winners of the European Space Agency (ESA)'s SysNova Challenge on LUnar Cubesats for Exploration (LUCE) in 2018. VMMO has been developed by a multi-national team consisting of MPB Communications Inc, Surrey Space Centre, University of Winnipeg and Lens R&D.

The proposed mission aims to address several key aspects of future lunar exploration:

- *Lunar Resource Prospecting*: *Mapping the location of relevant in-situ resources and volatiles in sufficient quantities to be operationally useful (fuel, life-support) for future sustained surface missions.* The VMMO's primary science payload (Lunar Volatile and Mineralogy Mapper or LVMM) is a miniaturised laser instrument that would probe Shackleton Crater, adjacent to the South Pole, for measuring the abundance of water ice. It uses a dual-wavelength chemical lidar at 532 nm and 1560 nm at relatively high SNR to improve the sensitivity to small changes in the water/ice content of the regolith. Scanning a 10m-wide path, LVMM would take around 260 days to build a high-resolution map of water ice inside the 20 km-diameter crater. LVMM would also map lunar resources such as ilmenite (TiFeO3) as it overflew sunlit regions, as well as monitoring the distribution of ice and other volatiles across darkened areas to gain understanding of how condensates migrate across the surface during the two-week lunar night.
- *Lunar Environment and Effects: Measuring radiation, lofted dust and diurnal temperatures in the cis-lunar environment to support planning for future manned missions.* A secondary radiation-detecting payload (Compact LunAr Ionizing Radiation Environment or CLAIRE) would build up a detailed model of the radiation environment for the benefit of follow-on mission hardware as well as human explorers.
- *Lunar Explorations Technology: Developing enabling technologies for beyond-LEO CubeSats.* VMMO adopts a low-cost 20kg 12U CubeSat design, incorporating beyond-LEO navigation methodology and sensor suite as well as qualification of key electronics for CubeSats in the cis-lunar environment. The laser payload offers a dual use to demonstrate high-bandwidth and 1560nm optical downlink to an existing optical ground station.

Mission Profile & Operation: VMMO has been designed for a potential flight opportunity within the Lunar Communications Pathfinder Mission currently being developed by Surrey Satellite Technology Ltd. (SSTL) and Goonhilly in partnership with ESA. The VMMO CubeSat would be injected by a mother spacecraft into a nominal high-eccentricity lunar orbit. It would then use its on-board propulsion to attain the desired operating lunar orbit.

The mission operation consists of the following sequence, as shown in Figure 1. After launch from Earth, the mission will take some time before the mother spacecraft Lunar Orbiter (LO) reaches its desired orbit around the Moon (approx. 15 days). The next step in the mission is to get from LO orbit to a Small Satellite (SS) release orbit at approximately 500 km altitude (approx. 15 days). At this point the VMMO will be released from SS orbit. Once released VMMO will perform de-tumbling and initial health monitoring prior to maneuvering into its final orbit (approx. 7 days). The maneuver length from the release orbit to VMMO final orbit is estimated to take 68 days using electrical propulsion. In the final orbit, VMMO will perform scientific measurements: Active, Passive and Radiation (approx. 260 days). Data transmission includes sending data to Earth via the LO relay or via a direct optical downlink. The total mission duration is expected to be approximately 1 year.

Spacecraft Design Overview: Figure 2 gives an preliminary overview of the VMMO 12U CubeSat, consisting of two payloads (LVMM and CLAIRE), three sets of deployable solar panels (one of them would be acting as a baffle for the LVMM payload), batteries, two electrical propulsion units, four reaction wheels with cold gas thrusters for momentum management, twelve attitude thruster nozzles, one star tracker, sun sensors, on-board computer and UHF and X-Band communication units and patch antennae.

The VMMO Cubesat will facilitate the selection and TRL advancement of low-cost microelectronics (FPGA, SRAM, PROM and flash memory, A/D, D/A, multiplexers and relevant analog and digital

electronics) for beyond-LEO space applications. The CLAIRE Radiation Effects Test Board will assess the performance of a range of relevant commercial-off-the-shelf (COTS) electronic devices operating in a real lunar radiation environment by monitoring for single-event-effects and power consumption changes due to total-dose damage. This will allow direct correlations to be drawn between effects on the selected electronics test bed and the real measured environment. The VMMO Cubesat will develop and flight qualify in a relevant lunar orbit environment an altitude and orbit control system (AOCS) for semi-autonomous spacecraft operation beyond LEO. VMMO will also validate a hybrid electric/cold-gas propulsion subsystem to enable acquisition of the low-eccentricity frozen operating lunar orbit and de-spinning of the onboard reaction wheels.

References: [1] R.V. Kruzelecky, P. Murzionak, J. Lavoie, I. Sinclair, G. Schinn, C. Under-wood, Y. Gao, C. Bridges, R. Armellin, A. Luccafabris, E. Cloutis and J. Leijtens, VMMO Lunar Volatile and Mineralogy Mapping Orbiter, ICES 2018, Albuquerque, NM, paper 227, July, 2018. [2] C. Pitcher, N. Kömle, O. Leibniz, O. Morales-Calderon, Y. Gao, and L. Richter. (2016) "Investigation of the properties of icy lunar polar regolith simulants." Advances in Space Research, 57(5), 1197–1208. [3] Y. Gao, A. Phipps, M. Taylor, J. Clemmet, I. A. Crawford, A. J. Ball, L. Wilson, D. Parker, M. Sweeting, A. Curiel, P. Davies, A. Baker, T. Pike, A. Smith, and R. Gowen, (2008) "Lunar Science with Affordable Small Spacecraft Technologies: MoonLITE & Moonraker", Planetary & Space Science, 56(3-4), 368-377.

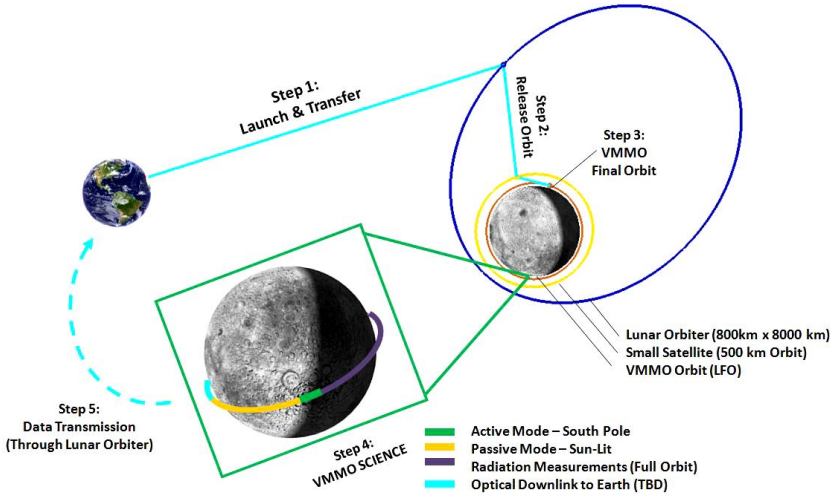

Fig 1: VMMO Mission Profile and Operation

Payload	**LVMM:** • Dual Band Laser Projection (532nm, 1560 nm) to detect Water/Ice presence at high resolution • Active Mode Res: 4 m x 44 m • Passive Mode Res: 20 m x 20 m **CLAIRE:** • Cis-Lunar Radiation Measurements
Structures	• 12 U Cubesat form factor (23 x 24 x 36 cm³) • < 24 kg total launch mass • 12 U Dispenser compatible
Electric Propulsion	• 2x IFM Nano Thrusters (0.35 mN at 35 W, total impulse of 10,000 Ns) • ΔV up to 750 m/s
C&DH	• Radiation Tolerant LEON 3 system: Xilinx XCKU060, 512 SDRAM, 4 M SRAM and 64 M PROM
Power	• Deployable Solar Arrays (6 arrays with 18 cells per panel) providing up to ~123 W of power. • LiFePO4 batteries with 8 cells at 10 A-hr, providing up to 236 W-hr total energy.
Comms	• DSN and CCSDS Compliant X-Band Transponder • UHF Transceiver (Variant STRX UHF VHF)
ADCS	• 4x Reaction Wheels (RW3-006) Sinclair Interplanetary: Momentum 60 mNms, Torque 20 mNm at 0.12 Nms • ST-16RT2 star tracker (5 arcsec boresight RMS) • Lens R&D BiSon64-B sun sensors and SINPLEX IMU • Butane Cold Gas Thrusters, 12 nozzles, 70s Isp, 0.27 kg of propellant
Orbit	• Polar Lunar Frozen Orbit • Semi-major axis 1858 km, Eccentricity 0.043

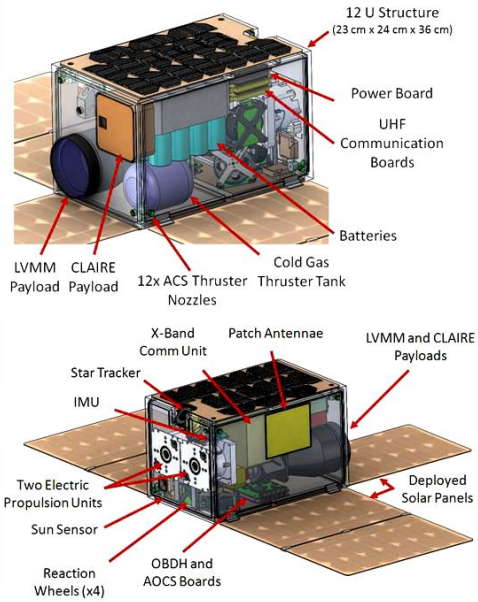

Fig 2: VMMO Spacecraft Preliminary Overview

LASER ADDITIVE MANUFACTURING USING INDIGENOUS LUNAR RESOURCES

Athanasios Goulas[1], Daniel S. Engstrøm[1], Ross J. Friel[2], [1]Wolfson School of Mechanical, Electrical & Manufacturing Engineering, Loughborough University, Loughborough, LE11 3TU (a.goulas@lboro.ac.uk), [2]Smart Electronic Systems, ITE, Halmstad University, P.O. Box 823, SE 301 18 Halmstad, Sweden.

Introduction: ISRU is considered as a necessity for any space architecture-related activity, since its substantial contribution towards mass saving and logistics will enable potential future lunar colonies and allow them to be less earth reliant. The target of this work is to reduce mass, costs and associated risk for human exploration. Success will further increase the viability of human space missions via the introduction of additive manufacturing concepts, instead of relying on the traditional method of shipping all mission assets from the earths surface [1], [2].

Additive Manufacturing (AM), also known as 3D printing, describes a range of layer based advanced fabrication techniques. Serving within the context of In-Situ Resource Utilisation (ISRU), AM is envisaged as a highly promising solution for autonomously producing a range of space mission physical and engineering assets [3]–[5] by using, as feedstock, the abundant and readily available natural resources onsite [6], [7].

A powder bed fusion (PBF) AM approach, such as that proposed in this work, could utilise thermal energy to fuse the indigenous particulate material that exists, in abundance, on the Lunar surface. The thermal energy source used for the current work is provided by laser however energy from an alternative source but could be provided; e.g. harnessing the significant thermal power from the sun at the moons surface through a system of lens (i.e. Fresnel optics) and mirrors. Additionally, using a thermal fusion process does not require additional transportion and utilisation of any solid, liquid or gas material additions to the lunar surface, which would be necessary for other AM techniques. Moreover, a Lunar-based PBF process would not require consumption of highly valuable human survivial resources, such as water.

The research discussed here details an experimental study focused on investigating the laser-based additive manufacture of JSC-1A lunar mare regolith simulant components. Such materials engineering research will aid in identifying the true potential of PBF-AM processing for delivering functional engineering assets, via ISRU, for future lunar manufacturing.

Materials & Methods: Laser additive manufacturing experiments were carried out using a Realizer SLM 100 selective laser melting machine, equipped with a λ1.06µm ytterbium doped fiber laser of 80µm beam dia. and 50W maximum power output. JSC-1A lunar mare regolith simulant was used as the feedstock for the study. The simulant was selected based on its close maching chemistry, mineralogy and glass content to the actual lunar samples collected during the Apollo missions [8]. AM test sample density and porosity were analysed using gas expansion pycnometry and scanning electron microscopy. Resultant mechanical properties were quantified using standardised compression testing and Vickers microhardness.

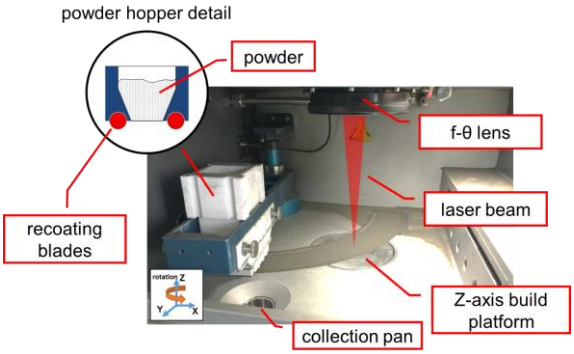

Figure [1] – Details of the SLM100's build chamber.

Results: This work has shown that a combination of laser processing perameters leading to a energy density range of 0.6 – 0.9 J/mm^2 produces repeatable, defect free and near netshape three dimensional parts (99%). The AM test samples exhibited a maximum density of 2.3 g·cm^{-3} and minimum porosity of 44%. Subsequent analysis of mechanical properties, revealed a maximum compressive strength of 4 MPa and 290 MPa elastic modulus, achieved via 0.92 J/mm^2 energy density input [9]. Early results (not shown here) from a post-processing study using conventional sintering, have revealed an increase in the resulting mechanical properties up to 3 times, when compared with the as-3D printed test samples.

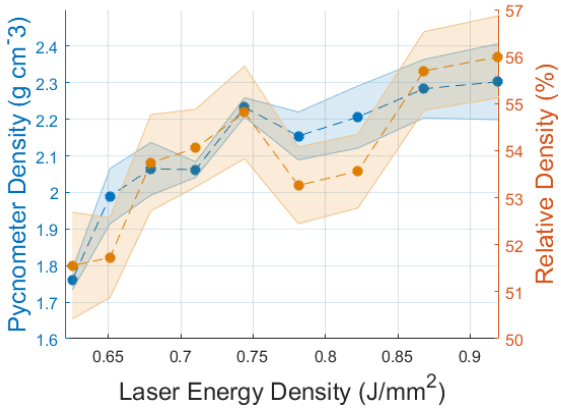

Figure [2] – Influence of laser energy on physical properties of 3D printed test samples.

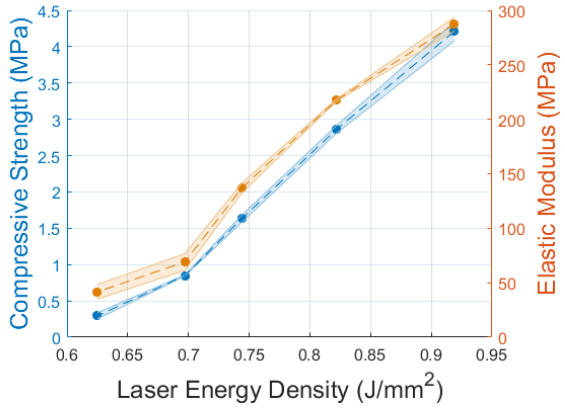

Figure [3] – Infulence of laser energy used on the mechanical properites of 3D printed test samples.

Conclusions: This experimental investigation has successfully demonstrated the ability and the applicability of a laser-based powder bed fusion AM technique to deliver three dimensional near net-shape parts from JSC-1A lunar regolith simulant. This has been achieved without the use of any process additives (i.e. binders, etc). The presented manufacturing approach could potentially serve within a future lunar facility, to provide functional engineering assets, directly via in-situ resources. Future work is further establishingsuitable post-processing techniques for improving mechanical and physical properties of lunar regolith AM components.

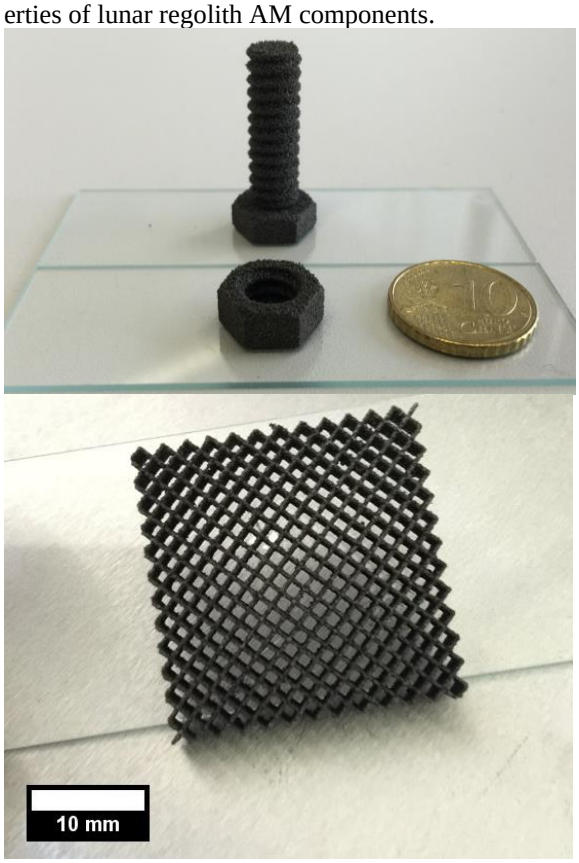

Figure [4] – 3D printed parts using JSC-1A.

Figure [5] – Near-netshape 3D printed part using JSC-1A.

References: [1] G. B. Sanders and W. E. Larson, "Progress Made in Lunar In Situ Resource Utilization under NASA ' s Exploration Technology and Development Program," J. Aerosp. Eng., vol. 26, no. 1, pp. 5–17, 2013. [2] J. Edmunson and C. McLemore, "In Situ manufacturing is a necessary part of any planetary architecture," in Concepts and Approaches for Mars Exploration, 2012, pp. 2–3. [3] F. Ceccanti, E. Dini, X. De Kestelier, V. Colla, and L. Pambaguian, "3D printing technology for a moon outpost exploiting lunar soil," 61st Int. Astronaut. Congr. Prague, CZ, IAC-10-D3, vol. 3, pp. 1–9, 2010. [4] R. P. Mueller et al., "Automated Additive Construction (AAC) for Earth and Space Using In-situ Resources," in Proceedings of the Fifteenth Biennial ASCE Aerospace Division International Conference on Engineering, Science, Construction, and Operations in Challenging Environments (Earth & Space 2016), 2016. [5] E. J. Faierson, K. V. Logan, B. K. Stewart, and M. P. Hunt, "Demonstration of concept for fabrication of lunar physical assets utilizing lunar regolith simulant and a geothermite reaction," Acta Astronaut., vol. 67, no. 1–2, pp. 38–45, 2010. [6] I. A. Crawford, "Lunar resources: A review," Prog. Phys. Geogr., vol. 39, no. 2, pp. 137–167, 2015. [7] M. Kallerud, B. Nguyen, T. Paladin, and A. Wilson, "In-Situ Resource Utilization: Investigation of Melted Lunar Regolith Simulant JSC-1A," pp. 1–10, 2009. [8] A. Goulas, J. B. Binner, R. A. Harris, and R. J. Friel, "Assessing extraterrestrial regolith material simulants for in-situ resource utilization based 3D printing," Appl. Mater. Today, vol. 6, pp. 54–61, 2017. [9] A. Goulas, J. G. P. Binner, D. S. Engstrøm, R. A. Harris, and R. J. Friel, "Mechanical behaviour of additively manufactured lunar regolith simulant components," Proc. Inst. Mech. Eng. Part L J. Mater. Des. Appl., 2018.

GROUNDTRUTHING LABORATORY EXPERIMENTS WITH DIVINER LUNAR RADIOMETER OBSERVATIONS

B.T. Greenhagen[1], K.L. Donaldson Hanna[2,3], C.N. Yasanayake[1], N.E. Bowles[3], C.M. Pieters[4] and D.A. Paige[5]; [1]Johns Hopkins Applied Physics Laboratory, [2]University of Central Florida, [3]University of Oxford, [4]Brown University, [5]University of California, Los Angeles. Email: benjamin.greenhagen@jhuapl.edu

Introduction: The Moon is the only planetary body for which we have extraterrestrial samples with known spatial context collected at a diverse range of sampling sites. These samples, an enduring legacy of the Apollo missions, provide a unique opportunity to validate planetary remote sensing datasets. Here we present results of a comprehensive study to best replicate a lunar environment in the laboratory, evaluate the most appropriate sample and measurement conditions, collect thermal infrared spectra of a representative suite of Apollo soils, and correlate these measurements with thermal infrared observations of the lunar surface.

Simulated Lunar Environment: In nearly 50 years of laboratory experiments, it has been established that thermal emission spectra measured in a simulated lunar environment (SLE) are significantly altered from spectra measured under terrestrial conditions [e.g. 1, 2, 3, 4]. The data for this study were collected in the Planetary Analogue Surface Chamber for Asteroid and Lunar Environments (PASCALE) at University of Oxford. The lunar environment is simulated by (1) pumping the chamber to vacuum pressures ($<10^{-4}$ mbar), which is sufficient to simulate lunar heat transport processes within the sample, (2) cooling the chamber (<125 K) with liquid nitrogen to simulate a surface radiating into a cold space environment, and (3) simultaneously heating the sample cups with heaters and illuminating the surface with a lamp to set up thermal gradients similar to those experienced in the upper hundreds of microns of the lunar surface.

Lunar Soils: Our reference sample suite is composed of bulk lunar soils from two NASA Curation and Analysis Planning Team for Extraterrestrial Materials (CAPTEM) requests: (1) the UCLA Bi-Directional Reflectance Function (UCLA-BDRF; 5 g mass; PI Paige) and (2) the Thermal Infrared Emissions Studies Lunar Soil Compositions Consortium (TIRES-LSCC; 3.5 g mass; PI Pieters) shown together in Table 1.

Diviner: NASA's Lunar Reconnaissance Orbiter Diviner Lunar Radiometer (Diviner) instrument produced the first global, high resolution, multispectral thermal infrared observations of an airless body. Diviner is a nine-channel, pushbroom mapping radiometer that measures broadband reflected solar radiation with two channels, and emitted thermal infrared radiation with seven infrared channels [5]. The three shortest wavelength thermal infrared channels near 8 μm were specifically designed to characterize the mid-infrared Christiansen feature (CF), an emissivity maximum, sensitive to silicate composition [1,6].

Table 1: Apollo soils available for this study.

Apollo Site	Station	Soil	Mass	Is/FeO
Apollo 11	LM	10084	5g	78
Apollo 12	LM	12001	5g	56
Apollo 14	LM	14259	3.5 g	85
Apollo 15	LM	15021	3.5 g	70
Apollo 15	Sta. 1	15071	5g	52
Apollo 15	Sta. 7	15411	3.5 g	43
Apollo 15	Sta. 9a	15601	3.5 g	29
Apollo 16	Sta. 1	61141	5g	56
Apollo 16	Sta. 6	66031	3.5 g	102
Apollo 16	Sta. 11	67701	3.5 g	39
Apollo 17	LM	70181	5g	47
Apollo 17	Sta. 2	72501	3.5 g	81
Apollo 17	Sta. 9	79221	3.5 g	81

Results: We conducted a preliminary suite of experiments on Apollo soils 15071 (maria) and 61141 (highland) using different environmental conditions and found spectral changes similar to [4]. We determined that the spectral effects causing by variable thermal environments were significant enough to reconsider our measurement methodology. For our new methodology, we heated each sample to the brightness temperature observed by Diviner at each sampling station for a 52.5° solar incidence angle (similar to the lamp incidence angle in PASCALE). The range was 323 K to 349 K. For comparison, we also heated each sample to the average noontime temperature of the sampling stations, 386 K.

We found that analyses of Diviner observations for individual sampling stations and PASCALE measurements of the returned Apollo soils in a relevant environment generally show good agreement. Furthermore, the agreement was improved when the illumination geometry of the laboratory experiments and Diviner observations are similarly constrained. In contrast, comparisons between Diviner observations and thermal infrared emission and reflectance measurements under terrestrial conditions do not agree well. These analyses underscore the need for SLE measurements to validate thermal emission datasets from the Moon and other airless bodies.

References: [1] Logan L.M. et al. (1973) JGR, 78, 4983. [2] Henderson B.G. et al. (1996) JGR, 101. [3] Thomas I.R. et al. (2012) Rev.Sci.Inst., 83 (12), 124502. [4] Donaldson Hanna K.L. et al. (2017) Icarus, 283, 326-342. [5] Paige D.A. et al. (2010) SSR, 150. [6] Greenhagen B.T. et al. (2010) Science, 329, 1507.

EXAMINING ISSUES EFFECTING THE APPARENT OPTICAL MATURITY OF LUNAR IMPACT CRATERS. J.A. Grier[1], A.M. Stickle[2], J.T.S. Cahill[2], R.N. Watkins[1], and M.E. Banks[3]. [1]Planetary Science Institute (Tucson, Arizona, USA; jgrier@psi.edu), [2]Johns Hopkins University Applied Physics Laboratory, [3]NASA Goddard Space Flight Center.

Introduction: Current investigations of the lunar surface are making substantial strides by integration of data sets (i.e. remote sensing spacecraft data and laboratory experiment data.) [1,2]. Such investigations rely first on understanding how remote sensing data at different wavelengths compare [3], and then tying these results to related laboratory work to provide 'ground truth' for age, grain size, composition, etc.

A key aspect of this work is the understanding of how the lunar surface changes with time, and how the processes driving that evolution affect the apparent ages of impact craters. Since limited absolute ages are available for lunar impact craters, the few ages that we have must be tied to relative measures from remote sensing in order to estimate the chronologies of lunar events.

The optical maturity (OMAT) of impact craters and their ejecta is a powerful tool in determining relative age, and is made even that much more useful by using absolute ages for calibration [4,5,6]. There are many important issues effecting OMAT that are currently under examination, including how various data sets compare at different wavelengths, how crater size effects relative age estimation, and how the nature of impact ejecta (blocks/grain size/secondaries) can influence the optical maturity of impact ejecta [7]. We discuss several of the most important issues, and their effects, here.

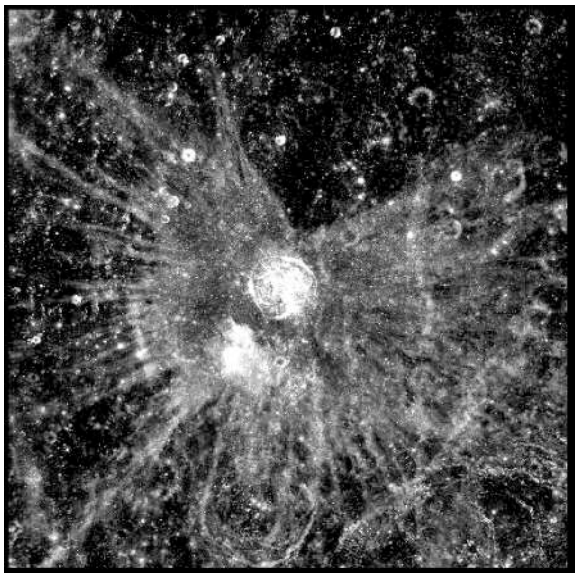

Figure 1: OMAT image (derived from Kaguya data) of Petavius B. Stretched to show detail in the ejecta structure, including continuous/discontinuous ejecta, rays, and exclusion zone from oblique impact.

Absolute and Relative Ages: Absolute ages of impact craters are determined by laboratory processes such as isotopic dating (K/Ar, $^{40}Ar/^{39}Ar$, Rb/Sr, etc.) or cosmic ray exposure (CRE). These absolute ages can then be tied to relative measures such as crater density (crater counting) or optical maturity (OMAT). Crater count ages for the Moon, as calibrated by absolute ages, have been extrapolated all over the lunar surface, to Mars, and beyond. Yet there are very few absolute ages that are available to calibrate these relative measures.

Absolute ages have been measured on many samples returned from the Apollo missions (Table 1, [8,9]. While substantially more ages of impact melts and impact breccias exist from laboratory analyses of lunar meteorites, on the ages in Table 1 can be directly tied by geologic context to specific craters. Additional references for ages can be found in [9].

Crater Name	Size (Diam)	Age	Mission	Reference(s)
Copernicus	93 km	810 Ma	Apollo 12	Bogard et al., 1992 Alexander et al., 1976, 77 Wasson and Baedecker, 1972 Silver, 1971
Tycho	85 km	109 Ma	Apollo 17	Drozd et al., 1977 Lucchitta, 1977 Wolfe et al., 1975
Aristillus	55 km	1.3 Ga	Apollo 15	Ryder et al., 1991 Bernatowicz et al., 1978
Autolycus	39 km	2.1 Ga	Apollo 15	Ryder et al., 1991 Bernatowicz et al., 1978
North Ray	1 km	50 Ma	Apollo 16	Arvidson et al., 1975
South Ray	800 m	2 Ma	Apollo 16	Eugster, 1999 Arvidson et al., 1975
Camelot	700 m	< 140 Ma ?	Apollo 17	Arvidson et al., 1975
Cone	340 m	26 Ma	Apollo 14	Arvidson et al., 1975
West	180 m	100 Ma	Apollo 11	Beaty and Albee, 1980 Geiss et al., 1977
Baby Ray	150 m	< 2 Ma ?	Apollo 16	Eugster, 1999 Arvidson et al., 1975
Shorty	110 m	19 Ma	Apollo 17	Eugster et al., 1977 Arvidson et al., 1975
Bench	~ 75 m	< 99 Ma ?	Apollo 12	Arvidson et al., 1975

Table 1: Absolute ages available for lunar craters as determined from Apollo samples, [8,9].

Impact Crater Diameter: It has been understood since early in the study of lunar craters that the diameter of a crater plays an important role in how that crater and its ejecta change with time (Figure 2) [10]. Larger impact craters remain fresher and younger-looking longer than smaller craters. This effect holds true not just for a crater's general morphology but also for crater ejecta. The OMAT profiles of craters at all sizes shows this same effect. Larger craters such as Copernicus (~100 km) will appear brighter in OMAT longer than smaller craters (especially those <10 km) [4].

This becomes a critical issue when we attempt to tie absolute ages to other relative age markers such as OMAT or crater count statistics. Very few absolute ages are available, and almost none exist for craters from 1km to 40km in diameter. This is a crucial size range to understand for dating and for determining impact hazards [9]. Linear interpretations of crater degradation with time are not likely to apply to craters of larger diameters.

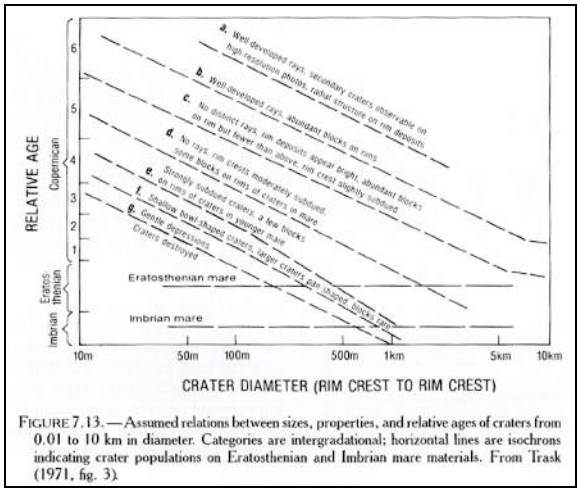

FIGURE 7.13.—Assumed relations between sizes, properties, and relative ages of craters from 0.01 to 10 km in diameter. Categories are intergradational; horizontal lines are isochrons indicating crater populations on Eratosthenian and Imbrian mare materials. From Trask (1971, fig. 3).

Figure 2: This plot from [10] was taken from [11] first published in 1971. It was an early attempt at a graphical quantification of the effect of impact crater size on the apparent age of the crater, and how that crater's morphology and ejecta change with time.

Composition, Grain Size, Blocks, and Albedo Features: Aside from crater diameter, there are other issues when considering the implications of optical maturity of impact craters and the general maturity of the surrounding terrain. Ongoing investigations include examination of Thorium anomalies and their relationship to surface properties including grain size and maturity [12,1]. Enigmatic features such as the lunar swirls may have a relationship to the ejecta from immature craters – the material may be feeding into and replenishing such zones, or may be simply protected from further maturation [13]. Relationships need to be established for these effects in order to quantify how ejecta mature over time.

Of particular note are how blocks (boulders) contribute to optical maturity [9,14]. It has long been considered that the erosion of blocks by micrometeorite bombardment provides a refreshing mechanism for immature materials. Thus larger, more energetic impacts that emplace bigger and more abundant boulders should exhibit a different pattern for ejecta maturation than do smaller impacts with less abundant blocks in their ejecta blankets. Slope or 'sharpness' of topography may play a role [15,16]

Acknowledgements: This material is based upon work funded by the NASA Lunar Data Analysis Program (LDAP) award number NNX15AV56G.

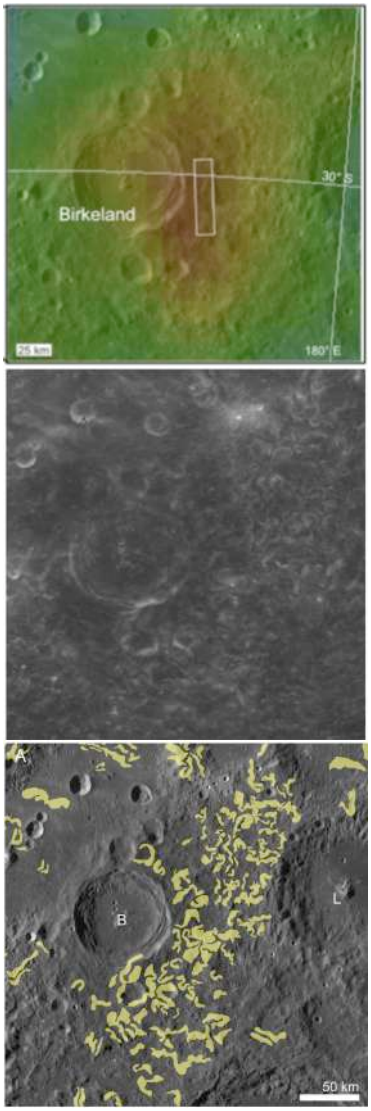

Figure 3: Top to bottom, Th abundances (red = higher) from [12], OMAT image from [1], and mapped lunar swirls from [13].

Additional funds were provided through a partnership between the TREX team supported by NASA Solar System Exploration Research Virtual Institute (SSERVI) (NNH16ZDA001N) and the NASA SSERVI VORTICES team (NNA14AB02A).

References: [1] Banks, M.E. et al. 49th LPSC, #2083, 2018. [2] Hendrix, A. et al. 42nd Cospar Assem. 2018. [3] Stickle, A.M. et al. 48th LPSC, 2017. [4] Grier, J.A. et al. JGR 2001. [5] Lucey, P.G., et al. JGR 1999. [6] Lucey, P.G. et al. JGR 1998. [7] Grier, J.A. et al. in Issues in Crater Studies, LPI 2015. [8] Grier, J.A. Dissertation 1999, Univ. of AZ. [9] Ghent, B. et al. Icarus, 2016. [10] Wilhelms, D.E. USGS 1348, 1987. [11] Trask, NASA-CR116408, 1971. [12] Moriarty et al, AGU 2018. [13] Denevi, B. Icarus, 2016. [14] Watkins, R. et al. AGU 2018. [15] Grier, J.A. et al. 31st LPSC, 2000. [16] Banks, M.E. et al. 50th LPSC, 2019.

FLUIDISATION OF LUNAR REGOLITH SIMULANTS FOR ISRU APPLICATIONS L. Grill[1] and P. Reiss[1], [1]Institute of Astronautics, Technical University of Munich, Boltzmannstr.r 15, 85748 Garching, Germany (l.grill@tum.de).

Introduction: The Moon is an important stepping stone on the way to interplanetary space. Since resupply flights from Earth for long-duration missions are cost-intensive, research on In-Situ Resource Utilization (ISRU) technologies has gained significance over the recent years. One major research focus is the production of oxygen from lunar regolith by means of different gas-solid reactions. Even though fixed bed reactors and rotary tube reactors have been investigated before [1,2], fluidised bed reactors seem to be the most suitable reactor type for this application.

Fluidised beds for ISRU applications: Lunar regolith has a wide particle size distribution from several nanometres up to larger than one millimetre [3]. Unlike most other reactor types for gas-solid systems, fluidised bed reactors can be operated using fine-grained powders with a wide size distribution. Solids in fluidised beds are rapidly mixed, leading to nearly isothermal conditions in the reactor, and to high heat and mass transfer rates between gas and particles. Furthermore, heat transfer rates between the fluidised bed and immersed objects are high. All of that is desirable considering the operating temperatures of the studied oxygen extraction processes close to the sintering temperature of lunar regolith. Rapid mixing can prevent sintering either by reducing contact times between the particles to prevent the formation of solid bonds, or by breaking apart previously formed bonds. Isothermal conditions in the fluidised bed as well as high heat transfer rates between heat exchangers and the fluidised bed prevent local temperature hotspots, thus minimizing the probability of sintering or melting of the solid. Isothermal conditions also allow to simply and reliably control the temperature in the reactor, making fluidised bed reactors suitable for large-scale operations. [4]

Due to complex hydrodynamics in fluidised beds, designing, upscaling and optimisation of reactors requires intensive lab-scale pilot testing to understand and to be able to predict intrinsic phenomena. Furthermore, prior studies [5–7] have revealed that gravity has a major impact on the flowability and hence the fluidisation behaviour of powders. This is why test results on the fluidisation behaviour of lunar regolith or suitable regolith simulants under terrestrial gravity can only be applied to lunar gravity in a limited way. The possibilities to test a reactor system under reduced gravity before a mission are limited and an incorrectly designed payload will lead to an inefficient or even insufficient operation. Numerical simulation is the most promising approach to understand and predict the behaviour of a fluidised bed. Many experiments have to be performed to help develop, verify and validate numerical models. In the following, results from a pre-study on the fluidisation behaviour of the lunar regolith simulants JSC-1A, EAC-1 and TUBS-M are presented.

Experimental setup: Experiments have been performed in a fluidisation test rig located at the Chair of Energy Systems at Technical University of Munich (Fig. 1). Nitrogen (preheated to 25 °C) was used as fluidisation gas. For each simulant, the bed expansion, pressure drop, and heat transfer coefficient between the bed and an immersed heat flux probe was determined. The measurements were performed at gas flow rates between 0.5 cm/s and 10 cm/s for JSC-1A, 0.5 cm/s and 12 cm/s for EAC-1 and 0.5 cm/s and 14 cm/s for TUBS-M.

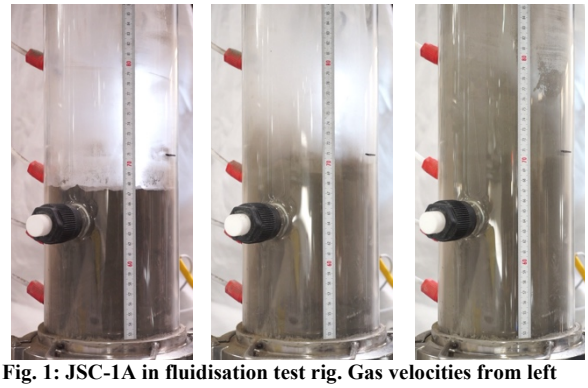

Fig. 1: JSC-1A in fluidisation test rig. Gas velocities from left to right: 0 cm/s, 4cm/s, 10 cm/s.

Results: The results of the study are shown in Fig. 2 to Fig. 4. The bed expansion was determined visually, thus results must be considered as qualitative reference values. The pressure drop through the bed was measured. The minimum fluidisation velocity was determined as the intersection point of the linear trend line of the measurement points before minimum fluidisation velocity and passing through the origin, and the linear trend line of the measurement points after minimum fluidisation velocity. The determined minimum fluidisation velocities are 4.3 cm/s for JSC-1A, 4.6 cm/s for EAC-1 and 5.2 cm/s for TUBS-M.

The experiments showed that the finest powder particles were blown out of the fluidised bed. Thus, the portion of fines in the powder bed decreased during the experiments, which can have an influence on the fluidisation behaviour of the powder. Furthermore, the powder seemed to demix during the experiments. The demixing became stronger over time, even though the powder was intermixed between every measurement point. This could be a result of the decreasing portion of fines in the bed. Particle size analyses will be performed in a next step in order to better understand possible explanations of this behaviour.

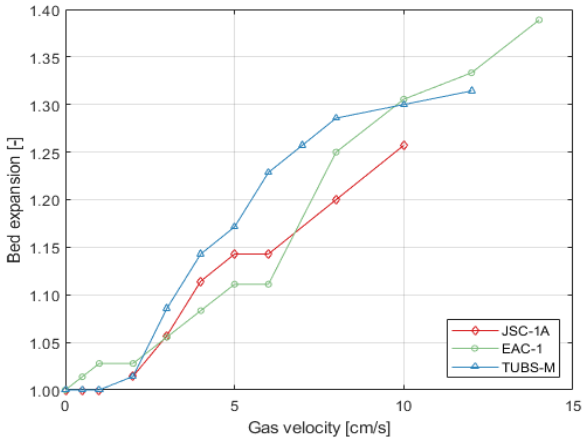

Fig. 2: Bed expansion of the simulants JSC-1A, EAC-1, and TUBS-M for different gas velocities.

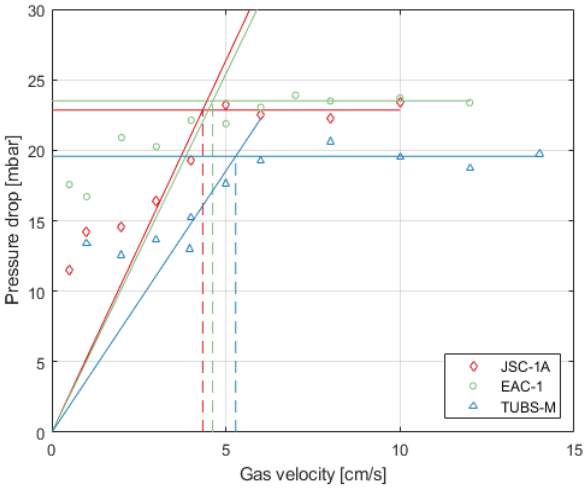

Fig. 3: Pressure drop in the fluidised bed of the simulants JSC-1A, EAC-1, and TUBS-M, and trend lines for different gas velocities.

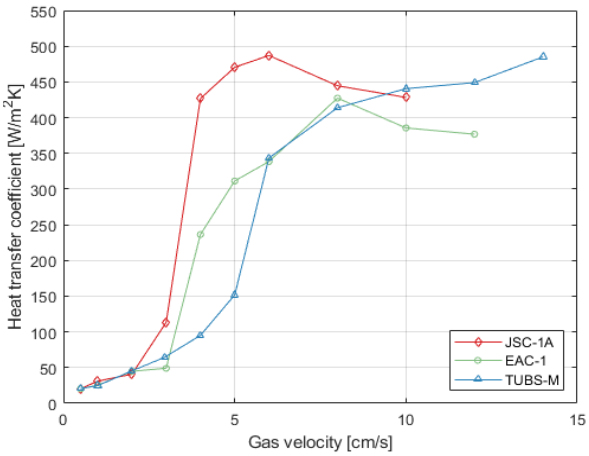

Fig. 4: Heat transfer coefficient between the bed of the simulants JSC-1A, EAC-1, and TUBS-M, and an immersed heat flow probe for different gas velocities.

Future work: Further characterisation (particle size distribution, sphericity factor, bulk density, cohesion, friction angle) of the lunar regolith simulants will be performed in order to select the most suitable one for the purpose of investigating the behaviour of lunar regolith in a gas-solid fluidised bed. In the long term, a numerical model shall be developed to simulate and predict the behaviour of lunar regolith in a fluidised bed under Earth gravity. This model can then be adapted for the purpose of predicting the behaviour of regolith under lunar gravity.

References:

[1] H. Yoshida, T. Watanabe, H. Kanamori, T. Yoshida, S. Ogiwara, K. Eguchi, Second Sp. Resour. Roundtable, Golden, 2000.

[2] D.L. Clark, B.W. Keller, J.A. Kirkland, Proc. AIAA Sp. Conf. Expo. (2009) AIAA 2009-6475.

[3] W.D. Carrier, Moon. 6 (1973) 250–263.

[4] D. Kunii, 国井大蔵, O. Levenspiel, Fluidization engineering, 1991.

[5] G.H. Qian, I. Bágyi, I.W. Burdick, R. Pfeffer, H. Shaw, J.G. Stevens, AIChE J. 47 (2001) 1022–1034.

[6] O.R. Walton, C.P. De Moor, K.S. Gill, Granul. Matter. 9 (2007) 353–363.

[7] R. Williams, R. Shao, R.A. Overfelt, Granul. Matter. 10 (2008) 139–144.

Bundle adjustment of LROC NAC Stereo Images for High Precision DTMs and Maps. I. Haase[1], P. Gläser[1,2] and J. Oberst[1,3], [1]Technical University Berlin (TUB), Dept. of Planetary Geodesy, Berlin, Germany (isabel.haase@tu-berlin.de), [2]Ronin Institute for Independent Scholarship, Montclair, NJ 07043, USA, [3]German Aerospace Center (DLR), Dept. of Planetary Geodesy, Berlin, Germany.

Introduction: Stereo image pairs of the Lunar Reconnaissance Orbiter Camera (LROC) Narrow Angle Camera (NAC) [1] are well suited to create Digital Terrain Models (DTMs) of the lunar surface, usually providing a lateral resolution of 2 m. Various teams, such as the LROC group at the Arizona State University (ASU), the University of Arizona (UA), the United States Geologic Survey (USGS), or NASA AMES (to name just a few), use commercial photogrammetric software, in-house developments or combinations of both to calculate adjusted and controlled DTMs. Within the photogrammetric processing chain a sophisticated and customized Block Adjustment (BA) is of fundamental importance. Different approaches, depending on how accurately and precisely the reality and the different sources of errors are modeled, will provide more or less accurate estimates of the ground truth. Here we present our efforts of providing DTMs of high relative and absolute accuracy as well as high lateral (1.5-2 m) and vertical resolution (0.1 m) for selected targets of interest, e.g. to support future lunar landings and mission planing. For this reason we implemented a BA specifically for image data as it is provided by the double-camera system LROC NAC of the Lunar Reconnaissance Orbiter (LRO) mission.

Challenges in Extraterrestrial Photogrammetry: The photogrammetric processing of planetary images to accurate DTMs is by far more challenging than the evaluation of terrestrial images. The calibrated values for the sensor model, i.e. the principal point, the calibrated focal length, and image distortion (parameters of the interior orientation), determined and documented in the laboratory before launch, are not necessarily stable. They are likely to change during the mission due to the extreme conditions in space (e.g. temperature changes) and because of physical shock effects during launch. Errors in the sensor model turn into systematic errors and are very difficult if not impossible to be accurately quantified by an on-orbit self-calibration due to insufficient geometric constraints and lack of accurate ground control. In addition, due to thermal stress the position and attitude of the camera relative to the spacecraft bus can change and thus its mutual alignment in case of multi-camera systems.

Furthermore, in order for the final DTM to be of correct scale and situated at the right position (absolute accuracy), either the position and pointing of the camera (the exterior orientation) must be accurately known or there must be global, geo-reference on the surface (control points) that can be identified in the images. Both prerequisites are usually not given with sufficient accuracy in extraterrestrial image data. The global accuracy of LRO's orbit data is given as 10 m [2], and only five (anthropogenic) features on the nearside are known with an accuracy at cm scale.

Nevertheless, in order to improve the mentioned parameters and to obtain useful results, the event of the image recording can be geometrically reconstructed in a weighted least-squares adjustment. However, the quality and reliability of the results of a BA highly depends on how well the functional model reflects the physical reality, and the achieved accuracy estimated by an adjustment calculation is only meaningful, if (and only if) the stochastic model of the BA is correct.

Bundle Adjustment: The BA implemented at the TU Berlin is embedded in a modified version of the German Aerospace Center (DLR) stereo processing chain [3], which was originally developed to process images acquired by the High Resolution Stereo Camera (HRSC) on board the Mars Express orbiter. A detailed description of the generation of LROC NAC DTMs by the TU Berlin group is given by [4].

The BA is based on a weighted least-squares adjustment (Gauss-Markov model), and the functional relationship between the image and the object space are the extended collinearity functions as proposed by [5]. They rigorously describe the alignment of the two cameras NAC-L and NAC-R mounted on the same platform. The position and pointing of the NAC-R are calculated relative to the NAC-L. We hold the lateral offset (~33 cm) of the right camera from NAC-L fixed, but leave some freedom to the attitude of NAC-R, to achieve an improved alignment of the two cameras. LRO's trajectory (the position of the NAC-L camera, to be more precise) and the orientation of NAC-L are modeled by 2nd degree Lagrange polynomials.

Control points providing the geodetic datum are provided by co-registered LOLA shots of the tracks available in the area of interest. To detect outliers in the image tie point observations, which were determined by applying the DLR automatic image matcher, we implemented an outlier detection approach following Baarda's Data Snooping. The unknown parameters, e.g. the exterior orientations and the LOLA shots, are additionally treated as pseudo observations and their a priori standard deviations were approximated by a variance component estimation within a pre-adjustment. This procedure has proved to be a decisive and suitable method for better as-

sessing the influence of the different observation groups on the overall result. The BA is carried out iteratively and usually converges after 6-7 iterations.

LOLA Co-Registration: Since the LRO mission, the globally available LOLA data have been used as global lunar reference frame (Smith et al., 2017). Instead of using the interpolated LOLA DTM, we integrate the nominal LOLA shots to our BA. As the laser altimeter shots are not correlated to specific features on the lunar surface, and thus are not detectable in the images, their unambiguous use as geodetic reference is limited and can only be achieved indirectly in roundabout ways. To provide a geodetic datum to our bundle adjustment we use the co-registration technique developed by [6]. The co-registration plays an important role, as it provides a mean to accurately tie LOLA shots to the image space. For selected, registered LOLA points their corresponding object points are identified in the object point cloud (derived from forward ray intersection) and are thus simultaneously correlated with the related image tie points. Usually, at least 20 LOLA orbits cover a typical NAC-L/-R model, and we use about 2 % of the shots of a track, but at least 15 shots per track.

Accuracy:

The variance component estimation ensures that the a priori accuracies and thus the weights are distributed among the observation groups in a stochastically reasonable way, so that after the BA the a posteriori variance factor ($\sigma_{0\ a\ post}$) amounts to 1.

The ray intersection (triangulation) accuracy of the stereo model is a valuable measure for assessing the quality of the adjustment and the relative accuracy achieved. Before the adjustment, the intersection error for a NAC-L/-R model is typically distributed unevenly across the model and usually lies between 1-10 m. Due to the improved exterior orientation of the images, after the BA the image rays coincide almost perfectly within a ground pixel. The average intersection accuracy after the BA is homogeneous for the involved stereo models and far below the image pixel size, at about 0.15 m on average. This also guarantees that the pixels in the overlapping area of adjacent images (e.g. the narrow NAC-L and NAC-R overlap) coincide during ortho-rectification and that mosaicing of images is possible without offsets and feature duplications (see Figure 1).

The achieved accuracy is also checked by a final co-registration to the LOLA tracks. The height difference between the registered LOLA shots and the adjusted and controlled NAC DTM is usually less than 2 m. The NAC DTM is optimally placed in the middle of the LOLA tracks used during adjustment. The adjustment also provides accuracy assessments of the used LOLA tracks, which can be useful for further LOLA related products.

Summary: We implemented a least-squares bundle adjustment for spaceborne CCD line-scan multi-camera systems. The BA was applied to LROC NAC images and it showed that the overall geometry of the stereo models could be much improved.

Acknowledgements: We gratefully acknowledge the LRO mission, the LOLA science team, and the LROC science team at Arizona State University. I. Haase was funded by the Federal Ministry for Economic Affairs and Energy (FKZ 50OW1702) and P. Gläser by a grant of the German Research Foundation (GL 865/2-1).

References:

[1] Robinson, M. S., et al. (2010) *Space Science Reviews*, 150, pp. 81–124. [2] Smith, D. E., et al. (2017) *Icarus*, 283, pp. 70–91. [3] Scholten, F., et al. (2015) *PE&RS*, 71(10), 1143–1152. [4] Haase, I., et al. (2019) *Earth and Space Science*, 6, pp. 59–95. [5] Ebner, H., et al. (1992) *ISPRS Archives – Volume XXIX Part B4*, pp. 458–464. [6] Gläser, P., et al. (2013) *Planetary and Space Science*, 89, pp. 111–117.

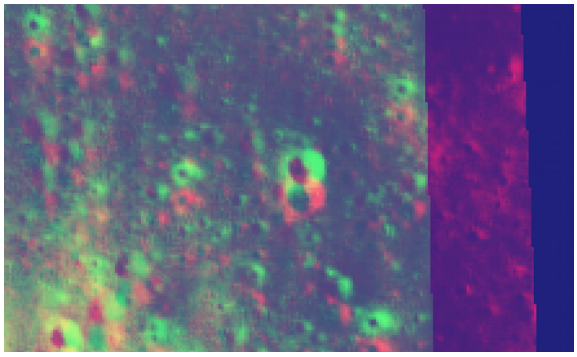

(a)

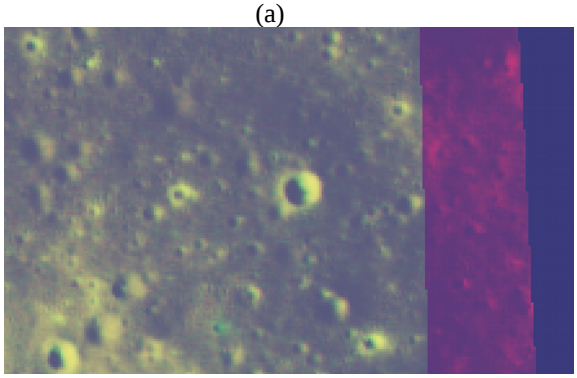

(b)

Figure 1: Image overlay of both NAC Left images acquired from different orbits (map projected and colored); red: M1159863525L; green: M1159877765L. (a) Before adjustment: Errors in the exterior orientation result in y-parallax of about 11 pixels and ambiguous feature locations. (b) After adjustment: The images coincide and there is no more (visible) parallax.

A UNIVERSAL FLOWSHEET AND TERMINOLOGY FOR IN SITU RESOURCE UTILISATION (ISRU)

K. Hadler[1], D. J. P. Martin[2], J. Carpenter[3] and J.J. Cilliers[1]
[1]Department of Earth Science and Engineering, Imperial College London, London, SW7 2AZ, UK
[2]European Space Agency ECSAT, Fermi Avenue, Harwell Campus, Didcot, Oxfordshire, OX11 0FD, UK.
[3]European Space Agency ESTEC, Keplerlaan 1, 2201 AZ Noordwijk, Netherlands.

Introduction: In Situ Resource Utilisation (ISRU) has the potential to be the breakthrough technology that enables the further exploration of space by humankind.

The use of in-space materials to provide water, fuel and building materials reduces significantly the launch mass, but also presents a multitude of challenges in numerous areas. These range from uncertainties in the mineralogical and physical characteristics of the local regolith [1] to the development of processes and associated technologies that are reliable under extreme environmental conditions, including varying temperatures, low gravity and abrasive dust [2].

The production of oxygen on the Moon using lunar regolith has received significant attention in recent years [3], since it can be used both to sustain human life and as fuel for further exploration. Furthermore oxygen is a major component of launch vehicles, spacecraft and lander masses, but comprises more than 40% of lunar regolith by weight [4], making it a prime in-situ resource. Other chemical and mineral resources such as metals and rare gases also may be considered valuable resources, particularly as they often are produced as by-products of extraction processes (e.g. [5]).

While a range of extraction processes to produce usable resources have been in development for some time, practical and successful implementation of ISRU requires that all the stages of the extraction flowsheet are considered. This requires a complete mine-to-product type approach, analogous to that of terrestrial mineral extraction.

A key high-level challenge is the unique cross-disciplinary nature of ISRU; it integrates space systems, robotics, materials handling and beneficiation, and chemical process engineering. This is underpinned by knowledge of the lunar or planetary geology, including mineralogy, physical characteristics, and the variability in local materials.

Combining such diverse fields in a coordinated way requires a universal framework, on which the different processes and systems can be mapped, in order to identify gaps in the knowledge and to progress the field towards implementation. In this paper, the foundations of this universal framework are presented.

A Universal Flowsheet: Much of the ISRU-related research has, to date, focused on specific processes for extraction of oxygen, for example hydrogen reduction of lunar regolith (e.g. [6]). Extraction of any valuable commodity, however, requires a suitable feedstock. Such a feedstock must be predictable and consistent in terms of composition and physical properties. This enables the extraction processes to be most efficient in recovering and transforming the valuable resource and to be autonomous or controlled effectively.

The production of the necessary, consistent feedstock is likely therefore to require beneficiation. Beneficiation increases the mass fraction of the component of interest (e.g. ilmenite, or specific mineral particle size range) in the feedstock by removing other components that are less useful or may interfere with the subsequent extraction. This must be accounted for in the overall ISRU process chain, or flowsheet.

Each extraction process can be described by a single, overall flowsheet, which is given in Fig. 1. This universal flowsheet comprises three key stages; excavation, beneficiation and extraction. This is analogous to terrestrial mining operations.

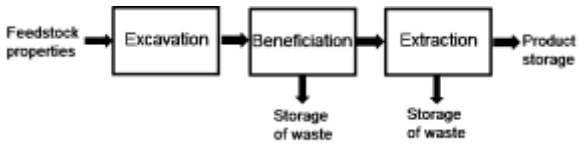

Figure 1: Universal flowsheet for ISRU processes

There is great benefit in mapping existing research onto the universal flowsheet, so as to identify weaknesses in the knowledge and technology base.

For ISRU to become a reality, all stages of the flowsheet must be integrated and function in the given environmental conditions (i.e. the planetary surface of interest).

A Universal Terminology: In developing a framework for ISRU, it is apparent that a clearly defined set of terms is required to describe the efficiency of a process. This is important for comparing the performance of different processes, in addition to enabling calculation of likely throughputs, and therefore defining requirements from the upstream processes of excavation and beneficiation. Many different terms are used in the literature, unfortunately they are neither consistent nor clearly defined.

The following key definitions are proposed:

Yield: Mass of product produced (e.g. O_2) per mass of feedstock (e.g. regolith into beneficiation)

Recovery: Mass of product produced (e.g. O_2) per mass of product in feedstock (e.g. O_2 in regolith into extraction process)

Grade: Mass of product (e.g. O_2 in feedstock) per mass of stream (e.g. total mass of feedstock)

Enrichment ratio: Grade of given species in outlet of process as a fraction of the grade of the same species into the process

Refresh ratio: Mass of fresh reactant required (e.g. H_2) per mass of product produced

Conversion: Mass of reactant consumed per fresh reactant input.

This list of terminology is not exhaustive, but these terms are the fundamental basis for ISRU systems design. Further, some terms are more applicable to certain stages of the flowsheet; e.g. *grade* and *enrichment ratio* are more appropriate to beneficiation, while *refresh ratio* and *conversion* are applicable to extraction (Fig. 1).

If the wider ISRU communities are to communicate their findings effectively, this terminology (and others, as required) must be adopted and used consistently.

Future Outlook: The aim of this work is to ensure that meaningful advances in ISRU are made, and that the process is considered as an entire system.

The Universal Flowsheet and Terminology are the beginning of this unified framework.

However, they must become the ISRU standard, and be consistently extended, to bring together effectively the research in this relatively new field.

In the next phase of development, the physical characteristics of local materials, specifically lunar regolith, will be defined in the context of ISRU feedstock.

References: [1] Schreiner S.S., Dominguez J.A., Sibille L., Hoffmann J.A. (2016a) *Adv Space Res, 57*, 1209-1222. [2] Colwell J.E., Batiste M., Horanyi S., Robertson S., Sture S. (2007) *Rev Geophys, 45*, RG2006. [3] Anand M., Crawford I.A., Balat-Pichelin M., Abanades S., van Westrenen W., Peraudau G., Jaumann R., Seboldt W. (2012). *Planet Space Sci, 74*, 42-48. [4] Schreiner S.S., Sibille L., Dominguez J.A., Hoffmann J.A. (2016b) *Adv Space Res, 57*, 1585–1603. [5] Schwandt C., Hamilton J.A., Fray D.J., Crawford I.A. (2012) *Planet Space Sci, 74*, 49-56. [6] Lee K.A., Oryshchyn L., Paz A., Reddington M., Simon T.M. (2013) *J Aerospace Eng, 26(1)*, 67-73.

Acknowledgements: This is part of the ESA Topical Team on 'A complete resource production flowsheet for lunar materials'. The authors would like to acknowledge the contribution of Andrew Morse (Open University), Philipp Reiss (TUM), Karol Seweryn (CBK), Alexandre Meurisse (ESA), Joshua Rasera and Stanley Starr (Imperial College London).

ASSESSING THE SURVIVABILITY OF TERRESTRIAL MATERIAL IMPACTING THE LUNAR SURFACE. S. H. Halim[1], I. A. Crawford[1], G. S. Collins[2] and K.H. Joy[3], [1]Department of Earth and Planetary Sciences, Birkbeck, University of London, Malet St., London WC1E 7HX, [2]Department of Earth Science & Engineering, Imperial College London, Kensington, London SW7 2AZ, [3]School of Earth and Environmental Sciences, University of Manchester, Oxford Rd., Manchester M13 9PL.

Introduction: The lunar surface has been impacted by a plethora of hypervelocity projectiles over its lifetime, leading to the heavily cratered surface we see today. This rich impact history is dominated by the Late Heavy Bombardment (LHB), an epoch circa 3.9 Gyr ago where it is suggested that the asteroid belt and terrestrial planets experienced frequent large-scale impact bombardment. During this time, Earth would have experienced many hypervelocity impacts, ejecting terrestrial material at velocities great enough to surpass escape velocity and take up Moon-crossing orbits. This has led to the proposal that such ejecta could be preserved on the lunar surface as terrestrial meteorites [1-4], if they survive impact. The lack of atmosphere, plate tectonics, and the low surface gravity, are all factors that enhance the likelihood that the Moon might still preserve a record of the early Earth. In some regions of the lunar surface, as much as 510 kg km^{-2} of terrestrial material may have impacted, with a globally averaged concentration of terrestrial material in the regolith between 1–2 ppm [4].

Previous modelling has been carried out to assess the survival of projectiles impacting the lunar surface, using ANSYS AUTODYN [5]. It considered solid, cube-shaped, basalt/sandstone projectiles impacting an unconsolidated sand target layer at 2.5 km s^{-1} and 5 km s^{-1} with varied impact angles. Here we update and improve previous analysis of terrestrial meteorite survival, using the two-dimensional version of the iSALE shock physics code [6-8]. We consider the effect of projectile shape and the equation of state (EOS) used, as well as considering target and impactor porosity. Previously, specific peak pressure thresholds have been used as a proxy for survivability in a variety of materials. Here we expand the previous work to include peak temperatures.

Methods: We simulated non-porous and porous sandstone (sst) projectiles vertically impacting a basalt target layer at 5 km s^{-1} (the upper limit found via analytical methods by [4] for vertical impact speeds of terrestrial meteorites on the Moon) in cylindrical geometry. The impactor was modelled in three different shapes: (1) 0.5 m diameter spheroid, (2) 0.5 × 1 m oblate spheroid, and (3) a 1 × 0.5 m prolate spheroid. An oblate spheroid describes a flattened spheroid, where the horizontal diameter, parallel to the target surface, is longer than the vertical diameter. Prolate spheroids are the opposite. Impact compaction of pore space was simulated using the epsilon-alpha porosity model [8]. Initial porosity of the target basalt layer was zero (solid), 30%, 50% and 70% for different simulations. The basis for a 30% regolith porosity stems from Apollo samples with intragranular porosities in lunar regolith of 21-32%, rising to 52% when including intergranular porosities [9]. An upper limit of 70% porosity was chosen based on the general area where the LCROSS mission impacted the lunar surface and suggested a surface porosity of >70% [10]. The porosity of the impactor was varied between 0% (solid) and 40%, at 10% intervals.

The solid component of the sandstone and basalt were modelled using equation of state tables derived using the analytical equation of state package (ANEOS). The strength of the impactor and target materials was modelled using the method described in [7]. Each model used 50 cells per projectile radius (cppr), improving resolution on [5], with tracer particles used to track material located within each projectile cell at time zero. These tracers record peak pressures and temperatures of the projectile material during the simulation. Simulations used lunar gravity (1.62 m s^{-2}), a surface temperature of 273 K and were run until peak pressures within the projectile stopped increasing (1.5 ms).

Results: Ten models were considered (Table 1): (A) sst into basalt, (B) sst into 30% porous basalt, (C) sst into 50% porous basalt, (D) sst into 70% porous basalt, (E-H) 10-40% porous sst into basalt, (I) oblate spheroid into basalt, and (J) prolate spheroid into basalt.

Table 1: Mean peak shock pressures and temperatures for projectiles in models.

Model	Pressure (GPa)	Temperature (K)
A	19.3	1400
B	14.6	1260
C	10.9	1190
D	6.3	1140
E	19.4	1540
F	18.9	1720
G	17.3	1920
H	16.1	2180
I	28.2	1270
J	9.7	1580

Comparing (A) with results from [5] shows how shock pressure is increased with the introduction of a solid basalt target layer. However, a 30% porous basalt layer (Model B) can be seen as comparable to the sand layer used in [3], according to mean peak pressures (14.6 and 12.8 GPa, respectively). Peak shock pressures in the projectile decrease with increasing target porosity (Fig. 1), as low as 0.49 GPa in the trailing half for model (D). The highest shock pressures are found in model (I), at 46 GPa, showing how shape of the projectile dramatically effects the survivability of the material. Model (J) indicates how prolate projectiles survive better than other shapes of projectiles. In porous projectiles (E)-(H), pressures decrease whilst temperatures increase (Table 1 and Fig. 2), with increasing porosity.

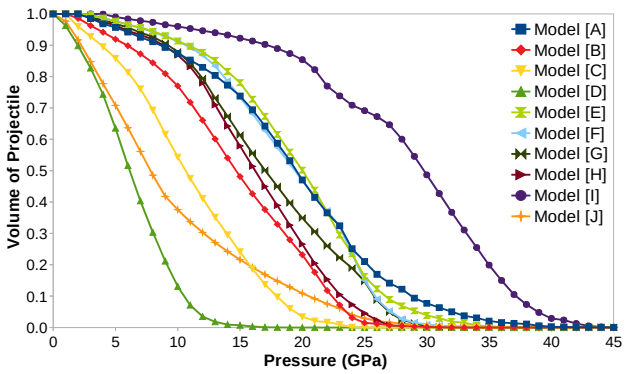

Fig. 1: Maximum peak shock pressures as a function of volume for projectiles in models [A]-[J].

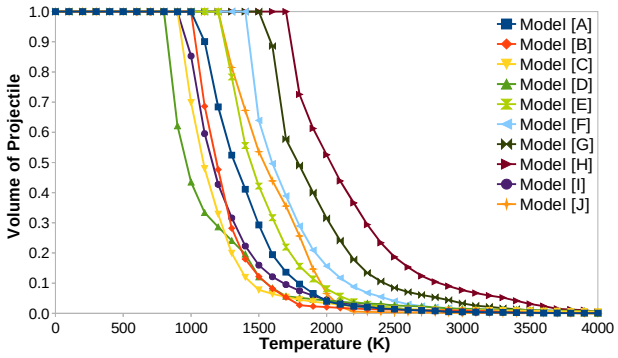

Fig. 2: Maximum peak temperatures as a function of volume for projectiles in models [A]-[J].

Discussion: Assessment of survivability has routinely been based upon threshold peak pressures, but temperatures must also be considered to gain a more accurate understanding of projectile survival. Initially, when considering a denser target than used by [5], peak shock pressures seem to remain low enough for significant proportions of impactor material to potentially survive the impact event. However, peak shock temperatures are higher than expected, compared to those predicted by Hugoniot data [11]. These peak temperatures could be due to significant shear heating experienced by the impactor during low-velocity impacts [12]. Including porosity in the projectile dramatically lowers the critical pressure required for melting. Porosity in the target has a great effect on survivability, as mean peak pressures and temperatures decrease in the projectile with increasing target porosity, highlighted most in model (D). Results from model (D) suggest that ~90% of the impactor would experience peak pressures <10 GPa, which would be low enough for the survival of constituents such as phyllosilicates, volatiles (poly-aromatic hydrocarbons, nitrogen and carbon) and potential biomarkers [5,13,14]. However, peak temperatures reach a minimum of 800 K within all projectiles (rising to over 4000 K in some cases), which will severely limit survivability of the organic molecules anthracene and stearic acid, with survival temperatures of 700 K and 650 K respectively [15]. Some alkanes and poly-aromatic hydrocarbons may survive in all of the models as survival pressures and temperatures are on the order of 30 GPa and 2500 K [16]. Melting and some vaporisation of sandstone is inevitable for a proportion of impactors even with the most favourable conditions [17]. In the future, a range of impact angles need to be considered in 3D models, as well as layered terrains in order to represent a more accurate lunar surface. Considering impacts at lower velocities could help estimate a range at which peak temperatures become more survivable.

Acknowledgements: We gratefully acknowledge the developers of iSALE-2D and STFC for funding.

References: [1] Armstrong, J. C. et al. (2002) *Icarus*, 160, 183–196. [2] Joy, K. H. et al. (2016) *Earth Moon Planets*, 118, 133-158. [3] Bellucci, J. J. et al. (2019) *Earth and Planetary Science Letters*, 510, 173-185. [4] Armstrong, J. C. (2010) *Earth Moon Planets*, 107, 43–54. [5] Crawford, I. A. et al. (2008) *Astrobiology*, Vol: 8 (2), 242-252. [6] Amsden, A. et al. (1980) *LANL Report*, LA-8095. [7] Collins, G. S. et al. (2004) *MAPS*, 38, 217-231. [8] Wünnemann, K. et al. (2006) *Icarus*, 180, 514-527. [9] Heiken, G. H. et al. (1991) *Cambridge University Press*, ISBN 0-521--33444-6. [10] Schultz, P. H. et al. (2010) *Science*, 330, 468-472. [11] Mimura, K. et al. (2003) *Carbon*, 41, 2547-2553. [12] Kurosawa, K. and Genda, H. (2018) *Geophysical Research Letters*, 45, 620-626. [13] Svetsov, V. V. and Shuvalov, V. V. (2015) *Planetary & Space Science*, 117, 444-452. [14] Tomioka, N. et al. (2007) *Meteoritics & Planetary Science*, 42, 19-30. [15] Burchell, M. J. et al. *Astrobiology* (2014) 14, 473-485. [16] Parnell J. et al. (2010) *Meteoritics & Planetary Science*, 45, 1340-1358. [17] Lintao, Y. et al. (2017) *Int. Journal of Physical Modelling in Geotechnics*, 12 (2), 65-90.

GEOCHEMICAL AND TEXTURAL COMPARISON OF METAL PARTICLES IN LUNAR AND ASTEROIDAL METEORITIC SAMPLES: A WINDOW TO IMPACTOR CHEMISTRY T.A. Harvey[1]. K.H. Joy[1] and R.H. Jones[1], [1]School of Earth and Environmental Sciences, University of Manchester, Oxford Road, Manchester, M13 9PL, UK (thomas.harvey@postgrad.manchester.ac.uk).

Introduction: Impacts are central to formation and evolution of planetary and asteroidal bodies, via accretion, surface modification and, in some cases, eventual breakup. There is a significant range of controlling factors which can influence the effects of a given impact, including impactor size, impact angle, target and impactor lithology, porosity and volatile abundance, as well as the state of the target body's atmosphere and hydrosphere [1].

The aim of this research is to investigate the textures and geochemistry of metal components in lunar samples and chondrites. We know that some of these metal particles form as a result of impact processes, but the processes (i.e reaction pathways dependent on impactor and target compositions, and physical mode of emplacement) and physical conditions (i.e. pressure, temperature, oxygen fugacity, and gravity) are not well understood. Our aim is to understand how metal behaves during impacts, and to do this we will compare metal-related processes on the Moon and asteroids. We aim to track backwards from an observed in-sample chemical composition of metal introduced by an impact to constrain the type of impactor that caused that collision [2]. Such knowledge would help to understand questions such as whether the types of Solar System impactors has varied over time [3].

Occurrence of metal in the Moon and Asteroids:

Lunar metallic components: In lunar crustal rocks, as on Earth, iron is predominantly found in its oxidised forms as a component of silicate or oxide minerals. However, in lunar impact breccia samples (both from sample return missions and lunar meteorites) it is common to find a metallic component, approximately 1 volume %. The metal is predominantly iron-nickel [4] although other species such as copper, cobalt and chromium have been identified. It occurs as interstitial phases in silicate assemblages in both crystalline impact-melt breccias and as discrete grains within regolith (soil and soil breccia) samples [5]. In 'pristine' lunar mare basalt samples it is magmatically derived as the lavas crystallised under very low fO_2. Metal is also partially derived from impactor (asteroids and micro-meteorites) components [4,6] and relics of the impactor can even survive in the target lithology [2]. Metal, indirectly derived from this impactor, may also form via the reduction of Fe^{2+} in impact melt sheets. Additional iron metal (known as nanophase iron) is thought to have been derived from the solar wind exposure-induced reduction of Fe^{2+} in minerals in the lunar regolith [7].

Meteoritic metal: Asteroid-sourced meteorite samples found on Earth commonly contain metal. The abundance of this metal varies depending on the type of meteorite. Iron metal is an important meteoritic component and its composition and associations with silicate mineral assemblages record information about a parent asteroid's formation and evolution.

Asteroids were formed initially as aggregates of particles which formed in the protoplanetary disk. Meteorites from chondritic asteroids contain metal particles which formed at this time [8], demonstrating that metal is an important component of primitive protoplanetary disk materials. Metal in chondrites carries chemical signatures of gas-solid condensation. Ordinary chondrites contain a range of metal abundances, with LL chondrites containing an average of 2 vol.% metal, L chondrites containing an average of 4 vol.% Fe,Ni metal and H chondrites containing 8 vol.% metal [8]. Carbonaceous chondrites of different groups have a range of metal concentrations, from zero to 80 vol.% [8]. In most cases, the metal is indigenous to the meteorite parent body. An unusual metal-rich group, the CB chondrites, contains rounded metal particles, up to centimetres in size, which are thought to have been derived via impact processes [9]. Heating of asteroids in the early Solar System allowed some, but not all, asteroids to differentiate and form metal-rich cores [10]. In iron meteorites, and iron-rich meteorites, such as pallasites and mesosiderites, metal carries a chemical signature of chemical differentiation and crystallisation.

Collisions with metal-bearing differentiated or metal-bearing chondritic asteroids can introduce exogenous metal to any asteroid. As in the case of the Moon, impacts on asteroids commonly melt a portion of the target lithology during the collision event, although we know that impactor material often survives the impact processes. For example, fragments of carbonaceous chondrites have been found in howardite meteorites [11].

Metal can also be melted and mobilized as a result of impact heating. In impact-melt lithologies, metal is texturally associated with silicate minerals in a variety of ways, such as metal veins in silicate grains, silicate grains entrained in metal, metallic melting textures, and silicate fragments included in metal particles [12]. This variation must reflect

some difference in reaction conditions such as pressure or temperature.

Approach: We will perform geochemical and textural analysis on metallic particles from a suite of meteoritic and lunar samples, with the goal of connecting geochemical evidence in the sample with the processes or reactions by which they formed, and the extent to which they were modified by being entrained in an impact melt. Scanning Electron Microscopy (SEM) will be used to acquire back-scattered electron images for the purpose of observing textures, as well as for qualitative EDS compositional analysis and X-ray mapping of the samples. Electron Probe Microanalysis (EPMA) will be used for quantitative analyses, in addition to quantitative X-ray mapping. Quantitative Evaluation of Minerals by Scanning Electron Microscopy (QEMSCAN) [13] analyses will be used to determine relative phase abundances, bulk sample chemistry, as well as grain size and shape distributions.

For chemical analysis, elements of interest include the major elements, typically Fe and Ni, as well as minor elements such as Co, Cr, S, P, Zn, Si and Mn. Iron meteorites are classified by their concentrations of trace elements such as Ge or Ga because their parent bodies formed with different volatile element abundances [14]. It would be useful to investigate whether such trace element signatures are recogniseable in impact-melt related or impactor relic metal particles for the purpose of linking observed geochemistry to potential parent bodies. Successful quantitative measurement of these concentrations would require the use of Inductively Coupled Plasma Mass Spectrometry (ICP-MS).

There are a range of avenues to be explored with regard to textural analysis. From preliminary analyses we have observed that metal grains entrained in impact melt consist of multiple sub-grains. We will investigate sub-grain orientation using Electron Backscattered Diffraction (EBSD) for evidence of strain-induced deformation which would provide information about the strain history of metal particles [15]. This can be used particularly in the case of lunar samples to determine whether a particle is an impactor relic [15]. In addition, characterisation of micro-scale metal-silicate interaction textures, in both lunar and meteoritic samples, and how these might be correlated with processes and conditions of formation will be useful to interpret how the textures vary with conditions [16].

We note that terminology used in terrestrial, lunar and meteoritic studies can differ. We will strive to use nomenclature which is geologically consistent across the differing rock types and planetary settings.

References:

[1] French, B.M. (1998) *Traces of Catastrophe,* 1-120. [2] Joy, K.H. et al. (2012) *Science,* 336, 1426-1429. [3] Korochantseva, E.V. et al. (2007) *Meteoritics and Planetary Sci., 42*, 113-130. [4] Goldstein, J.I. et al. (1972) *Proceedings of the Third Lunar Sci. Conf.,* 1, 1037-1064. [5] Wittman, A. and Korotev, R.L. (2013) *44th Lunar and Planetary Sci. Conf.* Abstract #3035. [6] Goldstein, J.I. and Yakowitz, H. (1971) *Proc. of the Second Lunar Sci. Conf.*, 1, 177-191. [7] Morris, R.V. (1980) *Proc. Lunar Planet. Sci. Conf., 11th,* 1697-1712. [8] Weisberg, M.K. et al. (2006) *Meteorites and the early Solar System II,* 19-52. [9] Srinivasan, P. et al. (2017) *Meteoritics and Planetary Sci.*, *52* 2193-2219. [10] Jeffrey, T.G. (1992) *Journal of Geophysical Research, 97*, 14,717-14,726. [11] Buchanan, P.C. et al. (1993) *Meteoritics, 28,* 659-682. [12] Kearsely, A. et al. (2013) *Meteoritics and Planetary Sci.*, *39,* 247-265. [13] Gottlieb, P. et al. (2000) *Microtextural Mineralogy: Testing & Analysis,* 24-25. [14] Scott, E.R.D. and Wasson, J.T. (1975) *Reviews of Geophys. And Space Phys., 13*, 527-546. [15] Morland, Z. S. et al. (2019) *50th Lunar and Planetary Sci. Conf.,* Abstract #1275. [16] Tomkins, A. G. et al. (2013) *Geochim. et Cosmochim. Acta, 100,* 41-59.

PETROGRAPHY AND MINERALOGY OF IGNEOUS CLASTS IN LUNAR METEORITE NWA11228.

T. S. Hayden[1], M. Anand[1], I. A. Franchi[1], G. Degli-Alessandrini[1] [1]School of Physical Sciences, The Open University, Walton Hall, Milton Keynes MK7 6AA, UK (tara.hayden@open.ac.uk).

Introduction: The lunar meteorite Northwest Africa (NWA) 11228 was found in 2017 as irregular-shaped fragments, exhibiting a sandblasted exterior and lacking a fusion crust. It has been classified as a feldspathic breccia [1].

NWA 11228 is proposed to be paired with the NWA 8673 clan of lunar meteorites, which in turn are compositionally indistinguishable from Dhofar (Dho) 925, 960 and Sayh al Uhaymir 449 [2]. This opens up the possibility that NWA 11228 contains mare basalt clasts, similar to that of Dho 925 and 960 [3,4]. In addition, Dho 961 (paired with Dho 960) is thought to have originated from the South Pole Aitken (SPA) basin on the lunar farside, based on its mafic composition and bulk Th concentration [5], raising the possibility that NWA 11228 may also contain some SPA material. Here we report on a preliminary study of the mineralogy and petrology of diverse igneous clasts within NWA 11228.

Methods: A polished thin section was examined using an FEI Quanta 200 3D Scanning Electron Microscope (SEM) fitted with an Oxford Instruments Energy Dispersive X-ray detector at The Open University. An electron beam current of 0.60 nA and an accelerating voltage of 20 kV was used to produce back-scatter electron (BSE) and X-ray maps to examine texture and compositional diversity. Quick acquisition of X-ray spectra for ~30-60s allowed for preliminary identification of mineral phases. Further quantitative analysis was carried out using a CAMECA SX100 electron microprobe (EPMA), using an accelerating voltage of 15 kV, a beam current of 20 nA, and a defocused beam with spot size of 5 μm to minimize mobilization of Na in feldspar. Modal proportions of plagioclase, pyroxene and olivine were calculated using MultiSpec (Version 2018.08.30) [6], and size of clasts was estimated using ImageJ software.

Results and Discussions:

Petrology and mineralogy: NWA 11228 is a polymict breccia containing 0.05-0.5 mm-sized mineral and lithic clasts in a dark brown matrix, which also shows vesiculation (Fig. 1). Mineral fragments are mainly plagioclase feldspar of anorthitic composition (An_{93-97}); Mg-rich olivine (Fo_{55-76}) and pyroxene of pigeonitic ($Fs_{18-53}En_{30-74}Wo_{6-20}$) and augitic ($Fs_{7-60}En_{17-53}Wo_{22-44}$) composition (Fig. 2). Accessory minerals are present as mineral fragments and include zircon, chromite, ilmenite, Fe-Ni phases, sulphide, merrillite, spinel and silica.

Clast Inventory:

Clast 1 is dominated by a glassy groundmass, the composition of which indicates mixing between mafic and feldspathic components. An-rich plagioclase laths (An_{97}) are also present.

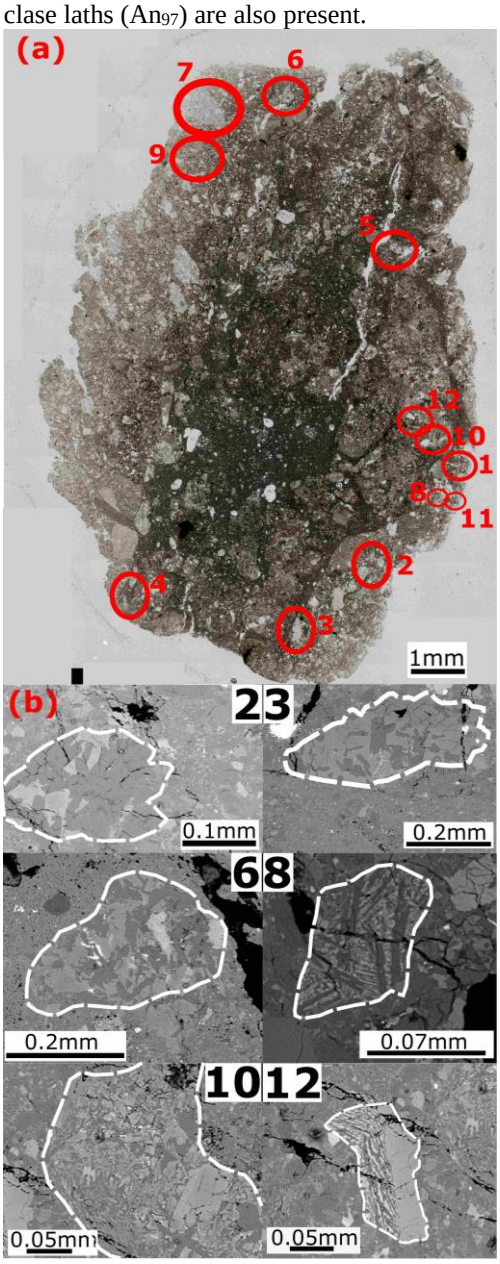

Figure 1: (a) Mosaic of NWA 11228 (in PPL); (b) BSE images of selected clasts (2-3, 6, 8, 10 and 12).

Clast 2 shows an ophitic texture (Fig. 1b), comprising pigeonite ($Fs_{28-33}En_{53-58}Wo_{14}$) and plagioclase ($An_{97}$) (Fig. 2). Pyroxene in this clast has very low-Ti contents (~0.4 wt% TiO_2), along with high Cr (~0.7 wt% Cr_2O_3), similar to that reported for a VLT clast in lunar meteorite MAC88105 [7]. A Fe# of 30-40 and Ti# of ~30 (Fig. 2b) is consistent with a VLT origin [10-13].

Clast 3 (0.5mm) (Fig. 1b) displays an equigranular texture of An-rich plagioclase (An_{92-93}) (43%) and

pigeonite ($Fs_{26-31}En_{61-69}Wo_{5-8}$) (56%). A relatively high Mg# (68-72) for pyroxene, along with an average Fe# of ~30, and Ti# of ~40 indicates a VLT to low-Ti mare basalt heritage [7-13].

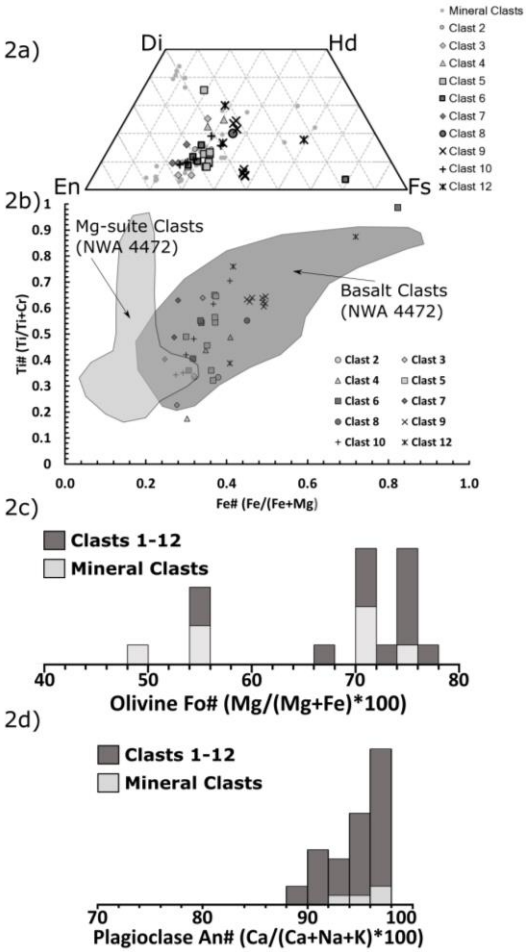

Figure 2. a) Pyroxene composistions in NWA 11228 clasts b) Pyroxene Fe# vs Ti# (compared to data from NWA 4472 [12]) c) olivine forsterite contents d) plagioclase anorthite contents.

Clast 4 is an igneous clast (~0.07mm) with intergrown laths of plag (An_{96-97}), augite ($Fs_{27-31}En_{44-51}Wo_{23-25}$) and pigeonite ($Fs_{28}En_{64}Wo_{8}$). Pyroxene has an average Mg# of 65, Fe# of 40 and Ti# of ~37, indicating a VLT basalt heritage [7-13].

Clast 5 has an equigranular texture comprising of plagioclase (An_{95-97}), pigeonite ($Fs_{31-34}En_{55-59}Wo_{8-13}$) and augite ($Fs_{19}En_{45}Wo_{35}$), similar to mare basalt clasts of NWA 4472 (Fig. 2b) [12].

Clast 6 exhibits intergrowth of forsteritic olivine (Fo_{55}), plag (An_{93}), pigeonite ($Fs_{28-30}En_{56-63}Wo_{9-16}$) and clinoferrosilite ($Fs_{79}En_{17}Wo_{4}$) (Fig. 1b), with modal abundances (47% plag; 46% px; 7% ol) similar to soils dominated by mare basalts [14]. Pyroxene has a Fe# of ~40 and Ti# of ~57, perhaps of a low-Ti mare basalt heritage [10-13].

Clast 7 exhibits an ophitic intergrowth of pigeonite ($Fs_{22-25}En_{61-68}Wo_{9-16}$), forsteritic olivine ($Fo_{68}$) and plagioclase ($An_{91-96}$). A high average Mg# (~73), Fe# of 30 and Ti# of ~51 for pyroxene hints at a low-Ti basalt parentage [7- 13].

Clast 8 exhibits an ophitic texture comprising plagioclase (An_{95}), pigeonite ($Fs_{36}En_{44}Wo_{20}$) and recrystrallized melt (Fig. 1b).

Clast 9 is predominantly a pigeonite crystal (~0.07 mm) ($Fs_{46-47}En_{47-48}Wo_{6}$), exhibiting augite exsolution lamellae ($Fs_{34-36}En_{41-42}Wo_{22-25}$). There appears to be shared boundaries with an anorthite (An_{96}) crystal of equal size and recrystallized melt. A pyroxene Fe# of ~50 and Ti# of ~60 plot close to the low-Ti mare basalt trend [10-13], indicating a low-Ti mare basalt heritage.

Clast 10 contains equant bytownite (An_{89-90}), anorthite (An_{91-97}) and pigeonite ($Fs_{25-34}En_{50-66}Wo_{9-19}$) (0.01-0.03mm), along with larger crystals of forsteritic olivine (Fo_{72-76}) (~0.08 mm) which exhibits gradational zoning (an increase in FeO (~2.4 wt%) towards the rim) (Fig. 1b). Pigeonite has a high average Mg# (~67), Fe# of 30 and Ti# of ~49, indicating a low-Ti mare basalt origin [7-13].

Clast 11 comprises olivine (Fo_{76} and Fo_{70-71}) sharing a boundary with a plag (An_{96-97}).

Clast 12 comprises a 0.12 mm augite crystal ($Fs_{29}En_{41}Wo_{30}$) and 0.01-0.06 mm intergrown pigeonite ($Fs_{35-59}En_{23-49}Wo_{17-18}$) and plagioclase ($An_{92-96}$) laths (Fig. 1b). Augite has an Mg# of ~59, Fe# of ~41 and Ti# of ~38, consistent with a VLT mare basalt origin [7-13].

The majority of igneous clasts analysed display a chemical affinity to mare basalts, indicating that this meteorite could have been sourced from close to a mare region. There is some possibility of Mg-suite material being present (see Fig. 2b), which will be explored during further studies.

References: [1] Gattacceca J. et al. (2019) *Meteoritics & Planet. Sci., 54,* 469-471. [2] Korotev R. L (2019)*http://meteorites.wustl.edu/lunar/stones/nwa8673.htm* [3] Russell S. S. et al. (2004) *Meteoritics & Planet. Sci., 39,* A215-A272. [4] Russell S. S. et al. (2005) *Meteoritics & Planet. Sci., 40,* A201-A263. [5] Jolliff B. L. et al. (2008) *Lunar Planet. Sci, 39,* Abstract #2519. [6] Purdue Research Foundation (2019) *Multispec Software Application Version 2018.08.30.* [7] Koeberl C. et al. (1991) *Geochim. et. Cosmochim. Acta 55,* 3073-3087. [8] Anand M. et al. (2006) *Geochim. et. Cosmochim. Acta, 70,* 246-264. [9] Papike J. J. et al. (1976) *Rev. of Geophys. And Space Phys., 14,* 475-540. [10] Arai T. et al. (1996) *Meteorit. Planet. Sci, 31,* 877-892. [11] Robinson K. L. et al. (2012) *Meteorit. Planet. Sci, 47,* 387-399. [12] Joy K. H. et al. (2011) *Geochim. et Cosmochim. Acta, 75,* 2420-2452. [13] Joy K. H. et al. (2014) *Geochim. et. Cosmochim. Acta, 144,* 299-325. [14] Lucey P. et al. (2006) *Reviews in Mineralogy & Geochemistry, 60,* 83-219.

Returning to the Moon with HERACLES. H. Hiesinger[1], M. Landgraf[2], W. Carey[2], Y. Karouji[3], T. Haltigin[4], G. Osinski[5], U. Mall[6], K. Hashizume[7], HERACLES Science Working Group, HERACLES International Science Definition Team; [1]Institut für Planetologie, Westfälische Wilhelms-Universität, Wilhelm-Klemm-Str. 10, 48149 Münster, Germany (hiesinger@uni-muenster.de), [2]European Space Agency (ESA), Directorate of Human Spaceflight and Robotic Exploration Programmes, [3]Japan Aerospace Exploration Agency (JAXA), Space Exploration System Technology Unit, [4]Canadian Space Agency (CSA), [5]University of Western Ontario, Centre for Planetary Science and Exploration, [6]Max-Planck Institut für Sonnensystemforschung, [7]Ibaraki University, Dept. of Earth Science.

Introduction: A human return to the Moon has many scientific (and strategic) benefits and offers unique opportunities for testing hardware and operational procedures beyond Low Earth Orbit (LEO), e.g., in preparation for human exploration of Mars [1]. The Human Enhanced Robotic Architecture Capability for Lunar Exploration and Science (HEREACLES) is an ESA-led international effort to prepare for such a return of humans to the Moon. HERACLES is primarily a technology-driven mission concept designed to demonstrate key elements and capabilities for sustainable human exploration of the Moon while maximizing opportunities for scientific knowledge gain [2-5]. Currently, HERACLES is a joint phase-A study of the European Space Agency (ESA), the Japan Aerospace Exploration Agency (JAXA), and the Canadian Space Agency (CSA) with NASA and Roscosmos having observer status. HERACLES will land on the lunar surface, demonstrate surface operations, and will return about 15 kg of samples from the surface to the lunar Gateway and eventually to Earth by the astronauts on board the NASA Orion spacecraft.

Mission Concept: Key objectives of HERACLES include: (1) Preparing for human lunar missions by implementing, demonstrating, and certifying technology elements for human lunar landing, surface operations, and return; (2) Creating opportunities for science, particularly sample return; (3) Gaining scientific and exploration knowledge, particularly on potential resources; and (4) Creating opportunities to demonstrate and test technologies and operational procedures for future Mars missions. For this purpose, HERACLES will consist of the Japanese Lunar Descent Element (LDE), the ESA-built Interface Element that will house the Canadian rover, and the European Lunar Ascent Element (LAE) that will return the samples to the lunar Gateway (Figs. 1,2). Details on the engineering aspects of the mission are provided by [4].

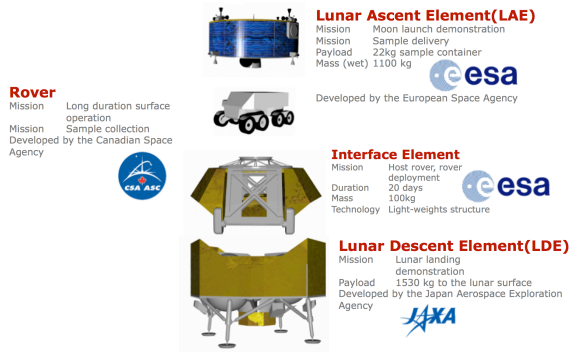

Fig. 1: The elements of the HERACLES mission.

The current concept forsees a 330 kg rover that will be deployed from the Interface Element via two ramps. It will be powered by a radioisotope power system, which will allow the rover to drive more than 100 km and to survive lunar night. While the rover will be operated for most of the time from Earth, it will be manipulated by astronauts on the lunar Gateway for particularly difficult taks (Fig. 2). The rover will immediately collect a contingency sample before it will collect additional samples along a ~35 km long traverse from about ten individual sampling stations. Samples will be returned to the LAE. The rover will have a payload mass of 90 kg, sufficient for a comprehensive a suite of scientific instruments that will allow us to study and document the sampling locations and the context of the samples, as well as the geology along the traverse. The HERACLES international Science Definition Team (iSDT) is currently discussing an appropriate instrument suite, which will most likely include cameras, spectrometers, a laser reflector, and potentially some geophysical instruments. After delivery of the samples to the LAE, the surface mobility demonstration phase will see the rover going on a >100 km long traverse with the instruments continuously collecting data while roving. For example, a Ground Penetrating Radar (GPR) could provide an unprecedented view into the regolith structure of various terrains visited by the rover. Similarly, a camera permanently looking at the wheels of the rover could

provide us with information on the physical characteristics of the regolith while spectrometers could provide geochemical/mineralogical information along the traverse.

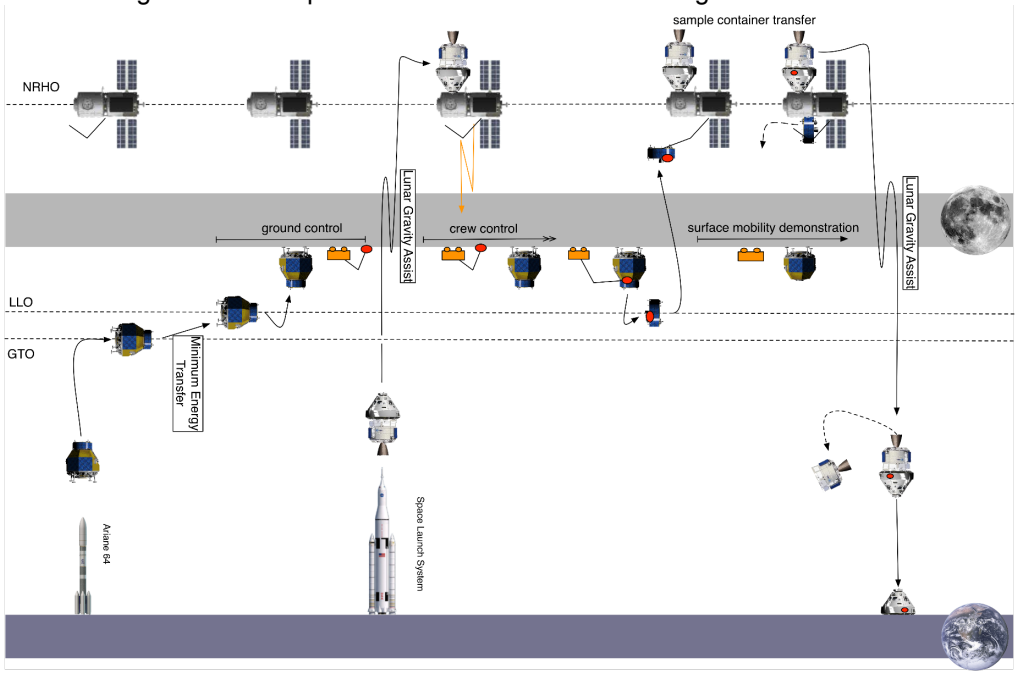

Fig. 2: The HERACLES mission concept.

Science: The iSDT identified five currently non-prioritized high-level science objectives that HERACLES will address: (1) Crustal anorthosite composition and crystallization age, (2) Mantle composition, (3) Improvement of chronology with crater counting of young basalts (<2.5 Ga), (4) Internal structure, i.e., subsurface, crust, mantle, and core, and (5) Mechanism of material transport (e.g., water) to the Moon.

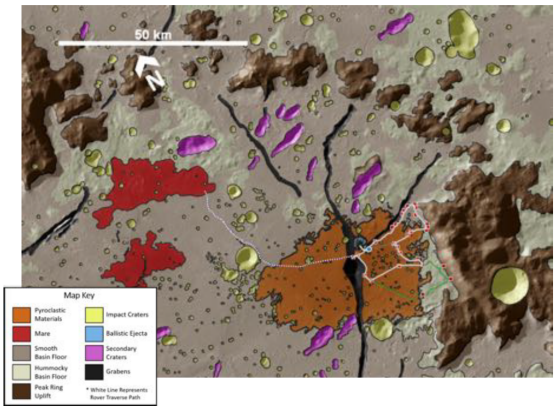

Fig. 1. Example of a potential traverse in Schrödinger basin.

The iSDT is evaluating a suite of potential landing sites, guided by the recommendations of the 2007 NRC report [6] and several subsequently published documents [e.g., 7]. Potential landing sites include the Schrödinger basin, the Moscoviense basin, Copernicus crater, Jackson crater, and some young basalts in the Flamsteed region [5]. Schrödinger is an extensively studied basin [e.g., 8-10] and currently serves as a case study for developing mission scenarios and scientific rationales. Landing in the Schrödinger basin, HERACLES could be the first mission to sample farside material, including material of the South Pole-Aitken impact, to sample a basin melt sheet and deep-seated crustal lithologies, and to evaluate the In Situ Resource Utilization (ISRU) potential. Thus, HERACLES will bridge the gaps between science, exploration and human space flight, and will allow us to accomplish many necessary steps in each of those domains.

References: [1] ISECG (2018), Global Exploration Roadmap; [2] Landgraf et al., (2017) LPSC 48th, 1790; [3] Hiesinger et al., (2019) LPSC 50th, 1327; [4] Landgraf et al., (2019) LPSC 50th, 1030; [5] Karouji et al., LPSC 50th 1736; [6] National Research Council (2007), The Scientific Context for Exploration of the Moon: Final Report, ISBN: 0-309-10920-5, 120 pages; [7] Kring and Durda (eds.) (2012), A Global Lunar Landing Site Study to Provide the Scientific Context for Exploration of the Moon, LPI Contribution No. 1694, 688 p.; [8] Kramer et al. (2013), Icarus 223, 131-148; [9] Potts et al. (2015), Adv. Space Res. 55, 1241-1254 [10] Steenstra et al. (2016), Adv. Space Res. 58, 1050-1065.

GEOLOGICAL MAPPING AND ABSOLUTE MODEL AGES AROUND THE APOLLO 17 LANDING SITE. W. Iqbal[1], C. H. van der Bogert[1], and H. Hiesinger[1], [1]Institut für Planetologie, Westfälische Wilhelms-Universität, Wilhelm-Klemm-Str. 10, 48149 Münster, Germany, (iqbalw@uni-muenster.de).

Introduction: The crater size-frequency distributions (CSFD) and their related *N*(1) values of the area around the Apollo and Luna landing sites are calibrated against the radiometric ages [e.g., 3] of the selected samples and provide important calibration points for the lunar cratering chronology [4,5], which were later modified to derive the absolute model ages on the various terrestrial bodies in the Solar System [e.g., 4-9]. Thus, the accuracy of the lunar cratering chronology can be reexamine by using up-to-date data [10-13] and sample analyses [e.g., 3]. The diverse geology [e.g., 1,2] around the Apollo 17 landing site provide insights for several key lunar geological events that feed into the lunar cratering chronology. Thus, we produced new geological maps at scales of 1:800,000 and 1:143,000 around the Apollo 17 landing site, and measured new CSFDs for the various units using data collected by recent missions. Subsequently, we compared our results with the previous analyses of [4] and [14] for the evaluation of lunar cratering chronology through the calibration points gained from the landing site.

Methods: We used Lunar Reconnaissance Orbiter Camera (LROC) images [10] for defining albedo contrasts, the LOLA/Kaguya merged digital elevation model (DEM) [11] for topographic analysis, and Clementine [12] and Kaguya Multiband Imager (MI) [13] data for investigating spectral differences. The used LRO Wide Angle Camera (WAC) data have pixel scales of 100 m and Narrow Angle Camera (NAC) data have a pixel scale of ~1.3 m. The data we used have incidence angles ranging from 69-76°. The WAC and NAC data was calibrated and map-projected in ISIS3 [15]. CraterTools [16] in ArcGIS was used to measure the CSFDs of the different units. We used CraterStats [17] for plotting the data in cumulative and relative plots with pseudolog binning. Although the obvious secondary crater chains and cluster were avoided during area definition and measurement, we still used randomness analysis [18] to avoid fitting diameter ranges where clustering of the craters may indicate the presence of secondary craters.

Geological Mapping: The geological events observed in Taurus Littrow Valley are divided into four time periods: Copernican, Post-Imbrian. Imbrian, and Pre-Imbrian (Fig. 1 and 2).

The Copernican events (Figure 1, 2a) include the deposition of light mantle material or LMD (*Cls1* and *Cls2*) and secondary crater material from the Copernican craters (*Csc*, *Cdec*, *Cld* and *Ccr*). These events have been widely considered to be Tycho-triggered [1,2,14]. However, due to spectral [1] and albedo [19] differences within the landslide deposits, it has been proposed that the landslide material may have been deposited during seismic shaking associated with the formation of the Lee Lincoln scarp. The ages determined around the scarp [20,21] are very similar to the ages determined for the light mantle deposit [14]. We also mapped and determined ages for the Paint-Splatter [1,2] feature and light mantle deposit (*Cld*), which is also considered to be the material related to the Tycho crater [2].

A variety of mare basalt units (*Im1, Im2, Im3, Im4, Im5, Im6, Im7, Im8, Im9* and *Im10*) were deposited in the post-Imbrian period, which were mapped on the basis of Clementine

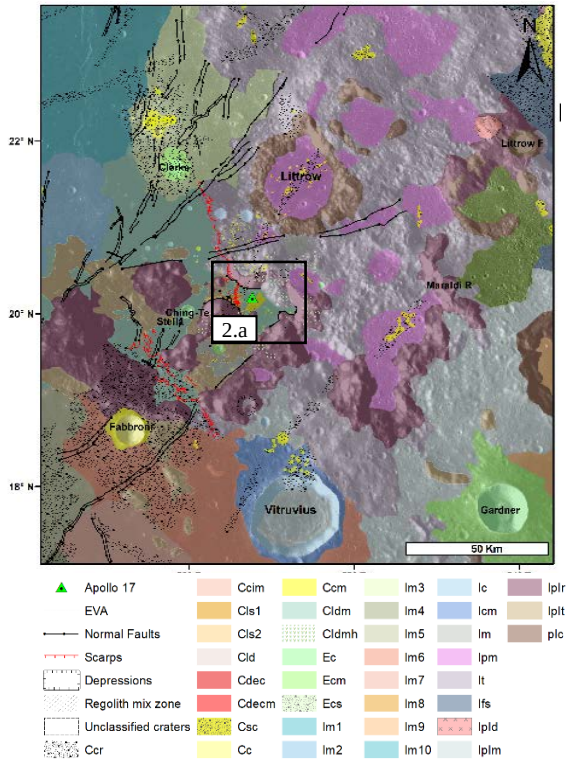

Figure 1. *New geological map of the region surrounding Taurus Littrow valley. The units include Imbrian and pre-Imbrian highlands, Imbrian basalts and plains, and different generations of the craters and structural features. Inset shows the area covered by a local geological map shown in Figure 2a.*

data (shown in Fig 1). The mare units in the mapping region was previously mapped by [22] on the Galileo data, which has slight differences in the mapped boundaries, due to different pixel scales of the both data set. The Taurus Littrow valley floor is covered with mare basalts and pyroclastic materials of similar ages (*CIdm*) [22,23]. Through observations of the albedo and spectral contrasts, we identified pyroclastic mantling in the depressions of the highlands (*CIdmh*) [1] around the Taurus Littrow valley. Potentially the pyroclastic material (*CIdm* and *CIdmh*) noticed in Clementine data, may originated from the rilles (Normal Faults in Fig. 1) in the west of the Taurus Littrow, and deposited in the valley with associated mare material as well as in the surrounding highland area via pyroclastic surges [2]. On the contrary, [1] argues the pyroclastic material deposited in the valley may originated from the "pyroclastic fissure" noticed on the Sculptured Hills. The highlands around the valley mostly consists of Imbrian terrain (*It*), likely ejecta material from the Imbrium basin. Though, the North and South massifs may belong to the pre-Imbrian Serenitatis crater wall or ejecta material [1,2], superimposed by Imbrian material (*IpIr*).

CSFD Measurements: CSFDs for the different geological units were determined using LRO NAC images and DTMs [7]. The CSFD measurements on the Paint Splatter (unit *Cld*)

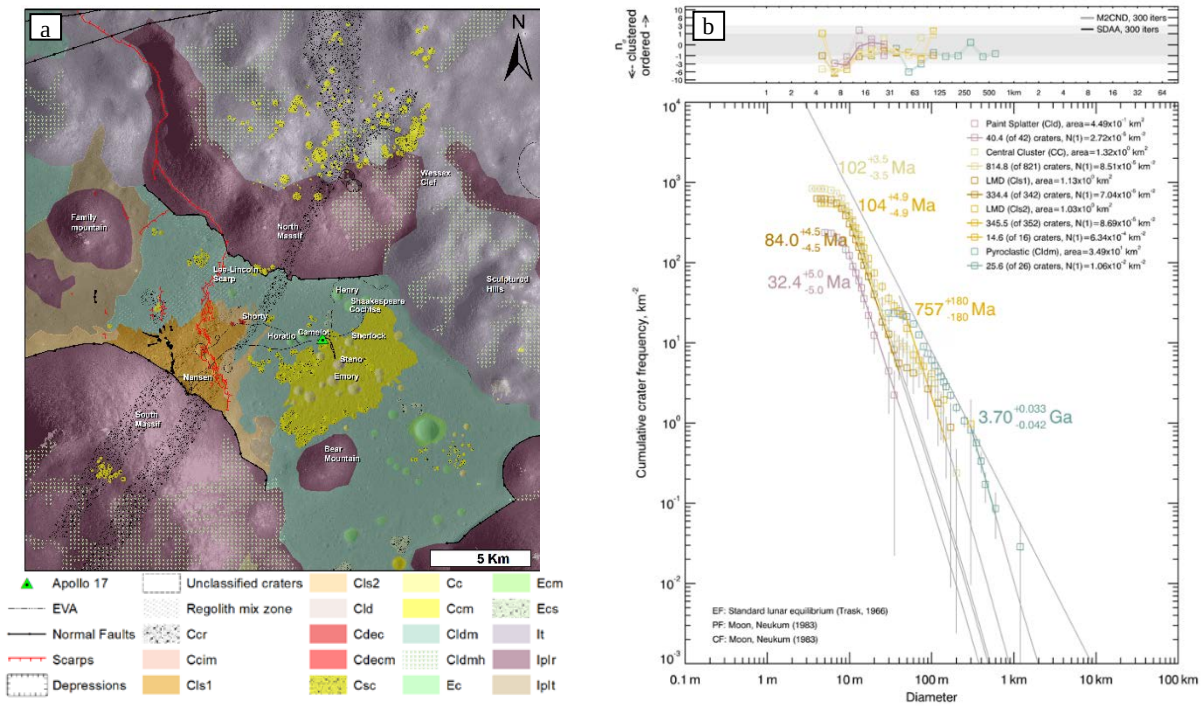

Figure 2. *(a) New geological map of the area around Apollo 17 landing site in Taurus Littrow valley. The map shows pre-Imbrian North and South Massifs (IpIr), Imbrian Sculptured Hills (It), valleys filled with pyroclastic and basalts material (CIdm), pyroclastic mantling (CIdmh) on the highland units, light mantle deposits (Cls1 and Cls2), secondary craters cluster (Cc), and other young crater materials (Csc and Ccr). (b) CSFD measurements and absolute model ages of selected geological units at the Apollo 17 landing site: the Paint-Splatter (unit Cld in map), the Central Cluster (unit Cc in map), the light mantle deposits (unit Cls1 and Cls2 in map), and the underlying pyroclastic unit (CIdm in map). All results are shown in cumulative form with cumulative age fits. The randomness analysis of the count area shows potential secondary crater contamination at crater diameters smaller than 10 m (panel above each plot), which were avoided while fitting the AMAs for each unit.*

show an $N(1)$ of 2.72×10^{-5} km^{-2} with a model age of 32.4±5 Ma, which is consistent with AMAs (~32-38 Ma) and $N(1)$ (~2.74×10^{-5} km^{-2}) values determined by [14] for Tycho impact melt pools. Although the nature of this unit is still unclear, it was previously interpreted as a possible impact melt deposit due to its relationship to other secondary materials from the Tycho crater [2,24]. However, the young age and the lobate features around the Paint Splatter may instead be related to seismic events. We also determined an $N(1)$ value of 8.59×10^{-5} km^{-2} and the age of 103±3.5 Ma on the Central Cluster (CC or *Cc* in the map), which is also consistent with the determined age of the Tycho crater [14]. Nevertheless, the values determined on the units *Cld* and *Cc* may be influenced by resurfacing, undetectable secondary craters contamination, and the small sizes of the selected areas.

On the basis of albedo contrast, we mapped and measured CSFDs for two units on the LMD; *Cls1* shows an $N(1)$ value of 7.04×10^{-5} km^{-2} and AMA of 84.0±4.5 Ma, and *Cls2* shows two $N(1)$ values of 8.69×10^{-5} km^{-2} and 6.34×10^{-4} km^{-2} and AMAs of 104±4.9 Ma and 757±180 Ma, respectively. [14] determined similar $N(1)$ values and AMAs on the unit *Cls1* for the determination of the calibration point for the Tycho crater on the lunar chronology curve [4,5]. The values determined on the *Cls2* unit are similar to the values determined by [20, 21] for the Lee Lincoln scarp. The origin of the older age appearing in the *Cls2* unit is not clear.

The CSFD measurements on the *CIdm* unit show an $N(1)$ value of 1.03×10^{-2} km^{-2} and model age of 3.70±0.037 Ga, which are consistent with values determined by [22,23], as well as radiometric ages of high Ti mare basalts [9].

In the future, we will compare our new geological maps and measured CSFD values with the most recent radiometric and exposure ages of the collected samples to evaluate and improve the lunar cratering chronology [4,5].

Acknowledgements: W. I. and H.H. were funded by the German Research Foundation (Deutsche Forschungsgemeinschaft SFB-TRR170, subproject A2) and C.vdB. was supported by EU H2020 project #776276, PLANMAP.

References: [1] Schmitt et al (2016) *Icarus 298*, 2-33. [2] Lucchitta (2018) *LPSC 49*, 2083 [3] Nemchin et al (2018) *LPSC 49*, 1936 [4] Neukum (1983) *Habil. thesis, U. of Munich.* [5] Neukum et al. (2001) *Space Sci. Rev. 96*, 55-86. [6] Neukum et al. (1975) *The Moon 12*, 201-229. [7] Hartmann (1970) *Icarus 13*, 299-301. [8] Robbins (2014) *EPSL 403*, 188-198. [9] Stöffler et al. (2006) *Rev. Min. Geochem. 60*, 519-596. [10] Robinson et al (2010) *Space Sci. Rev. 150*, 81-124. [11] Barker et al. (2016) *Icarus 273*, 346-355. [12] Pieters et al. (1994) *Science 266*, 1844-1848. [13] Ohtake et al (2013) *Icarus 226*, 364-374. [14] Hiesinger et al. (2012) *JGR 11*, E00H10. [15] Anderson et al. (2004) *LPSC 35*, 2039. [16] Kneissl et al. (2011). *PSS 59*, 1243-1254. [17] Michael et al. (2016) *Icarus 277*, 279-285. [18] Michael et al. (2012) *Icarus 218*, 169-177. [19] Hahn et al (2019) *LPSC 50*, 1963. [20] van der Bogert et al. (2019) LPSC 50, 1527. [21] van der Bogert et al. (2012) LPSC 43, 1847. [22] Hiesinger et al. (2000) *JGR 105*, 29239-29275. [23] van der Bogert et al. (2016) LPSC 47, 1616. [24] Lucchitta (1977) Icarus 30, 80-96.

NEW GEOLOGICAL MAPS OF THE APOLLO 11 AND 12 LANDING SITES. W. Iqbal[1], H. Hiesinger[1], and C. H. van der Bogert[1], [1]Institut für Planetologie, Westfälische Wilhelms-Universität, Wilhelm-Klemm-Str. 10, 48149, Münster, Germany, iqbalw@uni-muenster.de

Introduction: Geological mapping combined with crater size-frequency distribution (CSFD) measurements are important tools for understanding geological processes through out the Solar System [e.g., 1-8]. The Apollo missions played a vital role in deciphering the lunar geological history via the collection of samples that serve as important groundtruth for remote observations [e.g., 5,9]. By combining detailed geological mapping, CSFD measurements and sample analyses, we can determine absolute model ages (AMAs) on various planetary bodies [e.g., 6].

We used recent Lunar Reconnaissance Orbiter Camera (LROC) data [10] along with Clementine [11] and Moon Mineralogy Mapper (M3) [12] spectral data to reanalyze and map the geology of the Apollo 11 and 12 landing sites, and we produced new geological maps to provide an updated context for landing site-related sample and remote sensing studies.

Methods: ISIS3 [10] was used to calibrate and map-project the LROC Wide Angle (WAC; 100 m/pixel) and Narrow Angle Camera (NAC; ~1.2 m/pixel) data with incidence angles of 73-75°. The geological units were mapped on the basis of their morphology and albedo contrasts. The LOLA/Kaguya digital elevation model (DEM) [13] aided us in defining the units and related structures. Spectral data, including Clementine [11] and Chandrayaan-1 M3 [12], were used to subdivide units in the mare basalts around the landing sites.

We mainly used the stratigraphic scheme proposed by Wilhelms (1987) [1]. Thus, the mapped craters were classified as *Cc*-Copernican, *Ec*-Erathosthenian, *Ic*-Imbrian, and *pIc*-Pre-Imbrian craters. The symbology of the mapping units follows the standards of the Federal Geographic Data Committee (2006) [14], and the nomenclature used for the mapped craters and regions is consistent with the Gazetteer of Planetary Nomenclature (1999) [15].

Apollo 11 Landing Site Geology: The map covers the southwestern edge of Mare Tranquillitatis basin [16]. Based on variations in the iron and titanium concentrations observed in spectral data, we mapped five different mare units; *Im1, Im2, Im3, Im4* and *Im5* (*Fig. 1*). We observed rays (*Ccr*) around the landing site, which are directed towards Theophilus crater. However, a few rays probably belong to other young craters (*Cc*) (Fig. 1), such as Moltke, Alfraganus, Dionysius, and Tycho. We mapped few plains units in the highlands near the landing site on the basis of albedo and topography contrast, including: *Ifs*-Imbrian Fra Mauro smooth plains, *Ip*-Imbrian plains, and *IpIm*-undivided Imbrian or pre-Imbrian material observed in topographical depressions in the highlands. The mapped units in the highlands terrains are: *Ifm*-Imbrian Fra Mauro formation (Imbrium basin ejecta), and *IpIt*-undivided Imbrian or pre-Imbrian terrain, which does not have the northwest-southeast striation characteristic for *Ifm*. We observed a concentric pattern of graben (rilles) around the southwestern edge of Mare Tranquillitatis, which are mostly perpendicular to the radial pattern of the wrinkle ridges in the southwestern Mare Tranquilitatis.

Apollo 12 Landing Site Geology: The landing site is situated in Mare Cognitum on a southwest trending ray (*Ccr*) from Copernicus crater [17], in the Oceanus Procellarum. We observed mare units with Erathosthenian (*Em1, Em2*) and Imbrian (*Im1, Im2*) ages on the M3 data spectral contrast and crater density differences. Most rays (*Ccr*) in the mapping area point toward Copernicus crater, while a few may also belong to other young Copernican-aged craters (*Cc*), such as Gambert A and Lansberg B. Wrinkle ridges show a half concentric orientation in the east and south of the landing site. A few north-south and east-west trending graben are mapped to the west of the landing site. The highlands are covered with Imbrian ejecta (Fra Mauro formation; *Ifm*), while in the south and southwest of the landing site, a few areas in the highlands are mapped as undivided Imbrian and pre-Imbrian material (*IpIt*).

Implications: Detailed geological mapping supports not only a better understanding of the geological processes active at the landing sites, but is also necessary for defining homogeneous areas for the accurate measurement of CSFDs and deriving AMAs. We used our new maps to check and improve the previously selected count areas [e.g., 3,4] for determination of the $N(1)$ values at the Apollo 11 and Apollo 12 landing sites [16,17]. Our new values [16,17] compared with recently determined radiometric ages via modern sample analyses are consistent with those of [3,4,6,8], supporting the calibration of the lunar cratering chronology curve purposed by [3,4] via our updated landing site studies.

References: [1] Wilhelms (1987) *USGS Prof Paper* 1348. [2] Neukum et al. (1975) *The Moon 12*, 201-229. [3] Neukum (1983) *Habil. thesis, U. of Munich.* [4] Neukum et al. (2001) *Space Sci Rev 96*, 55-86. [5] Stöffler et al. (2006) *Rev Min Geochem 60*, 519-596. [6] Hiesinger et al. (2000) *JGR 105*, 29239-29275. [7] Hiesinger et al. (2003) *JGR 108*, E001985. [8] Hiesinger et al. (2012) *JGR 11*, E00H10. [9] Meyer (2012) *Lunar Sample Comp, ARES. NASA.* [10] Robinson et al. (2010) *Space Sci Rev 150*, 81-124. [11] Pieters et al. (1994) *Science 266*, 1844-11848. [12] Isaacson et al. (2013) *JGR 118*, 369-381. [13] Scholten et al. (2012) *JGR 117*, E00H17. [14] FGDC (2006) *FGDC-STD-013-2016.* [15] Blue (1999) Gazette of Plan Nom *USGS.* [16] Iqbal et al (2017) *LPSC 48*, #1258. [17] Iqbal et al (2018) *LPSC 49*, #1002. *Acknowledgement:* W. I. and H.H. were funded by the German Research Foundation (Deutsche Forschungsgemeinschaft SFB-TRR170, subproject A2) and CvdB was supported by EU H2020 project #776276, PLANMAP.

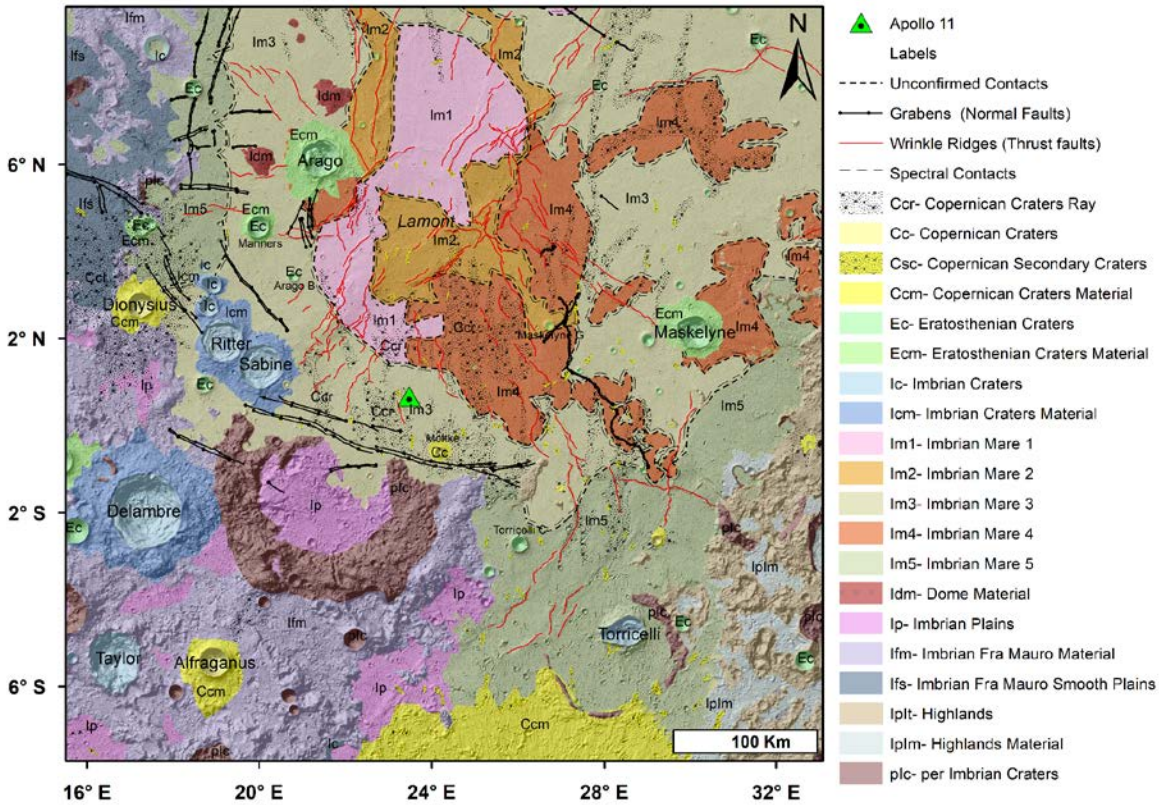

Figure 1: *New geological map of the southwestern part of the Mare Tranquillitatis around the Apollo 11 landing site (green triangle), showing mare units, various highland units (including the Fra Mauro and Cayley Formations), a radial pattern of wrinkle ridges, a concentric pattern of rilles, as well as different generations of craters and rays.*

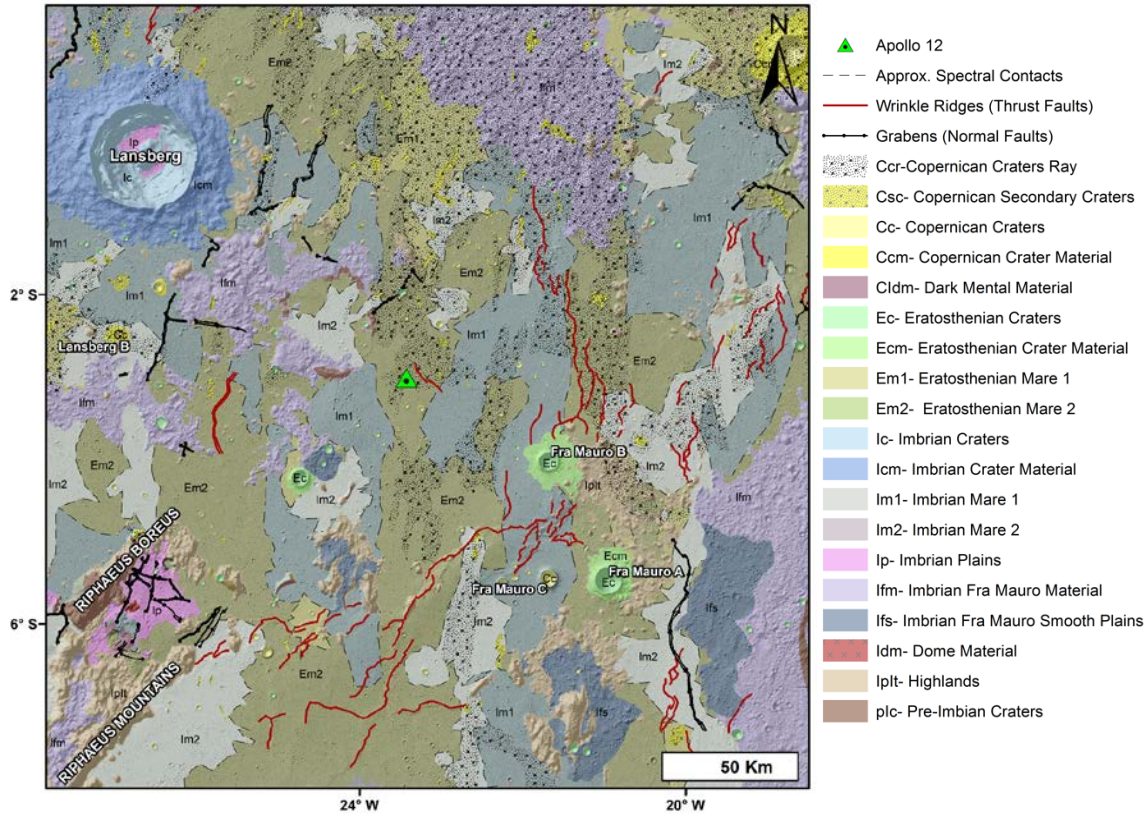

Figure 2: *New geological map of the Apollo 12 landing site (green triangle) in Oceanus Procellarum, which shows mare units, differently aged craters, rays crossing the landing site, highland units (including Fra Mauro Formation and older material), as well as wrinkle ridges and rilles.*

CRITICAL REVIEW OF REGOLITH EXCAVATION TECHNIQUES FOR LUNAR IN SITU RESOURCE UTILISATION AND SUGGESTED EXPERIMENTAL PARAMETERS. G. H. Just[1], K. Smith[1], K. H. Joy[2], and M. Roy[1], [1] School of Mechanical, Aerospace and Civil Engineering, University of Manchester (Oxford Road, M13 9PL, Manchester, UK; gunter.just@manchester.ac.uk), [2] School of Earth and Environmental Sciences, University of Manchester, (Oxford Road, M13 9PL, Manchester, UK.; katherine.joy@manchester.ac.uk).

Introduction: Space agencies have recently refocused on lunar exploration and are developing plans for a permanent human surface presence. China have landed a probe on the far side of the Moon and the first private lunar mission, the Israeli lander Beresheet, has just been launched. Returning to the Moon is of interest for many scientific fields, from investigating the origin and evolution of the Earth-Moon system, astronomy, earth observation, to life sciences [1]. The use of native lunar resources, referred to as In Situ Resource Utilisation (ISRU), is seen critical for extended exploration in cis-lunar space and the establishment of a sustained lunar surface infrastructure. Initial launch mass and therefore cost can be reduced significantly, while the need for resupply missions from Earth is also reduced [2].

Utilising the lunar regolith: Over the last 4.5 billion years the impacts of asteroids, comets, and their debris have created a regolith layer several meters thick [3]. Chemical elements present in the lunar regolith can potentially be used for mission support; for instance, more than 40% oxygen that can be used in life support systems or as propellant [4][5]. Several techniques for the extraction of oxygen from regolith have been proposed and are being investigated, for example hydrogen reduction [6], carbo-thermal reduction [7], and recently the promising FFC Cambridge process (molten salt electrolysis) [8]. Regolith is also of use for different applications, such as in-situ manufacturing or habitat construction. Technologies that are being developed include: sintering of regolith using concentrated sunlight [9], 3D printing for building habitats (D-shape) [10], selective laser melting [11], and direct energy deposition [12]. Other applications include radiation protection, metal production, or the extraction of solar-wind implanted volatiles.

Excavation and handling techniques for lunar regolith: The mutual requirement of all processing techniques is the constant delivery of pre-processed regolith. Efficient and reliable excavation, handling, and beneficiation processes have to be established. Several possible regolith extraction methods are being investigated at the moment, for example bucket wheels/ladders, pneumatic systems, or scrapers. Currently there is no consensus as to which option is favourable for different lunar surface conditions or manufacturing needs. The geotechnical properties of the lunar regolith, which are significantly different from terrestrial soils, have to be carefully considered. The regolith is highly abrasive (extremely irregular particle shapes), dense, very fine-grained, easily electrically charged, and adhesive [13]. The lunar "dust" damages surfaces, seals, and bearings, subsequently leading to malfunction of mechanical parts or thermal control problems [14]. Therefore, any ISRU hardware that is supposed to operate on the lunar surface for an extended period of time, has to be specifically designed to withstand the impact of these soil properties.

Critical review of excavation techniques and suggestions for future experimental work: A comprehensive review of regolith excavation and handling techniques for lunar ISRU is presented. To compare and evaluate the different mechanisms, a set of representative parameters was chosen, and additionally processes were grouped into different classes. Experimental and gravity conditions are considered in addition to process parameters and the types of simulants used. While performing the review, a need for more universal information and specific data during experimental campaigns became apparent. The encountered problems are presented, their impact explained, and possible solutions are suggested with the aim to enable easier categorisation, comparison, and evaluation of future excavation technologies.

References: [1] I. Crawford et al. (2012) *Plan. & Space Sci., 74,* 3-14. [2] P. Spudis and A. Lavoie (2011) *AIAA SPACE,* 7185. [3] K.H. Joy et al. (2016) *Earth, Moon, & Planets, 118,* 133-158. [4] M. Anand et al. (2012) *Plan. & Space Sci., 74,* 42-48. [5] I. Crawford (2015) *Prog. in Phys. Geo., 39(2),* 137-167. [6] C.C. Allen et al. (1996) *J. of Geophys. Res., 101 (E11),* 26085-26095. [7] R.J. Gustafson et al. (2009) *SAE Int. J. of Aero., 4(1),* 2442. [8] C. Schwandt et al. (2010) *Key Eng. Materials, 436,* 13-25. [9] A. Meurisse et al. (2018) *Acta Astro., 152,* 800-810. [10] G. Cesaretti et al. (2014) *Acta Astro., 93,* 430-450. [11] A. Goulas and R. Friel (2016) *Rapid Proto. J., 22/6,* 864-870. [12] V. Balla et al. (2012) *Rapid Proto. J., 18/6,* 451-457. [13] G. Heiken et al. (1991) *LSB,* Cambridge Univ. Press. [14] V. Badescu (2012) *Moon,* Springer.

Tracing Lunar Magma Ocean crystallisation with Mg-Ca isotope systematics of mare basalts.

M. Klaver[1,*], R.C. Hin[1], J. Lewis[1], T.-H. Luu[1], M. Anand[2] and T. Elliott[1];
[1]Bristol Isotope Group, School of Earth Sciences, University of Bristol. Wills Memorial Building, Queen's Road, Bristol BS8 1RJ, United Kingdom;
[2]School of Physical Sciences, The Open University, Milton Keynes MK7 6AA, United Kingdom
*martijn.klaver@bristol.ac.uk

Introduction: The strong isotopic similarity of the Earth and Moon sits uncomfortably with the giant impact hypothesis for the origin of the Moon. Without invoking a rather low-probability set of conditions for the collision, a giant impact scenario predicts that the Moon should consist predominantly of material derived from the impactor rather than the proto-Earth [1]. Isotopic equilibration of the lunar disk with a terrestrial vapour atmosphere in the aftermath of the collision has been suggested as a potential way to account for the isotopic similarity [2], yet it is potentially problematic for highly refractory elements such as Ti [3]. Mass-dependent ("stable") isotope fractionation of the major mineral-forming elements Mg, Si and Ca provides an excellent tool to critically evaluate the isotopic re-equilibration model. With increasing analytical precision, minute yet important differences in mass-dependent isotope composition between the Earth and Moon can, at least in theory, be resolved. As no samples representative of the bulk Moon are available, however, interpreting such high-precision isotope data is complicated by potential isotopic fractionation during magmatic processing of the Moon.

LMO crystallisation: The Moon is believed to have a differentiated mantle that formed as a result of equilibrium and fractional crystallisation of a lunar Magma Ocean (LMO). Whereas the anorthositic lunar crust is thought to be a direct product of LMO crystallisation through flotation of plagioclase cumulates, the mare basalts represent partial melts of the variably differentiated mantle [e.g., 4]. Crystallisation of the LMO and subsequent partial melting to form the parental melts of the mare basalts are likely to have been accompanied by mass-dependent isotope fractionation. As such, the mass-dependent isotopic composition of the mare basalts, which are commonly used as a bulk Moon datum, is unlikely to be representative of the bulk Moon. This is illustrated by the isotopic dichotomy between low-Ti and high-Ti basalts that is observed for many elements, including Mg, Fe and Ti [5, 6, 7]. Understanding the effects of mass-dependent isotope fractionation during LMO crystallisation is thus important for two reasons: i) it provides an independent constraint on the sources of the mare basalts and the evolution of the lunar mantle; and ii) it allows a bulk Moon composition to be calculated, which can then be compared to the bulk Earth to test the isotopic re-equilibration model.

Mg-Ca isotope constraints: We use high-precision Mg and Ca isotope measurements of low-Ti and high-Ti mare basalts to constrain the crystallisation history of the LMO. These elements are major components in the first phases to crystallise from the LMO (olivine, pigeonite, augite) and thus uniquely suited to trace the earliest stages of differentiation. Mass-dependent isotope measurements are, however, complicated by fractionation during sample preparation and analysis. In order to minimise such effects, we employ the critical-mixture double spike technique to obtain accurate and precise Mg isotope data [8, 9].

Our new data confirm a Mg isotope dichotomy between the low-Ti and high-Ti basalts [7]; the high-Ti basalts have ~0.06 ‰ lower $\delta^{25/24}$Mg than the low-Ti basalts. The latter have a homogeneous Mg isotope composition that is identical to a single KREEP basalt sample (15386) and, within uncertainty, to the bulk Earth [9]. Calcium isotope measurements, using the Proteus collision-cell MC-ICP-MS instrument in Bristol and a ^{42}Ca-^{43}Ca double spike to correct for instrumental mass fractionation [10], are in progress.

The isotopic evolution of the lunar mantle during LMO crystallisation and the composition of extracted melts will be modelled with the latest mineral-mineral and mineral-melt isotopic fractionation factors derived from experiments and *ab-initio* models. By comparing the Mg-Ca data for the mare basalts with the model, it will be possible to constrain mineralogy of the mare basalt sources and thus contribute to elucidating the early differentiation history of the Moon.

[1] Canup (2013) *Nature*, *504*, 27-29. [2] Pahlevan and Stevenson (2007*) Earth Planet. Sci. Lett.*, *262*, 438–449. [3] Zhang et al. (2012*) Nat. Geosc.*, *5*, 251-255. [4] Snyder et al. (1992) *Geochim. Cosmochim. Acta*, *56*, 3809-3823. [5] Sedaghatpour and Jacobsen (2019) *Proc. Nat. Ac. Sci.*, *116*, 73-78. [6] Liu et al. (2010) *Geochim. Cosmochim. Acta*, *74*, 6249-6262. [7] Millet et al. (2016) *Earth Planet. Sci. Lett.*, *449*, 197–205. [8] Coath et al. (2017) *Chem. Geol.*, *451*, 78-89. [9] Hin et al. (2017) *Nature*, *549*, 511-515. [10] Lewis et al. (2018) *AGU abstract* V43A-03.

INTEGRATING NEAR AND MID INFRARED DATA TO EXAMINE MAFIC MINERALS AROUND THE IMBRIUM, APOLLO, AND MOSCOVIENSE BASINS. Rachel L. Klima (Rachel.Klima@jhuapl.edu)[1], Jordan M. Bretzfelder[1,2], Benjamin T. Greenhagen[1], Debra L. Buczkowski[1], and Carolyn M. Ernst[1]. [1]Johns Hopkins University Applied Physics Laboratory, Laurel, MD 20723, USA. [2]University of Southern California, Los Angeles, CA, USA.

Introduction: Lunar missions in the last decade and the advancement of sample analysis techniques have resulted in a wealth of new information about the lunar surface. Integration of data across different subdisciplines is critical for addressing the outstanding science and exploration questions and identifying, as a community, what missions or advances would conclusively answer such questions. Recent studies [e.g., 1, 2], have shown the strength of integrating different remote sensing data sets with one another, or with sample studies. We here focus on a joint analysis using data from the Moon Mineralogy Mapper and the Diviner Lunar Radiometer.

Background and Approach: The Moon has experienced over a dozen impacts resulting in basins large enough to have excavated mantle material. With many of those basins concentrated on the lunar near side, and extensive regolith mixing since the lunar magma ocean crystallized, one might expect that some mantle material would have been found among the lunar samples on Earth. However, so far, only a small number of candidate mantle samples [e.g. 3] have been identified, and their provenance is still debatable [4].

From orbit, a number of olivine-bearing localities, potentially sourced from the mantle, have been identified around impact basins [5]. Based on analysis of near-infrared (NIR) and imaging data, Ohtake et al. [6] suggest that roughly 60% of these sites represent olivine from the mantle. If this is the case and the blocks are coherent and not extensively mixed into the regolith, these deposits should be ultramafic, containing olivine and/or pyroxenes and little to no plagioclase. In the mid-infrared, they would thus exhibit Christiansen features (CF) at wavelengths in excess of ~8.5 μm, which has not been observed in global studies using Diviner [7].

While olivine is certainly a major component of the lunar mantle, the composition of the upper mantle may also include significant amounts of ortho- or clinopyroxene. Using data from the Moon Mineralogy Mapper to search for Mg-suite norites, concentrations of low-Ca, high-Mg pyroxene have been characterized around the Imbrium and Apollo Basins [8], many of which occur in close proximity to olivine outcrops identified using Kaguya data [5]. These deposits may be exposures of Mg-suite plutons, may represent excavated material from deeper within the primary lower crust or mantle, or may be remnants of melt sheets (differentiated or undifferentiated). Less Mg-rich orthopyroxenes have been identified elsewhere, in smaller craters throughout the highlands crust, and within the South Pole-Aitken basin. While Diviner data has not identified any dunite deposits, some CF values could be consistent with pyroxenite or harzburgite compositions.

In this work, we examing mafic deposits excavated by the Imbrium, Apollo, and Moscoviense basin in detail using NIR, Mid IR, and imaging data to assess their bulk mineralogy and current geological context, and potential origins.

Imbrium Basin: The Imbrium basin is large enough to have excavated between 60-85 km into the Moon [9], deep enough to penetrate through the crust and into the mantle. It is also associated with the strongest thorium detections by Lunar Prospector [10], and is likely to be rich in KREEP [11]. The massifs surrounding the basin are clearly associated with the Imbrium basin-forming impact, but existing geological maps do not distinguish between whether they are likely ejecta or rather uplifted from beneath the surface during crustal rebound [12]. NIR data suggest that the massifs contain exposures of four dominant minerals: olivine, Mg-rich orthopyroxene, a second low-Ca pyroxene, and anorthite. Mid-IR results suggest that in the Montes Alpes region, the Mg-rich mafic material is present with substantial amounts of plagioclase. However, in the southeastern porting of Mare Imbrium, near Wolff Mons, the higher (~8.15 μm) CF values of these exposures suggest that these are more likely candidates for pyroxenite or very pyroxene-rich norite [13].

Moscoviense Basin: The Moscoviense basin is located on the far side, but despite being surrounded by relatively thck highlands crust, GRAIL data suggest that the basin floor may contain some of the thinnest crust on the Moon [14]. Based on the preliminary analysis of NIR spectra and CF data, the composition of mafic materials excavated in the SW portion of the basin, including orthopyroxene, olivine, and spinel [15] are unique to that location. Mid IR data suggest that the deposits may contain very little plagioclase. Spectral modeling is underway to more clearly characterize the bulk mineralogy of these deposits.

Apollo Basin: The Apollo basin is another example of a unique geologic setting, as it is superposed on the massive South Pole-Aitken (SPA), and sits above some of the thinnest crust on the Moon [14]. High Mg orthopyroxenes lie along inner ring

of Apollo [8]. Given the thin nature of the crust at Apollo, and the positioning of the high-Mg detections on the inner ring of the basin, it is possible that Apollo excavated deeper primary crustal (or mantle) material than is exposed elsewhere in SPA. However, preliminary Diviner analyses suggest that significant plagioclase is also present in the inner ring, as was found in the Montes Alpes region of Imbrium [13].

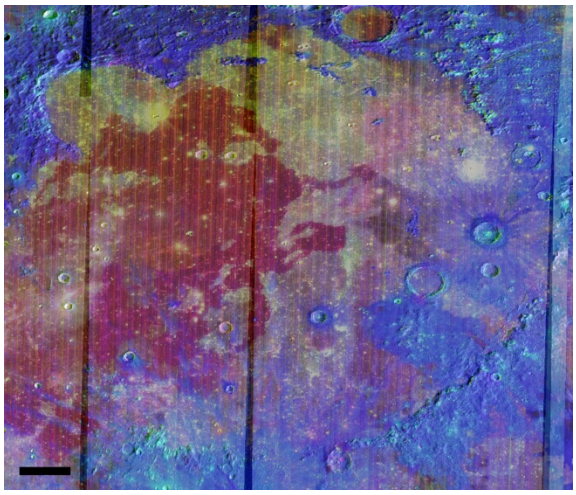

Figure 1: M3 standard color composite (R=integrated 1 μm band depth, G=integrated 2 μm band depth, B=1.58 μm reflectance). Orthopyroxene-rich regions appear as cyan. The highest concentration of Mg-rich orthopyroxene is in the massifs of Montes Alpes (NE corner). The center of Imbrium basin is located at 32.8°N 15.6°W and the scale bar is 100 km across.

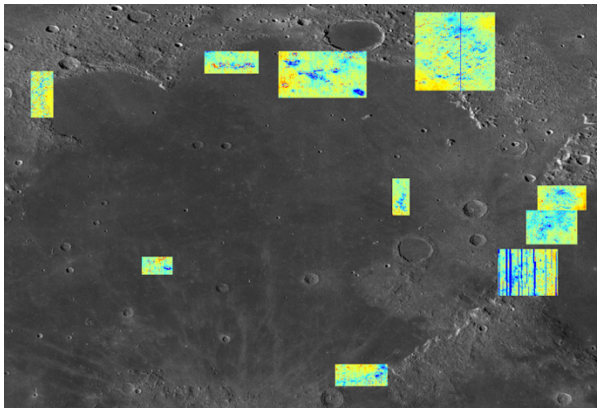

Figure 2: Diviner sites analyzed around Mare Imbrium. Low CF values (cool colors), consistent with anorthosite-dominated lithologies, while higher CF values (warm colors) are found among the mare deposits and in some of the massifs.

Initial Conclusions: Coupled NIR and Mid-IR analyses continue to suggest that large blocks of mantle (or even ultramafic lower crustal) material are rare, if present, on the lunar surface. However, some ultramafic material is excavated on the near-side in the SE of Imbrium, and on the far side around Moscoviense. We will present a comparative analysis of the mineralogical compositions of these materials as well as those excavated around the Apollo basin, to explore the compositional variations as a function of geological setting.

References: [1] Arnold, J. A., et al. (2016) *JGR* 121, 1342–61. [2] Crites, S. and Lucey, P., (2015) *Am. Min.* 100, 973. [3] Schmitt, H. H. (2016), *LPSC* 47, Abstract #2339. [4] Shearer, C. K. et al., (2015), *MAPS* 50, 1449. [5] Yamamoto et al. (2012) *GRL* 39, L13201. [6] Ohtake et al. (2017) *New Views of the Moon 2 – Europe*, Abstract #6016 [7] Greenhagen et al. (2010) *Science* 329, 1507. [8] Klima, R. L., et al. (2011), JGR, doi:10.1029 /2010JE003719. [9] Spudis, P., et al., (1988), LPSC XVIII, 155. [10] Lawrence, D. J. et al. (1998), Science, 281, 1484-1489. [11] Jolliff et al. (2000), JGR, 105, 4197. [12] Wilhelms D. E. et al. (1987), *USGS* Lunar map. [13] Bretzfelder, J. M. et al., (2018), LPSC 49, Abstract #1675. [14] Wieczorek et al. (2013), *Science* 339, 671. [15] Pieters et al. (2011), *JGR*, 116, E6.

Acknowledgements: We are grateful to the NASA LDAP program (grant #NNX16AN50G) and SSERVI VORTICES grant for supporting portions of this work.

AN ITERATIVE STEP IN ASSESSING THE RELATIVE CONTRIBUTIONS OF ACCRETING ASTEROIDS AND COMETS TO THE MOON DURING THE FIRST BILLION YEARS. David A. Kring[1,2], [1]Center for Lunar Science and Exploration, Lunar and Planetary Institute, Universities Space Research Association, 3600 Bay Area Blvd., Houston TX 77058 (kring@lpi.usra.edu), [2]NASA Solar System Exploration Research Virtual Institute.

Introduction: The ancient cratered highlands of the Moon provide the best and most accessible record of early bombardment in the Solar System. Samples from the highlands and, in particular, the margins of three nearside basins, reveal a surprising pattern. Their ages are dominantly ~3.9-4.0 Ga, which was interpreted to mean there was an increase in bombardment at that time (e.g., [1,2]) described as a lunar cataclysm. Strictly speaking, the samples only addressed the timing of the latter third of the basin-forming events. The timing of earlier events remain murky.

Testing the lunar impact cataclysm hypothesis is the highest priority science investigation when we access the lunar surface again [3]. The importance of bombardment to the evolution of the Moon and the need to better understand it is echoed in a recent document prepared at the behest of the NASA Associate Administrator for Science [4] and in a reaffirmation of a National Research Council report [3] by the Lunar Exploration Analysis Group [5].

While the magnitude and duration of the bombardment are immensely important, it is the implications those data have that really tug our interest. What caused the bombardment? What was the source (or sources) of the impacting material? What caused it to pummel the Moon and, by inference, the Earth and other terrestrial planetary surfaces? How did that bombardment affect the early evolution of those surfaces and, at least in the case of the Earth, the early evolution of life. In this paper, I address the progress we have made in assessing the sources of the impacting material.

Evolution of Ideas: Because astronauts recovered samples of impact melt from the basin-forming epoch, the samples can be probed for chemical signatures of any projectile material entrained in them. The preferred tracers are siderophile elements, because the Moon's native abundances were sequestered into the core and mantle. Thus, siderophile elements in impact melts produced in the lunar crust are largely derived from the impactors. Kring and Cohen [6] reviewed that data and found impact melts contained signatures of ordinary (OC) and/or enstatite chondrites (EC) and iron meteorites. Importantly, there did not seem to be any trace of CI or CM carbonaceous chondritic materials, which are our best proxies for comets. Thus, they concluded, "Comets were not important during this time."

We then posed another question: Is there a geological fingerprint of the impacting projectiles? The answer is yes – in the form of the size frequency distribution of craters produced in the highlands. In a novel integration of two methods, Strom et al. [7] measured the size frequency distribution of observed craters and then used pi-scaling techniques to evaluate the size frequency distribution of projectiles that produced them. While the impact parameters for any individual impact can vary, the values for the entire population can reasonably be assumed average (e.g., with a 45 degree impact trajectory). The calculated size frequency distribution matched that of main belt asteroids and not that of comets and Kuiper Belt Objects known at that time. It is important to note that the population of the largest basins is small, which implies greater uncertainty among the sizes of the largest impactors. Nonetheless, based on that analysis, they wrote "Because the impact signature in the crater record in the inner Solar System is asteroidal, we conclude that either comets played a minor role or their impact record was erased by later-impacting asteroids." Our unpublished analysis of the size frequency distribution indicated <15% of craters were produced by comets.

Attention then turned to the lunar regolith. Could fragments of the impactors have survived and be found as relics in ancient lunar soils? In ancient regolith samples, Joy et al. [8] detected relics with affinities to carbonaceous chondrites (CC) and properties distinct from comets. The lack of detectable comet fragments indicated <5 to 17% of the impactors could be comets, leading them to conclude "the impactor relics described here indicate that asteroids were the dominant objects hitting the Earth-Moon system at the end of the basin-forming epoch and that the flux of comets was small." The study also showed the types of impactors diversified after the basin-forming epoch ended.

Those studies collectively suggested the relative contribution of asteroids and comets during the basin-forming epoch, or at least the latter part of the basin-forming epoch, was dominated by asteroids. Can we probe deeper in time?

An obvious target for that question is water, which had, in the midst of the studies above, been detected in lunar samples [9] and, thus, inferred to be present in the lunar interior. Water in asteroids and comets has sub-equal abundances and distinct isotopic compositions. Two questions followed. When did that water accrete to the Moon? What was the

source of that water? Several teams addressed one or both of those questions. Saal et al. [10], Füri et al. [11], and Barnes et al. [12] determined that the water had affinities to asteroidal CC, although Greenwood et al. [13] preferred a cometary origin. Barnes et al. [12] went on to write "…we conclude that comets containing water enriched in deuterium contributed significantly <20% of the water in the Moon." They also argued most of the water was delivered before the Moon's crust solidified. If true, the asteroids delivered water to the Moon in its initial ~200 million years of evolution.

Dynamical Insights: The geological record of bombardment [7] has implications for the dynamical origin of the bombardment. Because the size frequency distribution of calculated projectile diameters matched that of main belt asteroids, the asteroid belt must have provided projectiles in a size-independent manner. That suggests gravitational resonances swept through the asteroid belt. That implied, in turn, that the orbits of Jupiter (and other giant planets) evolved.

In parallel with the geochemical, isotopic, and geological studies described above, several dynamical models for early Solar System evolution were being developed. Gomes et al. [14], for example, proposed an instability caused giant planets to migrate, which had the advantage of increasing the proportion of asteroids delivered to the inner Solar System over previous models [15]. The parameter space for those dynamical models continues to be explored (e.g., [16-18]).

New Directions: The work of [7] prompted a hypothesis: If resonances were sweeping inward, could we detect the early production of impactors from the outer belt, followed by impactors from the inner belt? Thus began an examination of the geochemical and isotopic fingerprints of impactors in lunar impact melts as a function of their age using new analytical techniques developed by Walker's group [19-21] and others. Their data are broadly consistent with a diverse set of chondritic impactors and an additional contribution from a fractionated core-composition impactor, although Fischer-Gödde and Becker [22] suggest the diversity is, instead, a mixing trend between a CC component and a type IVA iron meteorite component. If the compositions of Liu et al. [21] reflect multiple impactors rather than mixing, then compositions evolve from CC affinities at 4.2 Ga to OC and EC affinities at 3.75 Ga, which might be reflecting sweeping of resonances as postulated by [7] from the outer to inner portions of the asteroid belt. In the midst of that sweep, impactors with iron meteorite affinities occur, which could have been scattered from the terrestrial zone and deposited in the midst of the asteroid belt before the resonances moved. Materials with geochemical and isotopic affinities to OC and EC, along with type IAB irons, are also important components in the local feeding zone of the accreting Earth [23].

Conclusions: There sometimes appears to be a tangle of evidence, in part because of the challenge to separate sources during accretion (both before and after the giant impact, both before and after core formation) and subsequent impacts (both before and after lunar crust formation). A comprehensive solution eludes us. While it will be productive to continue probing the existing collection of lunar samples and explore dynamical models that may have delivered the projectiles, it is clear that substantial, potentially transformative [4], progress can be made if/when we collect new samples from the Moon at specifically targeted sites and return them to Earth for detailed analyses. It will be enlightening, for example, to determine the age and nature of the projectiles that produced the oldest basin (South Pole-Aitken basin) and one of the youngest basins (Schrödinger and Orientale). As has been explored elsewhere (e.g., [24]), a mission to the Schrödinger basin has the potential to provide all of those answers.

References: [1] Turner G., Cadogan P. H., & Yonge C. J. (1973) *Proc. Fourth Lunar Sci. Conf.*, 1889–1914. [2] Tera F., Papanastassiou D. A., & Wasserburg G. J. (1974) *EPSL*, *22*, 1–21. [3] National Research Council (2007) *The Scientific Context for Exploration of the Moon*. National Academies Press, 107p. [4] Pieters C. M., Canup R., Kring D. A., Head J. W. III, & Scott D. R. (2018) *Transformative Lunar Science*. NASA SSERVI, 8p. [5] Lunar Exploration Analysis Group (2018) *Advancing Science of the Moon: Report of the Special Action Team*, 67p. [6] Kring D. A. & Cohen B. A. (2002) *JGR*, *107*, 10.1029/2001JE001529, 6p. [7] Strom R. G., Malhotra R., Ito T., Yoshida F., Kring D. A. (2005) *Science*, *309*, 1847–1850. [8] Joy K. H. et al. (2012) *Science*, *336*, 1426–29. [9] Saal A.E. et al. (2008) *Nature*, *454*, 192–195. [10] Saal A. E., Hauri E. H., Van Orman J. A., & Rutherford M. J. (2013) *Science*, *340*, 1317–1320. [11] Füri E., Deloule E., Gurenko A., & Marty, B. (2014) *Icarus*, *229*, 109–120. [12] Barnes J. J. et al. (2016) *Nature Comm.*, *7*, doi: 10.1038/ncomms11684, 10p. [13] Greenwood J. P. et al. (2011) *Nat. Geosci.*, *4*, 79–82. [14] Gomes R., Levison H. F., Tsiganis K., & Morbidelli A. (2005) *Nature*, *435*, 466–469. [15] Levison H. F. et al. (2001) *Icarus*, *151*, 286–306. [16] Marchi S., Bottke W. F., Kring D. A., & Morbidelli A. (2012) *EPSL*, *325–326*, 27–38. [17] Morbidelli A., Marchi S., Bottke W. F., & Kring D. A. (2012) *EPSL*, *355–356*, 144–151. [18] Morbidelli A. et al. (2018) *Icarus*, *305*, 262–276. [19] Puchtel I. S. et al. (2008) *GCA*, *72*, 3022–3042. [20] Sharp M. et al. (2014) *GCA*, *131*, 62–80. [21] Liu J. et al. (2015) *GCA*, *155*, 122–153. [22] Fischer-Gödde M. & Becker H. (2012) *GCA*, *77*, 135–156. [23] Bermingham K. R., Worsham E. A., & Walker R. J. (2018) *EPSL*, *487*, 221–229. [24] Hurwitz D. & Kring D. A. (2015) *EPSL*, *427*, 31–36.

Luxembourg's Space Resources Initiative. B. Lamboray[1] and G. Martin[2], [1]Luxembourg Space Agency (Bob.Lamboray@space-agency.lu), [2]Luxembourg Space Agency (Gary.Martin@space-agency.lu).

Introduction: This presentation highlights Luxembourg's SpaceResources.lu initiative and recent results from an important study, 'Opportunities for Space Resources Utilization: Future Markets & Value Chains', conducted in 2018 by the Luxembourg Space Agency (LSA) in support of the initiative.

In 2016, Luxembourg launched the SpaceResources.lu initiative with the long-term vision to enable the exploration and utilization of space resources. The objective was also to create a framework supporting the broader commercialization of space activities by carving out an envelope of 200 M Euros for various activities to support the initiative. In 2017, Luxembourg passed legislation that enabled the creation of a regulatory framework needed to decrease risk and enable businesses to harvest and use space resources. In September of 2018, Luxembourg announced the creation of the Luxembourg Space Agency (LSA). These actions illustrate the strong determination of the country to reach their long-term vision of developing a thriving commercial space sector.

In line with the vision of Luxembourg's SpaceResources.lu initiative, the Luxembourg Space Agency conducted a year-long study to identify potential markets and the most promising value chains for using space resources in the next few decades. The analysis assessed the technical aspects and socio-economic benefits of this promising new industrial sector, and confirmed the enormous opportunities that appear on the horizon.

APPLICATIONS AND PLANNING FOR LUNAR LASER RETROREFLECTOR STUDIES. E. S. Law[1], G. W. Chang[1], N. Gallegos[1], S. Malhotra[1], S. Casini[2], B. H. Day[3], D. G. Currie[4], S. Dell'Agnello[2], [1]Jet Propulsion Laboratory (JPL), California Institute of Technology, [2] National Institute for Nuclear Physics-Frascati National Labs (INFN-LNF), Frascati (RM), Italy, [3]NASA Ames Research Center, Solar System Exploration Research Virtual Institute (SSERVI), [4]University of Maryland at College Park (UMCP), MD, USA

Introduction: NASA is collaborating with INFN-LNF and UMCP on the development of a tool targeted to facilitate Lunar Laser Retro-Reflector (LRR) and Lunar Laser Ranging (LLR) studies and mission planning. The tool called LRR/LLR Geometry Calculator will allow mission planners and researchers to find, visualize, and analyze images taken by the Lunar Reconnaissance Orbiter (LRO) that are applicable to LRR/LLR planning and research using NASA's Solar System Treks [1] Project's Moon Trek [2]. This presentation will provide an overview of LRR/LLR, and describe the tool and Moon Trek along with their LLR applications.

LRR and LLR: Five passive LRRs were installed on the Moon, three by the landing crews of Apollo 11, 14, 15 and other two mounted on the Lunokhod 1 and 2 rovers. LLR analysis provides high-precision measurements of ranges between observatories on Earth and LRRs on the Moon surface. LLR has become an essential technique to study geodesy, the dynamics of the Earth-Moon system, studies of the lunar interior, and is especially important for gravitational physics. LLR studies from various sites on the Earth have resulted in the relative positions of the arrays to be determined to the centimeter level. However, the limited number of points provided by the few retroreflectors on the lunar surface constrains the general accessibility of the LRR reference frame.

Resarchers at INFN-LNF and at UMCP are building and proposing to NASA, ESA, ASI (and other space stakeholders) next generation LRRs targeting a number of opportunities to return to the Moon (see Figure 1 and [3]). These include NASA's Commerical Lunar Payload Services (CLPS) and Lunar Surface Instrument and Technology Payload (LSITP) Announcements of Opportunities. The new LRRs will improve the knowledge of the lunar interior, the realization the lunar reference frame and the accuracy of several tests of general relativity, especially when deployed as a network and in combination with other geophysical instruments, like seismometers and heat flow probes [4].

Moon Trek: NASA's Solar System Treks Project (SSTP) produces a suite of interactive visualization and analysis Trek portals. The project is an integral element of NASA's SSERVI [5]. It is developed and operated at NASA's JPL[6]. These web-based portals enable mission planners, planetary scientists, and the public to access mapped data products from a wide range of instruments aboard a variety of missions, for a growing number of planetary bodies. Moon Trek offers data from past and current lunar missions and features a powerful set of analysis tools such as rock and crater detection, lighting and slope analysis.

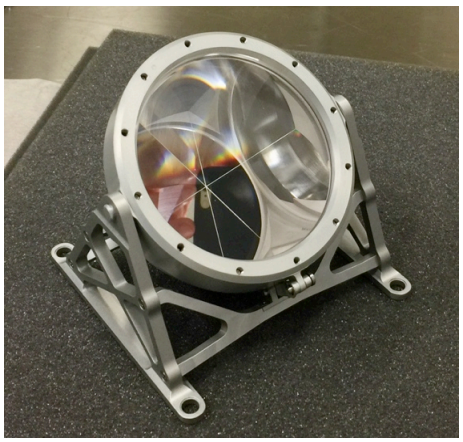

Figure 1. Next-gen LRR model (a single, large laser retroreflector in place of retroreflector arrays).

LRR/LLR Geometry Calculator: In collaboration with investigators from INFN-LNF and UMCP, the SSTP team is currently developing the LRR/LLR Geometry Calculator to support LLR planning and research. It will be used to predict geometries between Earth laser stations, LRRs, and LRO such that a pulse fired from Earth will reflect into the NAC instrument, and to identify NAC images showing reflections of the Sun or lasers off of the reflectors. The tool is to provide answers to six key questions: 1) When an LRR is visible from a ground laser station, so that station could shine its laser and hit the LRR? For a newly-deployed next-generation LRR, this means it must be correctly aligned to Earth. An LRR is *correctly aligned* to Earth when the normal to its retro-reflecting surface is pointed along the Earth line of sight from the LRR lunar location *averaged* over the full cycle of the lunar libration pattern. 2) When LRO cameras were pointing at the LRR? 3) When the Sun's Fresnel reflection from a LRR could be seen in a LRO image? The photometric observation of Fresnel solar glints from single retroreflector surfaces has been proven with the LAGEOS satel-

lites [7][8]. Here we look for Fresnel solar glints from 100 reflectors (Apollo 11, 14) or 300 reflectors (Apollo 15). 4) Which LRO images are available in the Planetary Data System (PDS) [9] that have the LRR in view? 5) Are there any LRO images available in the PDS that have the solar glint off the LRR? 6) Are there any LRO images are available in the PDS that have the Fresnel reflection from the LLR ground station? The answers to these questions will eventually allow Moon Trek users to find, access, visualize and analyze LRO NAC images that can greatly facilite existing LLR research and future LLR planning and studies.

Design And Development: The SSTP team has employed an incremental and iterative approach in the development of the calculator. Initially, a standalone prototype was implemented. The prototype was shared with the Italian partners whose inputs were used to fine tune the requirements and use cases. Once the next iteration of the prototype is completed, the calculator will be integrated with Moon Trek to make it widely available to the lunar community at large.

The standalone prototype comprises services using web-based APIs to compute geometries between a point on Earth, LRO, Sun, and one of 5 LRR sites on the Moon. The web-based services are designed to use all available CPUs on the machine to compute the time intervals when the specified geometries are satisfied with the constraint of time, the Earth, the LRO, and Sun angles at the specific LRR location.

The prototype also provides a user interface to visualize the geometries, used primarily to verify that the calculations are correctly computed (see Figure 2).

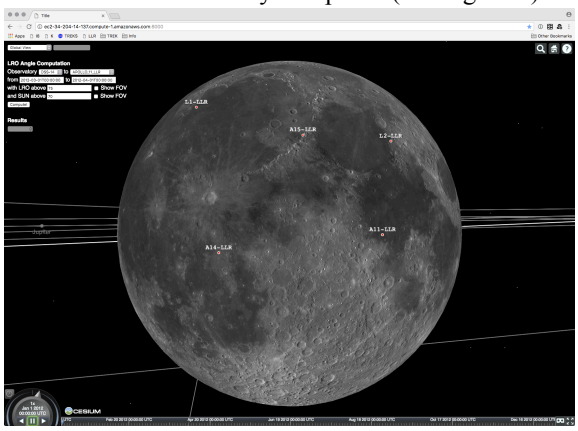

Figure 2. Standalone Prototype User Interface.

The prototype was designed to be scalable and configurable allowing users to specify six parameters: 1) Observatory – Discrete set of LLR stations; 2) LLR – Discrete set of LRRs; 3) LRO-MIN-DEC – Minimum declination (deg) of LRO; 4) SUN-MIN-DEC – Minimum declination (deg) of the Sun; 5) START-TIME – Start time of search window (ISO 8601); 6) END-TIME – End time of search.

Using the knowledge of LRO orbits, data from NASA's observational geometry system SPICE [10], and the specified parameter values, the final prototype will provide answers to all six questions.

Future Work: The next iteration of the prototype and its results will help validate the correctness of calculation and the answers. The results will be used to retrieve the LRO NAC images, which in turn will be map projected. Finally, the prototype will be integrated with Moon Trek. This will entail adding an user interface for users to specify required parameters and execute the web services via Moon Trek's backend infrastrucuture. Upon completion of the calculation, users will be able to select and view the resulted images on Moon Trek in 2D and in 3D. Prior to the official release of the calculator on Moon Trek, the lunar community will be invited to conduct beta testing and provide feedback.

Acknowledgments: We thank the Planetary Science Division and the Science Engagement & Partnerships Division of of NASA's Science Mission Directorate, and the Advanced Explorations Systems Program of NASA's Human Exploration Operations Directorate for their support in the development of Solar System Treks and Moon Trek. The activity is also part of the INFN Affiliation to NASA-SSERVI, of INFN's research program named "MoonLIGHT" and of the joint research activities of INFN-LNF and the ASI-Matera Laser Ranging Observagtory (MLRO). The latter is one of the three currently active LLR stations, together with APOLLO (Apache Point Observatory Lunar-Laser ranging Operation) in USA and Grasse in France.

References:

[1] Solar System Treks – https://trek.nasa.gov
[2] Moon Trek – https://trek.nasa.gov/moon
[3] S. Dell'Agnello. D. G. Currie et al (2019), The Return of Laser Retroreflectors to the Moon, proc. of Lunar Exploration Renaissance Conferenc
e, Brussels, Belgium.
[4] C. R. Neal et al (2019), The Lunar Geophysical Network Mission, 50th LPSC (LPI Contrib. # 2132).
[5] SSERVI – https://sservi.nasa.gov
[6] JPL – https://jpl.nasa.gov
[7] Avizonis, P. V. J. (1997), Ph.D. thesis, Univ. of Maryland at College Park, MD.
[8] T. Otsubo, R. A. Sherwood, P. Gibbs, R. Wood (2004), DOI 10.1109/TGRS.2003.817191.
[9] PDS – https://pds.nasa.gov
[10] SPICE – https://naif.jpl.nasa.gov/naif/

MICROWAVE HEATING EXPERIMENT OF LUNAR SIMULANT (JSC-1A) USING A BESPOKE INDUSTRIAL MICROWAVE APPARATUS. S. Lim[1] (sungwoo.lim@open.ac.uk), A. D. Morse[1], M. Anand[1,2] and A. Holland[1], [1]School of Physical Sciences, The Open University, Walton Hall, Milton Keynes MK7 6AA, [2]Department of Earth Sciences, The Natural History Museum, London, UK

Introduction: The Space Instrumentation Group at The Open University are investigating microwave sintering of lunar regolith/simulant as a potential fabrication method of 3D printing on the Moon to build lunar habitats. This has enabled us to integrate our existing expertise in 3D Concrete Printing [1, 2] and knowledge of lunar science and ISRU potential on the Moon [3] to perform a series of microwave sintering experiments aiming to develop a potential fabrication method of an extra-terrestrial construction process.

As part of this initiative, we have designed an industrial bespoke microwave heating apparatus. This apparatus will allow a thorough experimental investigation of the sintering mechanism of lunar regolith/simulant in the cavity. The mechanical properties of sintered specimens produced under optimal conditions can then be explored. The experiment will also be validated using COMSOL Multiphysics simulation software. In this contribution, we discuss the first outcomes using the bespoke microwave heating apparatus, and how COMSOL has been employed to understand the different characteristics of lunar regolith when subjected to microwave heating.

Microwave sintering: Microwave sintering of lunar regolith as a potential fabrication method of lunar habitat construction has become one of the favourite topics in recent years [4]. Previous research in this area, however, have been conducted using domestic microwaves, which are not ideal for sintering lunar simulants due to (i) incapable of withstand temperatures of up to 1,250 °C – the melting point of lunar regolith/simulant; (ii) not optimised to maximise microwave energy into a single hotspot; (iii) unable to mimic lunar atmospheric condition; (iv) it is not possible to measure sample surface temperature accurately; and (v) the fixed frequency at 2.45 GHz which is an optimal frequency to heat water molecules in food products but may not be optimal for inorganic solid materials such as lunar regolith.

Thus, an industrial bespoke microwave heating apparatus has been designed to overcome the current limitations. Figure 1 illustrates a design of the apparatus which includes two pyrometers, one viewfinder window, and a cylindrical cavity with a flange for a vacuum pump. The ports can also be connected to a mass spectrometer, permitting extraction and analysis of volatiles while specimens are heated. Volatiles in regolith can be extracted by heating the regolith between 300 and 900 °C [3, 5]. For example, a temperature of 700 °C is sufficient to obtain most of the H_2 and He [6]. Thus, the apparatus could also be used for measuring the types and amount of volatiles which could be used for propellant and life support (e.g. water). The new apparatus would allow to (i) maximise microwave energy in a single hotspot; (ii) measure the surface temperature and phase change of specimens under a near lunar atmospheric condition with more accuracy, and (iii) heating specimens of lunar simulant rapidly to be sintered/melted. This first version of the apparatus does not support multiple frequencies; however, this feature is planned to be added in a future upgrade.

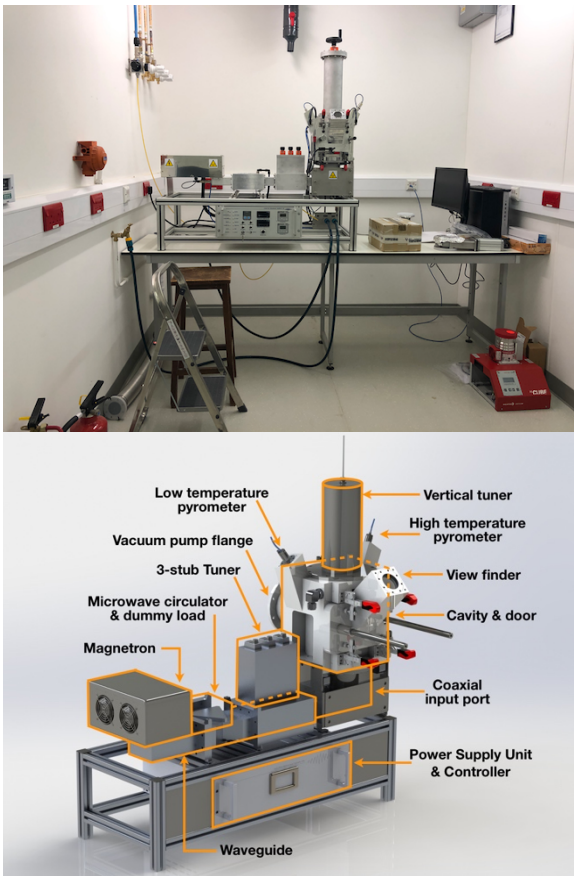

Figure 1: Bespoke microwave heating apparatus (above) and the detailed parts (bottom)

Numerical Modelling: As complementary research of the lab-experiment, we have chosen COMSOL (version 5.4), which has been used previously for a similar purpose [7]. COMSOL requires various parameters of material characteristics to simulate microwave heating phenomenon. The findings from the numerical modelling are (i) verifying the bespoke design of the cavity that could maxim-

ise microwave energy to heat specimens; (ii) understanding the sequence of sintering phenomenon by continual simulation of the surface and internal temperature of specimens; and (iii) identifying the different effects of sintering among frequencies in terms of the time and penetration depth.

Preliminary outcomes: A few preliminary experiments have been conducted, and the results show that 50 grams of lunar simulant JSC-1A, which has high iron contents, under 1,000 W of input power is well coupled with microwave energy and easily melted/sintered within 3 to 6 minutes. Figure 2 shows one of the sintered specimens with a partially melted core while the surface temperature of the specimen was 230 °C only. This is possibly caused by thermal runaway effect observed through the simulation of microwave heating behaviour of lunar regolith.

Figure 2: Microwave heated JSC-1A. Total 44 grams out of 50 grams was melted/sintered. Note that the white stuff on the surface of the sintered specimen is a residue of ceramic paper which prevents the specimen from being sintered to the crucible surface.

Our early simulation experiments using the material properties of lunar regolith indicate that highlands regolith, which has low iron contents – FeO 6.2 wt%, was struggling to be melted as the specimen temperature did not reach to the melting point (1,250 °C in this experiment) in 15 minutes. On the other hand, Mare regolith, which has high iron contents – FeO 16.6 wt%, exceeded the melting point in 7 minutes although it only happened to one hotspot point. The pre-defined mass was 35 grams, and the input power was 1,000 W. More data on the lab experiment and simulation would be given during the presentation.

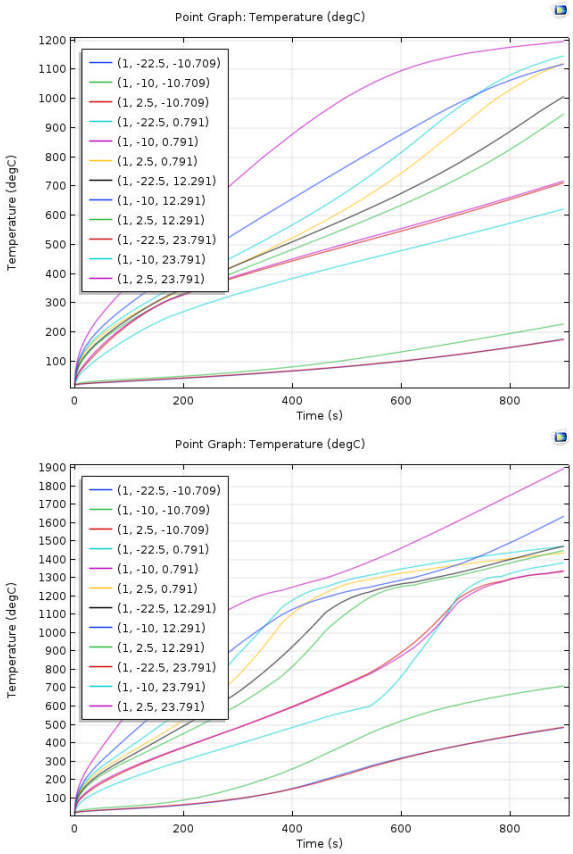

Figure 3: Simulation of the temperature curves of 12 sampled points in a specimen. Top – Highland regolith, Bottom – Mare regolith. Note that the red-dot curve represents the maximum temperature in the specimen.

Acknowledgement: The authors acknowledge funding from the Open University's Space SRA.

References:

[1] Lim, S., et al. (2016). *Additive Manufacturing*, 12(B), 216-230. [2] Lim, S., et al. (2012). *Automation in Construction*, 21(1), 262-268. [3] Anand, M., et al. (2012). *Planet. and Space Sci.*, 74(1), 42-48. [4] Lim, S., Prabhu V.L., Anand, M. and Taylor, L. (2017) *Adv. in Space Research J.*, 60(7), 1413-1429. [5] Ethridge, E. and Kaukler, W. (2012). *Concepts and Approaches for Mars Exploration.* [6] Crawford, I. (2015). *Progress in Physical Geography*, 39, 137-167. [7] Ethridge, E. and Kaukler, W. (2012) *50th AIAA Aerospace Sci. Meeting*, AIAA2012-0801.

FORMATION AND EVOLUATION OF THE MOON: THE KEY QUESTIONS ADDRESSED BY FUTURE LUNAR MISSIONS. Y. T. Lin[1], [1]The Key Laboratory of Earth and Planetary Physics, Institute of Geology and Geophysics, Chinese Academy of Sciences, Beijing 100029, LinYT@mail.iggcas.ac.cn.

Introduction: The modern knowledge of the Moon has been established mainly by about 50 years study of Apollo lunar samples and the numerous missions launched since 90's last century. However, the available lunar samples were collected from 6 Apollo and 3 luna mission landing sites, covering only 6-8% of the surface of the Moon. In addition, previous studies of Apollo samples reveal common contamination by the ejecta from Mare Imbrium. About 360 lunar meteorites have been approved[1], which are better representative of the Moon, but lack of petrographic settings. Another issue is to estimate quantitatively the characters and mass of impactors, which would have affected the distribution of water and volatiles in the Moon.

The Moon has become a hot spot and a main targets for space exploration before 2035. In addition, constructing of lunar research station has been considered in the future lunar missions, and there are proposals of sending astronauts back to the Moon. In order to take this unique opportunity to promote the lunar science, we need to review the remaining key questions of the Moon, which can be addressed by the future missions.

Key questions: The previous exploration of the Moon mainly focused on the near side, no missions landed on the far side except for Chang'E-4 roving in Von Karman crater within SPA. Furthermore, the returned lunar samples and remote sensing mainly obtain information from the surface of the Moon. Future well-designed missions can overcome these deficiencies and address below key questions.

The deep lunar interior. Because of very limited seismic data obtained in Apollo era, the deep interior of the Moon is poorly known. The size and status of the core, and the crust-mantle boundary are not well constrained, and the cause for velocity discontinuity at ~20 km is unsure. In addition, there were no seismic data from the far side. Installing seismographs in the South Pole and returning samples from SPA will shed light on the deep interior of the Moon. In addition, these robotic missions can be integrated with manned exploration, which has a unique advantage of setting up the observation network of broadband seismographs and other geophysical instruments.

Detailed impacting history of the Moon and the inner solar system. The Moon preserved the most complete impact history of the inner solar system. However, the impact flux were calibrated only for the period between 4-3 billion years by isotope geochronology of Apollo samples. Returning samples from the oldest impact basin South Pole-Aitken (SPA) and the youngest regions in Procellarum KREEP Terrane (PKT) will extend the impact flux curve to both sides, calibrate the crater dating method and clarify the Later Heavy Bombardment at about 3.9 billion years ago. The characters and mass of the impactors, which may vary with time, can be addressed via in situ separating of asteroid fragments from lunar soils at various sites with different ages.

Distribution of water and volatiles. The debate on water and volatile contents of the Moon was arisen mainly due to the discovery of high water content in the volcanic glass beads [2]. It is required to return pristine plutonic rocks from more geographic settings, in order to clarify the distribution of water and volatiles and possible correlation with highly siderophile elements. In addition, the presence of water ice in the permanently shadowed craters in both poles can be explored by in situ measurement with flying robots, and its possible reservoirs will be indicated by H isotopes. These new data will constrain the Giant Impact hypothesis of the Moon.

The surface history and processes. The lunar regolith has recorded up to 4 billion years surface history of the Moon. However, the maximum length of the lunar regolith drill cores returned by Apollo missions is about 2.4 m [3]. In contrast, the "rabbit holes" made by asteroid impact on basaltic tubes exposed up to 100 m thick regolith profiles. These "rabbit holes" supply with a unique opportunity to study the complete history and processes took place on the lunar surface. Another question is the presence of the Earth wind, which can be solved by returning lunar soil from the far side.

Lunar dichotomy. Beside the topography and the surface composition, exploration of the far side, especially SPA, will reveal if the deep interior maintains the dichotomy, and clarify the origin of lunar dichotomy.

References: [1] Meteorite Bulletin Database. [2] Saal A. E., et al. 2008. *Nature* 454: 192-195. [3] Heiken G., et al. 1991. *Lunar sourcebook: A user's guide to the Moon.* 736.

SUBMILLIMETER SOLAR OBSERVATION LUNAR VOLATILES EXPERIMENT (SSOLVE). T. A. Livengood[1], C. M. Anderson[2], Q. Bonds[2], D. C. Bradley[2], B. T. Bulcha[2], G. Chin[2], T. Hewagama[1], T. L. Jamison-Hooks[2], P. E. Racette[2]. [1]University of Maryland, timothy.a.livengood@nasa.gov; [2]NASA Goddard Space Flight Center.

Introduction: The Submillimeter Solar Observation Lunar Volatiles Experiment (**SSOLVE**) is a pathfinder for lunar exploration, a small and simple instrument to resolve broad uncertainty in the abundance of lunar water and processes for its supply, removal, and relocation. Water observed in the lunar surface and polar cold traps could be delivered by solar wind or meteoroids or it could be indigenous, with powerful implications for the Moon's formation history and evolutionary processes The key to distinguishing the source of lunar water and present processes controlling it is the abundance of water in the atmosphere/exosphere and its diurnal variability. SSOLVE is designed to make these measurements, with high sensitivity and precision.

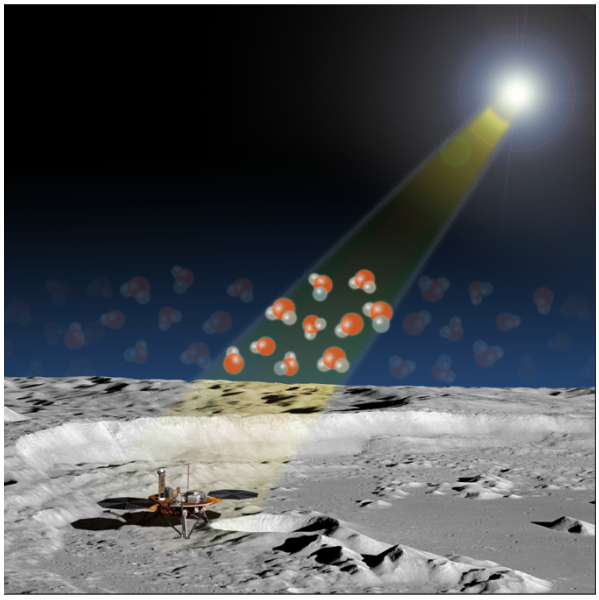

Fig. 1: SSOLVE will measure lunar water vapor against the bright Sun. SSOLVE will operate submillimeter spectrometers from a lander, using a heliostat to target the Sun to measure the column abundance of H_2O, OH, and HDO in the lunar atmosphere. H_2O and OH establish the chemical state of water and constrain current photolysis and loss rates, while HDO/H_2O constrains the history of hydrogen loss. Spectral absorption features can measure very small quantities of atmospheric water, $<10^{12}$ mol/cm^2 (~10^5 mol/cm^3 at surface). Vapor quantities inferred from diurnal variability of surface hydration, $>10^{14}$ mol/cm^2 (~10^7 mol/cm^3), could be detected in <10 min.

Technique: SSOLVE will use the Sun as a light source to illuminate the presence of water in the tenuous lunar atmosphere: its abundance, diurnal variability, chemical state (H_2O vs. OH), and the balance between sources and loss (Fig. 1). Water is critical to understanding lunar formation, the interaction between rocky bodies and space, and the potential for *in situ* resource utilization (ISRU) in lunar exploration and beyond. The SSOLVE design employs two bore-sighted heterodyne spectrometers: one spectrometer detects the 557 GHz transition of H_2O and the 509 GHz transition of HDO; the other spectrometer detects the 2510 GHz transition of OH. Doppler broadening in the absorption lines will measure the translational temperature of the gas to determine whether it is thermally accommodated to the local surface temperature as usually assumed. A sun-tracking scanner (heliostat) will acquire and track the Sun regardless of lander orientation, as well as enabling measurements on dark sky and on calibration targets. A radome and enclosure will shield the instrument from dust and visible-wavelength sunlight to enable staring at the Sun (Fig. 1).

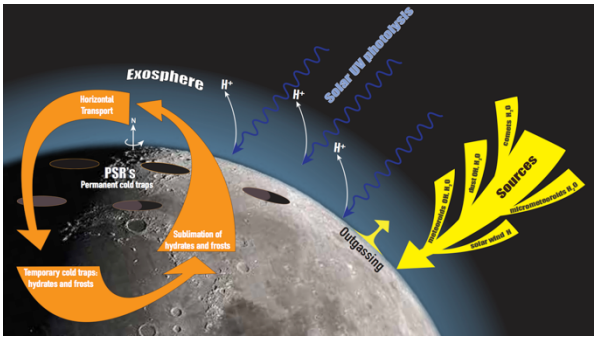

Fig. 2: SSOLVE will measure water vapor to learn which source(s) of water dominates the lunar atmosphere. The global inventory of water in the atmosphere/exosphere is in equilibrium between input sources (yellow) and losses to space and (potentially) permanent cold traps at the poles. Molecules migrate from the warm daylight surface across the terminator to be temporarily trapped on the cold night-time surface until the Moon's rotation brings the hydrated/frosted surface into daylight to thermally desorb the volatiles into the atmosphere, completing a hydration cycle (orange).

Measurement scenario: In a fourteen-day mission, SSOLVE will quantify the amount of water in the Moon's exosphere, retiring the controversy in the scientific community as to the amount of water and whether there is horizontal transport across the Moon's surface (Fig. 2.

The abundance of water in the tenuous atmosphere immediately above the daytime lunar surface has not been measured, although a wide range of estimates can be derived from measurements on orbit (Benna *et al.* 2018), remote sensing (Li and Milliken 2017; Livengood *et al.* 2015; Sunshine *et al.* 2009; Fig. 3), and equilibrium

between assumed supply and loss rates (Table I). These estimates vary by orders of magnitude. The instruments that were deployed by the Apollo missions were unable to measure the neutral atmosphere in daylight due to instrument problems, so neither the total gas pressure nor the composition of volatiles at the surface are known with any certainty (Cook *et al.* 2013; Stern *et al.* 2013; Hoffman and Hodges 1975).

Water is challenging to investigate in small quantities due to its presence as a contaminant on instrument surfaces, in sample handling environments, and in rocket exhaust. SSOLVE is designed to overcome these problems by measuring the total column of H_2O and OH above the lunar surface, in comparison with calibration measurements that can eliminate local contributions to water vapor in the line of sight. SSOLVE will use high spectral resolution to identify transitions of H_2O, OH, and HDO with certainty, to measure abundance, and to characterize physics in the exosphere using Doppler linewidth from translational motion.

Table I: SSOLVE will determine the abundance of lunar water vapor – or confirm near-zero abundance

basis		column abundance, H_2O or OH	volume density
Maximum above exobase	collisionless atmosphere	3×10^{14} mol/cm^2	3×10^{7} mol/cm^3
LADEE mass spectrometer	4 km above surface	$\leq 10^{10}$ mol/cm^2	$\leq10^{3}$ mol/cm^3
comparable to or greater than [H_2]	[H_2] ~10^9–10^{10} mol/cm^2	10^9–10^{10} mol/cm^2	10^2–10^3 mol/cm^3
micrometeoroid dominated	<100% H_2O	$<10^{12}$ mol/cm^2	$<10^{5}$ mol/cm^3
solar wind dominated	<100% efficiency	$<10^{13}$ mol/cm^2	$<10^{6}$ mol/cm^3
mineral hydrate concentrations	total surface reservoir ~10^{19} H_2O/cm^2	3×10^{16} mol/cm^2	3×10^{9} mol/cm^3

Gray shading indicates abundance less than the H_2O detection threshold of ~3×10^{11} mol/cm^2.

Mission concept: The SSOLVE instrument design and measurement goals assume a solar-powered lander outside the polar regions, within approximately ±60° latitude. The diurnal variability that SSOLVE will measure is diminished closer to the poles. Solar power restricts the mission to one lunar day, as surviving the lunar night cannot be assumed without power for survival heaters. We assume sufficient power for instrument operation in 12 days out of ~14 days of sunlight. The longest integration time that we consider assumes a duty cycle of ~16.7% to conserve average power, resulting in 48 hours' total integration time. Longer total survival or higher duty-cycle would reduce the minimum measurable column proportional to the square root of integration time.

References: [1] Benna *et al.* (2018). Lunar Soil Hydration Constrained by Exospheric Water Liberated by Meteoroid Impacts. *Nature Geoscience*, submitted. [2] Li and Milliken (2017). Water on the surface of the Moon as seen by the Moon Mineralogy Mapper: Distribution, abundance, and origins. *Science Advances* **03**, e1701471, doi: 10.1126/sciadv.1701471. [3] Livengood *et al.* (2015). Moonshine: Diurnally varying hydration through natural distillation on the Moon, detected by the Lunar Exploration Neutron Detector (LEND). *Icarus* **255**, 100–115, doi: 10.1016/j.icarus.2015.04.004. [4] Sunshine *et al.* (2009). Temporal and Spatial Variability of Lunar Hydration As Observed by the Deep Impact Spacecraft. *Science* **326**, 565–568, doi: 10.1126/science.1179788. [5] Cook *et al.* (2013). New upper limits on numerous atmospheric species in the native lunar atmosphere. Icarus 225, 681–687, doi: 10.1016/j.icarus.2013.04.010. [6] Stern *et al.* (2013). Lunar atmospheric H2 detections by the LAMP UV spectrograph on the Lunar Reconnaissance Orbiter. *Icarus* **226**, 1210–1213, doi: 10.1016/j.icarus.2013.07.011. [7] Hoffman and Hodges (1975). Molecular gas species in the lunar atmosphere. *The Moon* **14**, 159–167, doi: 10.1007/BF00562981.

DETERMINING THE VOLATILE HISTORY OF THE MOON THROUGH GEOMORPHOLOGICAL STUDIES OF ERUPTION DEPOSITS AND MODELLING OF VOLCANIC PROCESSES. M. Lo[1], M. Burton[1], K. Joy[1], G. La Spina[1], and M. Polacci[1]. [1]School of Earth and Environmental Sciences, University of Manchester, Oxford Road, Manchester, M13 9QQ, UK (marissa.lo@manchester.ac.uk).

Introduction: Volatile magmatic species play an important role in volcanic systems, affecting the transport and rheology of melts. Understanding the volatile content of the lunar interior is valuable for understanding the thermal and magmatic evolution of the Moon, as well as understanding how the formation of the Earth and Moon were related.

The volatile composition of the lunar interior can be studied using various approaches: petrological modelling, geochemical analysis of meteorites and returned samples, and satellite-based geophysical and geochemical data. Owing to improvements in instrument detection limits, measurements of the volatile contents of different lunar samples has become more precise. The identification and quantification of water and other volatile species in pyroclastic glass beads has been a key step in lunar volatiles research [1]. The isotopic composition of the lunar interior has been compared with that of Earth's and other planetary bodies, with important implications, such as the recognition that parts of the lunar mantle could be as enriched as MORB [2].

However, several problems still exist with these measurements: post-crystallisation diffusion of volatiles from apatite on the lunar surface, and terrestrial contamination of meteorites may have altered some water-bearing minerals [3]. Due to these problems, the volatile content of lunar magmas has yet to be constrained with certainty.

Objective: To use a volcanological approach to infer the volatile contents of different lunar magmas, consistent with the observed volcanic deposits.

Methods: Using existing literature on lunar magma properties – such as gas phase types and volume, temperature of the melt, and liquidus composition of the melt – the values for inputs of a magma ascent model will be set. This model has previously been used to calculate various eruption conditions for the 2007 Stromboli eruption, and for scenarios such as equilibrium and disequilibrium crystallisation [4]. With the parameters adjusted to lunar conditions for gravity and pressure, the model will produce values for mass eruption rates and other eruption conditions, such as gas volume fraction and melt viscosity.

Utilising the link between flow morphology and eruption conditions, satellite images of the lunar surface will also be analysed, in order to collect photogrammetric measurements of volcanic domes and cones. The ISIS3 (Integrated Software for Imagers and Spectrometers) image processing package will be used to manipulate LRO (Lunar Reconnaissance Orbiter) images to a GIS-compatible state and create digital elevation models [5]. The magma ascent model will essentially be inverted to provide estimates of the volatile content of the magmas consistent with the morphology of the lunar deposits.

These methods will be applied to a range of volcanic features on the Moon, including more prevalent mare features (mare domes, sinuous rilles) and non-mare features (cones, pyroclastic mantling deposits). For mare features, many regions of Mare Tranquilitatis and Mare Insularum would be apt study sites, while Taurus-Littrow, Alphonsus Crater, and Oppenheimer Crater are amongst well-studied sites containing pyroclastic deposits. The Marius Hills area provides an ideal study area, since it comprises both mare domes and cinder cones.

Project Outcomes: From this work, we hope to appraise the accuracy of values for lunar magma volatile contents in the current literature. Overall, we hope to greater understand the significance of volatiles in the Moon's volcanic history and the volatile relationship between the Moon and the Earth.

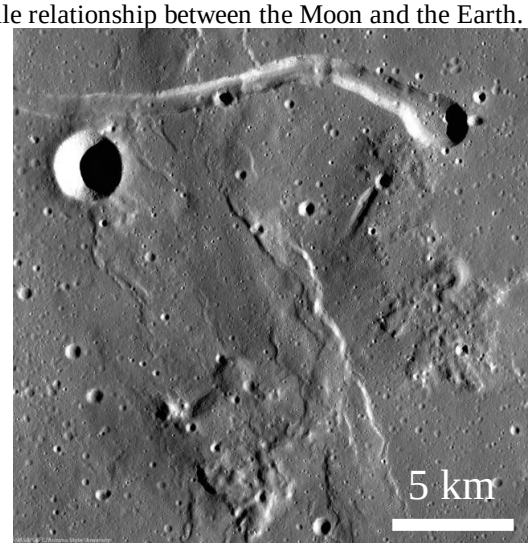

Figure 1: Cinder cones, lava flows, and a sinuous rille in Marius Hills, Oceanus Procellarum, a potential study site. Image: LROC, NASA/GSFC/ASU [6].

References [1] Saal A.E., et al. (2008). *Nature*, **454 (7201)**, 192. [2] Sarafian A.R., et al. (2014). *Sci. Rep.*, **346**, 623-626. [3] Anand M., et al. (2014). *Phil. Trans. R. Soc. A*, **372**, 1-33. [4] La Spina G., et al. (2016). *Nat. Commun.*, **7**, 1-10. [5] Gaddis L.R., et al. (1997). *Proc. LPSC*, **28**, 387-388. [6] Klem S.M., et al. (2014). *Proc. LPSC*, **45**, #2885.

The Metalysis-FFC-Cambridge process for efficient production of oxygen and metals on the lunar surface.

B. Lomax[1], M. Conti[2], N. Khan[2], A. Ganin[1], M. Symes[1]; [1]University of Glasgow, UK; [2]Metalysis, UK.

Introduction: Oxygen will undoubtedly be one of the most valuable resources in a self-sustaining space economy. As the largest weight component of any bi-propellant rocket, an efficient and plentiful source of liquid oxygen (LOX) on the lunar surface would reduce the reliance on mass transported from Earth. In-space lunar refuelling would impact not only lunar surface operations, but also activities in cis-lunar space, and deep-space missions.

While evidence is growing for ice deposits in the permanently shadowed craters at the lunar poles [1], the form, quantity, and accessibility of this resource remains unknown. The lunar regolith, on the other hand, is ubiquitous across the entire lunar surface and contains 40-45 wt% oxygen. Additionally, the lunar regolith contains a range of other elements that can be used to produce useful metals and alloys in-situ. Developing a single process that can efficiently extract the oxygen from regolith and produce useful materials will have a significant impact on the space resource economy. In this scenario, a process capable of both could operate synergistically with water extraction operations, should the lunar ice deposits prove to be a viable resource for oxygen. Furthermore, technology developed on the lunar surface that can produce metals and alloys is applicable to future Mars mission architectures, where processes that only produce oxygen become redundant in favour of simpler methods utilising the Martian atmosphere.

The FFC-Cambridge process: The Fray-Farthing-Chen (FFC)-Cambridge Process has been suggested as an efficient method for the production of both oxygen and useful materials from lunar regolith. The FFC-Cambridge process was invented at the end of the 1990s as a direct electrochemical method for producing metals from the corresponding metal oxides in molten salt [2]. At temperatures where the $CaCl_2$ salt is molten and can facilitate the transport of ions, approximately 900 °C, the metal oxide feedstock remains in the solid state throughout the entire process.

The metal oxide, which in the past has been in the form of a sintered pellet, forms the cathode and is electrochemically deoxidised to produce metal and oxygen ions:

$$\text{Cathode: } MO_x + 2x e^- \rightarrow M + x O^{2-}$$

In the terrestrial context, a carbon-based anode facilitates the removal of oxygen from the system in the form of carbon dioxide and carbon monoxide. In the lunar context an inert anode can be employed to directly produce oxygen:

$$\text{Anode: } 2O^{2-} \rightarrow O_2 + 4e^-$$

Some previous work has been done to investigate the reduction of lunar regolith using the FFC-Cambridge process [3]. The primary focus of this was the utilisation of lunar ilmenite as a feedstock, however, this process is distinguished by the fact it has the ability to remove 100 % of the oxygen from lunar regolith in the solid state, regardless of composition. Additionally, in the early years of this technological innovation, many aspects that would be relevant to a large-scale lunar operation were not yet proven.

Recent developments: In the almost two decades since this novel process was first reported, significant progress has been made in developing this technology. Metalysis (UK) have successfully scaled-up and commercialised the production of a number of metals and alloys. Innovations in the process have been made to allow for the production of metal powders for additive manufacturing, aerospace, and automotive applications directly from powder oxide feedstock.

Current work: The current research investigates the reduction of lunar regolith with the FFC-Cambridge process, applying the processing innovations of the Metalysis. Maximising efficiency, in terms of quantity of oxygen extracted and the functionality of materials produced versus energy consumption and process complexity are key goals. The processing knowledge gained in the years of terrestrial technology development will inform the design of a process that has the ability to be scaled up and operate sustainably and autonomously on the lunar surface.

References: [1] Li, S et al. (2018) *PNAS, 115 (36)*, 8907-8912. [2] Chen, G. Z. et al. (2000) *Nature, 407*, 361-364. [3] Schwandt, C. et al. (2012) *Planetary and Space Science, 74*, 49-56.

Research Support: This research is supported by Metalysis and by ESA's Network/Partnering Initiative.

FRICTION EXPERIMENTS ON IRON SULFIDE-BEARING ANORTHOSITE AND IMPLICATIONS FOR MECHANISM OF LONG RUNOUT LANDSLIDES ON THE MOON. G. Magnarini[1], T. M. Mitchell[1], S. Aretusini[2], G. Di Toro[3] and H. H. Schmitt[4], [1]Department of Earth Sciences, UCL, U.K. (corresponding author giulia.magnarini.14@ucl.ac.uk), [2]Istituto Nazionale di Geofisica e Vulcanologia, INGV, Rome, Italy, [3] Dipartimento di Geoscienze, Università degli Studi di Padova, Italy, [4] Department of Engineering Physics, University of Wisconsin-Madison, USA.

Introduction: Evidence for the presence of a long runout landslide at the Apollo 17 landing site (Fig. 1) opened important implications about mechanisms of reduction of friction on planetary bodies in the absence of an atmosphere and water availability [1]. Dry granular fluidization involving interaction between regolith particles has been considered the most likely process during emplacement of the Apollo 17 landslide [1], as well as for other lunar mass-wasting instances discovered in recent years thanks to new high-resolution imagery [2][3].

Following field work activity in Taurus-Littrow Valley and sample analysis, astronaut geologist Harrison H. Schmitt has speculated that gas fluidization is the principal mechanism involved in the emplacement of the Apollo 17 landslide [4]. Fluidization of lunar regolith could be a consequence of solar wind volatiles release by agitation of the granular material during the flow; solar wind hydrogen, nitrogen, carbon, helium have been found in lunar samples and the original abundance could have been as much as 200 ppm [5]. Contribution to the fluidization of the landslide could also derive from thermal decomposition of troilite induced by frictional heating. However, both hypotheses are lacking of theoretical and experimental support.

In recent years, experimental work has been used to support emplacement mechanisms of the terrestrial catastrophic Heart Mountain landslide [6]. Friction experiments were performed with a rotary shear apparatus (SHIVA, Slow to HIgh-Velocity rotary-shear Apparatus) at the Istituto Nazionale di Geofisica e Vulcanologia (INGV), Rome, Italy [7] in order to study the role of thermal decomposition of carbonates during landslide emplacement, for which only theoretical calculations were available [8]. The microstructures obtained during these experiments compared favourably with theoretical calculations and field observations.

Following the success of experimental work on terrestrial cases, we perform friction experiments with SHIVA in order to determine the viability of the thermal decomposition of troilite or other thermally activated dynamic weakening processes in anorthosites as mechanisms to explain the exceptional runout of the Apollo 17 landslide and the Tsiolkovskiy Crater landslide at the far side of the Moon (Fig. 2).

Methods: We use Proterozoic anorthosites of the Scandinavian Shield, provided by the European Space Agency Sample Analogue Curation Facility (ESA SAFC), as lunar analogue. Powders were prepared by crushing and sieving (< 250 µm) the anorthosites and pyrrohotite group minerals. Three different types of gouge are used in the experiments: one gouge of 100 wt% anorthosite, and two mixes including 1 wt% and 5 wt% of troilite. Powder samples and cohesive anorthosite rock samples are sheared simulating the landslide runout with a single slip pulse at constant slip rate of 1 ms^{-1} for up to 10 m displacement with a costant acceleration of 0.75 ms^{-2}. Experiments are performed in high vacuum (< 5e-4 mbar) to simulate the absence of a lunar atmosphere and at a constant normal stresses of 2 MPa and 8 MPa to simulate the overburden stress at the base of the estimated 500 m and 2 km thick collapsed slopes from which the Apollo 17 and Tsiolkovkiy Crater landslides developed, respectively.

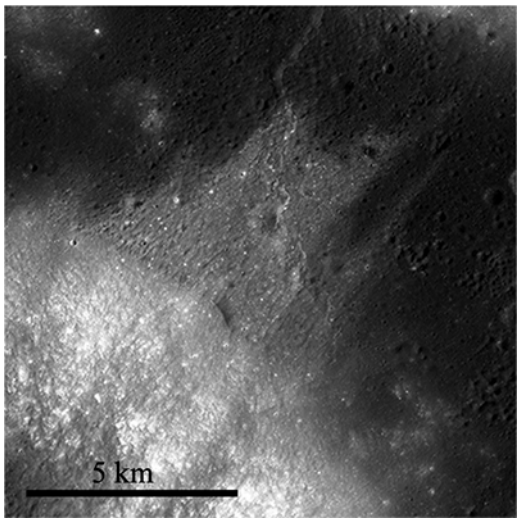

Figure 1: The Apollo 17 landslide (NASA/GSFC/Arizona State University).

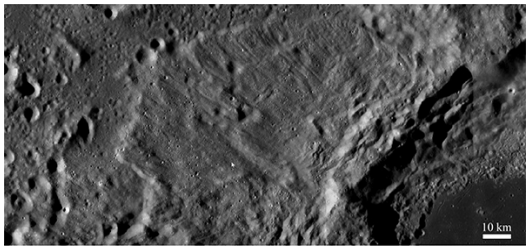

Figure 2: The Tsiolkovskiy Crater landslide at the far side of the Moon (LROC-QuickMap webtool).

References: [1] Howard K. A. (1973) *Science, 180,* 1052-1055. [2] Kokelaar B. P. et al. (2017) *JGR Planets, 122,* 1893-1925. [3] Senthil Kumar P. et al.

(2013) *JGR Planets, 118,* 206-223. [4] Schmitt H. H. et al. (2017) *Icarus, 298,* 2-33. [5] Schmitt H. H. (2006) *Springer,* 336. [6] Mitchell T. M. et al. (2015) *EPSL, 411,* 199-207. [7] Di Toro G. et al. (2010) *Rendiconto Lincei, 21,* 95-114. [8] Goren et al. (2010) *JGR Solid Earth, 115,* B10210.

LUNAR ROCK BOULDERS AS A TOOL IN COMPARATIVE PLANETOLOGY TO INVESTIGATE ROCK WEATHERING. U. Mall[1], H. Schmidt[1], D. Kloskowski[1], V.T. Bickel[1,2], R. Bugiolacchi[3], [1]Max-Planck Institute for Solar System Research, Göttingen, Germany (mall@mps.mpg.de), [2]ETH Zurich, Zurich, Switzerland, [3]Space Science Laboratory Macau University of Science and Technology, Macau – China.

Introduction: Lose rocks of various sizes have been observed on the surfaces of planets, asteroids and, recently, even on comets [1]. In the early days of planetary exploration, they were viewed just as critical potential hazards for landing and rover navigation. They are, however, not only important in the context of exploration but also as scientific targets worth of investigation. Rocks fragmented under diverse conditions have significantly different mass distributions [2]. The analysis of rock populations on a planetary surface can, therefore, provide important geological information related to the planet's origin, the timing of critical events such as meteorite bombardment, volcanism, and the evolution of its planetary crust.

In the field of Earth sciences, understanding the evolution and dynamics of brittle materials which form the crust is by itself a topic of great significance [3]. The time-dependent rock deformations in the crust influence a range of phenomena ranging from geohazards such as rockfalls, earthquake ruptures, volcanic eruptions, the integrity of underground mines to the long-term storage possibilities of hazardous materials. Of specific importance is the subject of which environmental factors drive the physical breakdown of rocks. Insolation, originally seen by Johannes Walther [4] as a splitting effect of expansion and subsequent cooling through solar heating on rock surfaces as a basic mechanism for brittle rock fracture, has in the last 100 years been the subject of an intense debate, with opinions alternating between general acceptance and flat rejection [e.g. 5].

On Earth, the time-dependent rock breakdown is controlled by numerous factors under a multitude of changing conditions, including the erosion power of the atmosphere and non-gaseous (vapour) water, which renders the disentanglement of concurrent factors complex. However, observations of a range of celestial bodies offer the opportunity of studying several of these factors at play under different conditions, including simpler settings (such as on airless bodies), operating over different timescales, thereby potentially offering the opportunity to assess the influence of a singular factor (i.e., heat excursions). The lunar surface, dry, devoid of atmosphere and plate tectonics represents an ideal laboratory to investigate certain aspects of mechanical rock weathering.

The investigation of boulders and boulder fields on the Moon would help to constrain the hypothesis of solar cycling as the main factor for rock breakdown. The insight gained from the study on degradation processes and the breakdown mechanisms of lunar boulders process would be key in understanding similar processes on other planetary bodies. This is highly relevant given that ejecta boulders around the crater edifice and over the rim must also derive from the excavation process ([6]). Thus, a temporal correlation between the boulders' spatial density and the crater age is most likely (e.g. [7]). By developing a reliable model of rock degradation on the lunar surface should help constrain the time of impact.

Studies that measure the size-frequency distribution of boulders have been carried out for decades [8], but the Lunar Reconnaissance Orbiter (LRO) narrow-angle camera (NAC) images [9] now allow the identification and mapping of boulders down to ~0.5m/pixel in scale. In this study, we are looking first at the boulders within the Taurus-Littrow valley and the Schrödinger crater to investigate how a lunar wide analysis of this topic can be made once a global map of lunar boulder distribution has been generated.

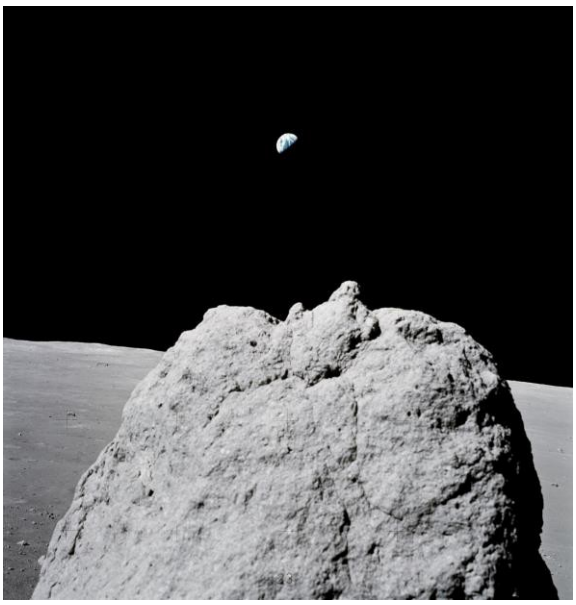

Figure 1. A boulder from the Apollo 17 mission archive, ©NASA (spaceflight.nasa.gov)

References: [1] Pajola M. et al. (2015) *A&A,* 583, A37. [2] Golombek M. and Rapp D. (1997) *JGR*, 102 E2, 4117-4129. [3] Hall K., (2014), *Geomorphology*, 206, 1-13. [4] Walther J. (1900) *Das Gesetz der Wüstenbildung in Gegenwart und Vorzeit*, Berlin: Reimer 1900. [5] Ryan, J. (1962), *JGR,* 67, 6, 2549-2558. [6] Melosh H.J. (1989) Impact Cratering: a Geologic Process. Oxford University Press, New York. [7] Basilevsky A. (2013) Planet. Space Sci. 89, 118-126. [8] Shoemaker E. and Morris E. (1968) *Surveyor project final report*, Part 2, 86-102. [9] Robinson et al. (2010) *Space Sci. Rev.* 150, 81-124.

ESA'S SAMPLE ANALOGUE CURATION FACILITY (SACF), AND EXPANDING ESA'S EXPLORATION SAMPLE ANALOGUE COLLECTION (ESA^{2}C). D. J. P. Martin and L. Duvet, European Space Agency ECSAT, Fermi Avenue, Harwell Campus, Didcot, Oxfordshire, OX11 0FD, UK (dayl.martin@esa.int).

Introduction: The European Space Agency's Sample Analogue Curation Facility (SACF) and associated analogue collection were developed to support ESA's Human and Robotic Exploration mission preparation programme. The main aim of this activity is to provide a long-term resource of planetary analogue materials for research and technology developments both within ESA and the wider scientific community.

Origins: The SACF and ESA's Exploration Sample Analogue Collection (ESA^{2}C) began their development at the Natural History Museum (NHM), London, who was the prime contractor to the activity from 2014 through to 2018. During this time, the NHM identified suitable and readily available resources for the analogue collection, obtained ~1 ton of various analogue materials, procured a range of analytical equipment and laboratory supplies, and performed baseline characterization of many of the analogue materials [1-3]. Since Q3-4 of 2018, the SACF has relocated to the Harwell Campus where it is now collocated with ECSAT, the UK ESA Centre.

Sample Analogue Curation Facility: The main aims of the SACF is to:

- curate a range of planetary analogues and simulants representing geological materials from various Solar System bodies.
- research and develop new analogues and simulants to fulfil current requirements within ESA and the wider research community.
- use the geological and sample expertise within the facility to support current missions and mission architectures within ESA.
- support learning and public outreach events with the analogue samples available at the SACF.

The dedicated facility on the Harwell Campus consists of an analytical laboratory for baseline characterization of the analogue materials, a sample preparation room for altering existing samples and creating new simulants, and a curation room for long-term storage of the analogue collection.

ESA^{2}C: The ESA Exploration Sample Analogue Collection (ESA^{2}C) is the reserve of analogues and simulants curated by the SACF. Currently, the ESA^{2}C collection consists of analogues representing various rock and soil types on the Moon, Mars, and Phobos that were collected from easily accessible sources (e.g. quarries) allowing replenishment of these analogues over time. Presently, the ESA^{2}C collection consists of 82 analogue and simulant materials, of which many are available in a range of prepared forms including polished blocks, cores, and powders for various applications. Also in the collection are a series of simulants that were developed during various international efforts including EAC-1, MGS-1, and OPRH2. Although some of the samples in the collection are voucher specimens (i.e. not available for loan due to their small quantities) [1], data pertaining to their properties and other information are available.

Much of the collection is available for loan for research projects, technology development and testing, and public outreach. Activities that have made use of the ESA^{2}C collection so far include in situ resource utilization studies (ISRU, e.g. plant growth in regolith) and technology developments (3D printing, ceramic coatings etc.), hypervelocity impact studies, geotechnical / chemical / spectral investigations of Mars analogues to aid the interpretation of ExoMars data, and as reference pieces for public outreach and engagement events. Loans have so far been allocated to projects in the UK, France, Hungary, Italy, Luxembourg, the USA, Hong Kong, and Australia. Within ESA, the SACF is supporting a number of mission teams and activities including PROSPECT, ExoFit, ExoMars, and the Mars Sample Return campaign. Support for these mission teams includes loaning of analogue materials, sample preparation, handling and analysis, and geological mapping and image analysis.

Expanding the ESA^{2}C collection: There are many planetary terrains and geological units that are not represented by the simulants currently available to the international community. Therefore, the SACF plans to expand the ESA^{2}C collection by creating a range of simulants produced in-house that represent some of these 'missing' simulants.

Lunar Dust Simulant: One such example is a 'lunar dust simulant' with grain size, shape, hardness, and abrasiveness representative of lunar regolith. This simulant would focus on the finer fraction (<25µm) of lunar regolith and would be used for testing parts that are designed to operate at the lunar surface. Such applications for the abrasive property include instruments with moving parts that will be in contact with the lunar surface, and parts designed to operate for long periods of time at the lunar surface such regolith transporters,

storage units, conveyers (and other ISRU machinery), robotic arms, and actuators (etc.).

Another potential application for this simulant would be to test the potential for instruments to overheat on the lunar surface when coated with regolith. Apollo 15, 16 and 17 astronauts encountered problems with the overheating of the battery unit and associated radiators on the lunar roving vehicle due to a coating of fine regolith that was highly thermally insulating, so laboratory testing with a suitable simulant would help to minimize any problems that may be encountered at the lunar surface [4].

A major problem encountered by the Apollo astronauts on all of the missions was the degradation of seals in suits and sample containers during their stay at the lunar surface. Development of seals designed to repeatedly operate at the lunar surface is essential for long-term missions and habitation at the lunar surface, and the lunar dust simulant could be used to effectively test the reusability of seals in the laboratory.

Source materials. One of the most representative terrestrial materials for creation of a lunar dust simulant would be Mistastin anorthosite, found in the Labrador province of Canada [5]. This material contains a high proportion of feldspathic glass and products of impact shock metamorphism, resulting in a more ideal starting material for simulating agglutinates and other shocked components found in lunar regolith. However, this material is difficult to obtain given its remote location, so may not be ideal as a sustainable analogue source material. Therefore, current efforts are focused on using an already sourced anorthosite from Sirevåg, Norway as the base material to create an initial version of the lunar dust simulant.

Lunar Pyroclastic Simulant: Pyroclastic deposits, found during the Apollo 15 and 17 missions, are of high interest within the ISRU area of research because of the potential for extracting trapped volatiles from within the pyroclastic glass beads. However, there are no pyroclastic simulants available for study at the time of writing, meaning some ISRU technologies cannot be tested with appropriate simulant materials. Such a simulant will be available either as a 'pure' pyroclastic deposit (i.e. only the glass beads, more representative of e.g. 74220) or as a pyroclastic-rich regolith simulant (a mixture of pyroclastic glass and a lunar regolith simulant, similar to Apollo samples 74240 or 15401).

Such samples would be useful not only for volatile extraction purposes, but may also be used for testing sample handling and processing equipment due to the varied flow properties of samples that contain higher proportions of spherical particles (in contrast to most lunar regolith samples that are dominated by highly angular particles). Also, as some Apollo regolith samples contain small proportions of glass beads (<1 wt%), the addition of a small portion of pyroclastic glass to any developed regolith simulant may be beneficial for more representative tests of certain technologies.

Simulant Recipes: Alongside developing new simulants for the ESA^{2}C collection, the methods to create the simulants, or 'recipes', will be also be publicly available. These recipes will detail source materials, processing steps, and the properties of the final products to allow reproduction of the simulants to take place outside of the SACF if required. This is particularly important for volatile samples (icy simulants, for example) where transporting the material is challenging and/or highly expensive.

Apollo Regolith Research: In order to create simulants with more representative properties of lunar regolith, a variety of analyses will be performed at the SACF on three lunar samples to further understand their physical properties. The samples will be sieved to obtain the finest size fraction, then subject to X-Ray Computed Tomography (XRCT) in collaboration with the Diamond Light Source, the UK's synchrotron facility also located on the Harwell Campus. A variety of simulants will also be analysed in the same way to enable direct comparison between Apollo sample and lunar simulant datasets. The electrostatic properties of the Apollo samples will also be investigated to further understand the particle interactions between material exposed to space weathering. As these physical properties may influence the way the material is handled and stored, it is of vital importance for designing more representative simulants and for adequate testing of ISRU technologies.

Future Scope: The need for a greater range of simulants will increase as Solar System exploration continues. The continued development of simulants is, therefore, vital for adequate testing of technologies being developed for future missions.

Also, new acquisitions to the ESA^{2}C collection will be characterized for a range of their physical and chemical properties to expand the available information for the analogues in the collection. For more information related to the SACF and ESA^{2}C collection, and to inquire into loaning of samples, please visit http://sacf.esa.int.

Acknowledgements: We warmly thank the Natural History Museum for their continued support with the SACF and curation of the ESA^{2}C collection.

References: [1] Smith C. L. et al. (2018) *LPSC XLIX,* Abstract #1623. [2] [2] Manick K. et al. (2017*) LPSC XLVIII,* Abstract #1220. [3] Manick K. et al. (2017) *LPSC XLVIII,* Abstract #1222. [4] Gaier J. R. (2005) NASA/TM-2005-213610. [5] Grieve R. A. F. (1975) GSA Bulletin 86 (12): 1617-1629.

EXPLORING THE LUNAR REGOLITH AT THE MICROSCALE. K. McCanaan[1], K. H. Joy[1], R. H. Jones[1] and D. J. P. Martin[2], [1] School of Earth and Environmental Sciences, University of Manchester, Oxford Road, Manchester, UK, M13 9PL (Kathryn.mccanaan@postgrad.manchester.ac.uk), [2]European Space Agency ECSAT, Fermi Avenue, Harwell Campus, Didcot, Oxfordshire, UK, OX11 0FD.

Introduction: The lunar surface is covered with a layer of unconsolidated, soil-like material which is known as the lunar regolith. The regolith is formed by a process known as space weathering; it is mostly caused by micrometeorite bombardment which constantly reworks rock exposed at the lunar surface. The regolith is composed of fragments and components of minerals and rocks as well as agglutinates (see Figure 1). Agglutinates are constructs which are composed of fragments of minerals, rocks and glasses that have been bound together by impact-melt glass; they are formed when micrometeorites impact their parent soils, causing some of the soil to melt [1]. Typically, the volume of agglutinates in lunar soils gives an indication of how 'mature' or space weathered that soil is: the longer the soil has been exposed to space, the more agglutinates it has [1]. Since agglutinates are formed during the space weathering process which forms lunar regolith, they are key to understanding regolith production, recycling and weathering processes [1].

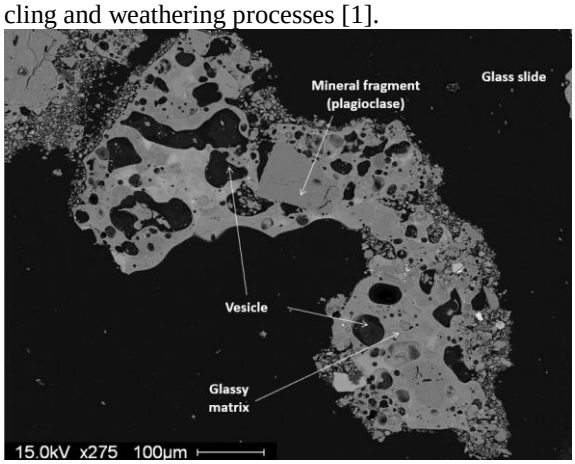

Figure 1: Example of a Back Scattered Electron image of an agglutinate from Luna 20 sample 22023,15 [author's own photo].

The process of agglutinate formation and their chemical relationships to their parent soils remains poorly understood. We aim to further understand these regolith processes through the analysis of agglutinates from a range of geographically and geologically distinct locations on the lunar surface, using samples from both the Apollo and Luna missions (see Figure 2).

Individual agglutinates will be selected from the sample soils to represent a range of grain sizes, mineralogies, core depths and collection locations on the lunar surface.

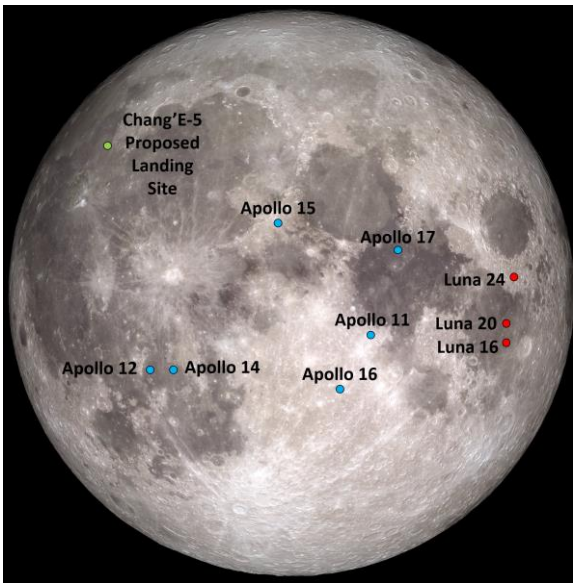

Figure 2: The near side of the Moon showing the approximate landing sites of the Apollo and Luna missions, as well as the proposed landing site of Chang'E-5, a sample return mission scheduled to launch in December 2019. Moon image was taken by NASA's Lunar Reconnaissance Orbiter Camera (LROC) [2].

Apollo samples: The NASA Apollo 11 mission made history when it returned the first lunar samples to the Earth in 1969; it was followed by a further five successful manned missions, Apollo 12, Apollo 14, Apollo 15, Apollo 16 and Apollo 17 [3]. The six Apollo missions returned a total mass of ~381.7 kg of lunar material to the Earth [3].

For this study we will be using the following four Apollo samples:

14163,135: This sample was collected during the Apollo 14 mission. The lithology of the soil is mostly breccia, it is described as sub-mature and was chosen as a reference soil for the lunar highland suite [3,4].

15101,319: This sample was collected during the Apollo 15 mission. The soil is described as mature and has a mostly basaltic composition [3,4].

61220,41: This sample was collected during the Apollo 16 mission. It is mostly composed of breccia and is described as an immature soil, containing <10% agglutinates [4].

62231,55: This sample was collected during the Apollo 16 mission. The sample is described as a mature soil [4].

Luna Samples: Three stratigraphic core samples were returned from the Moon between 1970 and 1976 by the Soviet Union robotic space missions:

Luna 16, Luna 20 and Luna 24; the cores contained soil samples of mass approximately 300 g [5].

The Soviet Academy of Sciences provided a sample from each of the three Luna sample return missions to the Royal Society in the 1970's [5].

Royal Society sample set: Many studies were conducted on the Royal Society Luna samples when they were first received, but little research has been carried out on these samples since the 1980s. The samples that were provided to the Royal Society are as follows: L1627 and L2016 from the Luna 16 and Luna 20 missions respectively as well as four samples from the Luna 24 mission: 24090, 24125, 24170 and 24196 [5,6]. As part of our investigation into regolith material we are first reviewing and cataloguing this existing material, so that we can best select samples for further study.

Methodology: Due to the limited amount of lunar material currently available for research, we are focussing on developing non-destructive techniques to study agglutinate regolith components. We will develop an analysis chain including:

X-Ray Computed Tomography (XCT): XCT scans of the agglutinates will be collected so that any trends in physical properties (such as size and porosity) based on the original location/depth of the sampled soil can be determined. Determining the porosity of individual agglutinates might help to shed light on the volatility of the parent soil or of the impactor which formed the agglutinate at the time of formation.

Fourier Transform Infrared Spectroscopy (FTIR): FTIR spectra will be collected for individual agglutinates to analyse their spectral properties to determine their bulk mineralogy [7]; this data can then be compared to the mineralogy of the bulk soil in which they were found to further understand the chemical relationship between agglutinates and their parent soils.

FTIR spectra can also be used to determine the shock history of samples by measuring the shock pressures of the different constituent phases [7]. This can be used to learn about agglutinate formation and subsequent weathering by further impacts.

Scanning Electron Microscopy (SEM) and electron microprobe analysis (EMPA): Texture and chemistry of the different agglutinates will be determined for constituent minerals and the bulk glass composition. This will help interpret what parent soils were melted to form the agglutinates in different soil types, and test ideas about which size fraction was preferentially melted during the regolith gardening process [8].

References: [1] McKay, D. S., Heiken, G., Basu, A., Blanford, G., Simon, S., Reedy, R., French, B. M. and Papike, J. (1991) *The Lunar Sourcebook*, 285-356. [2] NASA/Goddard Space Flight Centre/Arizona State University, 2017. *Lunar Near Side.* [3] Vaniman, D., Dietrich, J., Jeffrey Taylor, G. and Heiken, G (1991), *The Lunar Sourcebook*, 5-26. [4] Meyer, C. (2012) *The Lunar Sample Compendium*, https://curator.jsc.nasa.gov/lunar/lsc/. [5] Pillinger, C. T. and Gowar, A. (1977) *Phil. Trans. Royal Soc. A, 284*, 137-143. [6] Pillinger, C. T. and Gowar, A. (1980), *Phil. Trans. Royal Soc. A, 297*, 1-6. [7] Martin, D. J. P., Pernet-Fisher, J. F., Joy, K. H., Wogelius, R. A., Morlok, A and Hiesinger, H. (2017) *MAPS, 52*, 1103-1124. [8] Vance, A. M., Cristoffersen, R., Keller, L. P., Berger, E. L. and Noble, S. K. (2016) *47th Lunar and Plan. Sci. Conf., #2852.*

SEQUESTRATION OF HIGHLY SIDEROPHILE ELEMENTS INTO THE LUNAR CORE DURING A LATE MAGMA OCEAN CRYSTALLIZATION AND MANTLE OVERTURN. A. Morbidelli[1], D. Nesvorny[2], V. Laurenz[3], S. Marchi[2], D.C. Rubie[3], L. Elkins-Tanton[4], M. Wieczorek[1], S. Jacobson[1,3,5] and M.H. Zhu[6]. [1]Laboratoire Lagrange, Observatoire de la Côte d'Azur, Nice, France (morby@oca.eu), [2]Southwest Research Institute, Boulder, Co., [3]Bayerisches Geoinstitut, Bayreuth, Germany, [4]School of Earth and Space exploration, University of Arizona, Phoenix, Az, [5]Department Of Earth And Planetary Sciences, Northwestern University, [6]Space Science Institute, Macau University of Science and Technology, Avenue Wailong, Taipa, Macau

Introduction: The concentration of highly siderophile elements (HSEs) in the lunar mantle is 50 times lower than in the terrestrial mantle [1]. According to the ratio of collisional cross-sections between the Earth and the Moon and the relative masses of the two mantles, the HSE concentrations should be comparable. There is currently no convincing explanation for the observed imbalance.

HSE sequestration into the lunar core during LMO crystallization: We show that during the bottom-up crystallization of the lunar magma ocean (LMO) the HSEs concentrate, together with sulfur, in the top liquid mantle layer. At the end of crystallization, this creates a top layer in the mantle with high density material, like ilmenite-rich and FeS-rich cumulates, with HSEs bound to the sulfide due to their chalcophile behavior. This density imbalance drives a global mantle overturn. The high density layer can reach the core-mantle boundary. The decay of radioactive elements can melt this material, favoring the migration of FeS and HSEs into the lunar core. This process has two consequences: (i) the lunar mantle remains depleted of HSEs, so that its current HSE budget has to have been accreted after the mantle overturn event and (ii) the lunar core becomes enriched in S, which is consistent with the evidence for a 3-8 wt% S-rich core based on seismic velocity and core density determinations [2].

Implications of a late crystallization of the LMO: We show that a bombardment declining over time and consistent with the lunar crater record 3.5-4.0 Gy ago is consistent with the current HSE budget of the lunar mantle if LMO crystallization and mantle overturn occurred ~4.35 Gy ago [3]. This late LMO crystallization age is consistent with thermal evolution models of the Moon [4]. In this case, the Moon accreted after its formation an amount of material proportional to that accreted by the Earth by the ratio of cross-sections, but it lost into the core most of its HSEs during the late LMO crystallization event, explaining why the current HSE concentration in the Lunar mantle is only about 1/50 of that of the terrestrial mantle. Moreover, the high cratering rate in the 3.5-4.0 Gy period and the small amount of lunar mantle HSEs become consistent with a continuously declining bombardment perduring since the planet formation times [3]. There is no need to invoke a surge in the impact rate to explain the lunar crater record at the time of formation of the Imbrium and Orientale basins.

Simulations: We have conducted hydrodynamical simulations to evaluate which fraction of projectile material is implanted in the lunar mantle, in the lunar crust or is ejected to space, as a function of impact velocity and incident angle. The outputs of these simulations have been combined in a Monte Carlo model simulating a declining bombardment from a population characterized by a main-belt-asteroid-like size distribution. The results [5] confirm that the current HSE concentration in the lunar mantle require the sequestration of mantle HSEs into the lunar core 4.35Gy ago, while HSEs in the lunar crust might have been retained since an older time.

Conclusions: Altogether these results provide a coherent view of the Lunar thermal evolution, its current geochemical properties (HSE concentrations in mantle and crust, S concentration in the core) and the bombardment of the Earth-Moon system. The crystallization of the LMO about 4.35 Gy ago explains the deficit of HSEs in the lunar mantle with respect to the terrestrial mantle. The amount of material accreted in a smoothly declining bombardment since 4.35 Gy, deduced from the HSE lunar mantle inventory, is consistent with the lunar crater record during the so-called Late Heavy Bombardment (LHB) period (3.5-4.0 Gy ago). Thus, a surge in the bombardment rate at the time of the LHB is nolonger required to explain the data.

References:

[1] Day, J. M. D., Walker, R. J. (2015) *EPSL* 423, 114-124. [2] Antonangeli, D., et al. (2015) *PNAS*, 112, 39163919. [3] Morbidelli, A. et al. (2018) Icarus, 305, 262. [4] Elkins-Tanton, L.T., et al. (2011) *EPSL* 304, 326-336. [5] Zhu, M.H. (2019) to be submitted.

METAL IMPACTOR FRAGMENT FOUND IN LUNAR REGOLITH BRECCIA METEORITE NORTH WEST AFRICA 10989. Z. S. Morland[1,2], K. H. Joy[2], A. Gholinia[3] and G. Degli Alessandrini[1]. [1]School of Physical Sciences, Open University, Milton Keynes, UK., [2]School of Earth and Environmental Sciences, University of Manchester, UK. [3]School of Materials, University of Manchester, UK.
Corresponding email: zoe.morland@open.ac.uk

Introduction: The composition of material delivered to the inner Solar System throughout history remains a mystery [1,2]. Lunar meteorites, unlike samples returned from Apollo and Luna missions, provide a rich resource for understanding the whole surface of the Moon [3]. Here we analyse a recently discovered lunar regolith breccia meteorites, North West Africa (NWA) 10989 (Fig. 1 A), to see whether it holds preserved impactor material. We consider the implications of its existance under the context of regolith evolution and *in-situ* resource utilisation.

Methods: At the University of Manchester, the petrology of NWA 10989 was analysed using the following methods: (1) an ESEM to obtain whole sample merger and close-up BSE images, qualitative EDX point spectra, and whole sample EDS elemental maps; (2) a Raman spectrometer to identify Fe-oxide phases; (3) an EPMA to quantitatively measure major element concentrations; (4) a Broad-ion beam (Argon) mill to polish; and (5) an Oxford Instruments EBSD with AZtec software to study crystallographic structure.

Methods: The 1 cm sized fragment of NWA 10989 we investigated specifically contains highland granulites, glassy impact melt breccias (GIMBs), clast-rich impact melt breccias (CIMBs), monomineralic pyroxene and rare mare basalt fragments. These clasts are held within a glassy matrix that includes impact melt spherules and Fe-Ni metal. The Fe-Ni metal is dominantly contained within a single 1.90 × 0.85 mm grain (Metal_1) along with several other smaller grains and abundant fine particles in the matrix (Figs. 1 A & B).

Results: The metal grains are composed of predominantly kamacite (low-Ni), enriched in K (0.16-0.22 wt%). Metal_1 also contains minor amounts of taenitic (high-Ni) material and K-rich schreibersite. Comparison between the metals' compositions and the meteoritic field suggest they are similar asteroid-derived meteorite groups, and thus could indicate and exogenous origin [4]. However, silicates in contact with and ocassionally embedded within Metal_1 (Fig. 1 B) reflect native lunar compositions.

Metal_1's internal microstructure consists of an aggregate of 50-150 µm sized variably orientated grains (Fig. 2 A & B). The colour gradients within grains indicate the presence of lattice bending, which in places advanced to sub-grain development.

Discussion: The compositional dichotomy between the native lunar silicates and the sizeable, apparently exogenous, Fe-Ni metal suggests either (i) an almost intact fragment of meteorite or (i) a precipitate from an impact melt sheet composed of a vaporised impactor and lunar target rock mixture. Metal_1's complex internal structure, indicative of crystal plastic deformation, could be attributed to strain during regolith reprocessing.

This study advances current knowledge in ISRU through evidence of impactor survival and modification on the surface of the Moon, plus it aids in understanding what material was delivered to the inner solar system during its history.

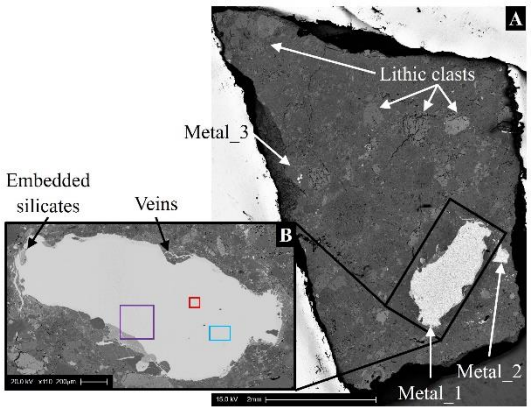

Figure 1: (A) Whole sample BSE image, *(B)* Metal_1 close-up BSE image with EBSD areas shown

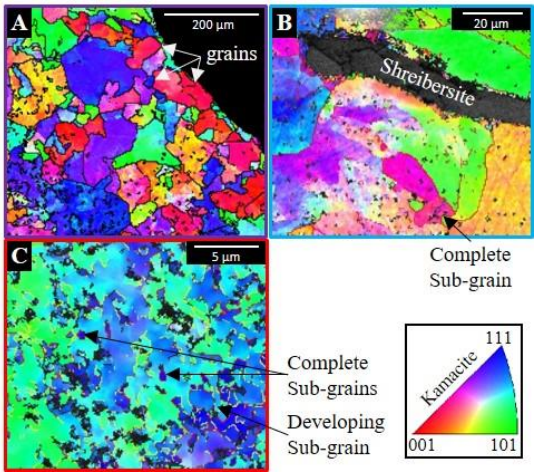

Figure 2: Inverse pole figures of parts of Metal_1, indicated in Fig. 1 B, where colours represent lattice orientation corresponding to the triangle key.

Acknowledgements: Thanks to Martin Goff, for donating the sample.

References: [1] Hartmann W. et al. (2000) In: R. Canup and K. Righter, eds. Tuscon: University of Arizona Press, 805-826. [2] Joy K. H. (2012) *Science*, 336(6087), 1426-1429. [3] Jolliff B. L. et al. (2000) *JGR*, 105, 4197-4216. [4] Goldstein J. I. and Yakowitz H. (1971) *P. Lunar. Plant. Sci*., 2, 177-191.

An Experimental Approach to Understanding Sublimation Water Ice Losses from Planetary Regolith Analogue Mixtures for ESA's PROSPECT Package. J. I. Mortimer[1], S. J. Barber[1], and M. R. Leese[1], [1]School of Physical Sciences, The Open University, Walton Hall, Milton Keynes, Buckinghamshire, United Kingdom, MK7 6AA, UK. (James.Mortimer@open.ac.uk).

Introduction: ESA's PROSPECT package, which is due to fly to the south polar region of the Moon on board Russia's Luna27 mission in 2024, consists of two main elements: the ProSEED sample drill, and the ProSPA volatile analysis instrument [1]. After drilling down to a depth of up to 1.2 metres, the ProSEED drill will then collect icy regolith material and bring it up to the lunar surface, before transferring it to the ProSPA oven carousel. From there, it will be rotated and positioned under a sample imaging system (SamCam) to work out the volume of the sample material in the oven, then rotated again to a tapping station, where it will be sealed, ready for heating and thus volatile release for analysis in the ProSPA instrument mass spectrometers. However, these processes of sample retrieval, positioning, transfer, imaging, and sealing all take time, during which the icy regolith sample is exposed to radiative and conductive heat sources, thereby potentially raising the temperature of the icy sample. Exposed to the high vacuum conditions of the lunar surface environment, such temperature rises may result in ice mass loss caused by sublimation, and this is important to quantify with some confidence in advance of lunar surface operations.

Previous studies conducted in support of PROSPECT have indicated that significant isotopic fractionation of the remaining water ice is unlikely until more than approximately 30% of the starting water ice mass has been lost [2]. Despite this, it is still necessary to have as much ice content remaining for analysis as is reasonably possible; the current ESA requirement is a maximum loss of 5% of the starting water ice mass across all of the processes outlined above, from retrieval to sealing. This limit on the amount of permissible mass loss then provides constraints on the maximum temperatures of different parts of the PROSPECT systems and so is of high importance to the thermal design of the entire package. Computer numerical simulation can model the expected water ice mass losses at various stages of this sample handling pathway, but these need to be verified by an experimental approach. If the models can be reconciled with real-world data at temperatures and pressures achievable in a laboratory setting, it increases confidence in the ability of the models to accurately predict likely sublimation losses at lunar-relevant temperatures and pressures.

Experimental Procedure: In brief, the set-up comprises a large vacuum chamber with a side-mounted hinged quick access door, on top of which sits a microbalance (CI Precision Recording Microbalance). The microbalance is capable of taking loads up to 5 g and of measuring differences in mass between the counterbalance and the sample of up to a maximum of 500 mg to an accuracy of 0.1 µg. The microbalance is controlled *via* its associated electronics and display box, or through its computer software, through which mass and temperature data (from a K-type thermocouple) are recorded at chosen time intervals (up to 60 measurements per minute) for any user-set experimental duration. Hanging down into the chamber from the microbalance head are two fine NiCr wires, one of which supports the counterbalance, and the other the sample weighing pan. The aluminium foil sample pan is suspended mid-way into a temperature-controlled copper jacket (cooled by liquid nitrogen and heated by a PID-controlled waterproof heating wire circuit), and is cooled from above by a liquid nitrogen cooled copper canopy. Both the jacket and the canopy are thermally isolated from the room-temperature metal walls and floor of the chamber as much as practical by the use of PTFE stilt legs.

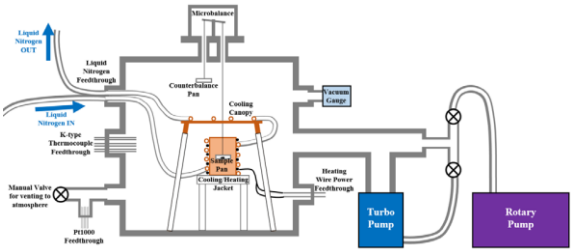

Figure 1: Schematic Diagram of the Sublimation Chamber and Microbalance Set-up

In a typical experiment, regolith simulant is first weighed out directly into the suspended sample pan. Once the sample pan contains a suitable mass of regolith simulant, the chamber is closed and pumped down to low vacuum overnight at room temperature. This removes most of the moisture already absorbed by and adsorbed onto the simulant particles. Immediately before starting an experiment, the chamber is quickly vented to atmosphere. At this point, the microbalance software is set to record both sample pan mass and temperature (typically in the region immediately above the sample pan), so that a record is kept of both the dry simulant starting mass and also the exact mass of water added to the sample pan. A syringe is used to add deionized water to the simulant in the sample pan, drop by drop. The increase in mass on the sample pan is monitored in real-time and recorded by the microbalance software. When the desired mass of water has been added to the sample pan, the pan is removed from the microbalance suspension wire and the regolith and water it contains are quickly mixed with a stainless steel spatula to

ensure a homogenous regolith/water mixture. The sample pan is then re-suspended from the microbalance inside the chamber, thermocouple and resistance thermometer positioning is checked, and the chamber closed again. A manual valve is opened to permit the flow of liquid nitrogen into the copper jacket and cooling canopy inside the chamber. When the temperature in the region of the sample pan has been stable at a minimum temperature (typically around -181 °C), for 5-10 minutes, the chamber is evacuated *via* a rotary vane pump and a turbomolecular pump; the measured base pressure in the chamber is typically around 10^{-6} mbar. As the pressure falls, the temperature of the icy regolith sample mixture on the sample pan begins to rise from near-liquid-nitrogen temperatures as radiative heat transfer through the vacuum overtakes conductive and convective heat transfers in an atmosphere, with the cooling effect of the liquid nitrogen pipework being increasingly offset by the warming effect of the room temperature chamber walls as the pressure falls. Sample temperatures eventually stabilise out (in the experiments conducted to date, sample temperatures range between -40 °C and -95 °C; see Results section; the range is caused by incremental changes to the thermal setup of the chamber in order to achieve lower temperatures).

Initial Results: Water ice losses as percentages of the starting ice mass for various initial experiments conducted with both JSC-1A (Fig.2) and NU-LHT-2M (Fig.3) regolith simulants are presented in this abstract. A range of water ice contents and temperatures of sublimation have been investigated, across timescales ranging from approximately 1 hour to over 4 hours.

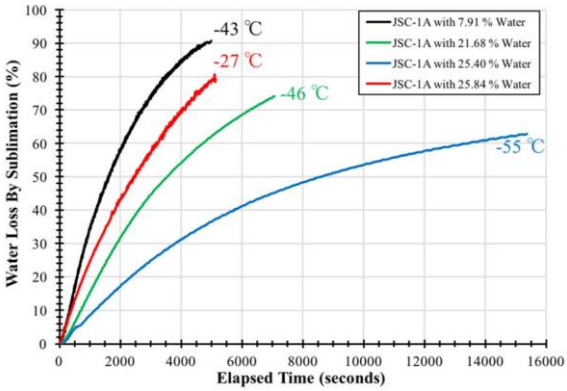

Figure 2: Water Ice Mass Loss Percentages over Time for Icy Regolith Mixtures made using JSC-1A simulant

In each case, the rate of water ice mass loss is observed to reduce as time passes, starting with a relatively rapid mass loss and becoming slower as progressively more water ice is lost. This is attributed to an increasing thickness of dehydrated insulating regolith simulant overlying the sublimation front at the top surface of the shrinking water ice mass as sublimation progresses, insulating the remaining ice and/or providing a more tortuous pathway for water vapour molecules to navigate before being lost from the sample. In comparison, experiments with water ice only (i.e. no regolith) display perfectly linear water ice mass loss rates over time.

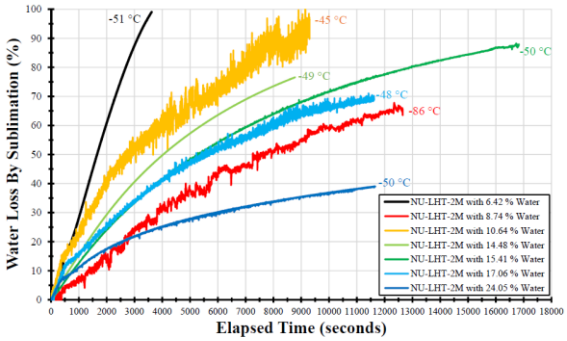

Figure 3: Water Ice Mass Loss Percentages over Time for Icy Regolith Mixtures made using NU-LHT-2M simulant

Interim Conclusions: All icy regolith samples, whether made with JSC-1A or with NU-LHT-2M, display logarithmic mass loss trends, in contrast to the linear mass loss behaviour of pure water. The more rapid initial rate of mass loss observed in icy regolith samples is comparable to that of the rates of pure water ice loss measured in this same study, for samples of similar exposed surface areas and temperatures. However, as sublimation progresses and the sublimating ice front moves deeper down into the sample mass, the rate of mass loss decreases. Given the importance of assumptions about sample surface areas to rates of mass loss when comparing experimental with modelled data, future experiments will use a fully representative part of a real ProSPA (prototype) oven with the microbalance, in order to more accurately replicate the sample geometries of the mission scenario. All samples at temperatures investigated so far (down to -86 °C) lose a mission-relevant 5 % water ice mass within the first 680 seconds or less, with warmer samples losing 5 % much more rapidly than colder samples (Table 1). The addition of multi-layer insulation to the chamber walls will aid the investigation of mass loss rates at lower temperatures, down to -100 °C.

Regolith Simulant	Initial Water Ice %	Initial Water Ice Mass (mg)	Temperature (°C)	Time taken to lose X % (seconds)		
				1%	2%	5%
JSC-1A	7.91	20.1857	-43	50	100	200
JSC-1A	21.68	65.0325	-46	150	230	430
JSC-1A	25.4	80.2928	-55	220	300	560
JSC-1A	25.84	81.8704	-27	50	90	110
NU-LHT-2M	6.42	18.1719	-51	120	160	260
NU-LHT-2M	8.74	34.4581	-86	100	300	680
NU-LHT-2M	10.64	24.8893	-45	50	70	150
NU-LHT-2M	14.48	34.1953	-49	50	70	240
NU-LHT-2M	15.41	36.6258	-50	100	150	400
NU-LHT-2M	17.06	41.7635	-48	80	100	250
NU-LHT-2M	24.05	64.5955	-50	50	100	260

Table 1: Time taken to lose 1%, 2% and 5% water ice mass

References: [1] Trautner R. et al. (2018) 69th International Astronautical Congress, Paper ID: 42773 [2] Mortimer J. et al. (2018) *Planet. Space Sci.*, *158*, 25-33.

MINI-RF RADAR OBSERVATIONS OF POLAR CRATERS: ARE THEY ROUGH, SMOOTH, OR ICY?.

G. W. Patterson[1], L. M. Jozwiak[1], R. Kirk[2], T. L. Becker[2], R. Perkins[3], L. M. Carter[4], A. M. Stickle[1], J. T. S. Cahill[1], B. J. Thomson[5], C. D. Neish[6] and the Mini-RF team [1]Planetary Exploration Group, Johns Hopkins University Applied Physics Laboratory, Laurel, MD (Wes.Patterson@jhuapl.edu), [2]U.S. Geological Survey, Astrogeology Science Center, Flagstaff AZ, [3]Department of Earth and Environmental Sciences, Wesleyan University, Middletown, CT, [4]Lunar and Planetary Laboratory, University of Arizona, Tucson, AZ, [5] Dept. of Earth and Planetary Sciences, University of Tennessee, Knoxville, TN, [6]University of Western Ontario, London, ON, Canada.

Introduction: The possibility that water ice could be present in lunar polar craters has long been postulated [e.g., 1,2]. More recently, measurements from instruments on a number of spacecraft have all pointed to the presence of water at the lunar poles [e.g., 3-7]. The Lunar Crater Observation and Sensing Satellite (LCROSS) impact into a permanently shadowed portion of Cabeus crater (84.9°S, 35.5°W; 98 km dia.) has provided the most direct evidence for the presence of water in the form of ice [8]. Measurements of near-infrared absorption and ultraviolet emissions indicated that water ice and vapor were present in the resulting ejecta plume at between 3 and 10% by weight.

Water ice can exhibit a strong response at radar wavelengths in the form of a Coherent Backscatter Opposition Effect (CBOE) and the circular polarization ratio (CPR) of the returned data can be a useful indicator of such a response—i.e., measured CPRs for icy materials typically exceed unity [9]. This effect has been observed in radar data for the floors of polar craters on Mercury [9,10]. However, ground-based radar observations of the lunar south polar region did not observe this effect [11]. This result was supported by later Mini-RF and Mini-SAR (Chandrayaan-1) monostatic observations of Cabeus [12] but was contradicted by Mini-RF bistatic observations that showed a clear opposition response, at S-band (λ=12.6 cm) for Cabeus crater floor materials [13].

Mini-RF is currently operating as part of the Lunar Reconnaissance Orbiter (LRO) Cornerstone Extended Mission to address driving questions related to the form/abundance of water on the Moon and its vertical distribution. To support this effort, Mini-RF has collected X-band (λ=4.2 cm) bistatic observations of the south polar craters Cabeus and Amundsen (84.5°S, 82.8°E; 103 km dia.) and will be releasing monostatic controlled polar mosaics with resolutions of 30 m/pixel for the north and south poles that provide > 95% coverage poleward of 80° (Fig. 1). Here we use these data to address the question of whether radar observations of the lunar poles indicate they are rough, smooth, or icy?

Mini-RF Operations: Mini-RF is a hybrid-polarized, side-looking synthetic aperture radar (SAR) that was designed as a monostatic system – i.e., the antenna operated as a transmitter and receiver. In this operational mode, it transmitted a left-circular polarized signal and received orthogonal linear polarizations [14]. In December of 2010 the transmitter experienced a malfunction and ceased to operate, precluding further monostatic data collection. Prior to this malfunction, Mini-RF was able to collect S-band data that covered > 66% of the lunar surface and > 95% of the lunar poles. Controlled monostatic mosaics of these data for both poles have been produced by the USGS following the methodology outlined in [15]. These mosaics provide shadow-free access to polar crater floors at a resolution of 30 m/pixel (Fig 1.).

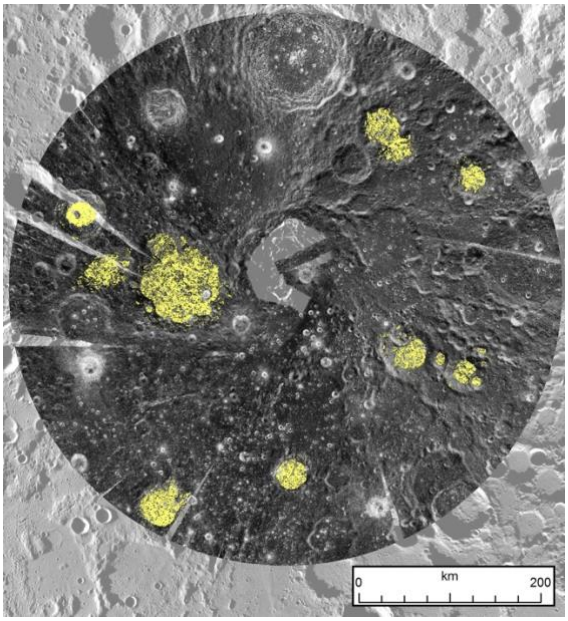

Fig. 1. Mini-RF controlled polar mosaic of the north polar regions (80°N to 90°N) overlain on WAC 100 m basemap. Yellow indicates crater floor areas analyzed in this study.

Shortly after the transmitter failed, Mini-RF began operating in concert with the Arecibo Observatory (AO) in Puerto Rico and the Goldstone deep space communications complex 34 meter antenna DSS-13 to collect bistatic radar data of the Moon. In this architecture either AO (S-band) or DSS-13 (X-band) transmits a circularly-polarized signal to illuminate a portion of the lunar surface, and Mini-RF's receives the

backscattered signal. This architecture allows for radar scattering properties of the lunar surface and subsurface to be measured over a range of bistatic angles (i.e., equivalent to phase angle for optical instruments), which was not possible in Mini-RF's original monostatic configuration (phase angle = 0º). In this bistatic configuration, 5 S-band observations of the floor of Cabeus crater and 3 X-band observations each of the floors of Cabeus and Amundsen craters have been acquired.

Analysis – Polar Mosaics: This analysis focused on comparing the radar response of permanently and non-permanently shadowed regions for the floors of craters polar craters with dia. > 15 km. The analysis regions were selected using LOLA-based shadow models and LOLA-based slope maps. Because sloped surfaces (such as crater walls or peaks) can result in spurious additions to the returned radar signal, we restricted our analysis to regions with slopes < 5°. These flat regions were then divided into permanently shadowed and non-permanently shadowed regions using the shadow model. Finally, we considered only craters where both the flat permanently and non-permanently shadowed regions were spatially expansive enough to be considered statistically significant (i.e., > 1 km^2 total).

Our final dataset included 10 north polar craters and 11 south polar craters (Fig. 1). Preliminary results indicate that the majority of the craters examined do not show an anomalous CPR signature indicative of the presence of water ice (for PSRs and non-PSRs within the craters). This is consistent with previous results from polar observations with bistatic angles < 0.5° [11, 12]. Three of the craters examined (Kocher, Wiechert E, and Wiechert J) have crater floor CPR values that are higher than surrounding terrain by a significant margin. Inspection of the floor morphology of those craters suggests that this signature is likely a result of surface roughness.

Analysis – Bistatic Observations: CPR measurements for the floor of Cabeus crater in S-band, as a function of bistatic angle, show a clear opposition surge; something not observed for the floors of nearby, similar-sized craters that were sampled during by Mini-RF bistatic observations (e.g., Casatus, Klaproth, Blancanus, and Newton A and G). Mini-RF X-band observations of the floor of Cabeus cover a smaller range of bistatic angles than were sampled at S-band. Based on the observations available, there is no indication of an opposition response. Data for the floor of Amundsen crater, on the other hand, do show an indication of an opposition response but it differs from what was observed for the floor of Cabeus at S-Band.

The Mini-RF bistatic data are currently being reprocessed with updated calibration parameters, adjustments to processing parameters that will reduce noise in the data, and the inclusion of low-resolution topography in the radar image formation process. These improvements to the data may impact the results of this analysis.

Conclusions: Preliminary analysis of the CPR of 18 polar craters in Mini-RF monostatic radar data suggest that a signature indicative of surficial/near-surface water ice is not present (i.e., at least not in quantities detectable at S-band wavelength). This is consistent with previous Mini-RF results from polar observations with bistatic angles < 0.5° [11, 12]. The CPR values of 3 other polar crater floors are elevated with respect to their surrounding but this signature is likely a result of surface roughness.

Mini-RF S-band bistatic observations, on the other hand, indicate that the floor of Cabeus crater is unique with respect to other materials observed on the Moon and has a CPR signature suggestive of water ice. That signature is not observed in shorter wavelength X-band bistatic observations of Cabeus and a different signature, indicative of surface roughness, is observed for the floor of Amundsen crater. Taken together, the bistatic observations could indicate that, if water ice is present in Cabeus crater floor materials, it is buried beneath ~0.5 m of drier regolith that does not include radar-detectible deposits of water ice.

Given some of the inherent ambiguities in interpreting radar data of silicate-ice mixtures, our continued objective is to integrate multiple wavelength observations over a range of bistatic angles (and concomitant penetration depths [16]) to help elucidate the structure of lunar polar regolith.

References: [1] Watson K. et al. (1961) *JGR, 66, 3033–3045*. [2] Arnold J.R. (1979) JGR, 84, 5659–5668. [3] Feldman W. C. et al. (1998) *Science 281*, 1496–1500. [4] Lawrence D. J. et al. (2006) *JGR, 111*, 08001. [5] Mitrofanov I.G. et al. (2010) *Science, 330*, 483–486. [6] Pieters C. M. et al. (2009) C.M. et al. (2009) *Science, 326*, 568–572. [7] Gladstone G. R. et al. (2012) *JGR, 177*, E00H04. [8] Colaprete A. et al. (2010) *Science 330*, 463–468. [9] Harmon J. K. et al., (1994) *Nature, 369*, 213–215. [10] Harmon J. K. and Slade M. A. (1992) *Science, 258*, 640–643. [11] Campbell D. B. et al. (2006) *Nature, 443*, 835–837. [12] Neish C. D. et al. (2011) *JGR, 116*, E01005. [13] Patterson G. W. et al. (2017) *Icarus 283*, 2-19. [14] Raney R. K. et al. (2011) *Proc. IEEE, 99*, 808–823. [15] Kirk R. L. et al. (2013) *LPSC XLIII*, Abstract #2920. [16] Prem P. and Patterson G. W. (2018) *LPSC XLIX*, Abstract #2134.

TRACE-ELEMENT SYSTEMATICS OF HIGHLAND ANORTHOSITES: IMPLICATIONS FOR UNDERSTANDING THE FORMATION OF THE LUNAR CRUST. J. F. Pernet-Fisher[*1]; E. Deloule[2]; K. H. Joy[1]. [1]SEES, University of Manchester, M13 9PL, UK. [2]CRPG, Université de Lorraine, Nancy, France (*john.pernet-fisher@manchester.ac.uk).

Introduction: In recent years, a wealth of mineral trace-element chemistry for lunar highland lithologies have been reported for lunar meteorites (e.g., [1, 2]), however, relatively few trace-element analyses have been reported from the Apollo collections [3, 4]. Here, we present plagioclase trace-element abundances for a suite of Apollo hand sample anorthosites, in addition to anorthositic clasts within Apollo 16 regolith breccias. This will enable us to explore the extent to which Apollo FANs display chemical heterogeneities, and test to what extent small (< 1 cm) clasts can be used to gain information about their parent lithologies.

Compositional heterogeneity of lunar primary crustal rocks: Studies have noted that some chemical differences are present between the Apollo FANs and the relatively Mg-richer anorthosite (MAN) clasts in lunar meteorites that are thought to have originated from the lunar farside [2, 5, 6]. This led workers to challenge the idea of a signal plagioclase flotation event during the crystallisation of the lunar magma ocean (LMO) (e.g., [5, 7, 8]). However, some have questioned the extent to which the modal mineralogy of small clasts within breccias represent their parent lithologies, further questioning the role that small clasts can play in identifying new highland rock types such as the MANs [9]. Trace-elements have the potential to circumvent these issues, due to their generally incompatible nature within the main rock-forming minerals. Not only can trace-elements distinguish between source lithologies [2], but also reveal the extent of geochemical diversity within lithological groups [1, 2, 4]. Here, we used extended mineral trace-element abundances (including Rare Earth elements, High Field strength elements, and Large-ion litholphile elements), combined with new mineral trace-element chemistry from Apollo 16 FAN hand samples to fully investigate the extent of chemical variability within FAN clasts, enabling the assessment of LMO crystallisation models.

Methods and Results: Major-elements were obtaining using a Camaca SX100 EMP using the methods described in [11], and X-ray element maps were determined on a Phillips FEI XL30 Environmental Scanning Electron Microscope-Field Electron Gun (ESEM-FEG) at the University of Manchester. Trace-element abundances were determined on an ASI RESOlution excimer laser ablation system (64 µm spot size) coupled to an Analytic Jena Plasma Quant MS Elite ICP-MS at the University of Portsmouth.

Polymineralic clasts investigated here range in size from ~ 1 cm to ~250 µm, and consist of plagioclase, clinopyroxene, and/or olivine of varying size and proportions. Clasts with clear igneous textures (i.e., minerals meeting triple junctions) and lacking Fe-metal blebs were preferentially targeted, however, in some cases, particularly for the smallest clasts, textures are ambiguous to distinguish from the poikiloblastic texture typically associated with granulites or phyric impact melts. Plagioclase major-element (e.g., An% vs. Mg#, [11]) systematics can be used to identify the parent lithologies of the smallest clasts and mineral fragments. All samples investigated here, regardless of their petrographic classification (i.e., mafic minerals > 5 modal %), are most similar to the anorthosite field; **Fig. 1**). The An% content of the plagioclase investigated ranges from 94 to 98, whereas MgO and FeO range from 0.03 to 0.50 wt. % and 0.06 to 1.45 wt. % respectively, falling within range of reported pristine FAN hand specimen samples [2, 12]. The REE abundances for the clasts encompass the range reported for the Apollo 16 FAN hand samples [4], Samples investigated here range in La/Sm_{CI} from 0.7 to 2.5, Eu/Eu* range from 4.79 to 119.

Discussion: Overall, investigations FAN hand samples and clasts within Apollo 16 regolith breccias greatly expand the trace-element systematics of Apollo 16 FANs available within the literature and highlights the value of trace-element for investing the petrochemical history of the FAN samples, particularly in cases were only small clasts/mineral fragments are available. [2].

The siderophile element abundances (Ni, Co) of plagioclase in the the clasts investigated here overlap reported pristine FAN hand samples, indicating they are 'pristine' clasts [12], and are not impact melts. Calculated melts in equilibrium with plagioclase mineral chemistry display correlations between ratios that are strongly controlled by fractionation crystallisation (e.g., Sr/Sm, Eu/Sm). Importantly variations in ratios such as Ti/Sm suggests that the FANs investigated here co-crystallised with pyroxene and ilmenite. This indicates that these samples are crystallization products of the LMO at >90 % solidification. Samples also display variations in incompatible element ratios (e.g., La/Sm, Th/Sm, Zr/Sm). These ratios do not display correla-

tions with compatible elements, suggesting that the observed variations are not the result of combined assimilation (of material chemical very difference to the FAN parent melts, e.g., KREEP) and fractional crystallisation (i.e., AFC).

We propose that the observed trace-element variations are related to overturn in the lunar mantle due to the onset of ilmenite accumulation within the lunar mantle. Ilmenite is denser than these underling minerals, and thus overtime will sink triggering mantle overturn events [17, 18]. During mantle overturn, the act of exhuming deep mafic-rich cumulates to the base of the lunar crust will result in decompression melting. Such melt are likely to be small-degree (< 10%) partial melts. Small-degree melts are typically rich in incompatible elements displaying LREE enrichments. Variable mixing between such melts, KREEP, and overlying plagioclase-saturated residual melts or plagioclase-rich lithologies will result in lunar anorthosites that display variable incompatible element enriched signatures (**Fig. 2**).

Implications and summary: The identification of potential source heterogeneities within the Apollo FAN suite clasts and hand specimen samples have implications for containing LMO crystallisation models. Modification of the 'classic' single event plagioclase flotation model has been proposed over the past few years. These include serial magmatism of discrete plagioclase plutons [5], and asymmetric plagioclase flotation [3, 7], both of which account of chemically diversity of anorthites lithologies on a global scale. The identification of source heterogeneities within the LMO supports these alternative suggestions.

References: [1] Cahill et al., (2004) *MaPS, 39*, 503-529. [2] Russell et al., (2014) *Phil. Trans. R. Soc. 372*, 20130241. [3] Floss et al., (1998) *GCA, 62*, 1255-1283. [4] Papike et al., (1997) *GCA, 61*, 2343-2350. [5] Gross et al., (2014) *EPSL, 388*, 318-328. [6] Takeda et al., (2006) *EPSL, 247*, 171- 184. [7] Arai et al., (2008) *Earth, Plan. Space, 60*, 433-444. [8] Ohtake et al., (2013) *Nat. Geo. 5*, 384. [9] Warren (2012) *2nd Lunar Highlands Conference* abstract #9034. [10] Joy et al., (2015) *MaPS, 50*, 1157-1172. [11] Warren (1993) *Am. Min., 78*, 360. [12] Warren & Wasson (1977) *LPSC, 8*, 2215-2235. [13] Aigner-Torres et al., (2007) *Contrib. Min. Pet., 153*, 647-667. [14] Warren & Wasson (1979) *Rev. Geophys. 17*, 73-88. [15] Hallis et al., (2014) *GCA, 134*, 289-316. [16] Shervais & McGee (1999) *Am. Min., 84*, 806-820. [17] Tronche et al., (2008) LPSC #1551; [18] Hess and Parmentier, (1995), EPSL, 134, 501-514. [19] Yamaguchi et al., (2010), GCA, 74, 4507-4530. [20] James et al., (1989) LPCS 19. 219-243.

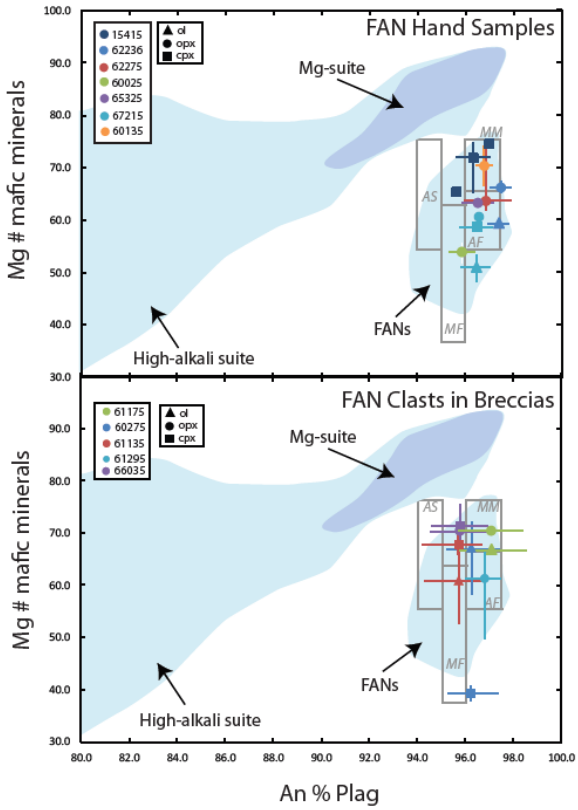

Figure 1: Plagioclase An% vs mafic mineral Mg# plot for Apollo FAN hand sample and breccias respectively. Background fields for FANs, Mg-suite and HAS are taken from [18]. Grey boxes represent the FAN sub-groupings defined by [19].

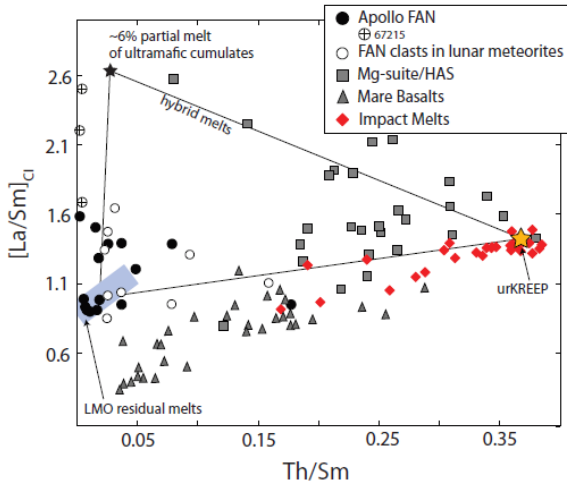

Figure 2: Chondrite-normalization La/Sm vs. Th/Sm plots for lunar lithologies. All circles represent compositions of melts in equilibrium within plagioclase. Yellow star represents the composition urKREEP. Black star represents a ~6 % partial melts of an ultramafic cumulate. Blue box represents range of residual LMO compositions <95% solidification. The black tie-lines between these three components represent mixing trajectories between 'pristine' LMO

residual melts and a hybrid melt from by small degree partial melts of ultramafic cumulates and urKREEP.

HALOGEN (Cl, Br, I) SYSTEMATICS OF LUNAR FERROAN ANORTHOSITES: EVIDENCE FOR SUB-CHONDRITC LUNAR VOLITAILS J. F. Pernet-Fisher[1], P. L. Clay[1], R. Burgess[1], K. H. Joy[1], [1]School of Earth and Environmental Sciences, University of Manchester, M13 9PL, UK (john.pernet-fisher@manchester.ac.uk).

Introduction: We report halogen (Cl, Br, I) abundances for a suite of 10 lunar Ferroan Anorthosites (FANs). The volatile elements, including the halogens, are crucial components in planetary differentiation and evolution as they influence melting temperatures, magma viscosity, and magmatic eruptions [1,2]. As crystallization products of the earliest phases of the Moon's history, anorthosites have the potential to shed light on the volatile systematics of the lunar magma ocean (LMO). Additionally, any such estimates will be important for evaluating existing apatite-derived volatile abundance estimates of the Moon, derived from partial melts of the lunar mantle (formed from mafic LMO cumulates). Apatite contains relatively high abundances of halogens (F+Cl) and water relative to other rock forming minerals (i.e., ol, pyx, plag). Thus, many studies have routinely used apatite to calculate magmatic water and halogen abundances, ultimately deriving water and halogen abundances for the lunar mantle [e.g., 2]. However, apatites are among the final phases to crystalize from a magma (~> 95 % solidification). Processes such as crustal assimilation or magmatic degassing over the lifetime of a magma can result in large uncertainness in any resulting apatite-derived volatile back-calculations.

Methods : We were allocated 10 FAN Apollo 16 samples from a range of different sampling stations, and one Apollo 15 sample. All these samples are thought to be 'pristine' and do not contain any impactor HSE component. Chips ~ 50 mg in mass were analyzed using the neutron irradiation noble gas method [4] on a Thermo-Fisher Argus VI multi-collector mass spectrometer at the University of Manchester. This method enables the precise determination of low abundance (sub-ppm) halogens such as Br and I.

Results: The Apollo 15 sample is within range of the Apollo 16. Ratios of Br/Cl and I/Cl for this suite of anorthosites generally overlap values reported for lunar volcanic glass beads, extending from chondritic compositions to sub-chondritic values (**Fig. 1**).

Discussion: Due to the volatile nature of the halogens, they can be easily modified by secondary processes such as impact modification and magmatic degasses/metasomatism. Therefore, before the FAN halogen systematics can be assessed in the context of a crystalizing LMO, the effects of secondary processes need to be considered first.

Role of Impact: Impacts have the potential to fractionate relative halogen abundances [5]**.** Pernet-Fisher et al. [6] characterized the extent of shock damages for a number of anorthosites investigated here. Samples display a range of shock states, ranging from near-pristine (< 3 GPa) displaying clear igneous cumulate textures to high shock states (~20 GPa; e.g., sample 60015) displaying cataclastic brecciated textures. No systematic relationships are observed between plagioclase shock state and halogen abundances, indicating that impact shock processing have had a minimal effect on modifying halogen systematics.

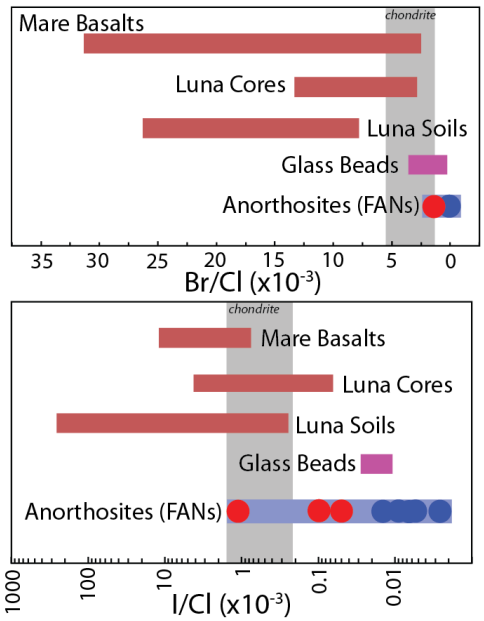

Figure 1: Plots of Br/Cl and I/Cl of lunar FANs in context with other lunar materials. Figure modified from [1]. Red symbols represent samples that display enrichments in halogens. Blue symbols represent samples that likely reflect LMO halogen ratios. Gray bar represents the reported range of carbonaceous and ordinary chondrites.

Role of metasomatism within the crust: Due to the water restricted nature of the Moon relative to the Earth, magmatic degassing can be dominated the volatilization of phases such as HCl and metal halides [7,8]. This will result in the gases/fluids that are enriched in Cl relative to Br and I. Such degassing has been linked to δ^{37}Cl enrichments in lunar samples [e.g., 3,7], and in extreme cases has resulted in low-T alterations around the rims of phases such as FeNi metal sulfides [9]. The best example of this is from Apollo 16 sample 66095 'rusty rock' which contains Fe-oxide alteration phases such as lawrencite ($FeCl_2$) [9]. No such alteration has

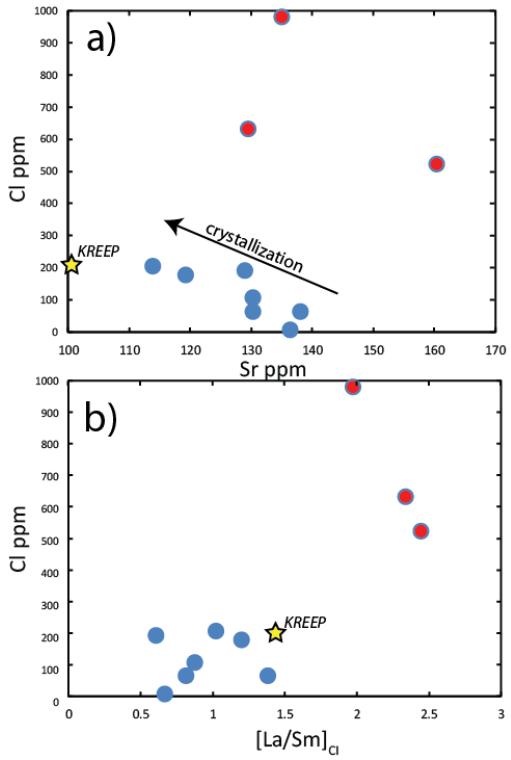

Figure 2: a) Cl vs. Sr ppm. Blue symbols display a negative correlation expected for a crystallizing LMO trending towards KREEP. b) Cl vs. [La/Sm]CI. For blue symbols Cl abundance does not vary with La/Sm as is expected during fractional crystallization. Red symbols in a) and b) display enrichments in Cl and LREE relative to trends expected in a fractional crystallization sequence. Sr and REE data from [10], KREEP from [14].

been reported for any lunar anorthosites, however, to date no Cl-isotope ratios have been reported for lunar anorthosites making it hard to assess the extent to which these samples have been affected by degassing.

Halogens in the LMO: It is anticipated that halogens should become progressively concentrated in residual LMO melts given the incompatibility of these elements in earlier crystallized olivine, pyroxene, and plagioclase [2]. Thus, within this suite of anorthosites, negative correlations are expected between indices of fractional crystallization (i.e., elements like Sr that are strongly affected by plagioclase fractionation) and halogen abundance. With the exception of 3 samples (red symbols in **Fig. 1 and 2**; 67635, 60135, 60515), such correlations are generally observed, indicating that fractional crystallization of a solidifying LMO is largely controlling FAN halogen abundance (**Fig. 2a**). The 3 noted samples above display both high halogen abundances and high Sr abundances, inconsistent with the trend expected for fractional crystallization. Indeed, these 3 samples also display large LREE enrichments ($La/Sm_{CI} > 2$; **Fig. 2b**). The observation of LREE enrichments within lunar anorthosites are not accounted for by the fractional crystallization of a single evolving LMO melt [10, 11].

Several mechanism have been proposed to account for the observation of LREE enrichments (and enrichments of KREEPy elements such as Th) in lunar anorthosites. These range from partial melts induced by mantle-over turn mixing with plagioclase-saturated LMO melts [10] to serial magmatism intruding plagioclase-saturated melts into the lunar crust [12]. In either case, it is clear that the mechanism that is introducing LREE enriched/KREEPy signatures to some FANs are also introducing enrichments in halogens.

Disregarding these three halogen-enriched samples, no to weak correlations are observed between halogens abundances (and ratios) and La/Sm (**Fig. 2b**), consistent with a simple crystallizing LMO melt. As such, these samples are the best available for constraining the volatile systematics of the LMO. As incompatible elements do not fractionate during fractional crystallization, the observed sub-chondritic Br/Cl and I/Cl ratios for these sample likely represent the halogen ratios of the LMO during solidification.

This interpretation is supported by the halogen systematics of lunar volcanic glass beads (**Fig. 1**). Due to the primitive nature of the glass beads, these samples are thought to have erupted through the lunar crust rapidly, having undergone minimal degassing relative to other eruptive volcanic products such as mare basalts [13]. Thus, the halogen ratios reported for these samples should represent a close approximation to the mantle signatures at the source of the glass beads. The observations that the FANs overlap these ratios, therefore, support our interpretation that the lunar mantle has sub-chondritic halogen signature.

In conclusion, we suggest that the Moon had an initial sub-chondritic halogen composition. This is consistent with the fact that Br and I are more volatile than Cl. Any volatile loss during the Moon-forming impact event is likely to have preferentially lost Br and I relative Cl, driving down Br/Cl and I/Cl values.

References: [1] Clay et al (2017). Nature, 551, 614; [2] McCubbin et al. (2015) Am. Min., 100, 1668-1707; [3] Barnes et al. (2016). EPSL, 447, 84-94; [4] Ruzié-Hamilton et al (2016) Chem. Geol., 437, 77-87; [5] Treiman et al (2014) Am. Min. 99, 1860-1870; [6] Pernet-Fisher et al. (2017) Sci. Rep., 7, 5888; [7] Sharp et al. (2010). Science, 329, 1050-1053; [8] Tartese et al. (2013) GCA, 122, 58-74; [9] Shearer et al. (2014) GCA, 139, 411-433; [10] Pernet-Fisher et al. (2017) LPSC 48 #1931; [11] Floss (1998) GCA, 62, 1255-1283; [12] Gross et al. (2014) EPSL, 388, 318-328; [13] Saal et al. (2008) Nature, 454, 192. [14] Warren (1988) Workshop on Moon in Transition.

INGENII FARSIDE SWIRLS HAVE EVERYTHING (EXCEPT ACCESS). C. M. Pieters[1], [1]DEEPS Brown University, Providence, RI, 02912 USA (Carle_Pieters@brown.edu)

The graceful but enigmatic albedo markings on the Moon's surface, called lunar swirls, continue to delight and perplex all who attempt to understand them. Their mysterious origin is likely to remain unsolved until one or more missions are sent to gather additional information that is applicable to their unique space environment. Properties derived from modern sensors of the Ingenii swirls found across diverse terrain in NW South Pole-Aitken basin are highlighted here to continue the discussion as the next several steps for lunar exploration are planned. Swirls exhibit no associated topographic expression but are associated with some of the strongest magnetic anomalies detected on the Moon [e.g. 1]. Although swirls are readily recognized in low albedo mare, several also occur in feldspathic highland areas.

M^3 data are used to distinguish compositional units and to sample and map local swirls across the Ingenii region on the farside. As illustrated below, Ingenii swirls are particularly interesting because they occur indiscriminately across neighboring feldspathic and basaltic materials. Assuming all Ingenii swirls have the same origin, it appears composition does not have a significant effect on swirl distinct properties.

The Ingenii swirls would make an excellent target to resolve major outstanding mysteries surrounding lunar swirls. Until global lunar access is truly achieved, however, such farside priority targets remain orphans or an expensive luxury which we crave.

Referemces: 1] Blewett et al. (2011) JGR, 116, E02002; Kramer et al., (2011) JGR 116, E00G18. [2] Moriarty and Pieters (2016) MaPS 51, 207-234.

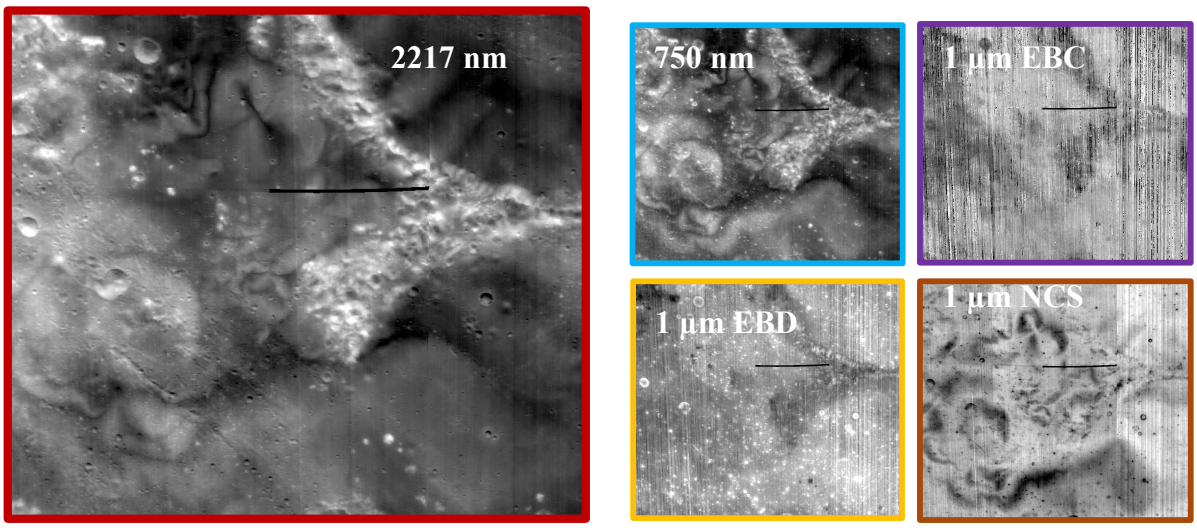

M^3 mosaic of several Ingenii swirls. Upper right corner is the SW rim of Thompson crater. The 2217 nm image is within a principal pyroxene absorption band, thus suppressesing the immature signature of basalts and allowing the albedo properties of swirls to be readily distinguished. Feldspathic materials associated with the highlands are identified by their high albedo, low 1 µm estimated band depth (EBD) and short wavelength 1 µm estimated band center (EBC) [see 2 for measurement technique]. All swirls exhibit a low 1 µm normalized continuum slope (NCS) compared to surrounding terrain due to their signature relatively uniform brightening across all wavelengths.

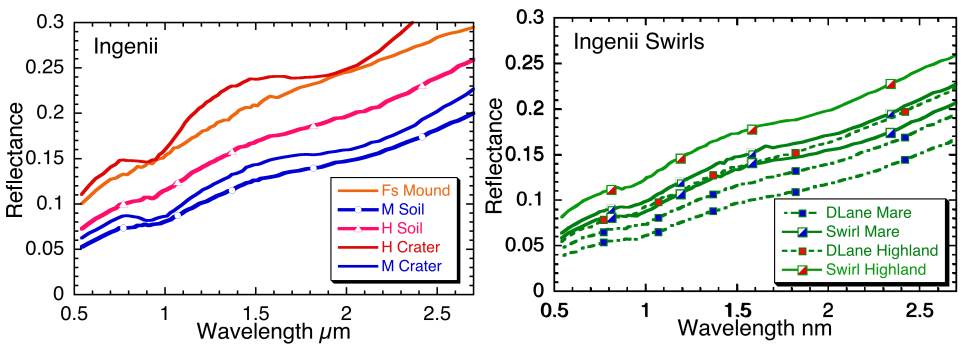

[Left] M^3 spectra for local highland (orange-red) and mare (blue) areas within the M^3 mosaic scene. [Right] M^3 spectra for dark lanes and swirls that occur in feldspathic areas (red symbols) and mare basalt (blue symbols). All swirls exhibit the general brightening across all wavelengths.

ADVANCED SPECTROSCOPIC SOFTWARE FOR OLIVINE DETECTION AND COMPOSITION DETERMINATION (ASS-OL). P.C. Pinet[1,2], S.C. Chevrel[1,2] and Y.H. Daydou[1,2]. [1]Université de Toulouse; UPS-OMP; IRAP; Toulouse, France, [2]CNRS/CNES; IRAP; 14, avenue Edouard Belin, F-31400 Toulouse, France (patrick.pinet@irap.omp.eu).

Introduction: We reassess the relationship between olivine composition and reflectance spectroscopy from an advanced MGM deconvolution approach which revisits the behavior of the three primary olivine absorptions near 1 µm (referred to as M1-1, M2, M1-2) and their interrelationships. We build on the previous works carried out [e.g.,1,2] to document at best the compositional variation of olivine from diagnostic absorption features across the visible and near-infrared wavelengths due to electronic transitions of Fe2+ in the crystal structure.

MGM implementation: The principle of the Modified Gaussian Model is to deconvolve overlapping absorptions of mafic mineral spectra into their fundamental absorption components. Spectra are modeled in the logarithm of reflectance space as a sum of modified Gaussian distributions superimposed on a baseline continuum [e.g., 3,4].The current procedure is described in [5,6].

Olivine Spectra Deconvolution / Methodology: MGM inverse modeling provides with band center, band width and band depth estimates. Band centers are used to determine trend line equations for each individual absorption band, with an assessment on the regression performance (rms spectral distance between bandcenter estimate from MGM and the one from the trend line). The olivine composition (Molar Forsterite Fo#) is then predicted based on minimizing the deviations in band centers from the established trends for the three absorptions simultaneously, using the integrated rms **s**pectral **d**istance to **t**rend quantity (**sdt**).

Synthetic olivine samples. A careful selection from [3] leads to a suite of 6 controlled and well-characterized synthetic olivine samples [2, 7] that can be considered to be the best examples of pure olivine for which the spectral optical properties are unaffected by the inclusion of minor cations. These samples, referred to as suite 1, span the range of Fo#0 to 70.

Our MGM approach is thus first implemented on this suite of spectra, referenced as table 6 in [2], and then extended (suite 2) to the range of Fo#0 to 90, using 10 synthetic samples. Fo#20 case is shown below (Fig. 1).

A systematic testing of the coherency is performed to assess the performance of each regression. For suite 1, the integrated Fo# rms deviation is 4.5, with a 6 nm rms **sdt**. For suite 2, the integrated Fo# rms deviation is 4.8, with a 6.5 nm sdt (see Fig. 2).

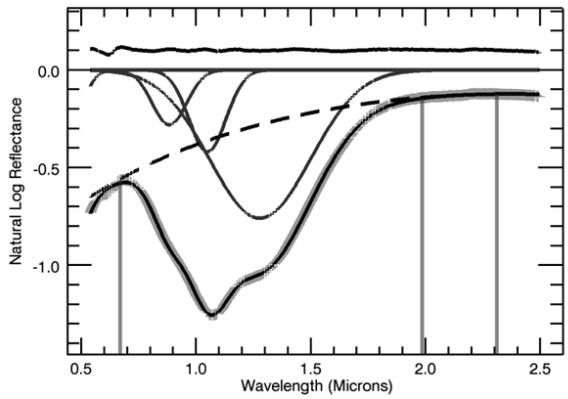

Figure 1. Case of C1DD96 (Fo#20). Measured spectrum (light grey crossed line) and MGM modeled one (thick black solid line) with the Gaussians (solid black lines) and polynomial (hatched line) and the residuals line along the spectral domain. Position of the local maxima along the spectrum used for the process of initialization (anchor points found at 670, 1985, 2310nm). For clarity, the residuals (observed – modeled quantity) are shifted by +0.1 which means that a perfect fit is displayed with a 0.1 flat line (rms : 0.005).

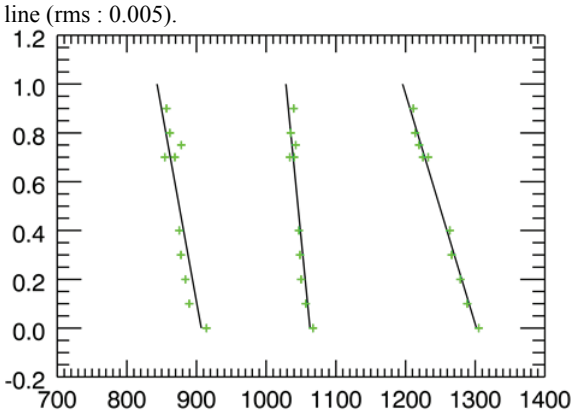

Figure 2. Composition Trend lines from our MGM (suite 2) in Molar % Forsterite vs band center (nm) graph. Spectra with grain size<45µm: C1DD[98 (Fo_0), 97 (Fo_{10}), 96 (Fo_{20}), 95 (Fo_{30}), 42 (Fo_{40}), 39 (Fo_{70}), 116 (Fo_{70}), 88 (Fo_{75}), 38 (Fo_{80}), 37 (Fo_{90})].

Natural olivine samples. We now consider the suite (suite 3) spanning the forsterite-fayalite solid solution series historically considered to derive the olivine composition [1] and apply our MGM approach on its 18 natural samples. The trend line equations established from suite 2 are then used to predict the composition variability based on the minimum deviation from the three trend lines simultaneously. While suite 3 presents an integrated Fo# rms deviation of 14.0, with a 16.9 nm sdt, we find that if one excludes spectra (A,C,E,F,G,P) the resulting suite 4 has an integrated Fo# rms deviation of 4.6 (i.e., comparable to suite 2), with a 12 nm sdt (see

Fig. 3). At the exception of P spectrum (Fo_{18}), all other spectra correspond to Mg-rich olivines (Fo#>84), for which our prediction underestimates Fo#. Along with [2, 7], we suspect these spectra are affected by impurities and/or heterogeneities arising from the presence of minor amounts of various cations (Ca^{2+}, Mn^{2+}, Ca^{2+},Cr^{2+} , Fe^{3+} ,…).

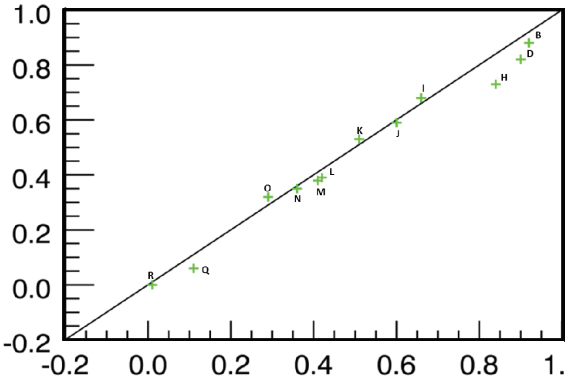

Figure 3. Predicted versus Actual Molar % Forsterite estimates for natural samples (suite 4) from [1], based on our suite 2 (synthetic samples) derived trend lines.

M3 orbital observations at Copernicus. This procedure is then implemented on M3 spectra with the objective of documenting the petrology at Copernicus crater from spectra acquired over exposed outcrops (e.g., central peaks, inner walls and rims). The present study has been made on a subset of the M3G20090416T122951_V01_RFL hyperspectral image (140m/pixel) acquired during the OP2A optical period. Based on a previous selection of olivine-bearing spectra across Copernicus [5], we choose 5 spectra (Fig. 4) taken in the central peaks and northern wall and derive their composition (Molar Forsterite Fo#).

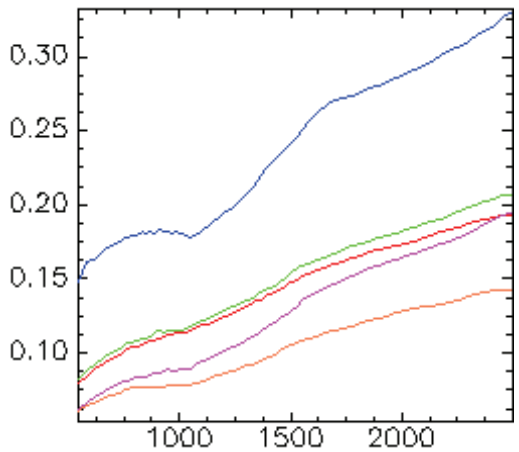

Figure 4. Selection of 5 spectra taken from the central peaks and the north wall of Copernicus crater.

A very interesting result is that for all spectra the Fo# is found in the range of 0.70+/- 0.05 consistent with the idea that there is no obvious local/regional variability in the subsurface petrology of the target.

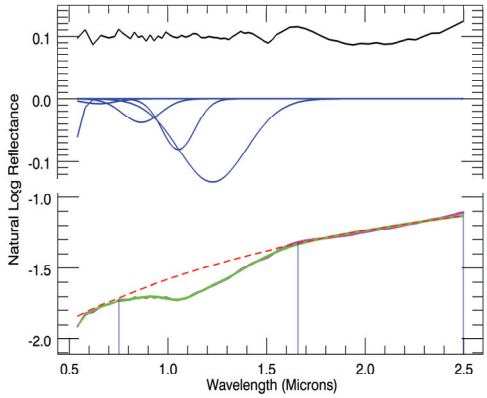

Figure 5. Measured spectrum (light pink curve below the green one) and MGM modeled one (green solid line) with the Gaussians (solid blue lines) and polynomial (red hatched line) and the residuals line (black line) along the spectral domain. Position of the local maxima used for the process of initialization (anchor points found at 750, 1560, 2500nm). Residuals (see Fig.1) (rms : 0.007).

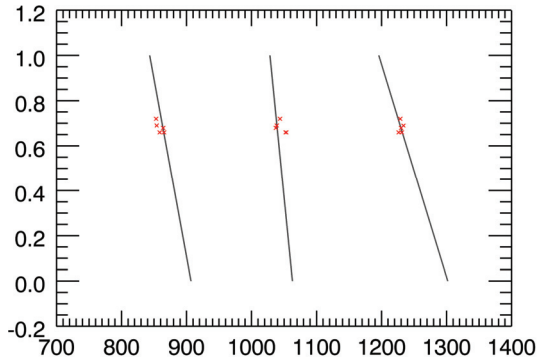

Figure 6. Olivine Composition estimates derived from our MGM for the 5 spectra shown on Fig. 4 in Molar % Forsterite vs band center (nm) graph.

Conclusions: The trend lines equations derived from the current MGM modeling do not depart very much from previous results. However, the band center positions of the three primary olivine absorptions near 1 µm (M1-1, M2, M1-2) can be used simultaneously to produce a better constrained prediction across an extended range of olivine solid solution composition from spectra measured on synthetic, natural samples and from orbital observations. This approach is of great interest for preparing the selection of potential landing sites and in situ characterization of samples to be collected for addressing the exploration of primitive mantle lunar rocks.

References: [1] Sunshine J. M. and C. M. Pieters (1998) *JGR, 103*, 13,675–13,688. [2] Isaacson P.J. et al (2014) *Am. Miner.*, *99*, 467-478. [3] Sunshine J.M. et al. (1990) *JGR, 95, B5*, 6955-6966. [4] Clenet, H. et al. (2011) *Icarus,* 213, 404-422. [5] Pinet et al. (2018) LPSC XLIX, Abstract #1899. [6] Pinet et al. (2019) LPSC XL, Abstract #1806. [7] Dyar M.D. et al. (2009) *Am. Miner.*, *94*, 883-898.

Acknowledgments : The support of CNES and CNRS to this project is duly acknowledged.

AGE AND ORIGIN OF THE LUNAR NORTHERN LIGHT PLAINS. C. M. Poehler[1], H. Hiesinger[1], and C. H. van der Bogert[1]. [1]Institut für Planetologie, Westfälische Wilhelms-Universität, Wilhelm-Klemm-Str. 10, 48149 Münster, Germany (c.poehler@uni-muenster.de).

Introduction: Lunar light plains are morphologically similar to dark mare plains, but differ in albedo, namely the light plains are brighter and have an albedo closer to the adjacent highlands [1]. Due to the morphological similarity a volcanic origin for light plains was proposed [2]. However, the Apollo 16 mission revealed that light plains consist mostly of impact breccias [3]. This led to several new hypotheses proposing an origin by one or two basin-forming events or several local impact events, and the deposition of fluidized ejecta [e.g., 1,4,5,6]. Meanwhile, other lines of evidence still seem to support a volcanic origin [7,8]. To investigate whether light plains have common ages and/or origins, we determined the absolute model ages (AMAs) of light plains in the northern hemisphere (see also [9]) to expand on existing data for light plains close to the equator [7], in the southern hemisphere [10], on the northern nearside [8], and around Orientale basin [11].

Method: On the basis of Lunar Reconnaissance Orbiter Wide Angle Camera image data (100 m/pixel) [11], we identified and characterized the light plains in our study area extending from the north pole to 45°N (***Fig. 1***). Shadowing effects prohibited light plains identification above 80°N latitude. On the nearside, mare basalts in Mare Frigoris and Oceanus Procellarum cover the area up to about 60°N.

We performed crater size-frequency distribution (CSFD) measurements and determined absolute model ages (AMAs) using the production and chronology functions of [12,13,14]. The CSFD measurements were made using CraterTool [15] in ArcGIS, and we used Craterstats [16] to determine the corresponding AMAs. The light plains units chosen for CSFD measurements were carefully examined for homogenous surfaces and special care was given to exclude secondary craters.

Results: We determined AMAs for 24 light plains occurrences. The light plains show AMAs ranging from 3.43+0.096/-0.28 to 3.98+0.019/-0.022 Ga (***Figs. 1, 2***). The light plains were divided into three different units *Ip*, *Ip1*, and *Ip2* by [17]. Unit *Ip1* was described as the older stratigraphic light plains unit with more craters than the younger *Ip2*. Light plains that cannot be distinguished into an older or younger unit were grouped as *Ip* [17]. We measured eight occurrences for each Ip type.

Plains type *Ip1* shows both the youngest (3.43 Ga) and oldest (3.98 Ga) AMAs. Some areas show signs of resurfacing in their CSFDs. For example, in Area 12 (61.1°N, 121.2°W), the light plains in a 40-km diameter crater gives two ages: 3.98+0.06/-0.071 Ga, representing an underlying older surface, and 3.43+0.096/-0.28 Ga, interpreted as the emplacement age of the light plains. Craters with a diameter smaller than 400 m appear to be in equilibrium. Two other areas also give two ages for the underlying surfaces: 3.93/3.60 Ga and 3.72/3.64 Ga. The older ages could indicate the presence of underlying cryptomare.

From the areas mapped as *Ip1*, four occur as crater fills and four are on intercrater plains. Some of the areas mapped as *Ip1* show CSFDs that can be easily fit to derive an AMA. The other areas mapped as *Ip1* seem to be either (1) affected by secondary cratering, which appears as small bulges in the cumulative CSFDs, or (2) exhibit equilibrium at small crater diameters.

The *Ip2* plains type occurs mostly on the nearside and to the east of the *Ip1* units. Areas mapped as *Ip2* show AMAs between 3.51 and 3.84 Ga. Five of these light plains fill large craters; the other three are intercrater plains. While *Ip2* was proposed to be younger than *Ip1* [17], the ages obtained in this study do not confirm this stratigraphic relationship, because both unit types span about the same time interval. However, in small-scale areas some differences can be observed.

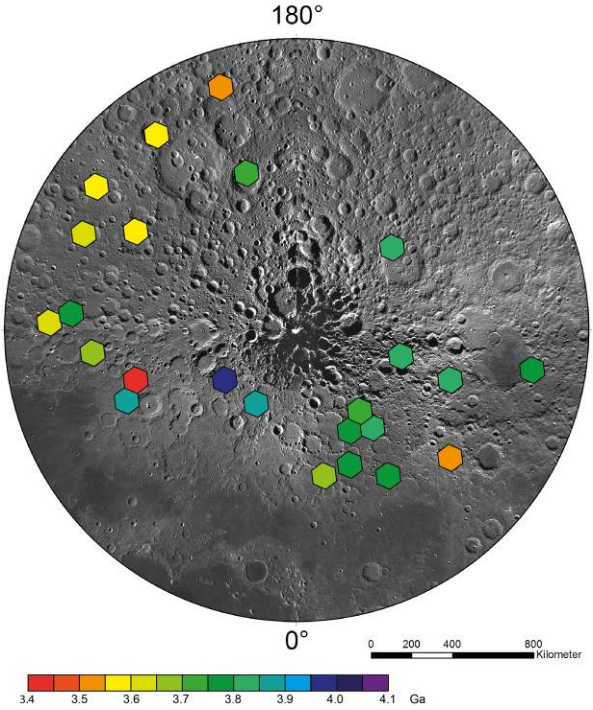

Fig. 1. *Locations and absolute model ages (AMAs) for light plains units in our study region from 45°N-80°N shown on LRO WAC mosaics [NASA/GSFC/ASU].*

Two areas directly east of Meton crater were selected to look at the small-scale age differences between the different types of light plains units. These areas border each other and were mapped as *Ip1* and *Ip2* [18]. Ages obtained for these plains show a younger AMA of 3.71+0.025/-0.03 Ga for the *Ip2*, whereas the AMA for the *Ip1* is 3.84+0.32/-0.42 Ga. Thus, in this case we can confirm a stratigraphic relationship where *Ip2* is younger than *Ip1*. On a larger scale, as shown in ***Fig. 2***, this stratigraphy could not be supported since both *Ip1* and *Ip2* include light plains of both older and younger ages.

Discussion: The two youngest large basins the Moon are Orientale (3.68-3.8 Ga [18,19]) and Imbrium basin (3.85 Ga [18]).The long time span over which the light plains of the study area formed excludes an origin by one or even two major events. With several light plains postdating the formation of the youngest basin (Orientale), an origin solely via basin forming events can also be excluded.

Nevertheless, our data shows a peak in the number of plains formed around 3.8 Ga. This peak becomes even more significant when combining our data with previous AMA determinations in other areas of the Moon (***Fig. 3***) [7,8,9,10]. The peak in ages around 3.8 Ga correlate to Orientale and possibly Imbrium basin formation, which might indicate a contribution to the formation of light plains by either one of these events either directly as ejecta or by triggering volcanism in those areas.

To investigate a potential volcanic origin of the light plains, we looked for volcanic features in the light plains in our study. While we were able to identify some structures that could be wrinkle ridges and might be linked to volcanic activity, most light plains in the study area did not show any evidence of typical volcanic features.

On the basis of all available CSFD measurements for light plains [7-10, this work], it appears that light plains in the northern hemisphere might be younger than those in the southern hemisphere. In addition, light plains in the western hemisphere seem to be younger than those in the eastern hemisphere. This supports an origin related to the Orientale basin for light plains units close to the basin.

Conclusions: The absence of volcanic features in the areas we studied supports an impact, rather than a volcanic origin, for light plains materials. The broad range of ages for light plains across the Moon precludes an origin via a small number of basin-forming events. Nevertheless, groupings of ages are likely associated with particular basin events, such as Orientale.

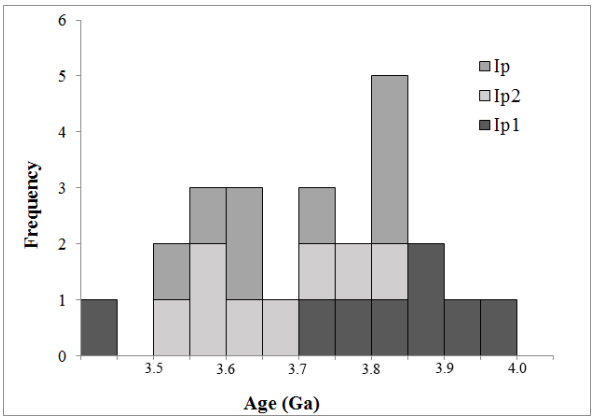

Fig. 2. *Age distribution of light plains AMAs in the northern lunar hemisphere sorted into units according to [17].*

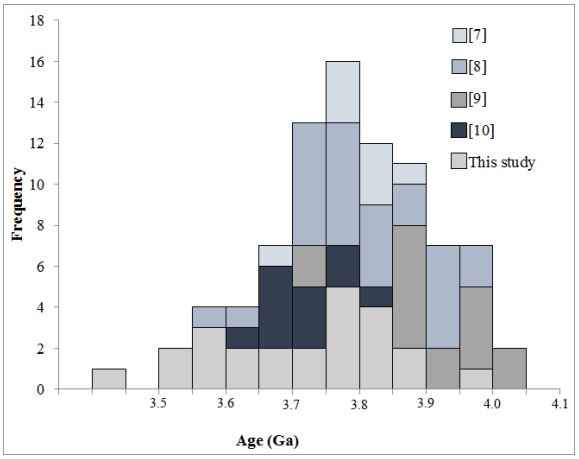

Fig. 3. *Distribution of light plains AMAs in this study combined with [7,8,9,10].*

Acknowledgements: This project receives funding from the European Union Horizon 2020 research and innovation programme under grant agreement No 776276.

References: [1] Eggleton and Schaber (1972) Apollo 16 PSR, 29-7–29- 16. [2] Wilhelms and McCauley (1971) USGS I-703.. [3] Muehlenberger et al. (1972) Apollo 16 PSR, 6-1–6-8. [4] Oberbeck et al. (1974) PLPSC 5, 111-136. [5] Head (1974) Moon 11, 327-356. [6] Oberbeck et al. (1974) PLPSC 5, 111-136. [7] Neukum (1977) Moon 17, 383-393. [8] Köhler et al. (2000) LPSC 31, 1822. [9] Pöhler et al. (2019) LPSC 50, 2310. [10] Hiesinger et al. (2013) LPSC 44, 2827. [11] Meyer et al. (2016) Icarus 273, 135-145. [11] Robinson et al. (2010) Space Sci. Rev. 150, 81-124. [12] Neukum et al. (2001) Space Sci. Rev. 96, 55-86. [13] Hiesinger et al. (2000) JGR 105, 29239-29276. [14] Crater Analysis Working Group (1979) Icarus 37, 467-474 [15] Kneissl et al. (2011) PSS 59, 1243-1254. [16] Michael and Neukum (2010) EPSL 294, 223-229.. [17] Lucchitta (1978) USGS I-1062. [18] Whitten et al. (2011) JGR 116, E6. [19]Wilhelms (1987) USGS Prof. P 1348.

GEOLOGICAL MAPPING OF THE SOUTH POLE AITKEN BASIN: A PROGRESS REPORT. C. M. Poehler[1], H. Hiesinger[1], W. Iqbal[1], C. Rueckert[1], C. H. van der Bogert[1], and M. A. Ivanov[2]. [1]Institut für Planetologie, Westfälische Wilhelms-Universität, Wilhelm-Klemm-Str. 10, 48149, Münster, Germany, c.poehler@uni-muenster.de, [2]Vernadsky Inst., RAS, Russia

Introduction The South Pole-Aitken (SPA) basin, situated on the lunar farside and centered at 53°S 169°W, is the largest [1-5] and oldest basin [6,7] on the Moon. Due to its morphological appearance it is argued that the SPA basin formed in an already solidified lunar crust [1]. Therefore, the timing of the formation of SPA basin gives valuable information on the evolution of the lunar crust. The large scale of the impact led to the hypothesis that it penetrated the crust and potentially exposed lunar mantle material [e.g., 8]. Thus, it might be possible to observe lunar mantle material or lower crustal material excavated by the impact event [e.g., 9]. Recently, the SPA has been the focus of several ongoing and upcoming missions [10-13]. On January 2, 2019, Chang'e 4 made the first soft-landing on the farside of the Moon in Von Kármán crater (175.9° E and 44.8° S) [11]. Sites in SPA are also being examined as possible landing sites for ESA's HERACLES mission study [14-16]. Here, we aim to compile a complete new geological map of the SPA basin in the context of PLANMAP [17]. The first part, the NE section surrounding the Apollo basin, has already been published by [12], and we are using the same units and stratigraphic relations to extend the map to the rest of the basin.

Method: We are using Lunar Reconnaissance Orbiter (LRO) Wide-Angle Camera (WAC) (100 m/pixel), Narrow-Angle Camera (NAC) (0.5m/pixel) [18], and Kaguya (10 m/pixel) data as base imagery to allow geomorphological and albedo contrast mapping, as well as crater size-frequency distribution (CSFD) measurements. We are also applying a hybrid spectral mapping approach, using Clementine [19], M3 [20], and Kaguya MI [21] data to aid in subdividing geological units. Topographic features are identified using Lunar Orbiter Laser Altimeter (LOLA) digital elevation models and the LOLA/Kaguya merged digital elevation model (DEM) that has the resolution of 512 pixel/degree [22].

We use the standards described in [23] for planetary mapping and the nomenclature is consistent with [24], in addition to project specific recommendations for presentation of nonstandard data sets and mapping products [25].

Unit descriptions: We identified different geological units based on their geomorphological, albedo, and spectral appearances. In general, the units can be divided into plains-forming units and craters/crater-related units. The stratigraphic relations of these units are identified and described by [12].

Several types of crater and crater-related units have been described in the SPA [12]. The specific characteristics of individual impact craters, such as the presence or absence of rays, discernible ejecta blankets and chains of secondarys craters, as well as the degree of degradation of the crater rims are used to classify different crater and crater-related units into a relative stratigraphy (***Fig. 1***). The ages of specific marker craters are then used to fix the relative ages to an absolute age scale [e.g., 12].

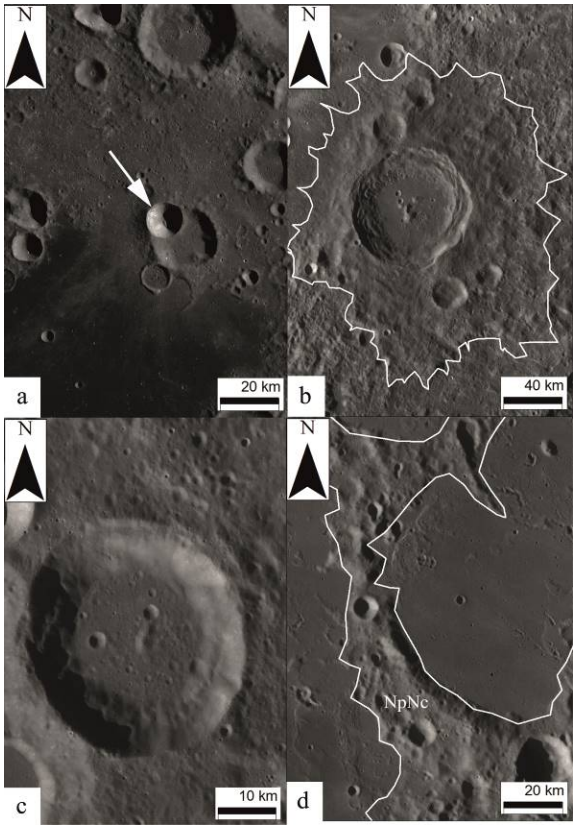

Fig. 1. *Examples of crater and crater-related units. (A) Cc with extensive ejecta and ray system, (B) Ec with prominent ejecta but without rays, (C) sharp-crested cratered unit Ic without discernible ejecta or rays, (D) unit with abundant degraded craters (NpNc).*

Copernican craters (Cc) are the youngest and freshest craters in the study area. They crosscut all other landforms and show extensive ejecta deposits and prominent systems of rays and secondary craters (***Fig. 1a***).

Erathostenian craters (Ec) are characterized by sharp-crested craters with no extensive ray system. They are often small and are numerous throughout the study area (***Fig. 1b***). However, some are larger craters such as Finsen crater (62 km diameter).

Imbrian craters (Ic) show a higher degree of degradion with subdued ejecta that indicates them to be older than Ec and Cc craters (***Fig. 1c***).

Nectarian, pre-Nectarian craters (NpNc) is a unit typically made of large, degraded craters that show mostly complete rims, rarely with visible ejecta deposits. The craters of this unit are abundant and often overlapping (***Fig. 1d***).

The oldest units are associated with the primary features of the SPA basin. These units represent areas of ancient rugged surfaces and consist of chaotically oriented short ridges and equidimensional blocks of several kilometers across. Both the ridges and blocks likely represent remnants of the oldest craters that have been destroyed by the formation of younger craters. According to their locations we divide these pre-Nectarian features into SPA Floor (pNm_SPAf) and rim material (pNm_SPAr). Whithin the SPA rim, materials of the unit pNm_SPAr surround the high-standing massifs of the basin rim (pNrm_SPA) (***Fig. 2***).

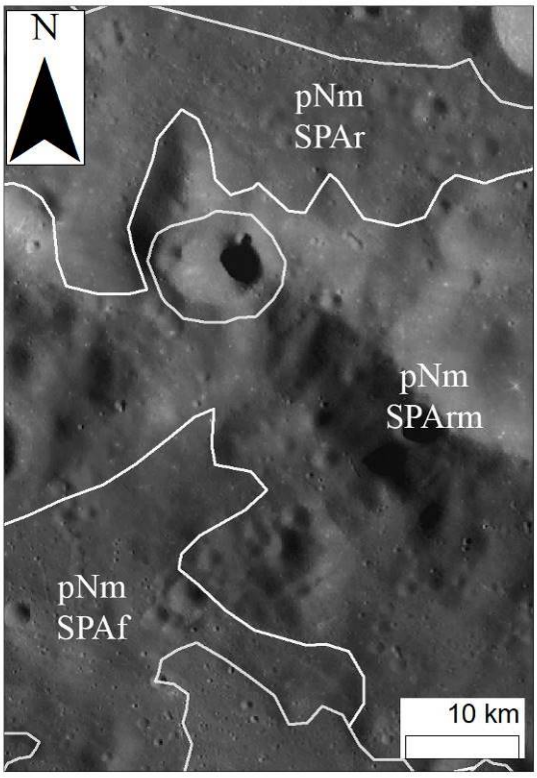

Fig. 2. *Examples of the oldest morphological units (pNmSPAr rim massif, pNmSPArm rim material, and pNmSPAf floor material) associated with the SPA rim.*

Within the study area three types of plains-forming units can be identified (***Fig. 3***). These units are set apart by their different albedos and morphological surface structures.

Upper Imbrian dark plains (UIdp) are identified by the noticeablely lower albedo compared to the surrounding terrains. The low albedo is often overprinted by higher albedo swirls, such as seen in Mare Ingenii. UIdp shows smooth surfaces and is predominantly found as filling in larger craters (***Fig. 3a***).

Imbrian light plains (Ilp) are similar in morphological appearance to UIdp, but differ in albedo. Ilp appear to have the same albedo as the adjacent crater-related landforms (***Fig 3b***). The light plains are scattered throughout the map area.

Lower Imbrian rugged terrain (LIrp) shows a rugged morphology due to numerous low, curvilinear ridges. LIrp appear as larger continuous plains especially towards the center of SPA.

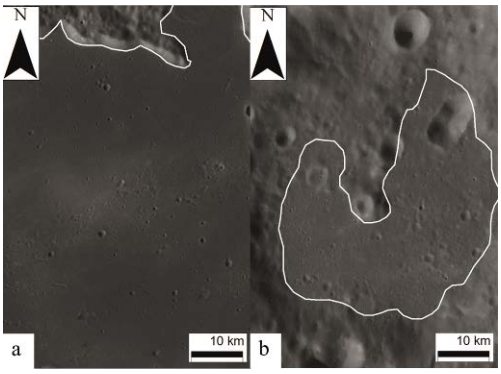

Fig. 3. *Examples of plains-forming units. (A) UIdp represents low albedo mare units. (B) Ilp is similar in appearance to UIlp but shows higher albedo*

Acknowledgements: This work receives funding from the European Union Horizon 2020 research and innovation programme under grant agreement No 776276.

References: [1] Stuart-Alexander (1978) USGS Map I-1047, 1978. [2] Spudis et al. (1994) Science 266, 1835-1839. [3] Hiesinger and Head (2004) PLPSC 35, 1164. [4] Shevchenko et al. (2007) Solar Sys. Res. 41, 447-462. [5] Garrick-Bethell and Zuber (2009) Icarus 204, 399-408. [6] Wilhelms (1987) USGS SP-1348, 302. [7] Hiesinger et al. (2012) LPSC 43, 2863. [8] Melosh et al. (2017) Geology 45, 1063-1066. [9] Yamamoto et al. (2010) Nature Geoscience 3, 533-536. [10] Hiesinger et al. (2018) LPSC 49, 2070. [11] Huang et al. (2018) JGR 123, 1684-1700. [12] Ivanov et al. (2018) JGR 123, 2585–2612. [13] Joliff et al. (2010) LPI Cont 1595, 3072. [14] Steenstra et al. (2016) Adv Space Res 58, 1050-1065. [15] Allender et al. (2018) Adv Space Res 63, 692-727. [16] Hiesinger et al. (2019) LPSC 50, 1328. [17] Poehler et al. (2019) LPSC 50, 2910. [18] Robinson et al. (2010) Space Sci. Rev 150, 81-124. [19] Pieters et al. (1994) Science 266, 1844-11848. [20] Isaacson et al. (2013) JGR 118, 369-381. [21] Ohtake et al (2013) Icarus 226, 364-374. [22] Barker et al. (2016) Icarus 273, 346-355. [23] FGDC (2006) FGDC-STD-013-2016. [24] Blue, J. (1999) Gazette. Planet. Nomen. USGS. [25] wiki.planmap.eu/display/public/D2.1-public

DUST STUDY, TRANSPORT, AND ELECTROSTATIC REMOVAL FOR EXPLORATION MISSIONS: THE DUSTER PROJECT. S. Ranvier[1], S. Hess[2], J.C. Matéo Vélez[2], J. Rodríguez Gómez[3], A. Alvaro Sanchez[4], and J. De Keyser[1], [1] Royal Belgian Institute for Space Aeronomy, Ringlaan 3, 1180 Brussels, Belgium (sylvain.ranvier@aeronomie.be), [2] Office National d'Etudes et de Recherches Aérospatiales, Département Physique Instrumentation Environnement Espace, Av. E. Belin, 31400 Toulouse, France, [3] Instituto de Astrofísica de Andalucia, Instrumental and Technological Development Unit, Glorieta de la Astronomía, 18008 Granada, Spain, [4] Thales Alenia Space Espana, Calle de Einstein 7, Tres Cantos, Madrid, Spain.

Introduction: One major environmental constraint during exploration missions is the presence of charged dust-like particles, which are present on the Moon, Mars, comets and asteroids. From an analysis of the effects of lunar dust on Extra-Vehicular Activity (EVA) systems during the six Apollo missions that landed on the lunar surface [1], it was found that these effects can take many forms such as external vision obscuration, false instrument readings, dust coating and contamination, loss of traction, clogging of mechanisms, abrasion, thermal control problems and seal failures. One of the most serious effects is the compromising of astronaut health by irritation and inhalation of lunar dust. The Apollo crews reported that the dust gave off a distinctive, pungent odour, (David Scott suggested it smelled a bit like gun powder) suggesting that reactive volatiles reside on the surface of the dust particles. Dust exposure and inhalation could have a range of toxic effects on human lunar explorers, especially if longer exposure times become the norm during future manned exploration missions [2].

Therefore, it is of utmost importance to characterise the properties of the dust particles present on the exploration sites and their transportation mechanisms to enable efficient mitigation techniques to be put in place. Several dust mitigation techniques have been studied and developed to, for instance, clean up dust-contaminated equipment [3, 4, 5], prevent the dust particles to fall and stick on optics [6] and to clean the air inside exploration shelters [7]. Nevertheless, to be effective all these mitigation techniques must be thoroughly analysed and validated by in situ measurements.

The DUSTER project: The overall objective of the DUSTER project is to develop instrumentation and technologies to study dust particles and electrostatic transportation for planetary and small body exploration missions. Specifically, the aim is to design, manufacture and test in a relevant environment a compact multi-sensor instrument for in situ analysis of dust properties (mechanical and electrical) and electrostatic transportation that can be used on a small lunar lander. To that end, the instrument includes:

- A dust collector: electrodes biased at high potential (a few kV) to attract/collect dust particles, coupled to an electrometer
- Langmuir probes
- E-field probes

Using this instrument the following parameters will be derived:

- Charging level of dust as a function of the environmental parameters (illumination, plasma density and temperature)
- (gravity + cohesive forces)/charge ratio distribution of dust layer

These two parameters will allow the determination of the electric field needed to attract/collect dust according to the environmental conditions (illumination, plasma density and temperature), which, among other applications, will allow designing electrostatic dust mitigation devices and dust sample collectors.

Principle: When charged dust particles are placed between two electrodes and a voltage is applied between these two electrodes, this creates an E-field that applies a force on the charged particles. When the voltage is high enough, the charged particles will move towards one of the electrodes (depending if the particles are positively or negatively charged) and ultimately will impact the electrode. By measuring the current resulting from the impact of the charged dust particles onto the electrodes, one can quantify the amount of charged dust that has been moved (when the gravitational acceleration is known, and assuming a relation between dust size and charge).

Furthermore, by gradually (step wise) increasing the potential between the electrodes, given some assumptions, the mass distribution can be inferred. The principle is pictured in Figure 1. This measurement principle is comparable to the Langmuir probe principle [8], where a probe placed in a plasma is biased to a positive or negative potential with respect to that plasma and attracts electrons and positive ions, respectively.

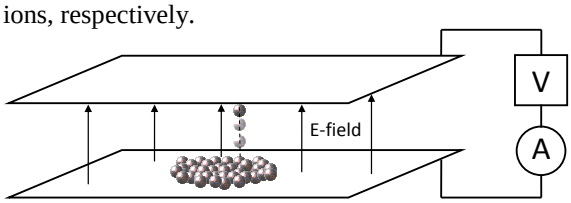

Figure 1. Measurement principle.

Physical parameters: For a layer of dust particles with given properties, the transport of those par-

ticles depends on several environmental parameters, namely:

- the level of charging (which depends on UV and soft X-ray fluxes)
- the gravity field
- the applied E-field
- the ambient plasma parameters (electron density and temperature)

The charge distribution as a function of depth is unknown for a soil composed of dust particles such as the lunar regolith, as no model of the charging of a granular material under space conditions has ever been published. It is assumed that the charge is carried by the uppermost layer of dust particles [9].

Using the Gauss theorem, the charging at the surface of the dust layer can be described as follows:

$$Q_{surf} = \varepsilon_0 \varepsilon_r E_{ext} A_{surf} \quad \text{(eq. 1)}$$

where ε_0 and ε_r are the permittivity of free space and relative permittivity, respectively, E_{ext} is the external E-field above the surface of the dust layer and A_{surf} is the area of interest. Thus, by measuring the electric field above the surface of the dust layer, the mean charging over the area of interest can be derived.

Measurements: The UV and soft X-ray fluxes and the surface gravity can be obtained by existing measurement data or reliable modelling. The E-field will be known accurately because it is applied by the instrument itself. Therefore, the remaining parameters that are needed to quantify dust charging and transportation are:

1) Charging level
2) Ambient plasma density and temperature
3) Current resulting from the impact of the dust particles onto the electrodes

The charging level of dust will be assessed by measuring the electric field above the dust layer with E-Field probes.

The solar illumination dependence of the charging properties of the dust will be studied by (a) performing potential measurements as function of solar zenith angle, and (b) performing potential measurements across the light/shadow terminator.

The ambient plasma parameters (electron density and temperature) will be measured with the Langmuir probe.

The current resulting from the impact of the dust particles onto the electrodes will be measured by the dedicated front end that will apply a given bias voltage (up to several kV) to the dust electrodes and measure the resulting current.

Laboratory test and validation: The E-field that is needed to move the charged grains, the current resulting from the impact of the charged grains onto the dust electrodes and the electric field at the surface of the dust layer will be measured in an existing dedicated measurement facility, the vacuum chamber called “dust regolith or particles” (DROP). This facility is a cylindrical tank of dimension 40 × 40 cm covered with a hemispherical cap. A pressure of 10^{-6} mbars is obtained with a cryogenic pump. The chamber is equipped with a Vacuum Ultraviolet (VUV) deuterium lamp emitting two intense spectral lines at 120 and 160 nm and a low continuum flux between 112 and 370 nm. The illuminated zone is a circle of 10 cm.

DROP, which has already been used at ONERA to study dust charging and transportation, will be upgraded to allow measuring the current resulting from the impact of the charged grains onto the dust electrodes. This current, which is a proxy for dust transportation, will be compared to the output of the existing optical detection method [10] (both detection methods will be used simultaneously). The optical detection method developed by ONERA uses images from a CCD camera with a resolution of 50 µm to analyse the amount of contamination on a surface. As an example of possible setup configuration for DUSTER, the experimental setup used previously at ONERA to characterise dust charging and transportation is shown together with the expected relative charging of surface, orientation of the electric field E, and particle trajectories (electrons and dusts) in Figure 2.

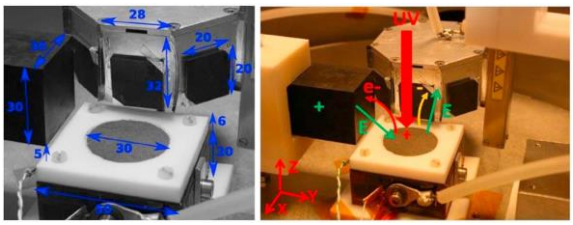

Figure 2. (left) Experimental apparatus dimensions (in mm). (right) Expected relative charging of surface, orientation of the electric field E, and particle trajectories (electrons and dusts).

References: [1] Gaier, J. R. (2007), Tech. Rep., NASA/TM-2005-213610/REV1, E-15071-1/REV1,. [2] Linnarsson D. et al. (2012), , Planet. and Space Sc., Vol. 74, 1, 57-71. [3] Biris A.S. et al. (2004), IEEE Ind. Appl. Soc. 39th IAS Annual Meeting, 1283-1286. [4] Calle , C. et al. (2006), 57th IAC. [5] Clark, P. et al. (2007), Proc. Space Tech. Appl. International Forum-STAIF, 400-406. [6] Afshar-Mohajer et al., (2011), AIAA 41st Int. Conf. Env. Sys. [7] Phillips, J.R. et al. (2016), Earth Space Conf. [8] Brace, L. H., (1998). Geophysic Monograph Series, American Geophysical Union, 102, 23–35. [9] Hess, S., et al., (2015), IEEE Trans. Plasma Science, Vol. 43 , 9, 2799 – 2807. [10] Champlain, A. et al.(2016), J. Geophys. Res. Space Physics, 121, 103–116.

THERMOGRAVIMETRIC ANALYSIS OF CHEMICAL REDUCTION PROCESSES FOR THE IN-SITU PRODUCTION OF OXYGEN FROM LUNAR REGOLITH. P. Reiss[1], F. Kerscher[2], and L. Grill[1], [1]Technical University of Munich, Institute of Astronautics, Boltzmannstr. 15, 85748 Garching, Germany (p.reiss@tum.de), [2]Technical University of Munich, Institute for Energy Systems, Boltzmannstr. 15, 85748 Garching, Germany.

Introduction: A variety of processes for producing oxygen from lunar regolith as part of In-Situ Resource Utilisation (ISRU) is known to date, most of which are derived from large-scale terrestrial applications of the metal processing industry. Taylor and Carrier [1] have identified over 20 relevant processes that are either based on solid-gas interaction, silicate-oxide melt, pyrolysis, or aqueous solutions. Schwandt et al. [2] more recently evaluated some of these methods and added the electro-chemical reduction of lunar regolith based on the FFC process [3,4].

The majority of past studies on oxygen production from lunar regolith has been focusing on the chemical reduction of regolith using hydrogen as a reactant gas (e.g. $FeTiO_3 + H_2 = Fe + TiO_2 + H_2O$). This is mainly because of the relatively simple process design, moderate temperature requirement, and high achievable hydrogen recycling rates. Moreover, the chemical reduction produces water, which could also directly be used instead of splitting it into oxygen and hydrogen via electrolysis. Instead of hydrogen as a reactant, carbon monoxide may be used in a comparable process to produce carbon dioxide, which then must be split into carbon monoxide and oxygen in a second step. Another process that has often been discussed for producing oxygen from lunar regolith is the chemical reduction with methane (e.g. $FeTiO_3 + CH_4 = Fe + TiO_2 + CO + 2H_2$). This process is expected to be more flexible on feedstock, but requires substantially higher temperatures and an additional reaction step. Here, the reduction of lunar regolith yields carbon monoxide, which then needs to be hydrogenated through the Sabatier reaction to produce water, and split to hydrogen and oxygen via electrolysis.

In the past, the aforementioned reduction processes have been studied theoretically and experimentally on different scales, with different sample materials, and under different process conditions. Although they have different characteristics and requirements, it is not entirely understood to what extent reactant gases could potentially be replaced with each other in an ISRU reactor and what the implications in terms of oxygen yield, reaction rates, and by-products are depending on the feedstock.

For an ISRU reactor it is advantageous to avoid temperatures in the melting range of lunar regolith, above 1100 °C [5]. It is questionable if and how well the reduction with methane works below this temperature, because earlier studies primarily investigated this process with melted regolith at around 1600 °C [6].

Because future resource prospecting missions will land in polar regions of the Moon, the applicability of potential ISRU processes to the highland type regolith needs to be understood. Earlier studies focused primarily on the processing of mare type regolith or selected lunar minerals.

To support the evaluation and selection of ISRU processes on a common basis we present a direct comparison of the reduction of ilmenite and NU-LHT-2M with hydrogen and methane up to a temperature of 1000 °C by means of thermogravimetric analysis (TGA).

Materials and methods: The investigated samples were 93-96 % pure ilmenite ($FeTiO_3$) as a reference with good susceptibility to reduction, and the lunar regolith simulant NU-LHT-2M as a chemical analogue for (polar) highland regolith. They were sieved to a 100-125 µm size fraction to make sure that the ilmenite particles in NU-LHT-2M are included in the sample (due to the production process of the simulant, ilmenite is only represented in the 75-150 µm particle size fraction [7]). The apparatus used for thermogravimetric analysis was a Linseis STA PT 1750. Samples with a mass of 70-80 mg were heated in a flow of nitrogen, hydrogen, or methane at 200 ml/min with a heating rate of 6 °C/min from room temperature to 1000 °C.

Results with hydrogen: The ilmenite sample showed a significant weight loss of 12.7 % between 500 °C and 850 °C due to the reduction with hydrogen, slightly larger than the the stoichiometrically expected weight loss of 10.5 %. An ilmenite sample that was baked out under nitrogen beforehand yielded a similar weight loss of 12.6 %.

For the NU-LHT-2M sample a weight loss of 0.7 % was measured between 550 °C and 700 °C. Another NU-LHT-2M sample that was baked out under nitrogen beforehand yielded a weight loss of only 0.2 % between 650 °C and 700 °C. This corresponds well with the expected stoichiometric weight loss for an ilmenite content of 1.5 % [7]. The higher weight loss measured for the first NU-LHT-2M sample is caused by additional thermal decomposition products, such as water, carbon monoxide, and carbon dioxide, as identified via evolved gas analysis by Reiss et al. [8]. Potential side reactions with these products complicate the interpretation of the weight change measured via TGA because they are on the same order as the expected weight loss due to reduction of the ilmenite content. It is therefore recommended to bake out NU-LHT-2M before using it for ISRU preparation

studies. An additional observation was that the NU-LHT-2M treated with hydrogen noticeably changed its visual appearance from white or bright grey to dark grey (Figure 1). This most likely is because of a chemical alteration of plagioclase, which makes up ~60 % of the sample.

Results with methane: In order to serve as a reactant, methane needs to be decomposed into hydrogen and carbon. Methane pyrolysis starts at temperatures as low as 700 °C to 800 °C [9]. While hydrogen can readily react with the sample, the solid carbon deposits on the sample and enables the reduction at higher temperatures. Correspondingly, the TGA shows two subsequent weight losses for the ilmenite sample, 1.5 % between 550 °C and 900 °C and 5.5 % between 900 °C and 915 °C. A sample that was baked out under nitrogen beforehand shows a similar weight loss of 1.8 % between 700 °C and 910 °C and 6.5 % between 910 °C and 940 °C. At temperatures above 915 °C and 940 °C respectively there is strong deposition of carbon, which overlays further weight loss through reduction (Figure 2).

The NU-LHT-2M sample did not exhibit a significant weight change under methane besides the expected weight loss due to thermal decomposition of the minerals and the strong weight increase due to carbon deposition above 900 °C. Again the potential side reactions with hydrogen pyrolysis products complicate a clear identification of the reduction processes of the sample in the TGA signal.

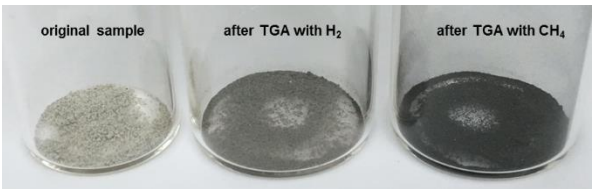

Fig. 1: NU-LHT-2M (100-125 µm sieved size fraction) before and after heating to 1000 °C in the presence of hydrogen and methane

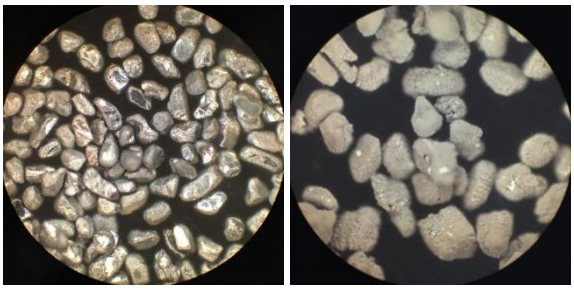

Fig. 1: Ilmenite (100-125 µm sieved size fraction) before (left) and after (right) heating to 1000 °C in the presence of methane, showing strong deposition of carbon on the particles

Conclusion: The results of the thermogravimetric analysis provide the following findings:

- Ilmenite and NU-LHT-2M were reduced with both hydrogen and methane below 1000 °C.
- Methane decomposition enables the reduction of ilmenite with hydrogen and carbon.
- Carbon deposition occurs above 900 °C and leads to significant contamination and corresponding weight increase.
- NU-LHT-2M noticeably changes its appearance after thermal treatment with hydrogen

References: [1] Taylor L. and Carrier W. (1993) *Resources of near-Earth space*, p. 69-108. [2] Schwandt C. et al (2012) *Planetary and Space Science* 74 (1): 49-56. [3] Chen et al (2000) *Nature* 407 (6802): 361-364. [4] Oosthuizen (2011) *Journal of the Southern African Institute of Mining and Metallurgy*, 111 (3): 199-202. [5] Colozza (1991) NASA Contractor Report 189073. [6] Rosenberg et al. (1966) *Aerospace Chemical Engineering*, 62(61), 228-234. [7] Rickman and Lowers (2012) NASA/TM-2012-217458. [8] Reiss et al. (2019), *Planetary and Space Science*, doi: 10.1016/j.pss.2019.05.001. [9] Chen et al. (1975) *Canadian Journal of Chemistry*, 53(23), 3580-3590.

EXPERIMENTAL DEVELOPMENT AND TESTING OF THE REDUCTION OF ILMENITE FOR A LUNAR ISRU DEMONSTRATION WITH PROSPA. H. M. Sargeant[1], F. Abernethy[1], M. Anand[1,2], S. J. Barber[1], S. Sheridan[1], I. Wright[1] and A. Morse[1]. [1]School of Physical Sciences, The Open University, Walton Hall, Milton Keynes, UK. [2]The Natural History Museum, London, UK. Email: hannah.sargeant@open.ac.uk

Introduction: In Situ Resource Utilization (ISRU) is the exploitation of the natural resources of a Solar System object beyond Earth (by robotic or human-mediated space missions). Future crewed missions to the Moon and beyond will require significant supplies of water and its constituents (hydrogen and oxygen) [1]. Therefore, ISRU can potentially reduce the costs of such missions.

There is direct and indirect evidence of deposits of frozen water in the lunar polar regions [2, 3]. However, the extreme environmental conditions at these locations pose a number of technological challenges for accessing and harvesting the water/oxygen. Instead, water/oxygen can be harvested at more accessible locations through reduction reactions on lunar minerals.

The PROSPECT payload, which is currently being developed by ESA for the Luna-27 mission, is intended for sampling the lunar regolith using a drill and subsequent analysis for volatiles by the ProSPA module [4]. It also aims to perform a proof-of-principle ISRU demonstration. ProSPA is being developed at The Open University and the present work considers the development of a breadboard model to test hydrogen reduction of the mineral ilmenite as a technique to produce water. The results of recent studies considering reaction temperatures and hydrogen concentrations are presented.

Ilmenite Reduction: Ilmenite is a common lunar mineral comprised of iron, titanium, and oxygen. When heated in the presence of hydrogen, water is produced in the equilibrium reaction as follows:

$$FeTiO_3 + H_2 \leftrightarrow Fe + TiO_2 + H_2O \qquad (1)$$

Ilmenite reduction has long been considered for lunar water production. The temperatures required are relatively low (700-1000 °C) [5] and there is the possibility of obtaining hydrogen feedstock from solar wind implantation into the lunar regolith. It is therefore planned to perform an in situ demonstration of this concept with ProSPA.

Generally, ilmenite reduction concepts include a dynamic, flowing gas system to enable the transport of the reactant and product gases [6]. Without the removal of water from the reaction site, the reaction will stall as equilibrium is reached. As ProSPA is a static system, other methods are required to transport water away from the ilmenite grains. A cold finger is utilized which condenses water and enables the reaction to proceed towards the further production of water [7].

The reduction of ilmenite in a static system was successfully performed using a benchtop demonstration model (BDM) of the ProSPA design [8]. A second iteration breadboard model was designed and built to perform further ilmenite reduction tests (ISRU-BDM). The new design allows improved quantification of the products through optimized thermal control.

System Development: The ISRU-BDM contains most components within a heated oven which operates at a temperature of ~120 °C. The hydrogen supply and mass spectrometer are located outside the oven (Fig. 1). A furnace that can reach >1100 °C heats a ceramic sample holder of 4 mm internal diameter (i.d.). The cold finger is thermally controlled with a chilled nitrogen gas supply and embedded heaters. This enables the cold finger to operate at -80 and +120 °C for condensing and releasing water.

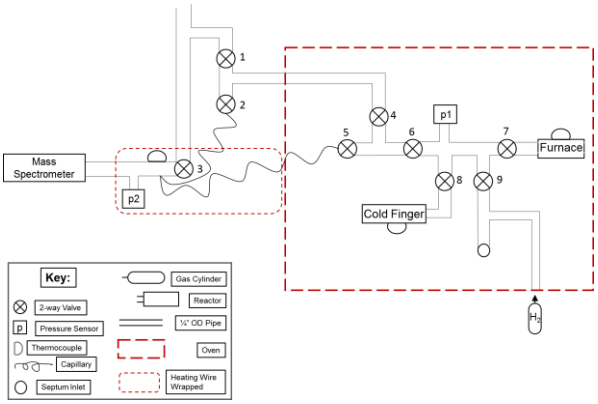

Fig. 1 ISRU-BDM schematic

The system was built with off-the-shelf parts and a series of calibration tests was performed. The successful trapping and release of water up to 5 µl demonstrates the system capability to trap and quantify the water produced from the reduction of >45 mg ilmenite.

Experimental Procedure: Experiments targeted two variables in the ilmenite reduction reaction: reaction temperature and hydrogen concentration. For both studies, 45 mg (0.3 mmol) of ilmenite (purity 95%; average grain diameter of 170 µm) was baked out to 500 °C for 1 hr [8]. Then hydrogen was added to the system. For the temperature studies 0.3 mmol of hydrogen was used for each experiment so that there is a just enough to reduce the whole ilmenite sample. For the hydrogen concentration studies the hydrogen: ilmenite ratio was varied as ~0.25:1, up to ~1:1. Next, the furnace was heated to the desired temperature. For the temperature studies, the reaction temperature was varied from 850 to 1050 °C. The optimal temperature of 1000 °C was used for the

hydrogen studies. The reaction was left to proceed for 4 hrs and the produced water was condensed at the cold finger operated at -80 °C. As each molecule of hydrogen converts to a single molecule of water, and the water then condenses, the pressure drops according to the amount of hydrogen reacted and therefore water produced. This pressure drop can be used to infer the quantity of water produced using the ideal gas equation. Finally, the cold finger was heated to 120 °C and water was released as vapour, where the pressure rise also indicates the amount of water produced. Pressure readings were recorded during each experiment to monitor the reaction and its products.

Results: *Temperature Studies:* The reaction rate is quicker at higher temperatures. However, after ~130 mins the 1050 °C reaction results in a slowing of the reaction rate. This is likely because 1050 °C is the melting point of ilmenite and the changing morphology of the outer grain results in the reaction slowing down. When the furnace is operating at 1000 °C (optimal reaction temperature for reaction times of 4 hrs), oxygen yields of ~3.4 wt.% are recorded after 4 hrs. However, the reaction is still only ~33% complete in this 4 hr time-frame, as calculated by the amount of water produced compared to what is expected (Fig. 2). A water production rate of ~0.43 µl/hr was estimated for a reaction temperature of 1000 °C.

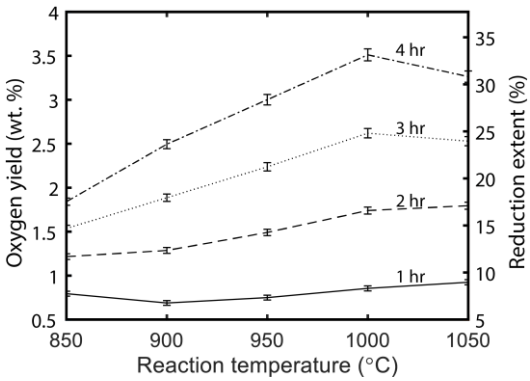

Fig. 2 Yield and reduction extent as calculated from pressure changes during the ilmenite reduction reaction for varying reaction temperatures.

Hydrogen Concentration Studies: With less hydrogen in the system, the initial reaction rate is increased as the water produced easily diffuses away from the reaction site and the reaction continues. However, as the reaction progresses, the reaction rate slows down. In the first hour, the best yields are achieved with a ratio of 0.25:1 of hydrogen to ilmenite with the fastest water production rate of ~0.50 µl/hr. However, in this static mode setup after 4 hrs the best yields are still achieved with 1:1 ratio of hydrogen to ilmenite (Fig. 3).

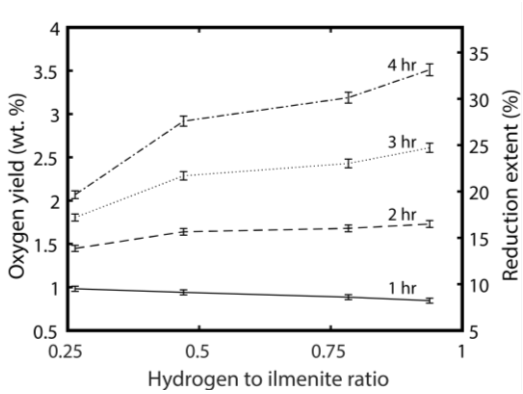

Fig. 3 Yield and reduction extent as calculated from pressure changes during the ilmenite reduction reaction for varying hydrogen concentrations.

A 'batch mode' study will follow where small amounts of hydrogen are let into the system at regular time intervals during the reaction to achieve the increased reaction rate when less hydrogen is present, but ensuring enough hydrogen is supplied to the ilmenite to allow complete reaction. This is a compromise between a static and flowing system that should be capable on the ProSPA setup.

Conclusions and Future Work: A static system can successfully produce water/oxygen from ilmenite. Using current operating conditions, the optimal reaction temperature is 1000 °C and the initial reaction rate can be increased with lower hydrogen pressures. A reaction time of >4 hrs is required for completion. A batch mode approach is proposed in order to optimize hydrogen pressure during the reaction to improve reaction times. Although a static system is not optimized for an ISRU reaction, it is a simple technique that can be used to perform a proof-of-principle reduction reaction of lunar ilmenite in situ. Future work will consider experiments involving lunar rocks and soils.

Acknowledgments: The funding by STFC of a studentship for H.S. is acknowledged. PROSPECT is a programme of and funded by the European Space Agency (ESA).

References: [1] Anand M. et al. (2012) *PSS, 74,* 42-48. [2] Fisher E. A. et al. (2017) *Icarus, 292*, 74-18. [3] Li S. et al. (2018) *PNAS*, *115*, 8907–8912. [4] Barber et al. (2018) *LPSC XLIX*, #2172. [5] Taylor L. and Carrier W. (1993) *Resources in Near Earth Space*, 69-108. [6] Schrunk D. et al. (2007) Appendix E of The Moon: Resources, future development, and settlement. [7] Williams R. J. and Mullins O. (1983) *LPSC XIV*, Special Session Abstracts 34-35. [8] Sargeant H. M. et al. *PSS* (submitted).

MIMOS II – AN OFF-THE-SHELF MINIATURIZED MÖSSBAUER SPECTROMETER FOR IN SITU LUNAR EXPLORATION AND ISRU. C. Schröder[1], G. Klingelhöfer[2,†], B. Bernhardt[3], M. Blumers[4], H. Gaber[2], R. Gellert[5], R. V. Morris[6], and F. Renz[7], [1]Biological and Environmental Sciences, University of Stirling, Stirling FK9 4LA, UK, christian.schroeder@stir.ac.uk, [2]Johannes Gutenberg-Universität, Mainz, Germany, [3]von Hoerner and Sulger GmbH, Germany, [4]Universitätsklinikum Bonn, Germany, [5]University of Guelph, Canada, [6]NASA-JSC, Houston, TX, USA, [7]Leibniz Universität Hannover, Germany, [†]deceased.

Introduction: The miniaturized Mössbauer spectrometer MIMOS II [1] is an off-the-shelf instrument with proven flight heritage. It worked successfully during NASA's Mars Exploration Rover (MER) mission [e.g. 2-5] and was on-board the UK-led Beagle 2 [6] and the Russian Phobos-Grunt missions [7]. There is a long history of investigations of lunar material returned e.g. by the Apollo missions using Mössbauer spectroscopy [e.g. 8-10].

Instrument Description: MIMOS II [1] consists of a sensor head (Fig. 1) and an electronics board. The sensor head can be mounted on e.g. a robotic arm (see Fig. 2 for a MER instrument) and needs to be brought in physical contact with the sample to be analyzed. Otherwise, no sample preparation is necessary. The sensor head carries the radiation source (^{57}Co, halflife 272 days) and detector system, and has a volume of 50×50×90 mm³. The electronics board holds data acquisition and instrument control units (CPU + FPGA), voltage converters, and electrical and data interfaces to the spacecraft. It is 100×160×25 mm³. The whole system including connecting cables weighs <500 g. Power consumption is 4W during data acquisition, and power can be switched off when the instrument is not in operation. The data product size per analysis is 512 kBytes (4 Mbit).

Adaptation to Lunar Operations: MIMOS II has demonstrated its reliability in the Martian environment (TRL 9) and can be easily adapted to the lunar environment. In contrast to the cold temperatures on Mars, solar radiation in the low pressure environment on the lunar surface poses the risk that the instrumentation is heated to high temperatures during the lunar daytime. To maintain detector performance, MIMOS II needs to be shielded so that temperatures do not overrun room temperature. Such shielding was analyzed and partially tested in the frame of a potential landing on Mercury (early BepiColombo mission scenario).

In Situ Lunar Exploration: Mössbauer spectroscopy determines iron-bearing mineral phases (e.g., silicates, oxides, and sulfides) and iron oxidation states, and determines the quantitative distribution of iron between mineral phases and oxidation states. It also yields insights into electromagnetic properties.

No sample preparation is necessary for a measurement with MIMOS II. Importantly, the instrument can "see through" more than a millimetre of basaltic dust and obtain information on the solid substrate beneath. Depth-selective information can be obtained by recording spectra at different radiation energies (6.4 keV and 14.4 keV) [11].

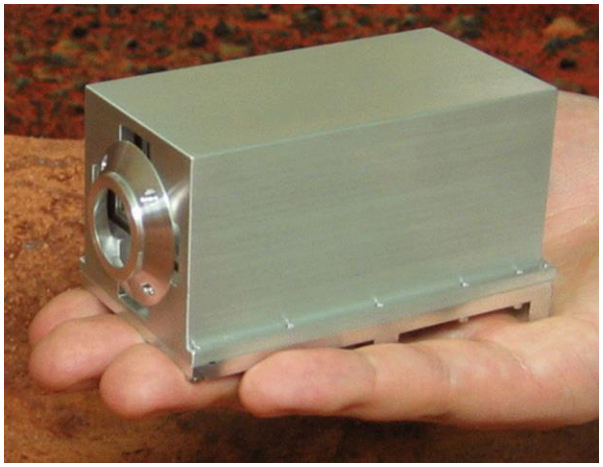

Fig. 1. The MIMOS II sensorhead. Credit: University of Mainz.

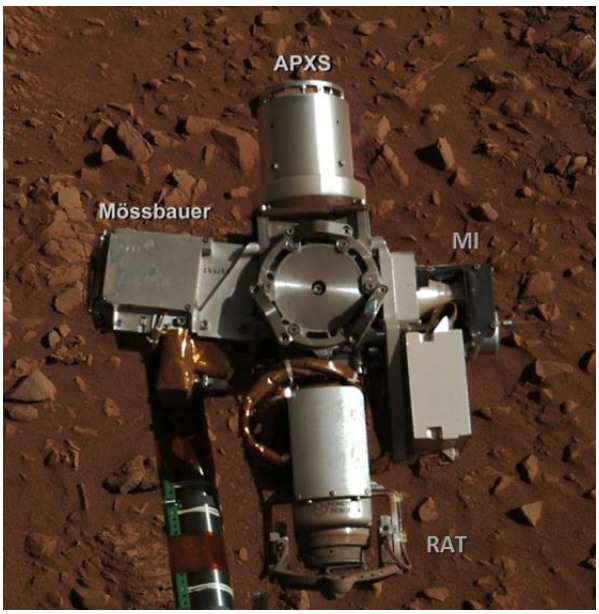

Fig. 2. A MIMOS II sensorhead (Mössbauer) mounted on Mars Exploration Rover Spirit's robotic arm, together with the Alpha Particle X-ray Spetrometer (APXS), the Microscopic Imager (MI), and the Rock Abrasion Tool (RAT). Credit: NASA/JPL/Cornell.

The information provided by MIMOS II allows to differentiate between the major constituents of the

lunar surface - i.e. maria, highlands or KREEP material – and to distinguishit between volcanic-ash regolith and impact-derived regolith [8]. The lunar South Pole has not been visited by landers yet. Given the size of the South Pole Aitken Basin and the depth from where material was excavated during the crater-forimg impact, new types of regolith have to be anticipated.

Micrometeoroid impacts as a form of space weathering reduces iron in the regolith. The metallic iron, Fe(0), content of surface fines is a measure of maturity, i.e. surface exposure time of regolith [8]. Measurement of the Fe(0) content of freshly exposed fines at the beginning of a lander mission and comparing it to subsequent measurements can help to constrain micrometeoroid flux at the landing site.

To understand the possible electrostatic mobilization of lunar dust, it is important to know the dielectric properties of its mineral constituents, for example by determining the abundance of insulating glass versus conductive iron metal.

In Situ Resource Utilisation: Oxygen can be extracted from lunar regolith, whereby the yield is directly proportional to the ferrous iron or FeO content [12,13]. FeO is reduced by hydrogen to form iron metal and water. The hydrogen source may be residual hydrogen in the tanks of a lunar lander. The water can be split electrochemically into oxygen and hydrogen. While the oxygen is consumed, the hydrogen is fed back into the reaction. Several such hardware concepts were evaluated during three field tests on Mauna Kea, Hawaii, in 2008 [14] and 2010 [15,16] and 2012 [17]. MIMOS II worked successfully as both a process monitor and a prospecting tool. As process monitor, iron oxidation states were determined before and after reductive treatment, and oxygen yield was calculated. As prospecting tool MIMOS II was mounted on a feedstock collecting rover. Feedstock would be selected for high FeO content and analysed for mineral content. The latter determines the optimum temperature during reduction: Ilmenite is reduced at 900°C, olivine at 1000°C and all other FeO-bearing phases at 1100°C.

In Memoriam: Göstar Klingelhöfer died unexpectedly in January 2019. Without him, this instrument would not exist. We would like to acknowledge his outstanding contributions to its development, to planetary science, and to our personal lives.

References: [1] Klingelhöfer G. et al. (2003) *J. Geophys. Res.* 108(E12), 8067. [2] Morris R.V. et al. (2004) *Science* 305, 833. [3] Klingelhöfer G. et al. (2004) *Science* 306, 1740. [4] Morris R.V. et al. (2010) *Science* 329, 421. [5] Morris R.V. et al. (2019) In *Remote Compositional Analysis: Techniques for Understanding Spectroscopy, Mineralogy, and Geochemistry of Planetary Surfaces*, ed. By Bishop J.L. et al., Cambridge University Press, in press. [6] Pullan D. et al. (2003) ESA SP-1240. [7] Rodionov D. et al. (2010) *Solar System Research*, 44, 362-370. [8] Morris R.V. et al. (1998) *Hyperfine Interact.* 117, 405-432. [9] Hafner S.S. (1975) In *Mössbauer Spectroscopy*, ed. by Gonser U., Springer. [10] Khasanov A.M. et al. (2001) *Mössbauer Effect Reference and Data Journal* 24(6), 195-199. [11] Fleischer I. et al. (2008) *J. Geophys. Res.* 113, E06S21. [12] Allen C.C. et al. (1994) *J. Geophys. Res., 99*(E11), 23173-23185. [13] Allen C.C. et al. (1994) *J. Geophys. Res., 101*(E11), 26085-26095. [14] Schröder C. et al. (2011) *Geochemistry: Exploration, Environment, Analysis, 11*, 129-143. [15] Klingelhöfer G. et al. (2011) *LPS XLII*, Abstract #2810. [16] Ten Kate I. et al. (2013) *Journal of Aerospace Engineering* 26,183-196. [17] Graff T. G. et al. (2013) *LPS XLIV*, Abstract #2974.

MIMOS IIA – ADVANCED MINIATURIZED MÖSSBAUER SPECTROMETER FOR RAPID SPECTRAL ACQUISITION AND WITH POTENTIAL X-RAY FLUORESCENCE CAPABILITY. C. Schröder[1], G. Klingelhöfer[2,†], B. Bernhardt[3], M. Blumers[2], H. Gaber[2], R. Gellert[4], R. V. Morris[5], A. Niculae[6], F. Renz[7], H. Soltau[6], and L. Strüder[6], [1]Biological and Environmental Sciences, University of Stirling, Stirling FK9 4LA, UK, christian.schroeder@stir.ac.uk, [2]Johannes Gutenberg-Universität, Mainz, Germany, [3]von Hoerner and Sulger GmbH, Germany, [4]University of Guelph, Canada, [5]NASA-JSC, Houston, TX, USA, [6]PNSensor GmbH, Germany, [7]Leibniz Universität Hannover, Germany, [†]deceased.

Introduction: MIMOS IIa [1,2] is an advanced version of the miniaturized Mössbauer spectrometer MIMOS II [3,4], which flew successfully with NASA's Mars Exploration Rover (MER) mission [e.g. 5-8], and which was part of the payload of the UK-led Beagle 2 [9] and the Russian Phobos-Grunt missions [10]. A new detector system in MIMOS IIa enables spectral acquisition that is faster by an order of magnitude when compared to MIMOS II.

MIMOS IIa was originally developed for the ESA ExoMars rover [11]. A prototype was used during lunar In Situ Resource Utilization (ISRU) field tests on Mauna Kea, Hawaii in 2010 [12,13] and 2012 [14]. MIMOS IIa has an ESA-assessed Technology Readiness Level (TRL) of 5.

Instrument Description: MIMOS IIa consists of (i) a sensorhead (Fig. 1) carrying Mössbauer drive, detector system and amplifiers, and radiation source, and (ii) an electronics board holding data acquisition and instrument control units (CPU + FPGA), voltage converters, and electrical and data interfaces to the spacecraft. No sample preparation is necessary. The instrument needs to brought in contact with the material to be analyzed.

Dimensions, mass, power consumption, data rate. The sensorhead volume is 50 × 50 × 90 mm³, the electronics board is 100 × 160 × 25 mm³. The whole system < 500 g. Power consumption is 4 W during data acquisition and can be turned off if the instrument is not in use. Data product size per analysis is 512 kBytes (4 Mbit).

Detector system and analysis time. MIMOS IIa uses Si Drift Detectors (SDDs) [15] instead of the Si PIN diodes used in MIMOS II. The high energy resolution of the SDDs (~200 eV vs ~2 keVat 14.4 keV) leads to an improved signal-to-noise ratio which, with the same detector area, reduces the required time for a Mössbauer spectrum by about an order of magnitude. They also open the potential for high resolution X-Ray Fluorescence (XRF) spectroscopy down to ~1 keV, i.e. detection of elements with Z ≥ Na, in parallel to Mössbauer measurements.

Radiation source. Decay of the radioactive isotope ^{57}Co in Rh matrix source provides 14.4 keV γ-rays used for Mössbauer spectroscopy, and 122 keV and 136 keV γ-rays as well as 6.4 keV Fe and 20.1 keV Rh K_α X-rays as excitation source for XRF spextroscopy. Compared to X-ray tubes used in commercial handheld XRF spectrometers, the radioactive isotope has the advantage of zero power consumption.

Fig. 1. MIMOS IIa Sensorhead with eight redundant SDDs (outer cover, amplifier electronics and detector windows opened).

Tab. 1. MIMOS IIa Specifications at a glance.

Volume	50×50×90 mm³ (sensorhead) 160 ×100×25 mm³ (control electr.)
Mass	350 g (sensorhead) 120 g (control electronics)
Power	4 W
Temperature range	−120 . . . +30C (operational) -150°C…+100°C (non-operating)
Energy resolution	140 eV at Fe-K_α at ≤-20°C
XRF-Energy range	0.8. . . 140 keV at lowest gain with a 5µm Be foil window
Irradiation	^{57}Co, typically 100 mCi
Spot diameter	14 mm
Spectral acquisition time	5. . . 30 min, typically

Potential XRF capability: The assessment of this capability is still in early development. The energy resolution of the SDDs of ~140 eV in principle allows identification of XRF spectral peaks. The ^{57}Co radiation source is not ideal, with higher unavoidable background and no Particle-Induced X-ray Emission (PIXE) excitation. The instrument will not deliver quantitative XRF data in the same quality as a stand-alone Alpha Particle X-Ray Spectrometer (APXS), for example. However, the ability to identify and quantify a select number of elements in parallel to obtaining Mössbauer spectra will be added science value.

In Situ Lunar Exploration: Mössbauer spectroscopy determines iron-bearing mineral phases (e.g., silicates, oxides, and sulfides) and iron oxidation states, and determines the quantitative distribution of iron between mineral phases and oxidation states. It also yields insights into electromagnetic properties.

No sample preparation is necessary for a measurement with MIMOS IIa. Importantly, the instrument can "see through" a thin layer of basaltic dust in Mössbauer mode and obtain information on the solid substrate beneath. Depth-selective information can be obtained by recording spectra at different radiation energies (6.4 keV and 14.4 keV) [15].

The information provided by MIMOS IIa allows to differentiate between the major constituents of the lunar surface - i.e. maria, highlands or KREEP material – and to distinguishit between volcanic-ash regolith and impact-derived regolith [17]. The lunar South Pole has not been visited by landers yet. Given the size of the South Pole Aitken Basin and the depth from where material was excavated during the craterforimg impact, new types of regolith have to be anticipated.

Micrometeoroid impacts as a form of space weathering reduces iron in the regolith. The metallic iron, Fe(0), content of surface fines is a measure of maturity, i.e. surface exposure time of regolith [17]. Measurement of the Fe(0) content of freshly exposed fines at the beginning of a lander mission and comparing it to subsequent measurements can help to constrain micrometeoroid flux at the landing site.

To understand the possible electrostatic mobilization of lunar dust, it is important to know the dielectric properties of its mineral constituents, for example by determining the abundance of insulating glass versus conductive iron metal.

In Situ Resource Utilisation: Oxygen can be extracted from lunar regolith, whereby the yield is directly proportional to the ferrous iron or FeO content [18,19]. FeO is reduced by hydrogen to form iron metal and water. The hydrogen source may be residual hydrogen in the tanks of a lunar lander. The water can be split electrochemically into oxygen and hydrogen. While the oxygen is consumed, the hydrogen is fed back into the reaction. Several such hardware concepts were evaluated during three field tests on Mauna Kea, Hawaii, in 2008 [2] and 2010 [12,13] and 2012 [14]. MIMOS IIa worked successfully as both a process monitor and a prospecting tool. As process monitor, iron oxidation states were determined before and after reductive treatment, and oxygen yield was calculated. As prospecting tool MIMOS IIa was mounted on a feedstock collecting rover. Feedstock would be selected for high FeO content and analysed for mineral content. The latter determines the optimum temperature during reduction: Ilmenite is reduced at 900°C, olivine at 1000°C and all other FeO-bearing phases at 1100°C.

In Memoriam: Göstar Klingelhöfer passed away unexpectedly in January 2019. Without him, this instrument would not exist. We would like to acknowledge his outstanding contributions to its development, to planetary science, and to our personal lives.

References: [1] Blumers M. et al. (2010) *Nucl. Instr. and Meth. A*, 624, 277-281. [2] Schröder C. et al. (2011) *Geochem.-Explor. Env. A.*, 11, 129-143. [3] Klingelhöfer G. et al. (2003) *J. Geophys. Res.* 108(E12), 8067, DOI: 10.1029/2003JE002138. [4] Schröder C. et al. (2019) this conference. [5] Morris R.V. et al. (2004) *Science* 305, 833-836. [6] Klingelhöfer G. et al. (2004) *Science* 306, 1740-1745. [7] Morris R.V. et al. (2010) *Science* 329, 421-424. [8] Morris R.V. et al. (2019) In *Remote Compositional Analysis: Techniques for Understanding Spectroscopy, Mineralogy, and Geochemistry of Planetary Surfaces*, ed. By Bishop J.L. et al., Cambridge University Press, in press. [9] Pullan D. et al. (2003) ESA SP-1240. [10] Rodionov D. et al. (2010) *Solar System Research*, 44, 362-370. [11] Klingelhöfer G. et al. (2008) LPS XXXIX, Abstract #2379. [12] Klingelhöfer G. et al. (2011) *LPS XLII*, Abstract #2810. [13] Ten Kate I. et al. (2013) *Journal of Aerospace Engineering* 26,183-196. [14] Graff T. G. et al. (2013) *LPS XLIV*, Abstract #2974. [15] Niculae A. et al. (2016) *Micros. Microanal.*, 22(S3), 40-41. [16] Fleischer I. et al. (2008) J. Geophys. Res. 113, E06S21, DOI: 10.1029/2007JE003022. [17] Morris R.V. et al. (1998) *Hyperfine Interact.* 117, 405-432. [18] Allen C.C. et al. (1994) *JGR, 99*(E11), 23173-23185. [19] Allen C.C. et al. (1994) *JGR, 101*(E11), 26085-26095.

TARGETING LUNAR VOLATILES WITH ESA'S PROSPECT PAYLOAD E. Sefton-Nash[1*], R. Fisackerly[1], R. Trautner[1], D. J. P. Martin[2], J. D. Carpenter[1], the ESA Lunar Exploration Team, the PROSPECT User Group and the PROSPECT Industrial Team. 1. ESA/ESTEC, Keplerlaan 1, 2201 AZ, Noordwijk, The Netherlands (e.sefton-nash@cosmos.esa.int). 2. ESA/ECSAT, Fermi Ave, Harwell, Didcot OX11 0FD, UK.

Introduction: The Package for Resource Observation and in-Situ Prospecting for Exploration, Commercial exploitation and Transportation (PROSPECT) is a payload in development by ESA for use at the lunar surface. Current development is for flight on the Russian-led Luna-Resource Lander (Luna 27) mission, which will target the south polar region of the Moon. PROSPECT will perform an assessment of volatile inventory in near surface regolith (down to ~ 1 m), and elemental and isotopic analyses to determine the abundance and origin of any volatiles discovered. Lunar polar volatiles present compelling science and exploration objectives for PROSPECT, but solar wind-implanted volatiles and oxygen in lunar minerals (extracted via ISRU techniques) constitute potential science return anywhere on the Moon, independently of a polar landing site. PROSPECT is comprised of the ProSEED drill module and ProSPA analytical laboratory [1] (Figure 1).

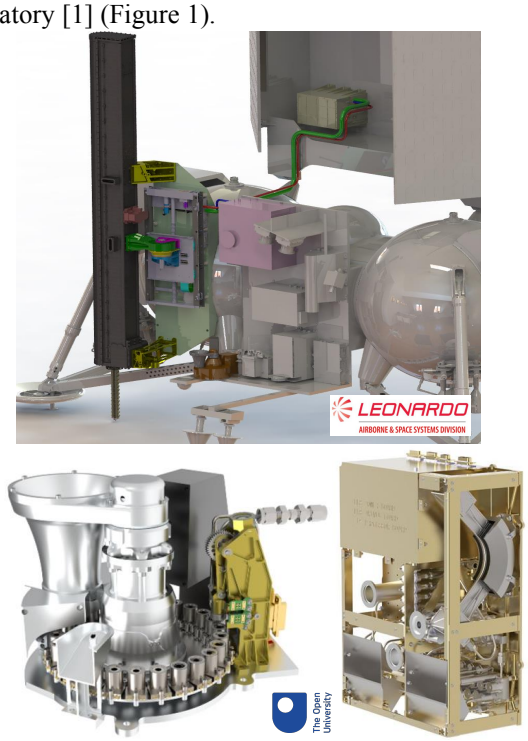

Figure 1. Renderings – Top: PROSPECT (non-grey items) mounted on Luna 27, including ProSEED drill module (left). Bottom left: Solids Inlet System to receive samples from drill sampling mechanism, with sample camera assembly (SamCam) and carousel of ovens for volatile extraction from regolith samples. Bottom right: ProSPA analysis package, containing magnetic sector and ion-trap mass spectrometers.

In ensemble, PROSPECT has a number of sensors and instruments (ion-trap and magnetic sector mass spectrometers, cameras, and sensors for temperature, pressure, permittivity and torque) that form the basis for a range of science investigations [2]. These investigations will be led by respondants from the lunar science community to an ESA Announcement of Opportunity released in 2018 for membership of to PROSPECT Science Team.

Development status and current activities: Tests of the PROSPECT Drill Module, ProSEED, in early 2019 are intended to demonstrate drilling and sampling functionality in ambient, cold and thermal vacuum (TV) laboratory conditions (at CISAS, University of Padova). The drill development model will be tested drilling into, and sampling from, lunar regolith simulant characterised and supplied by the Sample Analogue Curation Facility (SACF) at ESA/ECSAT [3]. Regolith density-depth profiles and grain size distributions in test materials are selected to cover plausible ranges expected for lunar regolith, informed by parameters measured from Apollo cores and retrieved from thermal infrared orbital observations [e.g. 4]. Most relevant to polar regions, material for tests in TV is prepared with water content representative of regolith that ranges from 'dry' to 'saturated' (0 - ~<12 wt. %).

Preservation of volatiles, via control of the thermal environment to minimise sublimation throughout the sampling and delivery process, is an important science requirement for PROSPECT, because sublimation of H_2O before analysis affects the retrieved volatile abundance, and may fractionate the samples' D/H ratio. Consequently, development requirements to minimise volatile loss drive design choices and operations strategies to maintain sufficiently low sample temperatures throughout the sampling process. Both completed work [5] and ongoing efforts seek to better quantify via laboratory experiments the potential effect on D/H of sublimation of lunar water ice.

Where is best to look for subsurface lunar volatiles? Abundant yet not totally aligned evidence regarding the presence of water ice on the lunar surface (visible to far-IR) and in the near subsurface (radar, neutrons, LCROSS [6]) leaves much to be determined regarding the distribution of lunar volatiles at the lunar poles.

Work by [7] identified regions of volatile stability, where temperatures never exceed a threshold (~110K, though this varies and depends on diffusion rates of water molecules in regolith) such that sub-

limation to vacuum results in loss rates < 1 kg m^{-2} Ga^{-1} (Figure 2). Many locations at the lunar south pole show such zones, and many zones extend to the surface (lightest blue in Figure 2).

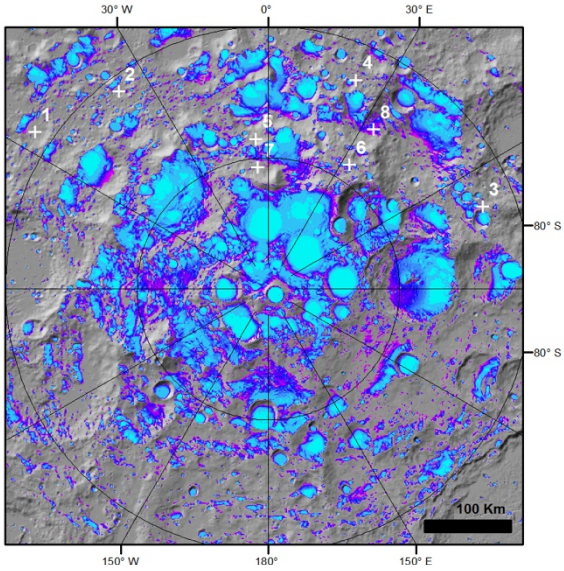

Figure 2. Polar Resource Product [7] for the lunar South polar region (pole to 80°S) illustrating depth to water ice stability criteria (where sublimation is expected to be < 1 kg m^{-2} Ga^{-1}). Purple is 1.09m depth, grading to lightest blue at the surface. Surface stability of water ice strongly correlates with regions of permanent shadow (PSRs). Study sites from [8] are illustrated in white crosses. Background is shaded relief of 20 m $pixel^{-1}$ LOLA altimetry.

Although the calculation in [7] was performed only down to 1m, the vast majority of zones of volatile stability lie much shallower than this (Figure 3). Thus, if water ice exists and is stable in the lunar polar sub-surface, it is likely to be accessible in the top few 10s of cm.

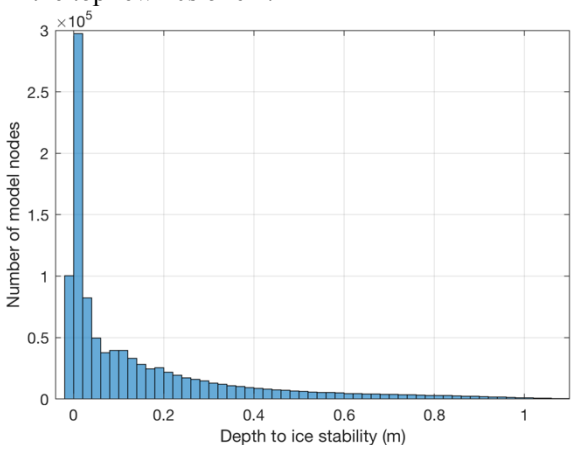

Figure 3. For locations where the water ice stability criterion is met in [4] (Figure 2), distribution of depth to stability.

This result introduces a trade-space where competing requirements are oppositely-sensed for solar-powered spacecraft, such that solar illumination must be maximized for the purposes of power and thermal operational constraints, but simultaneously minimised such as to target areas where illumination is not so high that volatile stability criteria are not met in the shallow subsurface. Indeed, for missions targeting subsurface volatiles it is clear that careful landing site selection and precision landing is of high importance.

The delivery function for lunar water is not well constrained over geologic time, and convolved with that uncertainty is another introduced by seasonal variation of insolation, which varies the extent of cold-traps (and therefore subsurface volatile stability zones) on ~18.6-year timescales [9]. Moreover, Ga-scale variations in lunar orbit and obliquity have likely greatly modified the available cold-trapping area over time. The implications of work by [10], which shows a decrease in lunar obliquity with time and a corresponding increase in the total area of lunar PSRs, is that much of the modern lunar cold-trap distribution may be geologically much younger (1-2 Ga) and may not have experienced as much cometary deposition of volatiles, e.g. compared to Mercury's cold traps, which have probably persisted for twice as long.

The relative importance of scattering and shadowing to the lunar thermal environment increases at high latitudes, which has led to [8] combining a 1D heat-flow parameterisation [4] and ray-tracing models [7, 11] in order to better constrain subsurface thermal environments in lunar polar regions. Such work will be of paramount importance in development of PROSPECT and planning for Luna 27 landing site selection in order to best target locations capable of harbouring volatiles.

Acknowledgements: The PROSPECT Industrial Consortium and development of ProSEED is led by Leonardo (Italy). The development of ProSPA is conducted by the Open University (UK).

References: [1] Barber et al., (2018), *Euro. Lunar Symp.* Abstract #099. [2] Sefton-Nash et al., (2018), *Euro. Lunar Symp.,* Abstract 114. [3] Martin, D. J. P. and Duvet, L., (2019) *50th LPSC*, LPI Contrib. No. 2132, Abstract #2663. [4] Hayne, P. et al. (2017), J. Geophy. Res., 10.1002/2017JE005387. [5] Mortimer, J. et al., (2018), *Plan. Space Sci.* **158**, p. 25-33. [6] Colaprete, A. et al., (2010), *Science* **330**, p. 463-468. [7] Paige, D. A. et al. (2010), Science, **330**, 479. [8] Warren, T. et al., (2019) *50th LPSC*, LPI Contrib. No. 2132, Abstract #2040. [9] Williams, J.-P. Et al. (2019), *50th LPSC*, LPI Contrib. No. 2132, Abstract #2852. [10] Seigler, M. A. et al. (2015), *Icarus* **255**, p. 78-87. [11] Vasavada, A. et al. (1999) *J. Geophys. Res.* **141**, 179-193.

Characterisation of the LUVMI Volatile Extraction and Volatiles Analysis package.

Sheridan[1], S. Barber[1], C. Pitcher[1] J. Biswas[2], P. Reiss[2], S., M. Reganaz[3], L. Richter[3] [1]The Open University, Milton Keynes, MK7 6AA, UK (simon.sheridan@open.ac.uk). [2]Institute of Astronautics, Technical University of Munich, Boltzmannstr. 15, 85748 Garching, Germany. [3]OHB System AG, Manfred-Fuchs-Str. 1, 82234 Weßling, Germany.

Introduction: Recent years have seen a growing interest in lunar exploration, with most international space agencies planning to return humans to the surface of the Moon, and to establish a long-term presence. In Situ Resource Utilisation (ISRU) offers the opportunity to make use of locally available resources and to potentially reduce the costs associated with transporting materials such as water, hydrogen and oxygen to the lunar surface. The polar regions of the Moon have long been known to be possible traps for solar system volatiles due to the low temperature of permanently shadowed areas [1,2]. Recent remote sensing missions have established the presence of volatiles (including water) at the surface and shallow sub-surface at these Polar Regions making them targets for in-situ missions to determine the ground-truth volatile inventory there. However, the Lunar Exploration Analysis Group (LEAG) Volatiles Specific Action Team (VSAT) findings state that there are enough uncertainties in the distribution of lunar volatiles from remote sensing techniques to imply that a non-mobile lander faces a significant risk of not finding volatiles or of "single data point" non-representative discoveries. To address the need for mobility, the Lunar Volatiles Mobile Instrumentation (LUVMI) [3,4] was developed (Figure 1).

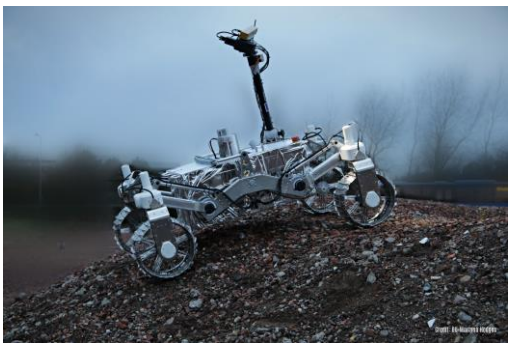

Figure 1 - The LUVMI prototype rover during testing in December 2018

Instrumentation description: The key LUVMI science package, comprising of the Volatiles Sampler (VS) and the Volatiles Analyser (VA) was developed to address key the current un-answered questions of what volatiles are present and the distribution on (and below) the lunar surface.

***Extraction of Volatiles*:** The VS consists of a hollow rotating drill shell and heating rod to penetrate approximately 10 cm into the lunar regolith. A central heating rod heats regolith inside the drill shell to release bound volatiles. The pressure within the drill shell will be monitored allowing the bulk volatile release during heating to be determined. In addition, a capillary leak will connect the drill internal volume to the VA to allow sampling of the dill volume during heating to enable real-time volatile characterisation to be performed.

***Volatiles Analyser*:** The VA is an ion trap mass spectrometer based upon the Ptolemy [5,6] flight-proven instrument (Figure 2). This is a low mass, compact and mechanically simple device capable of rapid detection of masses in the range of 10 to 150 *m/z*, enabling the detection of volatiles, including water, that may be released during regolith heating.

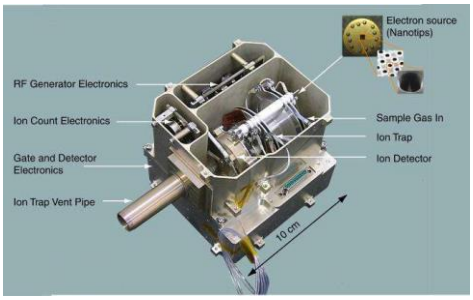

Figure 2 The Ptolemy Ion Trap Mass Spectrometer

Figure 3 shows the two instruments mounted in their flight configuration prior to volatile extraction testing.

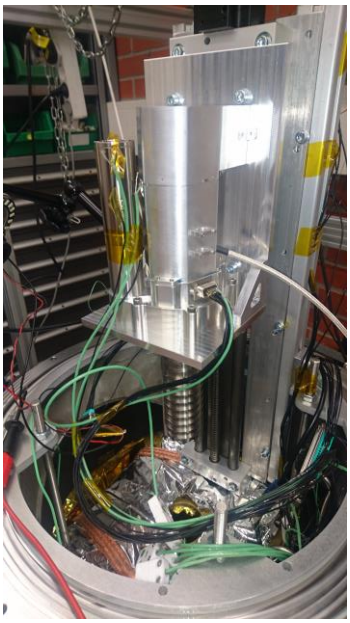

Figure 3 VA & VS prior to volatile extrction testing at TUM

Figure 4 – Thermal vacuum system

Volatile extraction tests: A thermal vacuum system was developed to enable testing of the VA (Figure 4) and allow volatile extraction from simulated regolith material under representative thermal lunar conditions. 200g of NU-LHT-2M simulant were used and doped with water content in a range similar to those seen by the LCROSS mission, where water contents of 5.6 ± 2.6% were observed in the ejecta plume created from an impactor striking the South Pole crater Cabeus [7]. A series of samples were prepared with 0, 0.5, 1 and 2% water (by weight). Samples were cooled to -150°C and evacuated to $<1\times10^{-5}$ mbar for 3 hours to investigate volatile loss in the temperature and pressure environment that tests were conducted .

Extraction of volatiles by heating were conducted with an in-house developed extraction probe that mimics the operation of the VS extraction system. The probe was heated to +300°C and lowered into the surface of the simulant whilst the output from the VA mass spectrometer was recorded.

Results: The doped samples were left under vacuum for 3 hours and then brought back to atmospheric pressure. Analysis of the sample masses revealed that, when stored at temperatures below 150℃, minimal water vapour were lost (a maximum of 0.25% water mass from the 2% sample). Although a mass loss was observed, if end-to-end testing are conducted within a 3 hour peiod then the procedure used will allow minimal volatile loss thus allowing meaningful measurments to be conducted.

A typical mass spectrum obtained with the VA during a volatile extraction experiment is shown in (Figure 5). During the extraction experiment a partial pressure of 1×10^{-6} mbar was measured within the vacuum chamber. In addition to the m/z 18 peak due to water a peak at m/z (CO_2) is present.

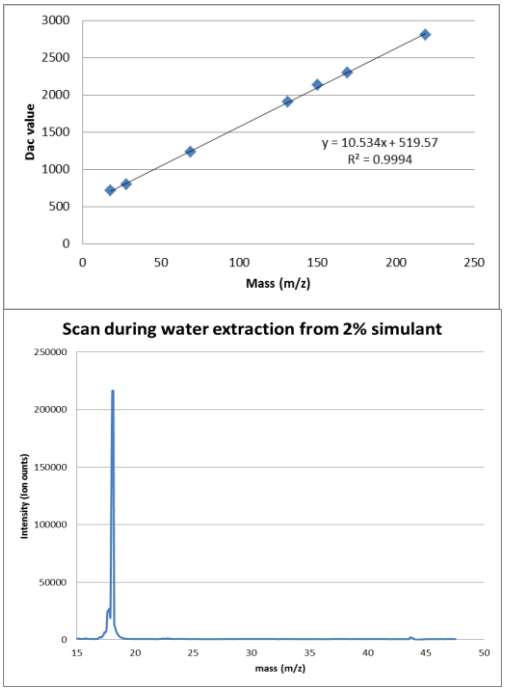

Figure 5 (top) mass calibration of the VA and (bottom) a typical mass specra during a volatile extraction experiment

Conclusion & Future Work: The VA results demonstrate that the mass spectrometer is capable of detecting and characterising volatiles evolved from simulated lunar regoilth under representative thermal conditions. The VA is capable of detecting and characterising volatiles in the mass range of 10 to 220 amu and offers the opertunity to perform ground truth in-situ measurments. Preliminary results demonstrate a dynamic range sufficient to differeniate between water doped regoliths of 0.5 to 3 %. Work will continue for the next 2.5 years under a new LUVMI-X grant.

Acknowledgments: This project is co-funded by the Horizon 2020 Framework Programme of the European Union, grant agreement 727220 and 822018

References:

[1] Paige et al. (2010) *Science*, 330, 6003, 479-482. [2] Vasavada et al., (1999) *Icarus* 141: 179-193. [3] Gancet J. et al. (2017) *ASTRA 2017*. [4] Biswas J. et al. (2017) *ELS V*. [5] Todd et al. (2007) *Journal Of Mass* Spectrometry. 42 (1):1-10. [6] Wright et al., (2007) *Space Science Review.* [7] Colaprete A. et al. (2010) *Science, 330*, 463-467.

EXPERIMENTAL AND ANALYTICAL CONSTRAINTS ON LUNAR MAGMA OCEAN CRYSTALLISATION. J. F. Snape[1], A. A. Nemchin[2], M. J. Whitehouse[3] and W. van Westrenen[1], [1]Faculty of Science, Vrije Universiteit Amsterdam, the Netherlands (j.f.snape@vu.nl), [2]Department of Applied Geology, Curtin University, Perth, Australia, [3]Department of Geosciences, Naturhistoriska Riksmuseet, Stockholm, Sweden.

Introduction: Recent studies have provided new insights into the crystallisation ages and initial Pb isotopic compositions of various volcanic lunar samples [1-4]. The results of these studies have been used to determine $^{238}U/^{204}Pb$ ratios (μ-values) for the magmatic sources from which these rocks were derived, and to place constraints on the starting μ-value of the primordial Moon [1-4]. A range of lunar formation times can be explained by varying the Moon's starting μ-value in order to generate the very radiogenic lunar initial Pb isotope compositions measured in the samples at different rates. For example, if the starting μ-value was very high (>1000), less time is required for the evolution of Pb isotopic compositions, and a young Moon remains a possibility (~4.4 Ga [5-6]). If on the other hand the Moon formed at 4.5 Ga [7-8], less extreme starting μ-values (~450) would be required.

In either case, these μ-values are significantly higher than those estimated for terrestrial mantle sources (typically ~8-10 [9-10]), and a significant range of source μ-values are also required to explain the Pb isotopic compositions for different lunar samples. In the case of the mare basalts with the least radiogenic Pb isotopic compositions, source μ-values of a few hundred are predicted [1,3], while KREEP-rich lithologies would require source μ-values of a few thousand [1-2]. Currently, it is not clear at what stage in the Moon's early magmatic evolution these elevated μ-values were established, or which process(es) could have generated such a wide range of μ-values.

In the past few years, several new experimental studies of lunar magma ocean (LMO) crystallisation have been published [11-13]. These studies aim to replicate the effects of fractional crystallisation in the LMO and provide more detailed information regarding the mineral assemblages and melt compositions formed towards the end of its crystallisation. However, there are still significant uncertainties associated with the partitioning behaviour of U and Pb [14]. Here we combine the results of the Pb isotopic sample analyses and these experimental studies, and aim to address these uncertainties with a series of new LMO crystallisation experiments.

Modelling approach: Initial modelling has been performed using the current best estimates for the mineral-melt partitioning behaviour of U and Pb [14]. For each stage of LMO crystallisation defined in the experimental studies, the concentration of U and Pb in the residual melt is calculated assuming Rayleigh fractionation. The concentrations of U and Pb in the cumulate assemblages are calculated assuming equilibrium partitioning. For the examples shown in Fig. 1, the starting μ-value of the LMO has been assumed to be 450.

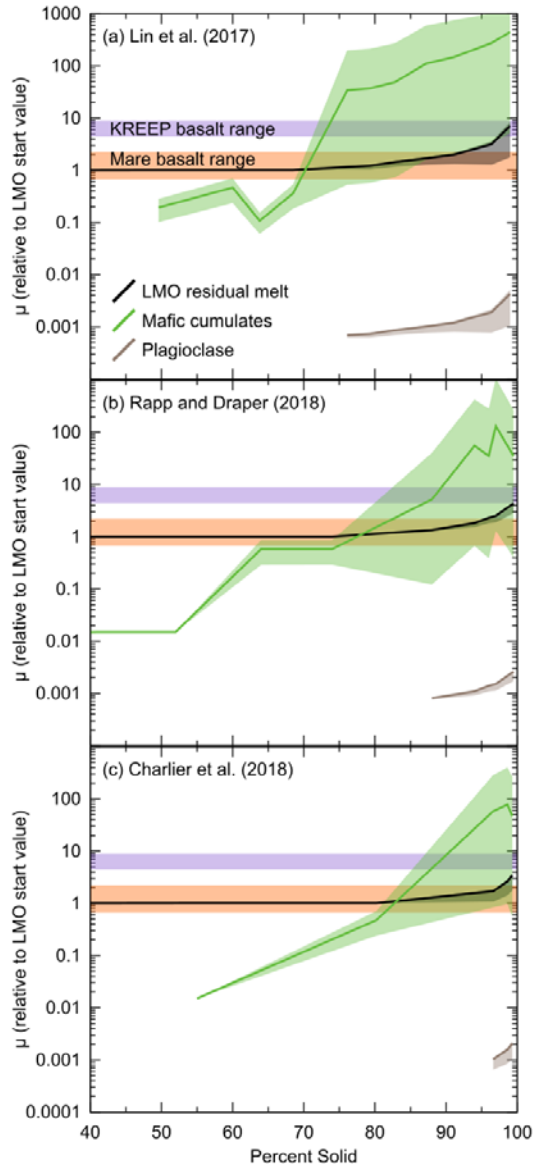

Figure 1: Evolving μ-values the LMO residual liquid, mafic cumulates and plagioclase predicted to form in the experimental studies previously published [11-13]. These are compared with predicted source reservoir μ-values of mare basalts and KREEP basalts [1,3]. The semi-transparent fields surrounding the model μ-values represent the potential range of values resulting from the uncertainties in the partition coefficients of U and Pb.

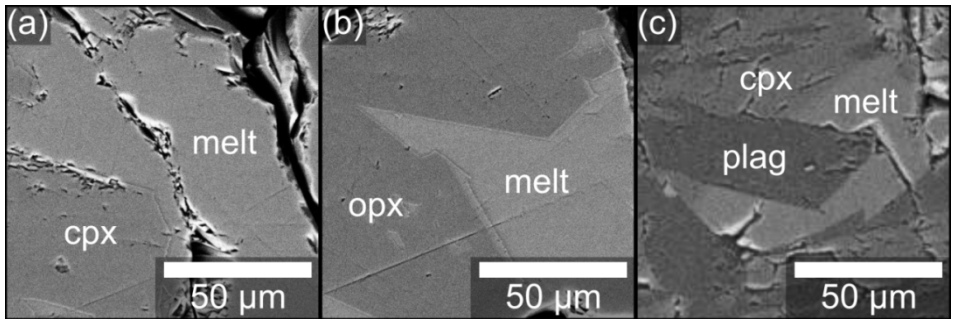

Figure 2: Backscattered electron images of run products from experiments with a pressure of ~0.8 GPa and a temperature 1250°C, using a starting composition taken from [12], equating to 88% LMO crystallization.

Experimental and analytical approach: The starting compositions for the new LMO crystallisation experiments are based on those in previous studies [11-13], and have been doped with radiogenic parent-daughter elements (U-Pb, Sm-Nd, Rb-Sr and Lu-Hf). These experiments are being performed in piston-cylinder apparatus in the VU high-PT laboratory. The run products from these experiments (Fig. 2) are then mounted in epoxy and polished for electron microprobe and laser ablation inductively coupled plasma mass spectrometry analyses.

Discussion: In the three LMO crystallisation studies [11-13], olivine and orthopyroxene are the only phases formed until approximately 70% of the LMO has crystallised. After this, cpx and plagioclase begin to crystallise, resulting in the most significant changes in the residual melt and the mafic cumulate µ-values (Fig. 1). Based on the calculations performed here, the uncertainties in U and Pb partitioning behaviour result in greater variations in the predicted µ-values than any differences between the three LMO studies.

µ-value of the residual LMO melt: The maximum µ-value of the residual liquid in the final stages of LMO crystallisation is <10× the starting µ-value. The majority of this increase results from the crystallisation of plagioclase, which acts as a significant Pb sink (Fig. 1). Assuming that the final LMO residual melt composition can be taken as a proxy for the composition of the "urKREEP" reservoir from which the KREEP-rich basalts obtained their high-µ signatures (~2000-4000; [1]), this provides a rough constraint on the starting LMO µ-value of (at least) several hundred.

µ-values of mafic cumulates: The early mafic cumulates (those comprising olivine and orthopyroxene) have µ-values lower than those of the LMO residual liquid. In general, the crystallisation of cpx, after approximately 70% crystallisation of the LMO, results in an increase of the mafic cumulate µ-values, such that it is possible to generate mafic cumulates with µ-values that are several orders of magnitude larger than those of the LMO residual liquid. As such, relatively low starting µ-values for the LMO would still be sufficient to produce mafic cumulate µ-values within the range of those previously predicted for the mare basalt sources [1,3] (Fig. 1). An exception to this is if one set of extreme clinopyroxene D_U values are used, which make it possible to generate mafic cumulates with consistently lower µ-values than the LMO residual liquid. Notably, the potential to generate lower µ-values for the mafic cumulate (relative to the LMO liquid) opens up the possibility of significantly higher starting LMO µ-values and, thus, later formation of the Moon.

Conclusions: The results of these initial calculations demonstrate how sensitive lunar magmatic evolution models are to uncertainties in U and Pb partitioning behaviour, and underscore the need for new experimental data. It is currently not possible to place very precise limits on the Moon's starting µ-value, leaving open the possibility for a range of lunar formation times. In spite of these uncertainties, there is still a requirement for the Moon to have acquired a high-µ signature early in its evolution, prior to the start of LMO crystallisation.

References: [1] Snape J. F. et al. (2016) *EPSL, 451,* 149–158. [2] Nemchin A. A. et al. (2017) *GCA, 217,* 441–461. [3] Snape J. F. et al. (2018) *Chem. Geol., 482,* 101–112. [4] Snape J. F. et al. (2018) *EPSL, 502,* 84–95. [5] Borg L. E. et al. (2011) *Nature, 477,* 70-72 [6] Carlson R. W. et al. (2014) *Phil. Trans. R. Soc., A372,* 20130246 [7] Avice G. and Marty B. (2014) *Phil. Trans. R. Soc., A372,* 20130260 [8] Barboni M. et al. (2017) *Science Adv., 3,* e1602365 [9] Zartman R. E. and Doe B. R. (1981) *Tectonophysics, 75,* 135-162. [10] Kramers J. D. and Tolstikhin I. N. (1997) *Chem. Geol., 139,* 75–110. [11] Lin Y. et al. (2017) *EPSL, 471,* 104–116. [12] Rapp J. F. and Draper D. S. (2018) *MAPS, 53,* 1432–1455. [13] Charlier B. et al. (2018) . *GCA, 234,* 50–69. [14] Blundy J. and Wood B. (2003) *Revs. Min. Geochem., 52,* 59-123.

Acknowledgments: This research was funded by the European Commission Horizon 2020 Research and Innovation programme, through a Marie Skłodowska-Curie Actions Fellowship grant (794287).

EXAMINING THE IMPACT PROCESS WITH PHOTOMETRIC IMAGE SEQUENCES. E. J. Speyerer[1], A. C. Martin[1], M. S. Robinson[1], A. Boyd[1], R. Z. Povilaitis[1], and B. W. Denevi[2], [1]Arizona State University, School of Earth and Space Exploration, Tempe, AZ, (espeyerer@ser.asu.edu), [2]Johns Hopkins University Applied Physics Laboratory, Laurel, MD, USA

Introduction: Observations of newly formed impact craters discovered by the Lunar Reconnaissance Orbiter Camera (LROC) enable detailed study of the impact process and its effect on the surrounding regolith. The LROC instrument began mapping the Moon in 2009 [1]. Nearly a decade later the twin Narrow Angle Cameras (NACs) and Wide Angle Camera (WAC) have collectively captured over 1,610,000 and 389,000 images, respectively of illuminated Moon. Using a subset of NAC images (50 to 150 cm pixel scale), we analyzed tens of thousands before and after temporal image pairs with similar lighting (incidence angle difference < 3°) and nadir viewing geometries to identify new surface changes. From these temporal pairs we located newly formed craters, secondary impacts, rock falls, and recent mass wasting events [2,3]. Discovery of larger impact craters (up to 70 m) and follow-up observations enables us to examine the cratering process in more detail than previous investigations.

Initial Investigations: On 17 March 2013, the NASA Lunar Impact Monitoring Program at Marshal Space Flight Center observed its largest impact flash at that time [3,4]. From images acquired before and after the impact event, the LROC team located a new 18 m diameter impact crater. Examination of ratio images (formed from the after image divided by the before image) revealed four distinct reflectance zones surrounding the newly formed crater (zones in order of appearance from the crater rim: proximal high reflectance, proximal low reflectance, distal high reflectance, and distal low reflectance) [3]. The broadest zone, the distal low reflectance zone, extended 500 m from the impact crater and discontinuous portions continued 1-2 km (~55 to 110 crater diameters) away.

Following this discovery, the LROC team went on to analyze other randomly targeted temporal observations identifying other surface changes. In the initial investigation, they discovered 222 newly formed craters [2] revealing that not all craters have the four distinct reflectance zones, but that almost all had a distinct distal low reflectance zone that extended out 10s to 100's of crater diameters. Continued analysis has increased our counts to over 500 newly formed (and resolved) impact craters with the largest crater having a diameter of 70 m.

Photometric Image Sequences: Follow-up observations acquired under different lighting and viewing geometries are enabling the study of the photometric properties of the disturbed zones. These photometric image sequences [5], enable one to infer changes in surface properties such as composition, grain size, porosity, and differences in sub-pixel roughness. Nearly 100 NAC observations of the newly formed craters have been collected to date with the goal of acquiring images across a full range of phase angles with some at low phase angles (<5°) to document the opposition effect [6] and higher phase observations to investigate the sub-pixel roughness of the surface.

Proximal Reflectance Zones: A photometric image sequence created from 19 NAC observations of a newly formed 50 m diameter impact crater enable examination of the continuous ejecta blanket surrounding the impact site. **Fig. 1a** shows a standard reflectance image (phase=65°) of the crater with both high and low proximal reflectance zones surrounding the crater and extending 175 m from the crater rim. **Fig. 1b** shows a low phase (2°) observation of the same impact site in which the proximal low reflectance zone is indistinguishable from the background indicating that this zone is not a compositional feature or a layer of nanophase iron as [7] has proposed, but rather an effect caused by changes in grain size or sub-pixel roughness. Additionally, the visibility of the proximal high reflectance zone in the low phase image is consistent with the exposure of immature regolith that was not previously visible on the surface prior to the impact event.

Fig. 1c shows a phase ratio image [5] where an image with 2° phase was divided by an image with 7° phase angle (both with incidence angle of 7°). In this ratio, the proximal high reflectance zone shows up as dark indicating a shallower slope of the phase curve between 2° and 7° relative to the background (mature mare). We can infer that this region, closest to the crater, has lower porosity possibly due to the emplacement of small rocks, increase in the relative grain size, and/or compaction of the surface. Meanwhile, the proximal low reflectance zone shows up as bright in the ratio image compared to the background that indicates an increase in the porosity possibly due to fewer

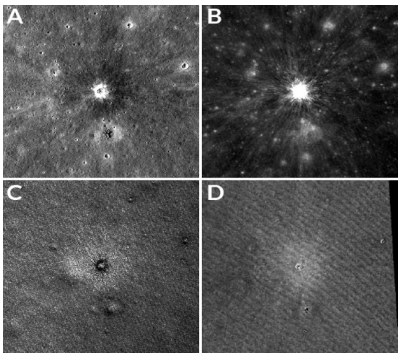

Fig. 1- A and B) Set of after images acquired at 65° and 2° phase, respectively. C and D) Phase ratio images of NAC observations C) 2°/7° D) 52°/79°.

rocks being present, decrease in the relative grain size, and/or dilation of the surface. However, when examining a second phase ratio image (**Fig. 2d**; 52°/79°), the difference in the two proximal zones seen in **Fig. 2c** disappear. This shows that sub-pixel roughness increases in both proximal zones compared to the background and is consistent with current impact models.

Distal Reflectance Zones: The impact that formed the crater on 17 March 2013 created two distal reflectance layers that extended 1-2 km from the impact site [3]. Additional observations of other craters discovered with temporal imaging revealed that these distal layers are common and can extend hundreds of crater diameters [2]. Further temporal image pair searches led to the discovery of a 70 m impact crater using before and after WAC observations. A ratio of a single pair of WAC images (100 meter pixel scale) shows a single bright pixel and a set of darker pixels surrounding the impact crater, which can be inferred as the impact crater itself and a low reflectance zone. Due to pixel scale and noise, no additional structure or reflectance zones are detectable in a single WAC ratio image. However, after its initial discovery and the collection of more WAC observations, an average temporal ratio image was created. First all WAC color observations covering the impact site were calibrated and a photometric correction was applied to each image [8]. The images were then map projected to a common map space. Finally, all the images acquired before the impact occurred were averaged together and all the images gathered after the event were averaged. The mean after image was divided by the mean before image. Using this technique, we increased the signal-to-noise ratio in the WAC temporal image to reveal subtle changes that were not detectable in the ratio of a single set of WAC observations (**Fig 2**).

As mentioned, a single pixel marks the location of the crater itself. Within 3 km of the crater are bright and dark markings that we infer to be the two proximal reflectance zones mentioned earlier. More strikingly, is the distal low reflectance zone that extends >80 km from the crater rim (>1100 crater diameters) and covers approximately 3400 km^2. These distances both in km and crater diameter units is far greater than any other new crater we have investigated to date. Based on this observation, even small < 100 m diameter craters can alter the reflectance of areas much larger (>10x) than previously expected.

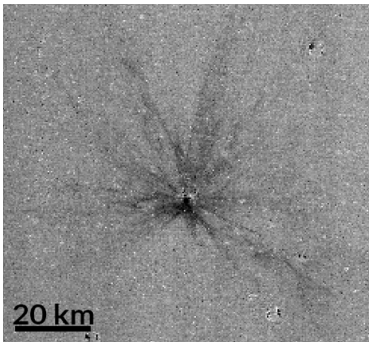

Fig. 2- Averaged WAC temporal ratio image showing the result of a 70m impact.

We investigated the photometric properties of the distal zones over a range of phase angles using WAC images. Due to the latitude of the impact site, we don't have any observations at phase angles <15°. Therefore, at this time we cannot conduct a complete Hapke [9] photometric analysis since we cannot characterize the opposition effect that occurs near 0° phase. However, we can study the basic shape of the phase curve by normalizing the reflectance by the Lommel-Seeliger Law [10] and analyzing the curvature and magnitude of the phase function with a simplified power law function:

$$\frac{IOF}{LS} = Ae^{-\propto g}$$

where A is the intercept and is related to normal albedo, α is the slope and indicates photometric roughness, and g is the phase angle associated with the pixel. While this function does not replace the Hapke function or completely capture the shape of the phase curve, it does provide two simple parameters that we can use to asses surface properties. **Fig. 3** shows the phase function and the corresponding fits for the reference area south of the impact site and a region within the distal low reflectance zone. From the initial fits we see that the parameter A remains the same between the two regions, but the α parameter increases from 0.72 to 0.81. This increase indicates a steeper phase curve slope for the low reflectance zone compared to the reference area. We interpret this change as an increase in surface roughness or dilation possibly caused by small particles colliding with the surface during impact induced jetting [2, 11]. Continued analysis and collection of photometric sequences will enable further study into the impact process and its effect on the surrounding regolith.

References: [1] Robinson M. S. et al. (2010) *Space Sci. Rev*., 150, 81–124. [2] Speyerer E. J., et al (2016) *Nature*, 538, 215-218 [3] Robinson M. S. et al. (2015) *Icarus*, 252, 229-235. [4] Suggs R. M. et al. (2014) *Icarus* 238, 23-36. [5] Martin A. C. (2019) *LPS L*, Abstract #2752. [6] Hapke B. (1981) *JGR*, 86, 3039-3054. [7] Kaydash V. et al. (2018) *Icarus*, 311, 258-270. [8] Sato H. et al. (2014) *JGR-Planets*, 119, 1775-1805. [9] Hapke (2002) *Icarus*, 157, 523-534. [10] Fairbairn M. (2005) *J. of the Royal Astro. Society of Canada*, 99, 92-93. [11] Johnson B.C. (2014) *Icarus*, 238, 13-22.

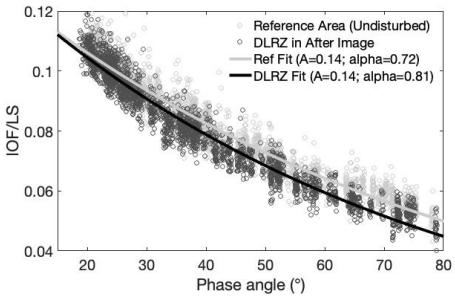

Fig. 3- WAC phase curve of the distal low reflectance zone and a reference area unaffected by the impact event.

HYDROGEN ISOTOPIC SIGNATURE OF THE MOON AS RECORDED IN MELT INCLUSIONS. A. Stephant[1], M. Anand[1,2], X. Zhao[1], G. Degli-Alessandrini[1] and I. A. Franchi[1], [1] School of Physical Sciences, The Open University, Milton Keynes, MK7 6AA, UK., [2] Department of Earth Sciences, The Natural History Museum, London, SW7 5BD, UK.

Introduction: Since the first report of the detection of water in lunar volcanic glasses (LVG) [1], the concentration and origin of this water is vigorously debated. Indeed, H_2O concentration estimated on the basis of volatile vs. refractory element abundances (Zn/Fe) points towards an anhydrous Moon (<1ppm H_2O) [2], while *in-situ* measurements on various lunar minerals, such as olivine (ol)-hosted melt inclusions (MIs) [1, 3-4], LVG [1,5], plagioclase [6] and apatite [7-8] strongly suggest a wetter Moon, with estimates ranging from ~1 to 300 ppm H_2O for the bulk silicate Moon (BSM) [1,3-4,6]; albeit still depleted relative to the Earth. Among all lunar minerals, ol-hosted MIs are thought to be more robust for preserving pre-degassed volatiles signature compared to later-formed phases such as apatite, although processes such as post-entrapment crystallization (PEC) and cosmic ray spallation effects need to be carefully considered in the case of MIs.

In terms of hydrogen isotopic composition (δD), multiple lunar reservoirs and processes have been highlighted by apatite measurements [7-9]. As the parent magma may have undergone significant degassing by the time apatites crystallized, MIs are preferable to unravel the juvenile δD value of the mantle source regions of mare basalts. Moreover, inferring the H_2O contents of parent magmas using apatite is nontrivial compared to silicate-hosted MIs. Few δD analyses have been reported on lunar MIs so far. 74220 and 74002 MIs and glassy beads recorded a juvenile lunar δD in between +187 and +274‰ [10-11]. A recent study on Apollo 12 basaltic MIs [12] reported a lower range of values from -183 to +138‰ (these values are not corrected for spallation and thus should be viewed as upper limit), arguing for a more terrestrial-like lunar δD for the source region of Apollo 12 samples. In this study, we analysed 56 MIs hosted in either olivine or pyroxene from nine different basalt types collected from four Apollo landing sites, in order to constrain the initial H_2O abundance and H isotopic signature of the lunar mantle and document any lateral heterogeneity for H in the lunar interior.

Samples: The samples studied are low-K ilmenite basalts 10020 and 10058, low-Ti Apollo 12 suite basalts 12002, 12004, 12008, 12020 and 12040, high-Al basalt 14072 and low-Ti basalt 15016. We selected these samples as H_2O abundances of MIs in 10020 and 15016 were previously measured [4]; while H isotopic compositions and abundances have been reported for 12040 [12]. Also we selected samples based on the confirmed presence of MIs as well as their young exposure age where possible (i.e. 21 to ~400 Ma).

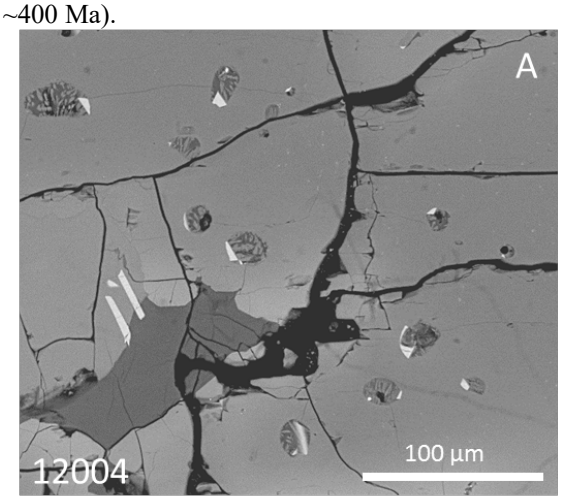

Figure 1: Back Scattered Electron (BSE) image of ol-hosted MI assemblage in 12004,51.

Analytical methods:

Olivine and pyroxene phenocrysts containing MIs were identified by optical microscopy and imaged using the FEI Quanta 200 3D scanning electron microscope (Fig. 1). Chemical composition of MIs and their hosts have also been analysed by Cameca SX 100 electron micro-probe.

Hydrogen concentration and isotopic composition. Measurements of D/H ratios and H_2O concentrations in the ol- and pyroxene (px)-hosted MIs were performed using the Cameca NanoSIMS 50L at The Open University. The H^-, D^-, $^{13}C^-$ and $^{18}O^-$ secondary ions were measured using a Cs^+ primary beam of 550 pA. $^{13}C^-$ was used to monitor contamination on the sample. The primary beam was rastered over a 8×8 µm². Blanking was made and only the 4×4 µm² (50%) interior of the surface area was analyzed, with each measurement consisting of 2000 cycles. Terrestrial MORBs were used as standards for calibrations.

Results: 45 ol-hosted MIs and 11 px-hosted MIs were analyzed. H_2O contents range from 2±1 to 194±51 ppm and from 6±1 to 212±27 ppm in ol- and px-hosted MIs, resp. (corrected for PEC- Fig. 2). δD measured in these MIs from 9 samples span over a large range, from -912±553‰ to +1942±611 ‰ (after spallation correction). Both, intra- as well as inter-

sample variations exist. As such, we can group samples into two main categories. The category 1 comprises low-Ti Apollo 12 basalts (12002, 12004, 12008 and 12020) except 12040. The category 2 contains high-Ti basalts 10058 and 10020, high-Al basalt 14072, and low-Ti basalts 12040 and 15016 with exposure ages >285Ma. Each category defines both a positive and a negative trend, in H_2O-δD space; category 2 displays a steeper trend (Fig. 2).

Discussion:

Hydrogen concentration in lunar mantle. The range in H_2O contents in ol-hosted MIs (2-212 ppm) is in good agreement with the range of 5-131 ppm measured in homogenized MIs from 10020 and 15016 [4] and the range of 28-156 ppm measured in crystallized MIs in 12040 [12]. The highest water content recorded by silicate-hosted MI in each sample varies from 65 ppm (in 12020) to 212 ppm (in 10058). For instance, a glassy MI found in 12040 recorded 194 ppm H_2O content. As such, it is highly probable that MIs in lunar basalts have lost some hydrogen (as H, OH or H_2O), hence the positive and negative H_2O-δD correlations (cf. Fig. 2). We considered the highest H_2O content measured (i.e. 212±27 ppm) as the closest to the pre-eruptive abundance of the mare basaltic parent melt. Assuming 10% partial melting in the lunar mantle, we estimate a water content for the BSM in the order of 19 to 24 ppm. This range is in agreement with most other studies (~1-80 ppm, recalculated for the same degree of partial melting) (Fig. 3), although our estimates are towards the lower range. 74220 MIs seem to record a more H_2O-enriched source (~100 ppm) [3-4] compared to other lunar material, which has been suggested to be a local anomaly [2]. However, MIs in 12018 also provide estimates with similar H_2O content for the BSM [12]. Crystallized MIs could have undergone some loss of hydrogen, either by trapping a degassed melt or during post-entrapment degassing, and, therefore, our estimated water concentration of ~25 ppm for the BSM should be viewed as a lower limit.

Hydrogen isotopic composition of the Moon. The two silicate-hosted MIs with the highest measured water contents (i.e. 194 and 212 ppm) are supposedly more primitive, and their associated δD values (i.e. ~ -250‰) is thus considered as a conservative estimate of the juvenile lunar δD. All the samples follow a slightly positive trend (dark grey dashed curve), which is the theoretical loss of H_2O from the initial basaltic melt. From this main trend, low-Ti Apollo 12 basalts (cat.1) and the rest of the samples show distinct negative trends (light grey curves), concordant with H_2 or H diffusive loss from the MI through its host, at different stage of the sample's petrogenesis. Finally, some MIs from the high-Ti, high-Al and low-Ti basalts of high CRE age (Cat. 2) point towards some solar wind (SW) mixing (light grey dotted line). After taking into account various processes that could have influenced the abundance and isotopic composition of H in these MIs, we make conservative estimates of 250 ppm H_2O in the primary lunar basaltic melt with an associated δD value of ~ -250‰.

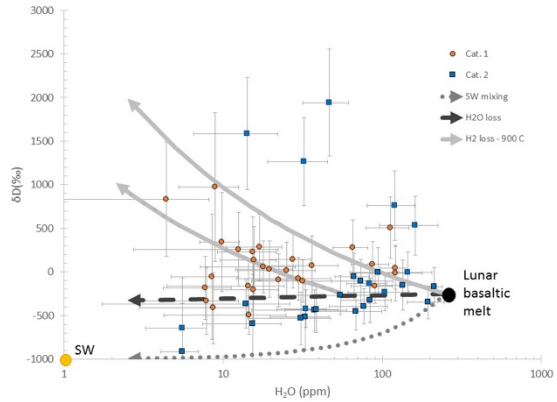

Figure 2: H_2O (ppm) vs. δD (‰) for lunar basaltic silicate-hosted MIs (see text for definition of Categories 1 and 2).

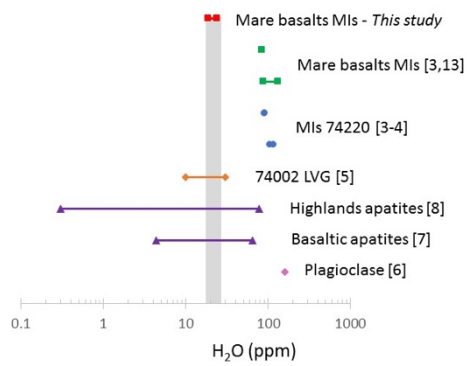

Figure 3: Estimation of BSM H_2O content from various lunar minerals. BSM H_2O contents recalculated based on parental melt H_2O concentrations [3-9], assuming 10% partial melting.

References: [1] Saal A. et al. (2008) *Nature*, 454, 192-195. [2] Albarede F. et al. (2013) *Icarus,* 222, 44–52. [3] Hauri E.H. et al. (2011) *Science,* 333, 213-215. [4] Chen Y. et al. (2015) *EPSL,* 427, 37-46. [5] Fueri E. et al. (2014) *Icarus,* 229, 109-120. [6] Hui 2013. [7] Tartese R. et al. (2013) *GCA*, 122, 58-74. [8] Barnes J.J. et al. (2014) *EPSL*, 390, 244-252. [9] Robinson and Taylor (2016) [10] Saal 2013 [11] Fueri et al. (2017) *EPSL*, 474, 76-82. [12] Singer J.A. et al. (2017) *Geochem. Jour.*, 51, 95-104. [13] Ni P. et al. (2019), GCA, 249, 17-41. [14] Huss G.et al. (2012) *LPSC*, 1709.

LUNAR CRATER EJECTA MATURATION ACROSS WAVELENGTH. A. M. Stickle[1], J.A. Grier[2], J.T.S. Cahill[1], G.W. Patterson[1], and B. Greenhagen[1], [1]Johns Hopkins University Applied Physics Laboratory, 11100 Johns Hopkins Rd., Laurel, MD 20723, USA (angela.stickle@jhuapl.edu), [2]Planetary Science Institute, Tucson AZ USA.

Background: The physical evolution of the lunar surface with exposure to the space environment (maturation) can take place over relatively short timescales, particularly with impacts. Maturation is attributed to the amount of glass and agglutinate content within the lunar soil [e.g., 1-8], the amount of trapped solar wind nitrogen [9], solar wind sputtering and vapor deposition [10-11], and/or the amount of sub-microscopic iron (SMFe) in the material. Studies show that the abundance of these glasses and agglutinates increases with regolith age and can account for large volume fraction of the regolith [e.g., 2,4,9]. Changes in physical properties of the lunar regolith are quantified in terms of specific maturity indices (e.g., Optical MATurity (OMAT) [13]). Regolith age is generally classified on the basis of one or more of these specific indices [3]. Comparisons indicate that maturity of the soil can be tracked across wavelengths, though different data sets may sample processes on different time- and depth-scales. New data from the LRO and Kaguya missions (coupled with Clemetine OMAT) provide important new ways to examine lunar surface maturity.

Observations of Crater Age Across Wavelengths: Impact craters expose immature material and distribute it across the lunar surface, often blanketing older more mature material. This provides a window to examine the ageing of lunar soils. One way to look at parameters such as OMAT locally around impact craters is to take profiles of the parameter of interest as a function of radius. Figure 1 shows an example of radial profiles of OMAT outward from the crater rim for three craters of interest. Using OMAT, [13] classify Byrgius A as "young", Dufay B as "intermediate" and Golitsyn J as "old". Higher values of OMAT indicate younger material, which correlates with the initial approximate ages of these three craters from morphology and crater counts.

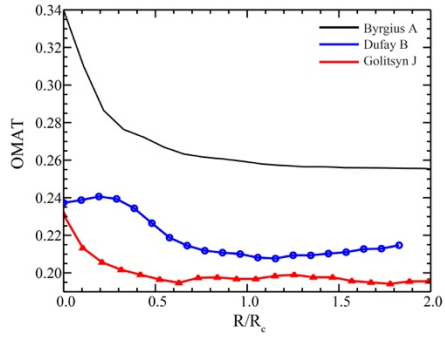

Figure 1. Radial OMAT profiles derived from Clementine data, outward from the crater rim. Higher OMAT indicates less mature material and a younger age.

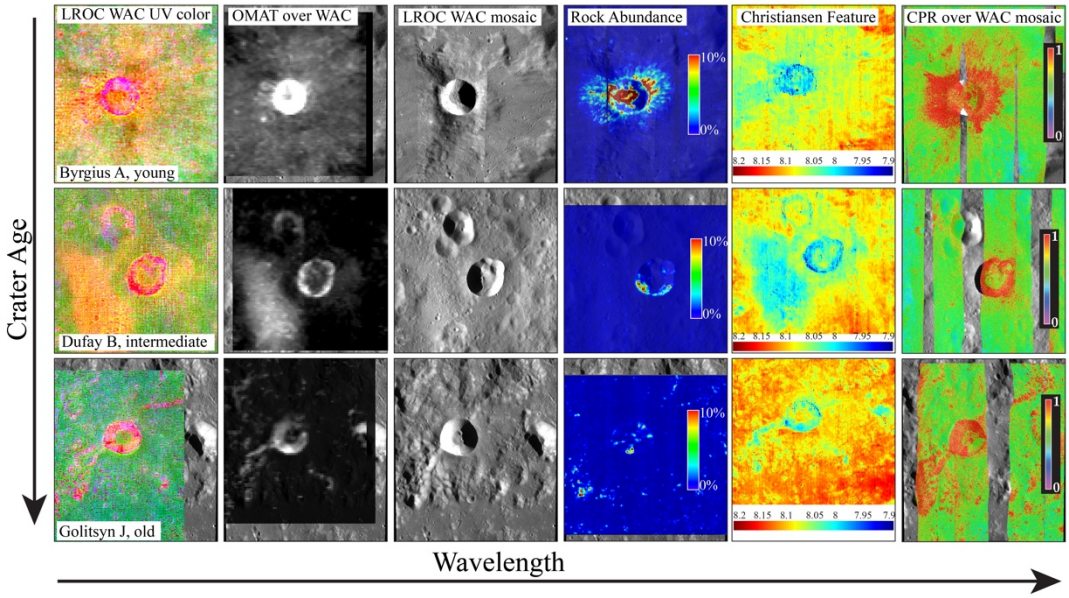

Figure 2. Variety of data sets collected for the three initially chosen craters. Maturity indices are being investigated across these data sets, with promising results. (top) Byrgius A (19.7 km, 24.6°S, 63.5°W), a young highlands crater, (middle) Dufay B (19.8 km, 8.3°N,171°E), an "intermediate" aged highlands crater, (bottom) Golitsyn J (19.5 km, 27.9°S, 102.9°W), an "old" highlands crater. The columns show the appearance of the crater across wavelengths, from UV (WAC UV, left) to radar (Mini-RF radar, right).

Comparisons of observations from UV to radar for these three craters (e.g., Fig. 2) indicate that maturity of the soil can be tracked across wavelengths. These comparisons suggest that specific "maturity parameters" manifest differently at different wavelengths. Further, more detailed comparisons are underway, and they are necessary to more fully understand when these maturity trends can be correlated and how to quantify the correlation. If trends can be correlated, this will provide a powerful tool when examining the surface evolution of the Moon and determining relative ages between features. These three craters are used as a basis for relative dating for other identified craters of interest.

Correlation of Maturity Indices: Using Byrgius A, Dufay B, and Golitsyn J as "type examples", other craters were examined across wavelengths. Specifically, 8 new craters of interest were identified: Proclus, Gambart A, Petavius B, Necho, Kepler, Peirce, and Picard. Here, data sets are compared to OMAT values at the crater rim, 1 crater radius out from the rim (approximate continuous ejecta blanket), and 2 crater radii out. The data sets examined to date include Diviner Christiansen Feature (CF) data v. OMAT; Mini-RF CPR v. OMAT, and Mini-RF m-χ v. OMAT 1 crater radius out from rim. Future exploration will include LROC WAC UV ratios and Diviner Rock Abundance values.

These comparisons, though preliminary, show promising trends (Figure 3). For the craters examined so far, differences in CPR profiles between mare and highlands craters are relatively clear. Less clear, however, is the effect of terrain on the Mini-RF m-χ [14] profiles. Preliminary analysis showed that both mare and highlands craters could be generally grouped into three classes, or "types" based on the shape of the m-χ decomposition of S_1. Our current study suggests Type 1 represents the freshest craters, and that Type 3 represents older craters. Our work also shows that trends can be seen with crater age across m-χ parameters (e.g., Fig. 3D), and that it may be possible to identify a functional form for scattering behavior of ejecta material with age.

A possible index for Diviner data might be the ratio of the CF band center at the rim compared with the surrounding background terrain, or perhaps CF as a function of OMAT near the crater. Figure 3A shows that the ages of our initial three craters can be picked out from the CF band center, and the relationship with OMAT is what is expected (e.g., younger craters (Byrgius A) have higher OMAT value across the space). CPR as a function of OMAT is also shown in Figure 3B and 3C, and shows expected trends: higher CPR with higher OMAT. This allows us to place the studied craters in a relative age order.

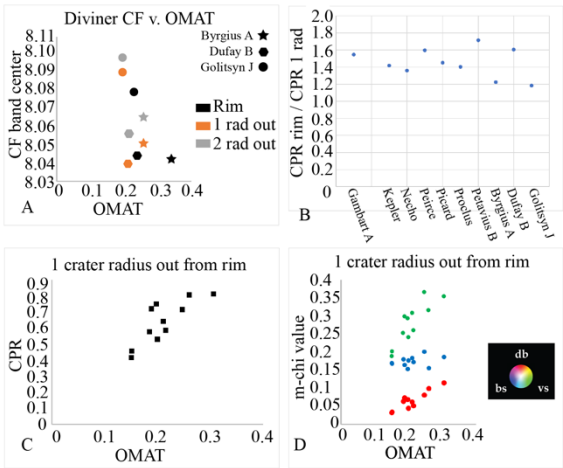

Figure 3. Initial comparisons of examined craters and proposed "maturity signifiers", showing promising trends. Here, data sets are compared to OMAT values at the crater rim, 1 crater radius out from the rim (approximate continuous ejecta blanket), and 2 crater radii out. A) Diviner CF data v. OMAT; B) proposed maturity index from CPR for 10 craters; C) CPR v. OMAT; D) m-chi v. OMAT 1 crater radius out from rim.

References: [1] Adams, J.B. and T.B. McCord (1971) *Science*, 171, 567-571; [2]McKay, D.S., et al. (1974) *Proc. Lunar. Sci Conf 5th,* p. 887-906; [3]Adams, J.B., and M.P. Charette (1975) *The Moon, 13*, 293-299; [4]Charette, M.P., et al. (1976) *Proc. Lunar Sci. Conf. 7th*, p. 2579-2592; [5]Wells, E., and B. Hapke (1977) *Science*, 195, 977-979; [6] Pieters, C. M. et al (1993) *J. Geophys. Res. Planet. 98*(E11), 20817-20824; [7] Britt, D.T., and C.M. Pieters (1994) *Geochim. Cosmochim. Acta 58*, 3905-3919; [8] Lucey, P. G., & Riner, M. A. (2011) *Icarus*, *212*(2), 451-462; [9] Charette, M.P., and J.B. Adams (1975), *Proc. Lunar Sci. Conf. 6th*, 2281-2289; [10] Gold, T., et al. (1976) *Proc. Lunar Sci. Conf. 7th*, p. 901-911; [11] Hapke, B., et al (1975) *Moon*, 13, 339-354; [12] McKay, D.S., et al. (1972) *Proc. Lunar Sci. Con;f. 3rd,* p. 983-994; [13] Grier *et al.* (2001) *J. Geophys. Res. 106*(E12), 32847-32862; [14] Raney, R. K., Cahill, J. T., Patterson, G. W., & Bussey, D. B. J. (2012). *Journal of Geophysical Research: Planets*, *117*(E12).

Investigating the Moon through a Hf/W lens

M.M. Thiemens[1,2], P. Sprung[1,3], R.O.C. Fonseca[1], F.P. Leitzke[4], V. Debaille[2], C. Münker[1], [1]Institute für Mineralogie und Geologie, Universität zu Köln; [2]Université libre de bruxelles, [3]Paul Scherrer Institut, Switzerland; [4]Steinmann Institute, University of Bonn

Understanding how planets formed in the early solar system is one of the most fundamental tasks of planetology. The Moon itself acts as a palimpsest which provides insights into when and how the Earth formed. Timing the Moon's formation divides scientists into two broad camps, one which favours an "old" Moon, (ca. 50 million years after solar system formation) while the other calls for a "young" Moon (older than 100 million after solar system formation). Key to these arguments is the observation of an excess of ^{182}W found in lunar samples compared to their modern terrestrial counterparts. The idea holds that a "late veneer" of material deposited after planetary formation would have deposited far less material on the Moon than the Earth, and that its inherited signature of unradiogenic W would thus overwrite the previous values.

To investigate this W signature and its origins, we combined recent experimental silicate-melt partitioning data with high-precision isotope dilution concentration analyses of W, Th, U, and high field strength elements on a large suite of lunar samples. Our results indicate that the Hf/W ratio of the lunar mantle (minimum 30) is higher than that of the bulk silicate Earth (Hf/W of 25.8). There are three broad scenarios that can account for the elevated Hf/W of the Moon. The first scenario holds that a late veneer of material with a Hf/W of ~1 lowers the Hf/W of the Earth-Moon system. As the Earth is struck by a proportionally larger amount of material, the bulk silicate Earth's ratio is lowered to 25.6, while the Moon retains a uniformly higher Hf/W closer to the original Hf/W of the system. The second explanation holds that the Moon forming event occurs while ^{182}Hf is extant, and the Earth's Hf/W is lowered following lunar formation by ongoing core formation and increasingly oxidized conditions on the Earth. The final explanation holds that the Moon forms while ^{182}Hf is extant, and the formation of the lunar core elevates the silicate Moon's Hf/W signature.

The results of our study imply that the ^{182}W excess is the result from in situ radiogenic ingrowth. These results lend credence to the idea of an "old" Moon, and diminish the need for a late veneer to explain the Moon's unique signatures.

Lunar Subsurface Exploration Technologies at the University of Glasgow: capabilities and the 'i-Drill' case study. R. Timoney[1], K. Worrall[1], P. Harkness[1], S. J. Barber[2], S. Sheridan[2] and N. Murray[3]. [1]School of Engineering, University of Glasgow, Glasgow, UK. G12 8QQ, r.timoney.1@research.gla.ac.uk [2]School of Physical Sciences, The Open University, Milton Keynes, UK. MK7 6AA. [3]Dynamic Imaging Analytics, Milton Keynes, UK. MK16 6GD.

Introduction:

A recent European focus on the exploration of the Moon, may provide the scientific community with opportunities to further understand our nearest neighbour, both in its own right and as an indicator of the rich history of our Solar System. Numerous missions are planned, starting with in-situ robotic exploration but envisaged to later involve sample return and new human sorties to the lunar vicinity.

Many missions will target previously unsampled high-latitude and/or Permanently Shadowed Regions (PSRs), in a quest to provide ground truth for orbital measurements that suggest elevated concentrations of water and other volatiles associated with these low-temperature environments. Such species are of high intrinsic scientific value; moreover the use of these materials as a potential feedstock within the emerging field of in-situ resource utilisation (ISRU) additionally makes them of particular interest to future mission planners. To this end, the authors propose technologies capable of the extraction and analysis of these volatiles, as candidate payload elements on these upcoming missions.

Drilling and Sampling Technologies:
Ultrasonic Planetary Core Drill (UPCD)

The University of Glasgow has experience in the development and testing of robotic planetary drilling and sampling systems which utilise a number of different technologies. The Ultrasonic Planetary Core Drill (UPCD) project [1], funded by an EC FP7 grant, ran from 2014-2017 and saw a consortium of European partners develop a drilling and caching system, based upon the ultrasonic-percussive technique, capable of autonomously extracting core samples of still-frozen regolith simulant as depicted in Figure 1.

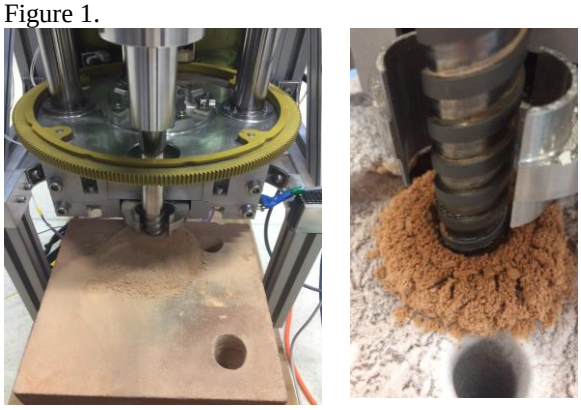

Figure 1: UPCD sampling dry (L) and saturated (R) Locharbriggs sandstone

This technology was tested at Coal Nunatak, Antarctica (73° S, 68° W) in December 2016 and proved to be a promising technology for use in potential Sample Return scenarios, capable of assembling, disassembling and caching in excess of three 10 mm core-containing drill bits, requiring 50 W of power on average to achieve this.

Percussive Rapid Access Isotope Drill (P-RAID)

The technologies developed for the UPCD project proved to be an excellent baseline for the development of a new system, the Rapid Access Isotope Drill (P-RAID), in collaboration with the British Antarctic Survey [2]. This cam-hammer driven rotary-percussive mechanism (Figure 2) was developed in order to sample subglacial bedrock cores – a longstanding aim within the field of paleoclimatology. Making use of the planetary drilling approach, P-RAID offers a solution to the problem which has a substantially lower resource demand than conventional, industrial approaches.

Figure 2: P-RAID architecture (L) and core samples of sandstone, limestone and microgabbro (R)

This technology has been tested in laboratory settings and also in a thermal vacuum chamber and has proven to be a robust means of obtaining samples of simulated planetary terrain, capturing cores with a diameter of 25 mm and as long as 300 mm. This can be achieved with as little as 70 W average power.

Ultrasonic Penetration of Granular Materials

The application of ultrasonic vibration to classic penetrometry tends to reduce both the overhead force and power required to insert the device to the required depths within granular terrain. Glasgow has

developed a knowledge base in this area through a longstanding expertise in the development of ultrasonic devices. Testing of these devices in settings such as the ESA ESTEC Large Diameter Centrifuge (LDC) suggests that they may be particularly suitable for use in low gravity environments [5]. Given that the reduced gravity found on the Moon may have a profound impact on the ability of lightweight landers and rovers to penetrate beneath the surface, ultrasonic penetrometers may be particularly useful. Furthermore, the fluidisation of granular material by the action of ultrasonic vibration may provide a useful means of conveying material against the direction of the gravity vector while benefiting from a reduction in mechanical complexity when compared to convention screw conveying/augering.

Ultrasonically Assisted Drilling (UAD)

In a manner not dissimilar to the previously discussed ultrasonic penetrometry, the application of ultrasonic vibration directly to a drill bit will reduce the weight on bit required to penetrate a target material [6]. While this technology has predominantly seen application in industrial-scale machining, testing at Glasgow suggests that it may be beneficial to apply this technology to planetary exploration.

'i-Drill' – an instrumented drill

i-Drill is an instrumented drill concept optimised to access the upper ~1 m of the lunar regolith. Thus i-Drill accesses both the surface layer that may exhibit signatures of transient surficial volatile enhancement and/or of contamination from the host spacecraft, and the deeper subsurface probed by remote sensing observations such as neutron detectors.

The concept shares many of its objectives with the Luna-27 PROSPECT package [3], with regolith being sampled by a drill and volatiles being released by heating for analysis in a mass spectrometer. However, whereas PROSPECT employs a complex, coring drill and an intermediate sample receiving and manipulation device to seal the cored sample and release volatiles by heating, i-Drill removes the need for precise robotic manipulation. This is accomplished by i-Drill employing a hollow drill-string, such that volatiles bound to the regolith are released through the drilling process and diffuse up the string for analysis in a (PROSPECT-type) ion trap mass spectrometer supplied by The Open University (OU). Further advantages accrue because the drill can be operated for maximum penetration performance, and the resultant heat generated is beneficial in enabling efficient release and transfer of evolved volatiles. This is in contrast to a coring drill, which must be operated carefully in order to minimise the generation of heat at the bit that may introduce unwanted thermal alteration of the sample.

i-Drill also supports imaging of the sampled lunar regolith, enabling the volatiles profiles obtained to be interpreted in the wider geological context of the site. Imaging of the bottom of the borehole and of the cuttings is proposed and shall be achieved through the use of a dual camera suite of LUVMI heritage [4] and provided by Dynamic Imaging Analytics (DIA).

i-Drill was conceived at Glasgow, OU and DIA in response to a ESA RFI call on European payload contributions for future lunar missions. Harnessing knowledge gained through a rich heritage of technology development in their respective fields of subsurface sampling, in-situ analysis tools and space imaging, i-Drill provides a low resource solution for locating and extracting volatiles on future lightweight landed missions. Crucially, it occupies a 'sweet-spot' in the trade between payload mass/power requirements and its capability in terms of accessing ~1 m sub-surface and performing crucial volatiles investigations supported by contextual imagery. It is envisaged that this package of drill integrated with powerful and complementary mass spectrometer and imagers shall form a mass- and power-efficient payload applicable to various near-term small lunar landers.

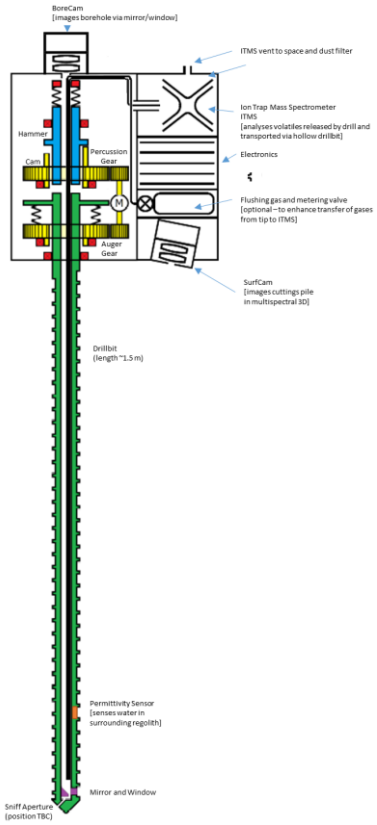

Figure 3: i-Drill Conceptual Schematic

References:

[1] Worrall K. et al. (2017) ASTRA 2017. [2] Timoney R. et al (2018) AGU Fall 2018. [3] Trautner R. et al. (2018). IAC 2018. [4] Urbina D. et al. (2017) IAC 2017. [5] Firstbrook D. et al. (2017). Royal Soc. [6] Firstbrook D. et al. (2017) Springer.

NOVEL APPROACHES TO ISRU: AQUEOUS ALKALINE PHASE ELECTROLYTIC REGOLITH REDUCTION AND OTHER WORK AT SPACESHIP EAC. L. Turk[1], A. Cowley[1] , L. Offermann[1], [1]European Astronaut Centre EAC, European Space Agency, 51170 Köln, Germany,

Introduction: In-Situ production of oxygen and other resources on the Moon is a significant technical challenge in enabling mass-efficient and sustainable human space exploration thereon. Spaceship EAC aims to develop and validate operational concepts and low-TRL-level technologies in support of lunar human exploration scenarios, as part of the ESA E3P/ExPeRt (European Exploration Envelope Programme/Exploration Preparation, Research and Technology) programme.

Using regolith simulant as starting material, in this instance EAC-1, this project has been looking at novel, yet industrially proven methods of oxide reduction such as the Molten Salt (FFC Cambridge and OS processes) Reduction and the Aqueous Alkaline Electrolysis. While there are various different promising pathways to achieve a reliable and cost-effective way to oxygen production [1], the aim of this work is to draw the scientific community's attention to novel approaches that have not been explored, or only partially, but have significant potential.

Aqueous Alkaline Regolith Electrolysis – Previous workers have suggested that low-temperature (383 K) electrolysis of pure Fe_2O_3 in extremely alkaline (pH 15+) suspensions can be done at remarkably high (95%+) efficiencies. This method finds its use in terrestrial ultra-low CO_2 steelmaking and in the production of high-purity iron [2]. As it works only at 100 °C, the Aqueous Alkaline Regolith Electrolysis could be an efficient, low energy process and simple in terms of implementation.

We have investigated the feasibility of reducing pure Fe_2O_3 and EAC-1 regolith simulant in similar conditions to Allanore et al. [2] and preliminary results indicate that partial de-oxidation does occur. We are presently working on better cell configurations and improved electrolyte parameters to better access the oxygen bound in the EAC-1 regolith simulant.

Novel molten salt approaches – It has been shown by Liu et al. [3] that, similarly to the FFC Cambridge and OS processes, partial reduction of Regolith simulants in near equimolar NaF / AlF_3 mixes, similarly to terrestrial Aluminium electrowinning, is feasible and produces an Al/Si alloy at the cathode and pure Oxygen at the anode. The challenge in selecting a corrosion-resistant anode can also be potentially tackled with the use of a Ni/Fe alloy.

The effect of low pressure is also investigated as high vacuum conditions will have to be dealt with in a Lunar setting, where evaporation of the hot, liquid electrolyte will occur. It has been shown that evaporation of $CaCl_2$ salt at typical operating temperatures of 1173 K is significant (5% loss over 30 min at 0,1 mbar). At Spaceship EAC, various electrolyte compositions are investigated that take into account the unique thermodynamic landscape of a mixed oxide. On the one hand, existing metallurgical processes are reviewed to better fit the unique characteristics of regolith, and on the other hand, thermodynamical simulations are conducted to help identify the ideal electrolyte for mare-type regolith simulants.

References:

[1] M. Anand et al. (2012) *Planetary and Space Science 74* 42–48

[2] A. Allanore, H. Lavelaine, G. Valentin, J.P. Birat, F. Lapicque, and P. Delcroix (2010) Observation of the reduction of iron oxide particles to metal in alkaline solution by electrolysis", *Electrochimica Acta, 55*, 4007.

[3] A. Liu et al. Lunar Soil Simulant Electrolysis Using Inert Anode for Al-Si Alloy and Oxygen Production *Journal of The Electrochemical Society, 164* (2) H126-H133 (2017)

LOOKING BACK 50 YEARS TO APOLLO 11. Grenville Turner, School of Earth and Environmental Science, University of Manchester, Manchester M13 9PL, grenville.turner@manchester.ac.uk

Introduction: On May 25th 1961 President John F Kennedy declared the goal, 'before this decade is out, of landing a man on the moon and returning him safely to the Earth'. So began the Apollo program, leading to the landing of the Apollo Lunar Module Eagle on the Moon's surface on July 20th, 1969. The intervening eight years had seen intense activity with a major setback in January 1967 with the tragic deaths of astronauts Roger Chaffee, Ed White and Gus Grissom in the fire of the Apollo 1 command module. Major redesign led to the first manned launch, Apollo 7, on October 22nd, 1968, and two months later Apollo 8. On Christmas Eve Apollo 8's orbit took it out of radio contact behind the Moon. Radio audiences across the world waited anxiously for the radio silence to end and were memorably rewarded with a reading by the crew of a passage from Genesis. Further testing followed on Apollos 9 (March) and 10 (May) with a 'dress rehearsal' partial descent towards the lunar surface by the latter.

Science and Planning for Apollo: Scientific exploration of the Moon was seen by some as a distraction from the daunting engineering task. Nevertheless members of the small community of lunar scientists pursuaded NASA to set up in 1962 an ad hoc working group to provide guidelines for an ambitious Apollo science program. The Sonett report published in December 1963 was extremely ambitious but many of its proposals survived in the program developed for the six lunar landings. An early result was the automated Lunar Orbiter spacecraft, used to provide the basis for site selection. Amazingly, because of limitations to 1960s digital technology the Orbiters used actual photographic film, developed chemically in situ in the spacecraft providing images to be scanned for telemetry to Earth.

Surface Activity; Activities on the lunar surface, in addition to sample collection, included setting up passive and active seismometers (A11,12, 14,15,16), corner cube laser ranging retro reflectors (LRRR), solar wind collecting foils (Swiss flag experiment), heat flow measurements (A15, 17), lunar neutron probe (A16), cosmic ray detection, magnetometry, and other experiments. An exciting early result came from the passive seismometer (A11). Seismic events from meteorite (and spacecraft) impacts gave unusual traces having 'emergent' beginnings and very long (1 hour) duration, leading to newspaper reports that 'the Moon rang like a bell'. This was explained as a result of low attenuation (high Q) and intense scattering in the crust, leading to the view of a very dry Moon and a 20km deep 'mega regolith'. The seismic array was switched off in 1977 but has provided vital data on the structure of the Moon, including evidence from deep (800km) moonquakes. In an early 'geodetic' result from LRRR the laser pulse round trip travel time between Earth and Moon indicated an error in the published co-ordinates of the Lick Observatory!

NASA Policy and Lunar Sample Analysis: After extensive consultation with expert panels NASA chose 142 Principal Investigators and teams, to provide a full scientific coverage but without unnecessary duplication. Generously 31 of these PIs were from outside the USA. NASA had a number of 'worries' concerning the sample analysis: (1) A worry over possible bio-contamination of Earth was 'solved' by feeding lunar soil to mice and other fauna. (2) The possibility of a black market in lunar samples was solved by careful legal contracts and rules on PI storage facilities. (3) A wish to avoid an unseemly scramble for publication of early results led NASA to place an embargo on publication until after the Apollo 11 Lunar Science Conference, held in downtown Houston from 5th to 8th January, 1970. On a personal level this helped balance the playing field for a small group such as mine.

Early Sample Analyses: The 1970 Conference must be unique in the vast amount of new information and conflicting ideas presented to conference delegates over such a short period of time. What were the highlights? Sample ages? A reading of the chronology papers in the 'Moon Issue' of Science indicates only two groups presented accurate ages; five Ar-Ar ages from Sheffield (Turner) and four Rb-Sr ages from CalTech (Wasserburg). A confusion of 4.6 Ga Pb-Pb 'ages' from lunar soil led to much inconclusive discussion. John Wood (Smithsonian) found fragments of anorthosite in coarse fines and presented a model of a 25 km anorthositic crust. Why didn't I arrange to get some from him for Ar-Ar?. Much discussion on the Europium anomaly and the suggestion of a matching positive Eu anomaly in the crust, later confirmed. REE enrichments in the basalt were explained in terms of low degrees of partial melting of a clinoperoxenite mantle. Presentations on petrology and mineralogy were amazing for the beauty of thin sections of completely unweathered 3.6 Ga basalts. Noble gas analyses of lunar soil by several groups showed similar elemental and isotopic patterns to Howardite meteoritic regolith breccias. $^{40}Ar/^{36}Ar$ ratios were accounted for by a memorable interjection from the audience by Thomas Gold. Enrichments of Ir and other elements indicated a 2% meteoritic component, while solar wind was a major source of carbon. Nuclear tracks provided hours of fun and neutron stratigraphy began providing data for statistical models of regolith development. By 1975 our view of the Moon had matured including a theory of how it formed.

RECENT EVENTS AT THE APOLLO 17 LANDING SITE: AGES OF THE LEE LINCOLN SCARP, LIGHT MANTLE DEPOSIT, AND TYCHO CRATER. C. H. van der Bogert[1], H. Hiesinger[1], W. Iqbal[1], J. D. Clark[2], M. S. Robinson[2], B. L. Jolliff[3], T. M. Hahn Jr.[3], T. R. Watters[4], M. E. Banks[4,5], H. H. Schmitt[6]; [1]Institut für Planetologie, Westfälische Wilhelms-Universität, Wilhelm-Klemm-Str. 10, 48149 Münster, Germany (vanderbogert@uni-muenster.de); [2]Arizona State University, Tempe, AZ, USA; [3]Washington University in St. Louis, St. Louis, MO, USA; [4]Smithsonian Institution, Washington DC, USA; [5]NASA Goddard Space Flight Center, Greenbelt, MD, USA; [6]University of Wisconsin-Madison, WI, USA.

Introduction: The Apollo 17 landing site exhibits a complex geological history that is in part characterized by several relatively recent events: (1) the Lee Lincoln lobate scarp (LLS), (2) a light mantle deposit (LMD), and (3) a cluster of secondary craters, known as the Central Cluster (CC). The latter two features were previously related to the formation of Tycho crater [1-7], and ages derived from these features were used for the Tycho crater lunar cratering chronology calibration point [5]. However, recent work dating the LLS determined an age similar to Tycho crater [8], which raised the possibility that the formation of the LMD was instead triggered by seismic shaking from a LLS event [1,8,9]. Here, we review and discuss the origins and ages of these recent events.

Background: Both the CC and LMD are argued to have an origin related to Tycho crater, because (1) both units exhibit distinct, fine-structured, birdsfoot patterns characteristic of Tycho ejecta, which point toward the South Massif and Tycho crater, (2) the downrange extent of the LMD is similar to downrange extents of individual Tycho secondaries, (3) the craters in the CC and at the summit of the South Massif are similar in size and morphology, and (4) both sets of craters are part of a larger cluster (10's of km long) aligned in a trajectory from Tycho crater, that includes additional secondaries on North Massif and Littrow crater [5,7]. Additional analyses of the elongation directions of crater clusters, azimuth trends in the V-shaped grooves, in addition to CSFD measurements, were argued to support a Tycho origin for the secondaries on South Massif and in the CC [6].

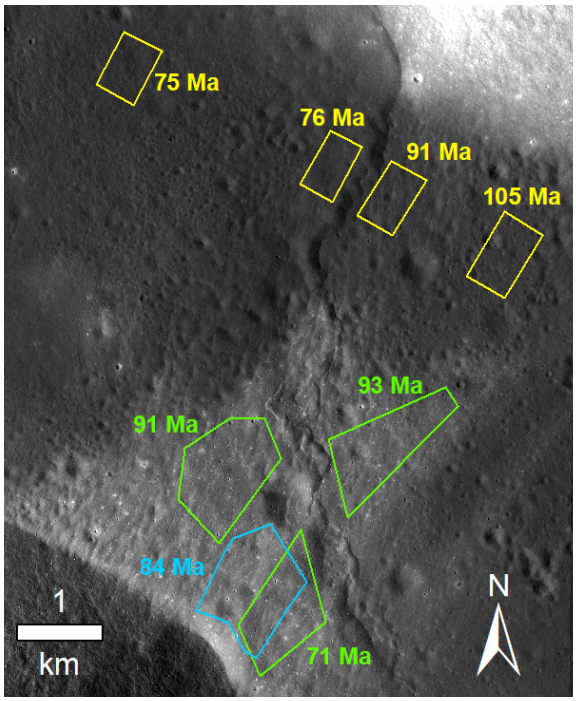

Figure 1. *Locations of count areas on the light mantle deposit (green, [23]; blue, [24]) and Lee-Lincoln scarp (yellow, [8]). The errors on the AMAs (see text) mean they are not significantly different from one another or from NAC-derived ages determined for Tycho.*

The exposure ages of three samples from the CC and one from the LMD led [6] to conclude that both the LMD and CC formed ~100 Ma ago. Additional exposure ages were determined by [10] for the CC and Sculptured Hills areas, but not for the LMD. In sum, the results from [10] indicated an age of ~109±4 Ma for the CC and LMD, which [10] interpreted as the age of Tycho crater. However, an unexpectedly broad range of exposure ages were measured at the Apollo 17 landing site, in contrast to similar studies at North Ray, South Ray, and Cone craters. As a result, [10] postulated might result from (1) more complicated shielding histories than the assumed single-stage exposure model, (2) failure of the dating analyses, or (3) an absence of a "single dominant event" at the Apollo 17 site [10]. Drozd et al. [10] rejected the latter option as being unnecessarily complicated, but the result of [8] motivates a reevaluation.

Data and Methods: Crater size-frequency distribution (CSFD) measurements were made using CraterTools [11] on Lunar Reconnaissance Orbiter Narrow Angle Camera (LRO NAC) images and products in ArcGIS, and plotted and fit with CraterStats [12,13], using techniques described in [14,15]. The derived absolute model ages (AMAs) use the production and chronology functions of [15].

Absolute Model Ages of the Lee Lincoln Scarp: The absence of many >~100 m diameter craters superposed on the scarp, along with its morphological freshness, indicates that the LLS is young [16-19]. Recently, [14] also showed that CSFD measurements can be used to derive scarp age estimates. Using this approach, we determined that the last significant activity on the LLS occurred ~75 Ma ago (***Fig. 1***, yellow; [8]). Preliminary buffered CSFD

measurements give an age <75 Ma. However, the validity of this approach is challenged by the fact that the LLS crosses significant topography (North Massif), making the technique non-ideal due to the erasure of small craters via mass wasting, including downslope creep [e.g., 14,20,21].

Absolute Model Ages of the Light Mantle Deposit(s): CSFDs on the LMD and CC were shown to be consistent with CSFDs at Tycho crater [22]. New count areas of the LMD using recent NAC data (***Fig. 1***, green; combined age of ~86 Ma) match NAC measurements on Tycho ejecta (85+15/-18 Ma) [23]). We also determined a new AMA of 84±5 Ma (***Fig. 1***, blue) that excludes Tycho ray material [24]. Based on Monte Carlo simulations, the errors for count areas of about 1 km^2 in size and 100 Ma in age are ~±10 Ma [25].

Discussion: In addition to morphological evidence, [7] used the results of other studies to infer that the LMD and Tycho ejecta were coeval (e.g., similar crater densities, equilibrium diameters (C_s), largest unshadowed crater diameter (D_L), and regolith thicknesses on the LMD and Tycho ejecta deposits). The similarity of the CSFDs [6,7,22,23] and exposure ages of samples [6,10] from both the CC and LMD also point to a common origin. However, our work on dating the LLS, particularly in the context of the errors on the AMAs determined in the Taurus Littrow valley, suggests the LLS is also statistically coeval with the LMD and Tycho crater. The spread in the exposure, as well as CSFD ages, is plausibly explained by the occurrence of multiple events ~75-110 Ma, rather than one discrete event. Given that the Tycho secondaries and LLS are unrelated, the question remains – which event triggered the formation of the LMD?

As described, many earlier studies found morphological and other support for a Tycho event origin, and [1] also observed fresh scarp morphologies on the LMD, suggesting that the LLS post-dated the LMD. The small back-scarp graben, both on the LMD and Taurus Littrow floor are likely younger than the LMD itself [26]. However, it is unclear whether multiple scarp slip events could account for both pre- and post-LMD morphologies.

In addition, photometric analysis of the LMD [9,27,28] may indicate the presence of more than one landslide deposit. The different photometric characteristics of the LMD must then be explained either by different thicknesses across the deposit, or by multiple slides due to repeated slip events on the LLS or by both Tycho secondary impacts and LLS slip.

Despite giving an AMA of ~75 Ma, the LLS might still currently be active, with some level of activity causing continued slip and the creation of small <50 Ma old back-scarp graben [26,29], possibly also triggering boulder accumulations [29] and falls, such as Boulder 1, Station 2 (exposure age of ~45 Ma, [30]). Activity on the LLS, which erased craters <30 m in diameter, could have also reset the AMA of the LMD such that the surface reflects the age of a coseismic slip event, rather than the formation age of the LMD. Seismic shaking associated with the scarp might be expected to have reset or complicated the exposure history of collected samples, which might also help explain the broader than expected range in exposure ages reported by [10], including boulders with young exposure ages.

New geological maps and interpretations for Taurus Littrow valley [e.g., 24], plus more CSFD measurements, may provide the means to constrain the timing of the recent events near the Apollo 17 landing site.

Implications: While the exposure ages of samples primarily from the CC underpin the formation age of Tycho crater for the lunar cratering chronology, using the CC to obtain an $N(1)$ for Tycho is complicated by the fact that it is a cluster of secondary craters. CSFD measurements rely on the observation of primary craters and require the elimination of counting areas containing known secondary craters. Thus, the $N(1)$ value for the Tycho crater lunar cratering chronology calibration point is primarily measured on the LMD, due to the presumed common origin with Tycho crater. If the LMD is not in fact related to Tycho crater, what does this mean for the Tycho crater calibration point? Currently, our study indicates that the AMAs of the LMD and Tycho crater ejecta deposits are still statistically similar. Thus, the calibration of the lunar cratering chronology for the $N(1)$ of Tycho is not likely to be significantly in error.

References: [1] Lucchitta (1972) USGS Map I-800, 2. [2] Scott and Carr (1972) USGS Map I-800, 1. [3] Muehlberger et al. (1973) *Apollo 17 Prelim. Sci. Report*, NASA SP-330, 6-1. [4] Howard (1973) *Science* 180, 1052. [5] Wolfe et al. (1975) *PLPSC* 6, 2463. [6] Arvidson et al. (1976) *PLPSC* 7, 2817. [7] Lucchitta (1977) *Icarus* 30, 80. [8] van der Bogert et al. (2012) *LPSC* 43, 1847. [9] Schmitt et al. (2017) *Icarus* 298, 2. [10] Drozd et al. (1977) *PLPSC* 8, 3027. [11] Kneissl et al. (2011) *PSS 59*, 1243. [12] Michael and Neukum (2010) *EPSL 294*, 223. [13] Michael et al (2016) *Icarus* 277, 279. [14] van der Bogert et al. (2018) *Icarus* 306, 255. [15] Neukum et al. (2001) *Space Sci. Rev. 96*, 55. [16] Lucchitta (1976) *PLPSC* 7, 2761. [17] Schultz (1976) *Moon Morphology*, Austin, TX. [18] Binder and Gunga (1985) *Icarus* 63, 421. [19] Watters et al. (2010) *Science* 329, 936. [20] Basilevsky (1976) LSC 7, 1005. [21] Meyer et al. (2016) LPSC 47, 2740. [22] König (1977) PhD Thesis, Univ. Heidelberg, NASA TM-75023. [23] Hiesinger et al. (2012) JGR 117, E00H10. [24] Iqbal et al. (2019) LPSC 50, 1005. [25] van der Bogert et al. (2015) Wkshp on Crater Studies, 9023. [26] Watters et al. (2012) *Nature Geoscience* 5, 181. [27] Hahn et al., LPSC 49, 2637. [28] Hahn et al., LPSC 50, #1963. [29] Watters et al. (2015) Geology 43, 851. [30] Leich et al. (1975) *The Moon* 14, 407.

IMPROVING OUR KNOWLEDGE OF LUNAR SUB-SURFACE AND INTERNAL STRUCTURE AND COMPOSITION WITH GRADIOMETERS AND GRAVIMETERS.

J. Guérard[1], B. Christophe[1], R. Lévy[1], O. Le Traon[1] and J.-C. Matéo-Vélez[2], [1]ONERA BP72 - 29 avenue de la Division Leclerc - FR-92322, Châtillon, France (Jean.Guerard@onera.fr); [2]ONERA BP74025 - 2 avenue Edouard Belin, FR-31055 Toulouse, France

Introduction: We present two instruments that could be developed for future lunar missions using heritage in gradiometers and gravimeters. On one hand, as it was proved by GOCE mission, the gradiometer can provide a very accurate static gravity field, allowing to improve our knowledge of the structure and composition of the lunar interior. A gravity gradiometer with 1E/Hz$^{1/2}$ noise spectral density on a 50 km altitude polar orbit could improve by a factor 10 the GRAIL accuracy objective [1]. In [2], a gradiometer with a performance of 10 to 1 mE/Hz$^{1/2}$ is proposed to improve the gravity field from the GRAIL mission. On the other hand, an identified issue of future human settlement on the Moon is the harmful effect of radiations, from both Solar wind and Cosmic rays. An efficient and commonly discussed solution is the existence of lava tubes offering shielded sub-surface void spaces. Such tubes have been suspected on the Moon surface thanks to previous orbital cartography missions (LRO, SELENE). Once localized by visible skylights, the tubes shall be mapped underground. It is known that a 20m diameter 30m deep tube is responsible for a gravity anomaly of 1 mGal at ground level. This can be achieved by gravimetry.

Gradiometer on orbit: Cubstar Electrostatic Gradiometer for Lunar Orbiter (CEGLO) is a gradiometer based on the heritage of electrostatic accelerometer developed for Earth gravity missions GRACE, GOCE and GRACE-FO. It is based on the electrostatic accelerometer CubSTAR, a miniaturized version of the accelerometers which have already flown, with a cubic proof-mass to provide the same performance along the 3 axes.

The gradiometer could be composed by the association of 2 to 8 accelerometers, providing the gravity gradient along 1 or 2 directions or the complete tensor, see Figure 1. The gravity gradient along one direction is obtained by the difference of acceleration measurement from both accelerometers along the axis, after substraction of the centrifugal acceleration. The centrifugal acceleration is deduced from the accelerometers which measure the angular accelerations around the 3 axes. It is also possible to deduce the angular acceleration from the comparison of linear acceleration measurement as in GOCE. The accelerometers developed by ONERA are based on the electrostatic suspension of a proof-mass. The principle of the acceleration measurement consists in the measurement of the voltage necessary to maintain a proof mass in electrostatic levitation in the centre of a cage placed at the centre of gravity of the satellite. This electric voltage represents the effect of surface forces only when the accelerometer is located at the satellite center of gravity. In case of an accelerometer not located at the center of gravity of the orbiter, the accelerometer measures also the gravity gradient with respect to the center of gravity, as well as the inertial acceleration due to the attitude motion of the orbiter. This is the configuration proposed for a gradiometer in lunar orbit.

Figure 2 presents the Sensor Unit Mechanics (SUM). It consists of a ULE proof mass, suspended inside an electrode cage (gold coated silica): the proof mass motion is servo-controlled using capacitive sensors. This core (mass and electrode cage) is enclosed by a sole-plate and a housing in which vacuum is maintained with a getter. Proper operation of this getter is insured on ground by periodic reactivation of the getter material by a heat-out process. The SUM vacuum unit is surrounded by four boxes containing front-end electronics.

The main contributors of CubSTAR noise as well as the one of one gradiometer arm with a distance between both accelerometer proof-masses of 140mm have been identified. The gradiometer performance achieve 10 mE/Hz$^{1/2}$ in [10-100] mHz bandwidth and 40mErms in [0.1-100]mHz, making it relevant for measurements on-board an orbiter at 50 km altitude.

The following table provides the budget for the different configuration with 2, 4 or 8 accelerometers.

	CEGLO-2	CEGLO-4	CEGLO-8
Mass [kg]	6	12	24
Size (SUM part) [cm]	14x28x16	28x28x16	28x28x32
Size (PCU part) [cm]	12x12x10	12x12x20	24x12x20
Power Consumption [W]	16	32	64
Data Rate [Mbits/s]	4.6	9.2	18.3

Gravimeter on rover : gravity acceleration can be measured by means of a vector accelerometer with Miniature surface Unveiling Gravimeter (MUG). The core of the instrument is the Vibrating Beam Accelerometer developed and patented at ONERA [3], and transferred to industry [4]. It shows excellent stability of its scale factor (the ratio between the output signal of the sensor and the applied acceleration) guaranteed by monocristalline α-quartz properties. The patented geometry allows an excellent stability of the measurement bias compared to other miniature accelerometers.

More recently, an improved version of the accelerometer shown on Figure 3 has been developed and validated, together with a new generation of highly integrated digital electronics. Enhanced performances in resolution, scale factor and bias stability enable to use it for gravimetric measurements. The low mass and power consumption of the payload enables it to be embedded in a rover. It enables to perform gravimetric measurements with a 0.3 mGal resolution making it relevant for measurement on-board a rover to map 10m scales lava tubes. Total mass is less than 0.8 kg. Volume is less than one cubesat unit. Science data is 520 kbit/day. The current TRL of the accelerometer is TRL 9 as it has been transferred to industry and is already manufactured and used in systems. The other parts of the payload to be developed in the frame of lunar exploration have been identified.

References: [1] Carroll, K. A. (2011) *LPSC XLII*. [2] Zheng, X., et al. (2015) *Surv Geophys* 36:111–137. [3] Le Traon O. et al. (1999) U.S. Patent No. 5,962,786. [4] Loret, T., et al. (2014) *Inertial Sensors and Systems Symp.*

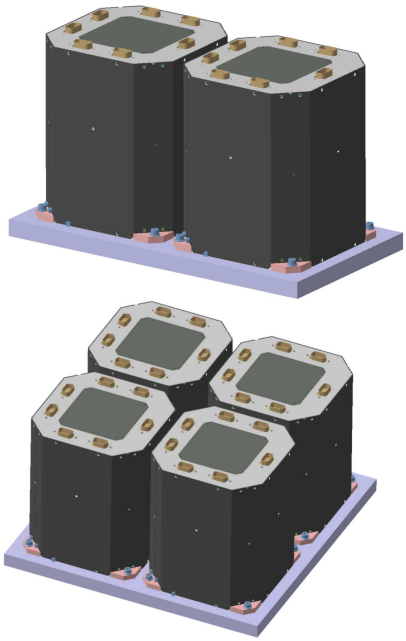

Figure 1: 2 different configurations of the CEGLO gradiometer with 2 CubSTAR accelerometers (top) and 4 Cubstar accelerometers (bottom). 8 Cubstar accelerometers is a third possible configuration (not represented).

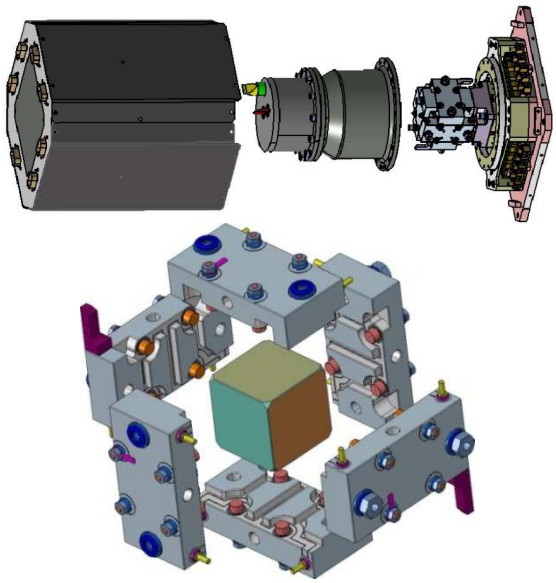

Figure 2 : CubSTAR Accelerometer Sensor Unit (exploded view of SU on top and of the electrode core with the proof-mass on bottom)

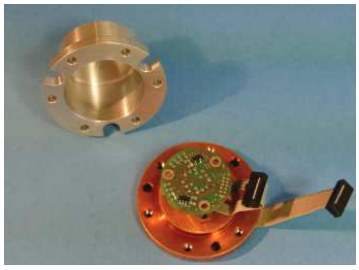

Figure 3: Packaged MUG sensor including the vibrating beam micro accelerometer core (1 inch diameter)

A QUANTITATIVE EVOLVED GAS ANALYSIS FOR LUNAR AND METEORITIC MATERIALS. A. B. Verchovsky, M. Anand and S. J. Barber, School of Physical Sciences, The Open University, Walton Hall, Milton Keynes MK7 6AA, UK, sasha.verchovsky@open.ac.uk

Introduction: Evolved gas analysis (EGA) is a powerful tool widely used in different fields of research from investigations of chemical compounds in chemistry (polymers, complexes, catalysts, composite materials etc.) to technology (coating, food production, batteries etc.) to environment and Earth Sciences [1]. It consists of linear heating of a material with registration of the released volatile compounds by different methods such as gas chromatography, infrared spectroscopy and mass spectrometry (MS). The latter seems to be the most popular and effective method of volatiles registration since it provides a quick scan for a wide range of masses if quadrupole mass spectrometer (QMS) is used.

This method was successfully applied to Apollo lunar samples in the early 1970s [2, 3]. Gases from solar wind, inclusions and chemical reactions between different phases have been identified. Different lunar samples can be compared with each other in terms of the release patterns of different gas species. But quantitative comparison of the amount of gases present in different samples was not possible. By developing Quantitative EGA (QEGA), we enable new insights into laboratory analyses of extraterrestrial samples. QEGA also informs the design and operation of spaceflight instruments being developed to perform analogous experiments *in situ* on the lunar surface such as within the European Space Agency's PROSPECT package [4]. The quantitative determination of volatiles within lunar regolith is also important for *in situ* resource utilization (ISRU).

In this study we developed a QEGA just for QMS system without a carrier gas by calibration of the measuring instrument with reference gases, for which flow rate is determined independently in order to convert the signals from different gas species from samples into their flow rates, ultimately leading to their quantification and comparison with different samples. The method has been applied for analyses of the Murchison reference sample and lunar soils.

Experimental technique: We used our custom-built Finesse mass-spectrometer system [5, 6], which contains a Hiden Analytical quadrupole mass spectrometer (QMS) equipped with an electron multiplier and evacuated by turbomolecular and ion pumps. The sample is wrapped in Pt foil and heated linearly within a furnace capable of reaching 1500 °C.

Several reference gases for calibration (single gas or gas mixtures) at 5-10 bar pressure were placed into a vessel connected to the vacuum system via a capillary leak or piezo-electric (PZT) metering valve. The (mostly viscous) flow rate was regulated either manually with a crimp (in the case of capillary) or automatically through software control of the voltage applied to the PZT valve. The flow rate was determined using a high sensitivity and precision MKS Baratron® capacitance manometer.

In addition we used a number of pure chemical compounds such as $CaCO_3$, $NaHCO_3$, $CaC_2O_4*H_2O$ etc., which are decomposed according to their stoichiometry into gaseous components upon heating.

Calibration procedures: For calibration, we used pure gases or a gas mixture with 11 gas species (H_2, He, CH_4, Ne, N_2, CO, O_2, Ar, CO_2, Kr and Xe with the following relative abundances: 56.78, 15.91, 1.452, 0.1011, 15.42, 1.03, 2.98, 1.002, 5.288, 0.02022, 0.01516 vol %, resp.) with well determined relative abundances (~1% rel.) resembling those observed in lunar soils. First, the gas flow rate was determined. For that, the reference gas was accumulated during a certain time in the volume of Baratron and the pressure was recorded after equilibration. The procedure was repeated several times with different accumulation time, which gives flow rate expressed in mbar/s. Subsequently, the reference gas was directed to the QMS and signals for a number of masses in the range from 2 to 132 (2, 4, 12, 14, 16, 18, 20, 22, 28, 29, 30, 32, 36, 40, 44, 84, and 132) were recorded in the continuous flow, using peak jumping mode and ion counting. For the same reference gas the procedure was repeated several times for different flow rates in the range from 10^{-8} to 10^{-4} mbar/s. Flow rate in mbar/s can be converted into ml/s, if the volume in which the gas is accumulated during Baratron measurement is determined. By integrating the release curves the gas concentrations in ml/g can then be obtained.

For calibration with chemical compounds we used the same heating rate as for the sample. In this case direct comparison of the areas under corresponding peaks for the reference material and sample gives concentration of gases.

Calibration results: The dependence of the signal intensities at different masses on the gas flow rate are in general non-linear but can be well approximated by a power law (Fig. 2). Although the calibration gas mixture contains 15% of N_2 and 1% of CO, we do not see a contribution of CO on mass 28, since calibrations with pure N_2 and the gas mixture yield the same line within scatter of the experimental points. For this reason the mass 12 has been used for calibration of CO, since pure CO also gives signal at that mass, which is about only 30 times less strong comparewd to that at mass 28.

The use of pure gases for calibration enables the characterization of second order signals produced by

some molecular gases as a result of their dissociation in the QMS. The second order mass for N_2 is 14, for CO is 12, for O_2 is 16, and CO_2 gives masses 28 and 16 in nearly equal amounts. Knowing the ratios between the main and second order signals for these gases allows us to calculate contribution of different gas species when they are present in a mixture and therefore, may contribute towards similar isobaric interferences, e.g. for N_2, CO and CO_2 at mass 28.

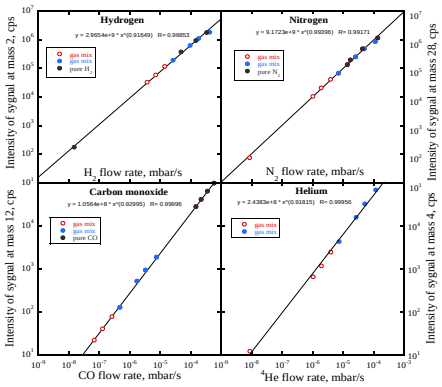

Figure 1. Representative QMS calibration curves for various gases.

Analysis of the PROSPECT reference Murchison meteorite sample: As part of ESA's PROSPECT lunar exploration activity, a reference sample of Murchison (CM2) meteorite has been developed as a standard for volatile species investigations. A 3 mg powdered sample was heated at a rate of 6°/min from 200 to 1400 °C with recording of signals at 17 masses mentioned above, every second, such that about 10 scans were made at each temperature. A blank correction was applied through subtraction of the signal produced through a 'blank analysis' of an empty furnace.

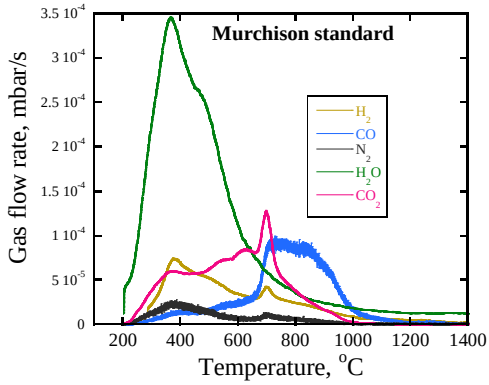

Figure 2. Release pattern of the major gas components from Murchison meteorite standard.

The release pattern for each gas has been recalculated into flow rate variations using corresponding calibration curves (Fig. 3). As can be seen, water is the major component and this is only a lower limit for its amount since a part of it was condensed in the vacuum line between the furnace and the QMS. However, the release pattern of water seems not to be affected by its condensation in the pipes. Mass 28 is represented essentially by CO because it shows identical spectrum with mass 12. Therefore, for calculations of N_2 amounts, we used signal at mass 14. Release pattern of CO_2 is almost identical to that for mass 16, suggesting the presence of a small amount of methane. Mass 20 is almost exclusively associated with water ($H_2{}^{18}O$). Among the minor components, we observe ^{4}He, oxygen, Ar and Kr (Fig. 4).

Water, hydrogen and nitrogen are released mostly at lower temperatures (200-600 °C), whereas CO_2 and especially CO are released at higher temperatures. For most gases, except for water and CO, a spike at ~700 °C is observed reflecting probably chemical reactions or structural transformation of the heated material.

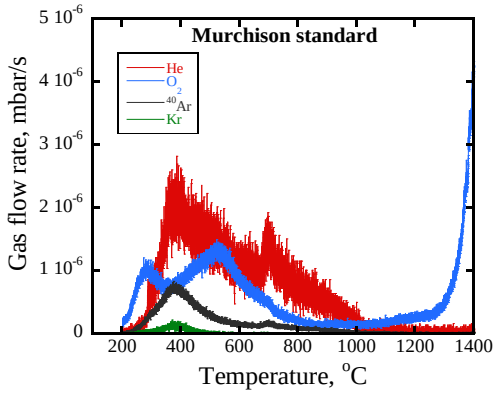

Figure 3. Release pattern of minor components from Murchison

The results for gas concentrations in ml/g in the Murchison standard obtaind by EGA and their comparison with those obtained by combustion [7] will be presented at the conference.

Conclusion: For the first time a quantitative method for EGA has been developed and successfully applied for the analysis of Murchison meteorite. We plan to improve calibration of the system for water and apply the method for the analyses of lunar samples. The method will also be implemented *in situ* on the Moon within the PROSPECT project.

Acknowledgement: This work was funded by UKSA (grant# ST/R001391/1 to MA and SB). PROSPECT is a program of and funded by ESA.

References: [1] Risoluti R and Materazzi S. (2018) *Applied Spectroscopy Reviews*, 1-29. [2] Gibson E. K. Jr. and Jonson S. M. (1971) *Proc. 2-nd LSC*, 2, 1351-1366. [3] Gibson E. K. Jr. and Moor G. W. (1973) *Proc. 3-d LSC*, 2, 2029-2040. [4] Barber S. J, et al. (2018) *VXIX LPSC*, abstr. #2083. [5] Wright I P. et al. (1988) *J. Phys. E* 21, 865-875. [6] Verchovsky A. B. (2017) *Geochem. Intern*. 55, 957-970. [7] Mortimer J. et al. (2017) ELS, abstr.

USING THE EUROPEAN SPACE AGENCY (ESA) TECHNOLOGY DEVELOPED FOR MARS RETURN FOR A MOON CRYO-SAMPLE RETURN. John Vrublevskis[1], Mark Jones[1], Lucy Berthoud[1], Michael Guest[1], Ysatis McCulloch[1], Portia Bowman[1], Steve Duncan[1], Russell Hills[1], John Holt[2], John Bridges[2], Caroline Smith[3], Allan Bennett[4], Francois Gaubert[5], Ludovic Duvet[6], Michel van Winnendael[5], Frank van der Hulst[5], Ray Robins[7], Doina Pisla[8], Calin Vaida[8], Bogdan Gherman[8], Michael Hofbaur[9], Bernhard Dieber[9], Narendrakrishnan Neythalath[9], Guido Breitenhuber[9], [1]Thales Alenia Space UK Limited, Building 660, Bristol Business Park, Bristol, BS16 1EJ UK john.vrublevskis@thalesaleniaspace.com, , [2]Space Research Centre, Department of Physics and Astronomy, University of Leicester, Leicester, LE1 7RH UK jmch1@leicester.ac.uk, [3]The Natural History Museum, Cromwell Road, London SW7 5BD UK caroline.smith@nhm.ac.uk, [4]Public Health England, Porton Down, Wiltshire SP4 0JG UK allan.bennett@phe.gov.uk, [5]ESA-ESTEC, Keplerlaan 1, Postbus 299, 2200 AG Noordwijk NL Francois.Gaubert@esa.int, [6]ESA-ECSAT, Fermi Avenue, Harwell Campus, Didcot, Oxfordshire, OX11 0FD UK Ludovic.Duvet@esa.int, [7]Felcon Ltd, Euro Business Park, New Rd, Newhaven BN9 0DQ Ray.Robins@felcon.co.uk, [8]Technical University of Cluj-Napoca, Research Center for Industrial Robots Simulation and Testing, 28, Memorandumului, Cluj-Napoca, 400114 Cluj, Romania doina.pisla@mep.utcluj.ro, [9]Joanneum Research Forschungsgesellschaft mbH, Institute for Robotics and Mechatronics Lakeside B08a, 9020 Klagenfurt am Wörthersee, Austria Bernhard.Dieber@joanneum.at

Introduction: The European Space Agency (ESA) technology currently developed for Mars sample return [1] and can be readily adapted for a moon cryo-sample return [2].

ESA have initiated two 'breadboard' developments to demonstrate the key technologies used in isolators using robotic manipulation. Commercial Off The Shelf (COTS) hardware is being employed at room temperatu,re very clean dry nitrogen environment, to demonstrate current technology capabilities. Results from the isolators and robotic manipulation breadboards have shown the system to be feasible. The breadboards aim to give a first insight and assessment for the sample management in total isolation from human handling. A set of automated robotic systems will be housed inside the isolators and robotic manipulation used to provide both manipulation of the sample at macroscopic & microscopic level. The isolator will be fully integrated with instrumentation for preliminary analysis of sample material (Environmental SEM, Raman Spectroscopy, X-Ray Tomography & Microscopy) as well as GC-MS to analyse isolator gas.

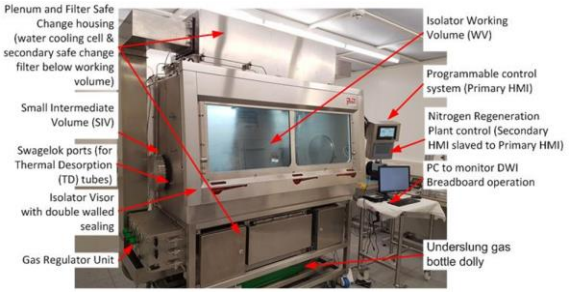

Fig. 1 Double Walled Isolator Breadboard at the Space Research Centre, clean room University of Leicester.

This breadboard could be modified for use at the low temperature required by a moon cryo-sample return. The robotic manipulation would enhance operator capability (e.g. autonomous actions in certain regions of the isolator) and remove mundane tasks (e.g. automatic isolator internal wipe down at end of working day).

References:

[1] J. C. Bridges and M. Guest, "Planetary Protection and Mars Sample Return," Journal of Aerospace Engineering, vol. 225, no. 2, pp. 239-246, 2011.

[2] J. Vrublevskis et al., "Concept for a Lunar and Asteroid Receiving Facility (LaARF)", Science and Challenges of Lunar Sample Return Workshop, 19 February 2014

BULK DENSITY AND POROSITY OF THE UPPER LUNAR CRUST FROM HIGH-RESOLUTION GRAIL AND LOLA DATA. D. Wahl[1], M. A. Wieczorek[2] and J. Oberst[1,3] [1]Technische Universität Berlin, Chair of Planetary Geodesy, 10623 Berlin, Germany (daniel.wahl@tu-berlin.de), [2]Observatoire de la Côte d'Azur, Laboratoire Lagrange, 06108 Nice, France, [3]German Aerospace Center (DLR), Institute of Planetary Research, Department of Planetary Geodesy, 12489 Berlin, Germany.

Introduction: The lunar interior reveals insights about the formation and evolution of the Moon and the terrestrial planets. From the characteristics of the lunar crust we can learn more about the development of an ancient magma ocean and subsequent alterations through impactors during the late heavy bombardment.

Latest investigations of the bulk density depend on remotely determined gravity and topography data. Wieczorek et al. [1] investigated lateral variations in bulk density and porosity using a gravity model from Gravity Recovery and Interior Laboratory (GRAIL) mission [2] of degree and order 420. The resulting maps have a grid size of 60 km, where each point was calculated using circles of 6° radius. A mean density of 2550 kg m^{-3} was found, significantly lower than in earlier studies.

Gravity and topography data: We used the most recent GRAIL gravity model GL1500E and truncated the dataset to an upper limit of degree 700, to avoid contribution of noise from high degree coefficients. In addition, we used topography data from the Lunar Orbiter Laser Altimeter (LOLA) [3] reduced to the same resolution as the gravity field.

Bulk density from correlation analysis: We applied the method proposed by Wieczorek et al. [1], truncating the gravity data at a lower boundary of degree and order 150, to exclude long wavelength gravity contribution (the remaining coefficients represent gravity from topography only). Calculating Bouguer correction, the resulting signal will be zero if the correct density is applied. If a wrong density is used, the Bouguer anomalies will correlate with the topography. Testing different density values, we minimized the correlation between Bouguer anomalies and topography to find the bulk density in small analysis circles of 3° radius.

Bulk density from Bouguer anomaly roughness: We slightly modified the approach from Wieczorek et al. [1] and estimated the roughness of Bouguer anomalies for different density values, by calculating the standard deviation. Maximizing the smoothness of the Bouguer anomalies we found the bulk density for each analysis area.

Bulk density map: The bulk density map (Fig. 1) has a grid size of 0.75°. The truncated gravity field starting from degree and order 150 constrains the depth of the analysed bulk densities to a few kilometers.

Since lunar maria consist of basaltic material, being of different origin and composition as the anorthosite crust, we exclude analysis regions where the mare contribution [4] exceeds 2.5%.

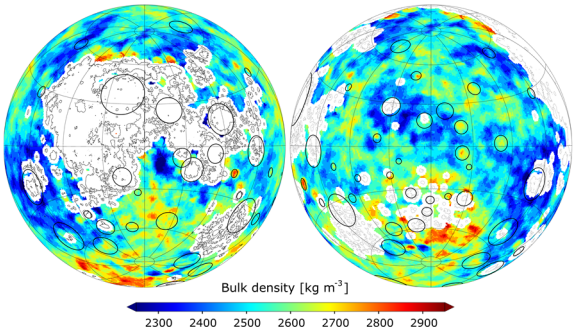

Figure 1: Bulk density from correlation analysis, mapped in lambert azimuthal equal-area projection, covering a 240° latitude and longitude range (nearside: left; farside: right). Prominent impact basins are marked with black circles, mare regions were excluded in our investigation (white).

Both applied methods yield similar results in most (97%) of the investigated areas. Differences of up to 700 kg m^{-3} were found in regions of smooth surface, indicating that both methods suffer from a lack of topographical features.

The average densities of 2536 ± 21 kg m^{-3} (correlation analysis) and 2503 ± 22 kg m^{-3} (Bouguer anomaly roughness) agree with earlier studies [1], where an average of 2550 ± 18 kg m^{-3} was estimated.

Porosity map: Variations in crustal porosity were determined by considering the well-known relation between bulk and grain densities of

$$\phi = 1 - \frac{\rho_{bulk}}{\rho_{grain}} \quad .$$

The analyses of lunar samples revealed a correlation between average grain densities of rocks and their iron and titanium abundances [6]. Following Huang and Wieczorek [6] we used remote sensing data from Lunar Prospector mission [5] to map the porosity of the upper lunar crust (Fig. 2).

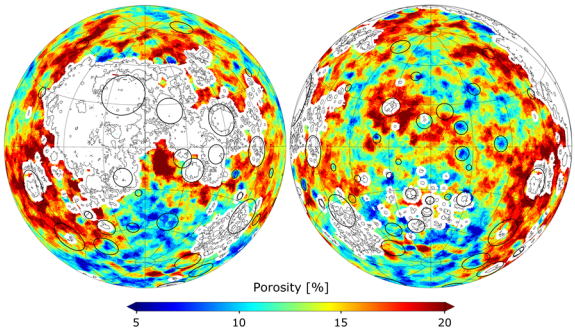

Figure 2: Porosity of the upper crust, mapped with the same conditions as Fig. 1

Conclusion and Outlook: Our maps of lateral variations in bulk density and porosity of the upper crust have a spatial resolution two times higher than in former studies [1]. Areas of high crustal porosity correlate with the location of lunar impact basins, which confirms earlier ideas, that the high porosity of the lunar crust is most likely impact induced.

We will use high-resolution bulk density and porosity maps to study lunar impact basins in more detail. Furthermore, global mass anomalies in the lower crust may be modelled in more detail when applying bulk densities, which have been presented in this study.

References: [1] Wieczorek, M. A. et al. (2013) *Science, 339,* 671–675. [2] Zuber, M. T. et al. (2013) *Science, 339,* 668-671. [3] Smith, D. et al. (2017) *Icarus, 283,* 70-91. [4] Nelson, D. M. et al. (2014) *LPS XLV,* Abstract #2861. [5] Prettyman, T. H. et al. (2006) *JGR Planets, 111(12),* 1-41. [6] Huang and Wieczorek (2012) *JGR Planets, 117(5),* 1-9

MINERALOGICAL CHARACTERISTICS OF U-PB DATABLE MINERALS IN LUNAR METEORITE NORTHWEST AFRICA 2995: IMPLICATION FOR ITS MULTI-IMPACT HISTORY.

N. Wang[1,2], R. Tartèse[1], J.R. Darling[3], K.H. Joy[1], J. F. Pernet-Fisher[1], Y. T. Lin[2]. [1]School of Earth and Environmental Sciences, The University of Manchester, UK (nian.wang@postgrad.manchester.ac.uk), [2]Institute of Geology and Geophysics, Chinese Academy of Sciences, Beijing, China, [3]School of Earth and Environmental Sciences, University of Portsmouth, UK.

Introduction: The Moon has preserved the most abundant information about early impact history of the Solar System, and is the best and most accessible place for us to evaluate this bombardment and its consequence [1-2].

Accurate dating of these events that occured on the Moon depends both on high precision, and high spatial resolution, analysis of isotopic and trace element systematics, and correct interperation of the chronology results. Here, we investigate the mineralogical characteristics of mineral phases that are datable using the U-Pb and Pb/Pb isotopic systems using several integrated laboratory methods in lunar meteorite Northwest Africa (NWA) 2995. In the future we will combine these results with age dating using NanoSIMS, providing a systematic study of the geochronology of lunar meteorite NWA 2995.

NWA 2995 is a feldspathic fragmental breccia containing numerous highland fine grained lithologies [3]. Its paired sample NWA 2996 has been inferred to come from in or around the South Pole-Aitken (SPA) impact basin. These meteories are, therefore, potentially highly significant as they could shed light on the timing of formation of the biggest lunar impact episode [4]. NWA 2995 contains approximately a 5% KREEP chemical composition [4], offering us relatively abundant suitable accessory minerals to study the chronology of the Moon's early history.

Methods: A polished thick section of NWA 2995, about 1 cm long and 0.6 cm wide, was studied. Datable minerals, identified using Scanning Electron Microscope (SEM) mapping (both backscatter electron (BSE) and X-ray imaging), are mainly zircon, apatite and merrillite with minor baddeleyite. Petrological observations were conducted with BSE and cathodoluminescence (CL) imaging, and structural analyses with Raman and FTIR spectroscopy [5]. Additionally, we used NanoSIMS to image the distribution of Si, Ti, Y, Zr, Pb, U and Th in several zircon grains displaying interesting microstructures in BSE and CL images. In order to account for the shock deformation features in several zircons, high resolution electron backscatter pattern (EBSP) and diffraction (EBSD) mapping were also collected with nanoscale step sizes following the technique previously reported in Darling et al. [6]. All of the analyses were carried out at the University of Manchester, except EBSP and EBSD that were measured at the University of Portsmouth.

Results and Discussion: In total, 10 zircon grains, 1 baddeleyite, and 56 Ca-phosphate grains > 3 microns in size were identified on the exposed surface of NWA 2995.

Zr-bearing minerals. All the zircon grains in NWA 2995 are isolated mineral fragments in the matrix, which potentially means that they have experienced multi-impact events before they were consolidated together within the surrounding matrix. Five zircon grains with obvious internal CL features show Raman and FTIR specta typical of unshocked zircon. Two grains, around 25 µm and 5 µm in size, have internal regions that are homogenous in BSE and dark in CL images. These areas show a broad and smooth peak feature in Raman spectrum, corresponding to a flat FTIR spectrum . This implies a lack of crystallinity, suggesting that the grains have been completely transformed into amorphous phase. This transformation implies that these grains have either underwent shock metamorphism or accumulated high levels of radiation damage [7-8], or a combination of both. Three other zircon grains also show diverse internal structures: two of them display small internal relict grains that are darker on BSE images, and brighter (more active) in CL (Fig. 1A-B). These relict grains have lower concentrations of trace elements such as Y, Th, and U than the surrounding more homogenous looking grain (Fig. 1D-E). Raman, FTIR and EBSD analyses have confirmed that these internal relict grains are crystalline zircon, while the host material has been transformed into amorphous phase (Fig. 1C). As shown in Figure 1, the small relict grains in the core shows the lowest Y concentration. The surrounding middle zone has the highest Y abundance, while the zircon rim displays intermediate Y abundance. Raman spectroscopy and the diffraction intensity in EBSD map indicates that these two latter zones are amorphous, while relict grains show around 10° orientation difference in total. These characteristics indicate that this whole zircon grain has experienced at least three stages of evolution, with the two latest stages likely involving shock metamorphism. These grains will be targeted to understand if there are age differences between the relict grains and the surrounding shocked structure.

Baddeleyite. We only found one baddeleyite grain within a mafic-rich clast. This grain has no obvious fractures features, and will have likely retained a crystallization age.

Ca-Phosphate. Two types of phosphate, apatite and merrillite, are common in NWA 2995 (the two can easily be distinguished using Raman spectroscopy) and most of them are isolated in the matrix with only 7 grains related to lithic clasts. All the phosphates analysed using Raman spectroscopy in NWA 2995 are crystalline phases that do not show any indication of high pressure phases or shock polymorphs [9-10]. Furthermore, most of the grains do not show any fractures or deformation features. This suggests that phosphates have either crystallized after the latest deformation event, or that they have been thermally annealed after formation and have not been subsequently deformed by impact reprocessing. This could imply that Ca-phosphate grains crystallized in the matrix in response to late metamorphic events, after formation of the zircons, an effect that has been seen in Apollo samples [11-12].

Future work: Zircon, baddeleyite and Ca-phosphates respond differently to metamorphism. Some of the relict zircons may have preserved very old ages correspondiong to formation of their parent protoliths for example, while other minerals more sensible to thermal events such as Ca-phosphates may have recorded later impact events that affected NWA 2995. These will be achived by combining a systematic study of the geochemistry, microstructures, and *in situ* dating of accessory phases should allow constraining the timing of the multi-stage formation history of NWA 2995.

References: [1] Joy K. H. et al. (2016), *Earth, Moon, and Planets*, *118*(2-3), 133-158. [2] Norman M. D. and Nemchin A. A. (2014) *Earth and Planetary Science Letters*, *388*, 387-398**.** [3] Carpenter P. K. et al. (2017) *LPS XLVIII*, Abstract #2607. [4] Mercer C. N. et al. (2013) *Meteoritics & Planet. Sci.*, *48*(2):289-315. [5] Martin D. J. et al. (2017) *Meteoritics & Planet. Sci.*, *52*(6)*:*1103-1124. [6] Darling J. R. *Earth and Planetary Science Letters*, *444*, 1-12. [7] Timms N. E. et al. (2012), *Meteoritics & Planet. Sci.*, *47*(1), 120-141. [8] Zhang M. et al. (2000), *Journal of Physics: Condensed Matter*, *12*(8), 1915-1925. [9] Chen M. et al. (1995), *Lunar Planet. Sci.*. [10] Xie, X. et al. (2002), *Geochimica Et Cosmochimica Acta*, *66*(13), 2439-2444. [11] Nemchin A. A. et al. (2009), *Meteoritics & Planet. Sci.*, *44*: 1717-1734. [12] Grange M. L. et al. (2013), *Journal of Geophysical Research: Planets*, *118*(10), 2180-2197.

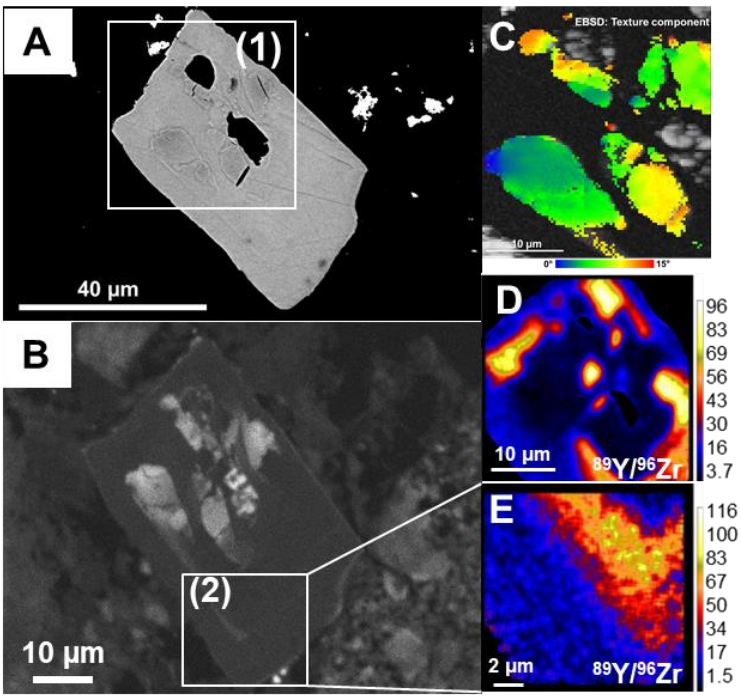

Figure 1. A large zircon grain in NWA 2995 showing internal structures that implies at least a three-stage formation history. A) BSE image shows darker relict grains, surrounded by a more homogenous light grey area, and a zoned-like rim. The areas appearing black within the zircon are filled with Si-rich melt. The same features are seen in the CL image (B), except that relict zircon cores appear brighter than the amorphous surroundings. C) EBSD texture component mapping of area (1) in A shows around 10° orientation difference across the relict grains. NanoSIMS images of the $^{89}Y/^{96}Zr$ ionic ratio in D (square (1) in A) and E (square (2) in B) indicate that the relict grains contain the lowest Y concentration, the surrounding middle zone has the highest Y abundance, and the zircon rim displays intermediate Y abundance

The Oxford 3D Thermophysical Model with application to PROSPECT on the Luna-27 Lunar Lander Mission. T. Warren[1], O. King[2], N. Bowles[1], E. Sefton-Nash[3], R. Fisackerly[3], R. Trautner[3]. (1) Atmospheric, Oceanic and Planetary Physics, University of Oxford, UK, (tristram.warren@physics.ox.ac.uk neil.bowles@physics.ox.ac.uk), (2) Department of Physics & Astronomy, University of Leicester, UK (ortk1@leicester.ac.uk), (3) ESTEC, European Space Agency, Keplerlaan 1, Noordwijk 2201AZ, Netherlands (e.sefton-nash@cosmos.esa.int).

Introduction: To investigate potential in situ near surface volatiles that might be present in the lunar Polar regions, the European Space Agency (ESA) is developing the PROSPECT instrument package to fly to the South Polar region of the moon on-board Russia's Luna-27/Luna Resurs mission, which is scheduled to launch in the early 2020s [1,2]. PROSPECT will consist of a drill (ProSEED) that will collect samples from the regolith at depths of up to 1 m below the lunar surface and transfer them into a miniaturised chemical laboratory (ProSPA), where samples will be heated to 1000° C in the presence of different reagent gases to extract a range of different volatile species including water. For 8 study landing sites of the Luna-27 mission, to investigate the depth at which water ice is likely to be stable we have modelled the lunar surface and subsurface (<2.5 m) temperatures using the new Oxford threedimensional thermophysical model. These sites have been identified as of specific interest as potential candidate sites for Luna 72/Luna Resurs, in part due to proximity to permanently shadowed areas and/or proximity to topographic features resulting in local shadowing of the site.

Oxford 3-D Thermophysical Model: One dimensional thermophysical models are poor predictors of the lunar polar surface and subsurface temperatures due to the importance of shadowing and scattering at high latitudes. To accurately model the surface and subsurface temperatures at the lunar poles requires a 3-D thermophysical model (3DTM). A new 3DTM that includes a discreet subsurface exponential density profile, surface shadowing and scattering effects has been developed at Oxford University to simulate the lunar surface and subsurface temperatures to account for these environmental effects at the poles [3,4,5]. The Oxford 3DTM combines the one-dimensional subsurface heat flow from the Hayne model [5] and the 3-D shadowing and scattering effects used in standard 3DTMs such as the Paige and Vasavada models [3,4]. To compute the shadowing and scattering effects the Oxford 3DTM uses the LOLA topography and albedo datasets. However, since the LOLA albedo measurements are performed using a 1064.4 nm laser the albedo values are scaled to represent the broadband solar albedo value using the method described in [5]. All other thermophysical modelling parameters are taken from [5]. There is currently no in situ data for the Polar regions to compare to our modelled values, so the simulations have been compared to measurements from the Lunar Reconnaissance Orbiter's Diviner Lunar Radiometer instrument ("Diviner") for validation [6].

The central location of each site studied is given in Table 1. The sites were simulated at 3 different resolutions (4 ppd, 16 ppd and 128 ppd - pixels per degree). Each model simulation was kept to ~2 hours in simulation time on a standard desktop personal computer by adapting size of the area simulated to that shown in Table 2.

Site	Latitude	Longitude
1	-79.30	-56.00
2	-80.56	-37.10
3	-81.24	68.99
4	-81.35	22.80
5	-84.25	-4.65
6	-84.33	33.19
7	-85.33	-4.78
8 *	-82.70	33.50

Table 1 : Study landing sites of the PROSPECT mission

Resolution	Latitude buffer size	Longitude buffer	Simulation size	Surface element
4ppd	4.00°	20.00°	~ 245 km	~ 8 km
16ppd	2.00°	10.00°	~ 122 km	~ 2 km
128ppd	0.15°	0.75°	~ 9 km	~230m

Table 2 : Area of simulated region around each study landing site for each resolution used.

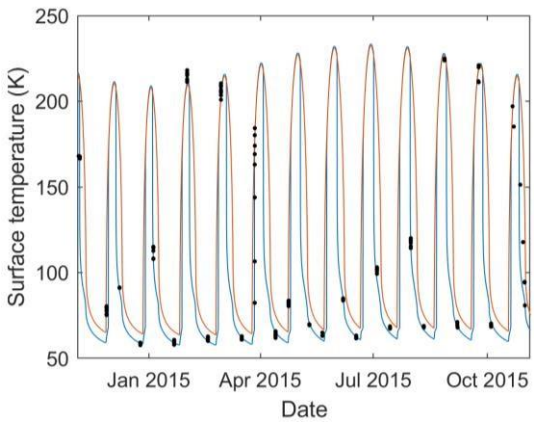

Figure 1 : Blue line is the 3D modelled surface temperature including shadowing and scattering, orange line is a 1D thermal model for the same location not including shadowing and scattering. Black dots are Diviner measurements at site 8. There are multiple Diviner measurements at each time due to the simulation surface elements covering multiple Diviner pixels.

Model Accuracy: We will present an overview of modelling results from all 8 sites and provide the 16 ppd resolution for site 8 as an example in this

abstract. Figure 1 shows the comparison between the Diviner measured surface temperature and the modelled surface temperature for the element that contains the central location of site 8. As can be seen in Figure 1 the 3DTM is in good agreement with the Diviner measurements with the absolute temperature deviation being typically less than 5 K. Where the absolute temperature deviation is defined as being the time averaged absolute difference between the modelled temperature and the Diviner measured temperature.

The modelled temperature deviates from measured Diviner surface temperatures greatest during sunrise and sunset when the surface temperature is changing rapidly. During these periods the modelled temperature deviation from the Diviner measurements can be ~10 K due to a timing or geometry error where the modelled temperature changes slightly earlier or later than the Diviner temperature. This deviation is likely due to the model only simulating the sun as a point source. The absolute model deviation from Diviner surface measurements is also high in regions that are in near permanent shadow such as pole facing shallow slopes and surface elements on the boundary of permanently shadowed regions. For many of these areas the model of the sun as a point source and the discrete simulation grid causes the model to treat them as permanently shadowed, even though they are only partially shadowed during the summer. This can cause deviations of > 30 K as the model under estimates the temperatures in these regions. The absolute temperature deviation from Diviner surface measurements for the 16 ppd simulation of site 8 can be seen in Figure 2.

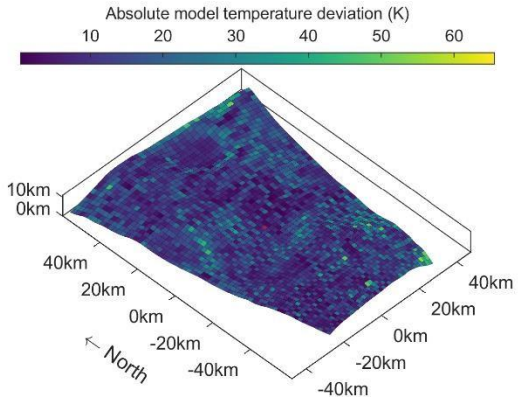

Figure 2 : Absolute difference between Diviner surface temperature measurements and 3DTM surface temperatures at site 8. Red dot shows center of site 8.

Ice Stability Depth: Despite the limitations of the model outlined above, it is still possible to make deductions on the ice stability in these regions. From the thermal model it was possible to define the depth required to drill to reach subsurface temperatures where water ice is expected to be stable by assuming water ice is stable if the temperature remains below 112 K throughout the seasonal cycle [3]. The minimum stable ice depth can be calculated as the depth required to drill to get to a subsurface layer that has a stable temperature < 112 K

The minimum stable ice depth for site 8 is shown in Figure 3, which shows there are large regions where ice is not stable at any depths and in those locations where ice is stable the minimum ice stability depth is relatively shallow (< 0.5 m). Across all landing sites it was found the simulated minimum constant temperature typically occurs at a depth of ~ 0.5 m. These results show that, assuming careful selection of landing site. The current design depth of the PROSPECT drill (~1 m) should be sufficient to sample trapped water ice.

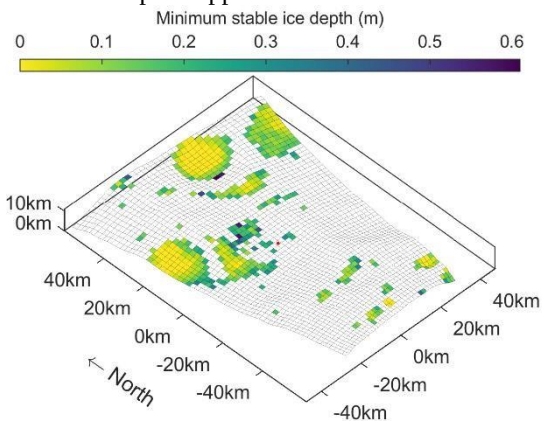

Figure 3 : Minimum depth of stable water ice for region surrounding site 8.

Conclusions: Depths at which ice would be expected to be stable are generally near the surface (i.e. between 0 - 0.5 m deep), so the choice of landing site location and the precision landing capability of the lander are essential given the engineering constraints on the sampling system.

There is an obvious correlation between the illumination fraction and the volatile stability conditions. Luna-27/PROSPECT will therefore have a trade-off to select a site that will satisfy both critical power/operations requirements and science objectives of the PROSPECT mission.

The Oxford 3DTM is currently being improved to including a multiple point solar source and if available updated results will presented.

Acknowledgements: We would like to thank the UK Science and Technology Facilities Council, the Leverhulme Trust, the UK Space Agency and the European Space Agency for supporting this work.

References: [1] Trautner, R. et al. (2018) IAC18, 42773 [2] Sefton-Nash, E. et al. (2018) LPSC 2740 [3] Paige, D. A. et al. (2010), Science, 330, 479. [4] Vasavada, A. et al. (1999) GJR, 193. [5] Hayne, P et al. (2017) Space Sci Rev. [6] Paige, D. et al. (2009), Space Sci. Rev.150, 125-1

DURATION AND SIGNIFICANCE OF VOLCANICALLY INDUCED TRANSIENT ATMOSPHERES ON THE MOON. Lionel Wilson[1,2], James W. Head[2], and Ariel N. Deutsch[2] [1]Lancaster Environment Centre, Lancaster University, Lancaster, LA1 4YQ, UK, l.wilson@lancaster.ac.uk, [2]Department of Earth, Environmental and Planetary Sciences, Brown University, Providence, RI 02912 USA.

Background: Lunar basaltic magmas released volatiles when they erupted, albeit in small amounts when compared with terrestrial basalts [1]. This has led to the suggestion [2] that, at times in the past, especially around the peak in lunar volcanism ~3.5 Ga ago, the Moon may have had a transient atmosphere comparable to that of present-day Mars for periods of tens of Ma. Such conditions might have provided niches in which primitive living organisms could have evolved [3], and released water might have migrated to the poles to explain the excess hydrogen signatures there [2]. We have recently reassessed the mechanisms of generation, ascent and eruption of lunar basaltic magma [4, 5]. This has led to detailed predictions of the pattern of activity during eruptions [6]. Specifically, we are able to predict the variation with time during a typical eruption of the mass flux of magmatic liquid and released gas species, the style of activity (relatively steady hawaiian fire-fountain; intermittent strombolian explosions) and also to give values for the eruption durations, and hence the ranges of values of total magma volume and total gas mass. By combining this information with measurements of lava flow thicknesses and of the total volume of lava in each of the mare basins [7] we arrive at estimates of the typical intervals between volcanic eruptions on the Moon as a function of geologic time. Finally, we address the timescales for the dissipation of transient atmospheres after their production.

Input data: We review the information required to quantify volcanically-generated lunar atmospheres.

Individual eruption volumes: Typical volumes, V, of the visible and therefore most recent mare lava flow deposits [4] are at least ~200-300 km^3, with some potentially up to 1000-2000 km^3. The minimum volumes of lava needed to thermo-mechanically erode the visible sinuous rille channels were of order 100 km^3 [8]. These values are summarized in Table 1.

Total mare basalt erupted volumes: Estimates of the total thickness of lava in each of the mare basins imply that the total volume, V_t, of all volcanic products erupted on the Moon over its lifetime was close to ~10^7 km^3 [7]. Accurate values for the absolute dates of specific eruptions cannot be determined, but crater size-frequency distributions can give approximate ages of units mapped from orbit. Combined with stratigraphic relationships, this allows estimation of the overall duration, τ_v = ~2 Ga, of the vast majority of the Moon's volcanic activity [7, 9].

Table 1. Parameters of various types of lunar eruptions. Cobra Head is the source of Schroeter's Valley [5] and FFC is a typical floor-fractured crater [11-12]. Released volatiles assumed to be dominated by CO and to form n = 1000 ppm by mass of a magma that has a liquid density ρ_m = 3000 kg m^{-3}. V = lava volume; F_l = lava volume eruption rate; τ_e = eruption duration; G = total gas mass released; F_g = gas mass release rate. Typical values for parameters are quoted but individual eruption values may vary by a factor of at least 2 to 3.

Feature	V/km^3	F_l/(m^3 s^{-1})	τ_e/days	G/kg	F_g/(kg s^{-1})
Cobra Head	2000	1.4×10^5	165	6×10^{12}	4×10^5
FFC	1000	~10^5	115	3×10^{12}	3×10^5
long flow	300	10^6-10^4	30	9×10^{11}	3×10^6
small flow	200	10^5-10^3	100	6×10^{11}	3×10^5
sinuous rille	100	~3×10^4	50	3×10^{11}	10^5

Number of eruptions, average rates and estimated repose periods: Using an average magma volume of 100-300 km^3 for a single eruption, the ~10^7 km^3 total erupted volume of mare basalts, and the time-span, from ~2 to ~4 Ga ago, encompassing most of lunar volcanism, we calculate that a total of ~30,000 to 100,000 eruptions took place, with an average interval between eruptions of 20,000 to 60,000 years. Accounting for lunar thermal evolution in terms of mare mantle production rates and the evolving state and magnitude of stress in the lithosphere we predict [4] that greater volumes were generated and released in earlier periods than later. Assuming that three times as much magma was erupted in the 4-3 Ga period than in the 3-2 Ga period, this suggests that the earlier eruptions could have occurred every 13,000 to 40,000 years, with longer gaps between more recent eruptions.

Volatiles and release patterns: Modern measurement techniques [e.g., 1] and thermodynamic arguments [10] indicate that lunar volatiles were dominated by CO (mass fraction, n, from several hundred to ~1500 ppm by mass) released at depths > 50 km with significant additions of H_2O (up to 900 ppm), SO_2, H_2S and S_2 (totaling ~500 ppm), F (up to 40 ppm) and traces of Cl, all released at depths < 1 km.

Eruption durations: Analyses of the dynamics of lunar eruptions allow us to estimate the volume fluxes, F_l, of the lava forming surface flows and leading to the erosion of sinuous rilles [4-6]; coupled with the dense-rock-equivalent erupted volumes, V, these give values for the typical durations, τ_e, of these eruptions. Table 1 contains the results.

Volatile input to the atmosphere: Multiplying the erupted volume V by the typical density of lunar basaltic magma, ρ_m = ~3000 kg m^{-3}, yields the magma mass erupted, and multiplying the magma mass by the released gas mass fraction n gives the total gas mass released, G. Finally dividing G by τ_e yields the average gas mass input rate to the atmosphere, F_g. Table 1 summarizes these values.

Analysis: For each of the released gas masses in Table 1 we can find the properties of the lunar atmosphere that would be created if the gas were released from the erupted magma at a much greater rate than the total loss rate into space of the atmosphere by all relevant mechanisms. Based on the proportions of the various components [1] we find that the mean molecular mass of the volatiles would have been m = ~25 kg/kmol. The scale height, H, of the resulting atmosphere would have been equal to $[(Q\ T) / (m\ g)]$ where Q is the universal gas constant, 8.314 kJ kmol^{-1} K^{-1}, T is the mean lunar surface temperature, ~235 K, and g is the acceleration due to gravity at the lunar surface, 1.62 m s^{-2}. These values imply H = 48 km. The surface density of the atmosphere, ρ_s, would have been equal to its mass, G, from Table 1, divided by the volume equivalent to the surface area of the Moon multiplied by the scale height, i.e. $\rho_s = G/(4\ \pi\ R^2\ H)$ where R is the lunar radius, 1738 km. Finally the surface pressure would have been $P_s = \rho_s\ g\ H$. Table 2 lists the values of ρ_s and P_s corresponding to eruption types in Table 1.

Table 2. Initial values of the surface density, ρ_s, and surface pressure, P_s, in a transient atmosphere produced by the five types of volcanic activity listed in Table 1. The maximum duration of the atmosphere, τ_d, is indicated.

Feature	ρ_s/(kg m^{-3})	P_s/Pa	τ_d/years
Cobra Head	3.3×10^{-6}	0.26	19,000
FFC	1.6×10^{-6}	0.13	9,500
long flow	4.9×10^{-7}	3.8×10^{-2}	2,900
small flow	3.3×10^{-7}	2.6×10^{-2}	1,900
sinuous rille	1.6×10^{-7}	1.3×10^{-2}	950

Discussion: Table 1 shows that typical styles of lunar volcanic activity would have produced atmospheric gas masses of order a few times 10^{11} to a few times 10^{12} kg. A hypothetical volcanically-induced atmosphere with a total gas mass of 10^{14} g, i.e., 10^{11} kg, was assumed by Stern [13, his section 5.2.2] as part of a review of three possible types of lunar atmosphere, and his example is at the lower end of the range of masses that we predict. This mass implies that a collisionally dominated atmosphere would have typically formed. If this were the case, then the loss rate of gas from such an atmosphere would have been of order 10 kg s^{-1} [14], and the timescales for atmospheric decay, τ_d, would have been between ~1,000 and ~20,000 years, with most values less than ~3000 years, as shown in Table 2. These atmosphere preservation times are likely maxima, because as the density becomes very small, other loss mechanisms come into play. We can compare these loss times with the likely intervals between eruptions on the Moon. With a total magma volume, $V_t = 10^7$ km^3 [7], a typical erupted volume of 200 ± 100 km^3 (Table 1), and a total duration of volcanism of τ_v = ~2 Ga, the average interval between eruptions is ~13,000 to 40,000 years, on average more than an order of magnitude greater than the time needed for the previous transient atmosphere to be lost.

Thus, for most lunar volcanic eruptions, any transient atmosphere formed in a single eruption is likely to be dissipated well before the next eruption occurs. However, some lunar eruptions would have produced more massive atmospheres with a longer survival time - the extreme example is the eruption that produced the Schroeter's Valley sinuous rille. Also some events linked to the formation of floor-fractured craters could have produced unusually long-lasting atmospheres. These events were rare, however. In general atmospheres were lost in about 5% of the interval before the next eruption. Only if all of the Moon's ~10^7 km^3 of basaltic volcanism were to have taken place within a 200 Ma interval would the time scales be comparable.

Conclusions: The implied intervals between typical lunar eruptions, ~20,000 to 60,000 years, are more than an order of magnitude greater than the likely durations of the vast majority of individual transient atmospheres, between ~1,000 and 3,000 years. It is therefore unlikely that the Moon ever had a semi-permanent volcanically-driven atmosphere. We attribute the differences between our estimates and those of others [2, 3] to their use of maximum impact basin depths as average depths, and to their assignment of all lava volumes stratigraphically below datable units to a single age, e.g., 5.9 x 10^6 km^3 of lava assigned to 3.5 Ga in the case of Mare Imbrium.

References: [1] Rutherford M. J. et al. (2017) *Amer. Mineralogist, 102*, 2045-2053. [2] Needham D. H. & Kring D. A. (2017) *EPSL, 478*, 175-178. [3] Schulze-Makuch D. & Crawford I. A. (2018) *Astrobiol., 18*, 985-988. [4] Head J. W. & Wilson L. (2017) *Icarus, 283*, 176-223. [5] Wilson L. and Head J. W. (2017) *Icarus, 283*, 146-175. [6] Wilson L. & Head J. W. (2018) *GRL, 45*, 5852-5859. [7] Head J. W. & Wilson L. (1992) *GCA, 56*, 2155-2175. [8] Head J. W. & Wilson L. (1981) *LPS, XII*, 427-429. [9] Hiesinger H. et al. (2011) *GSA Special Paper 477*, 1-51. [10] Renggli C. J. et al. (2018) *GCA*, 206, 296–311. [11] Jozwiak L. et al., (2015) *Icarus* 248, 424-447. [12] Wilson L. & Head J. W. (2018) *Icarus* 305, 105-122. [13] Stern S. A. (1999) *Rev. Geophys., 37*, 453-491. [14] Vondrak R. R. (1974) *Nature, 248*, 657-659.

FIVE DECADES OF INSIGHT INTO SOLAR SYSTEM PROCESSES FROM THE APOLLO SAMPLE SUITE: A GUIDE TO FUTURE EXPLORATION. Ryan A. Zeigler. Astromaterials Acquisition and Curation Office, NASA Johnson Space Center, 2101 NASA Parkway, Mail Code XI2, Houston, TX, 77058 USA. ryan.a.zeigler@nasa.gov.

Overview: The Apollo program was the seminal moment in modern human history and the crowning technological achievement of the 20th century. The Apollo program has a profound historical, cultural, and technological significance. Additionally, scientific results from the Apollo samples have had a lasting impact on a range of scientific fields, particularly planetary science and cosmochemistry. Over the past five decades, studies of Apollo samples have yielded significant insights into planetary bodies throughout the solar system. Despite the Apollo samples being a static collection, recent and ongoing studies continue to make new significant discoveries. Here we will discuss the history of Apollo samples collection, curation, and study, and also look forward to expected new developments in the coming years.

Background: The Astromaterials Acquisition and Curation Office at NASA's Johnson Space Center (hereafter JSC curation) is the past, present, and future home of all of NASA's astromaterial sample collections [1-3]. Our primary goals are to maintain the long-term integrity of the samples and ensure that the samples are distributed for scientific study in a fair, timely, and responsible manner, thus maximizing the science return on each sample. JSC curation currently houses all or part of nine different astromaterial sample collections, with two more sample return missions underway: (1) Apollo samples, (2) Luna samples, (3) Antarctic meteorites, (4) Cosmic Dust particles, (5) Microparticle Impact Collection, (6) Genesis solar wind atoms, (7) Stardust comet Wild-2 particles, (8) Stardust interstellar particles, (9) Hayabusa asteroid particles, (10) Hayabusa2 asteroid particles (2021), and (11) OSIRIS REx asteroid particles (2023). Additionally, JSC curation houses some combination of space exposed hardware, contamination knowledge samples, and spacecraft coupons for all NASA-led sample return missions, including future sample return missions like OSIRIS-REx and Mars 2020.

Apollo Samples: From 1969 to 1972, the Apollo astronauts collected 382 kg of rock, regolith, and core samples from six geologically diverse locations on the Moon. The Apollo samples span an incredible range of sample types, including: large rock samples (e.g., the 11.7 kg 61016); multiple rocks chipped from large boulders (e.g., 76235/55/75/95 from Boulder 1, Station 6, Apollo 17); bulk surface, trenched, and shaded lunar soils (e.g., 60500, 61220, and 69920/40/60 respectively); multiple 30-60 cm drive tubes and deep drill cores samples up to ~3 meters in depth (these preserved the regolith stratigraphy); and several different types of special vacuum-sealed regolith and drive tube samples [4].

In the 50 years since the Apollo samples were collected, there have been 3158 unique lunar sample requests from >500 different Principal Investigators from over 15 different countries. The total number of samples allocated is not precisely known, but a conservative estimate is >50,000 Apollo samples have been allocated over the past 50 years (Figure 1). Studies of Apollo samples continue as new scientists and new instruments push the boundaries of what can be done with the samples. Currently 145 active lunar PIs are studying >8,000 samples in fields as disparate as biology, medicine, astronomy, engineering, material science, chemistry, and (of course) geology.

Discussion: Studies of the Apollo samples, both early and more recent, continue to yield significant insights into the formation, evolution, and maturation of the Earth-Moon system, as well as many other planetary bodies in both the inner and outer solar system. A comprehensive listing of significant results from the study of Apollo samples in this space is impossible (even in a long-form abstract), but listed below are a subset of results that highlight the wide-ranging, long-lasting, and diverse nature of studies of Apollo samples: (1) The Moon formed from the debris of a giant impact between the proto-Earth and a large bolide early in the solar system history [4,5]. (2) The Moon had a Lunar Magma Ocean, and evolved akin to a global (though asymmetric) layered-mafic intrusion [6,7]. (3) A prevalence of ~3.9 Ga ages of lunar impact melts suggests that there might have been a "Lunar Cataclysm" at that time, which would have affected all of the inner solar system [8]. (4) The potential prevalence of impacts ~600 Ma after solar system formation (i.e., the "Lunar Cataclysm") was one of the factors leading to new dynamical models for the evolution of the entire solar system, e.g., the Nice Model [9]. (5) By tying the ages of Apollo basalts to the crater densities in the regions of the Apollo landing sites, relative crater counting ages can be given absolute ages on the Moon, as well as elsewhere in the inner solar system [10]. (6) Despite decades of null results for volatiles in lunar samples (e.g., H_2O), recent results [e.g., 11,12] have shown that the Moon is not "bone dry" and these volatile abundances inform the models for lunar formation. (7) The way light interacts with the surface of airless bodies changes over time due to space weathering caused by micrometeorite bombardment and solar wind implantation; studies of Apollo samples form the basis for understanding this process and thus correctly interpreting remotely sensed observations of these bodies [13]. (8) The composition of Apollo samples have directly contributed to the interpretation of remotely sensed data sets, including their use as ground truth for both

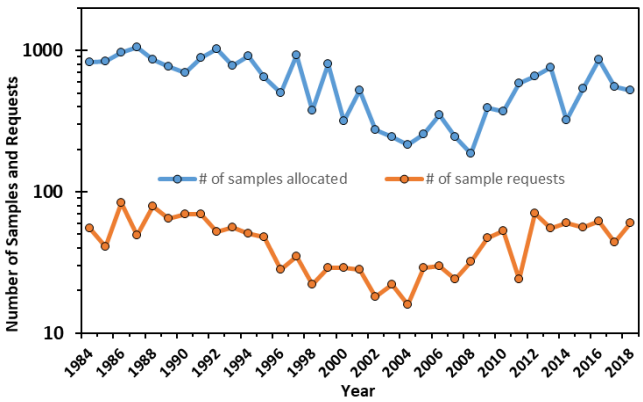

Figure 1: Number of Apollo sample requests and sample allocations per year since 1984. These represent about 40% of the total requests made since 1969.

Clementine and Lunar Prospector global geochemical maps [14,15]. (9) Studies of the toxicity of Apollo samples provide the basis for safe exposure limits for future human exploration of the solar system [16]. (10) Apollo samples have been requested as analogs for studies of Mercury, the martian moons, and near-Earth asteroids, as well as to better understand how to detect potential life on exoplanets.

Future Apollo Studies: Despite the Apollo Sample Suite being a static collection, "new" samples are still being made available for study through several avenues. NASA recently solicited proposals as part of the Apollo Next Generation Sample Analysis (ANGSA) program [17]. The ANGSA program includes previously unopened, vacuum-sealed drive tubes and bulk soil samples, cold-curated samples (-20°C), and samples only handled in a He-purged environment. Furthermore, JSC Curation can now scan samples using X-ray Computed Tomography (XCT); XCT scans of polymict breccias are expected to identify "new" lithic clasts for PIs to study. Similarly, there are 10,000s of small particles in the >110 kg of bulk lunar regolith, and a portion of these will also be classified and made available to PIs after a retroactive preliminary examination process utilizing XCT, micro X-ray Fluorescence, and Imaging micro-Raman Spectroscopy. Additionally, a new searchable database for lunar geochemical data called MoonDB has been brought online [18].

Conclusions 50 years of study of Apollo samples yielding important insights into a wide-variety of topics and planetary bodies has shown that sample return missions are "the gift that keeps on giving." Many of the results highlighted in this abstract were not yet conceived of (or the instruments not yet invented) when the samples were first brought back. However, because the samples have remained available, and been maintained in a pristine manner, future generations of scientists continue to extract greater and increasingly novel value beyond the initial studies. Despite the costs, complexity, and risk (real or perceived) associated with sample return missions, the long-lasting legacy of scientific return for sample-return missions more than offsets these mitigating factors. This is not to say that sample-return missions and sample-related studies are the only type of planetary science that should be pursued, but rather that they are a key component of a holistic way of studying the solar system, combined with remote-sensing and *in-situ* missions, as well as modelling-based and experimental-based studies on Earth.

References: [1] Allen, C. et al., (2011) Chemie Der Erde Geochemistry, 71, 1-20. [2] McCubbin, F. M. et al., (2016) 47th LPSC, abstract #2668. [3] Calaway M. J. et al., (2018) 50th LPSC, abstract #1690. [4] Canup R. M. and Asphaug E. (2001) *Nature*, **412**, 708-12. [5] Cuk M. and Stewart S. T. (2012) *Science*, **338**, 1047-52. [6] Wood J. A. (1975) *PLSC*, **6**, 1087-1102. [7] Elkins-Tanton L. T. et al. (2011) *EPSL*, **304**, 326-336. [8] Marchi S. et al. (2012) *EPSL*, **325-36**, 27-38. [9] Morbidelli A. et al., (2007) *The Astronomical J.*, **135**, #5. [10] Hiesinger H. et al., (2012) *JGR Planets*, https://doi.org/10.1029/2011JE003935. [11] Hauri E. H. et al. (2011) *Science*, **333**, 213-15. [12] McCubbin F. M. et al. (2010) *PNAS*, *https://doi.org/10.1073/pnas.1006677107*. [13] Pieters C. M. et al., (2010) *MAPS*, **35** 1101-07. [14] Blewitt D. T. et al., (1997) *JGR Planets*, **102**, 16319-25. [15] Lawrence D. J. et al., (2002) *JGR Planets*, **107**, 13-1-13-26. [16] Lam C. W. (2013) *Inhal. Toxicol.*, 25, 661-78. [17] Specially Curated Apollo Samples – Programmatic Information Package. [18] Lehnert, K. et al., (2018) 50th LPSC, Abstract #2996.

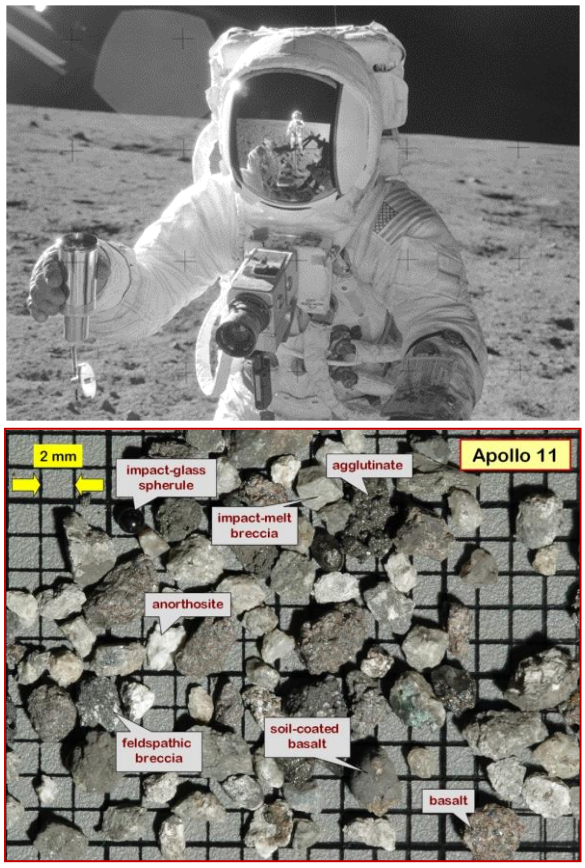

Figure 2: Apollo 12 astronaut Alan Bean collecting a GASC sample (top). 2-4 mm particles separated from an Apollo 11 soil.

LUNAR IMPACT GLASSES: PROBING THE MOON'S SURFACE AND CONSTRAINING ITS IMPACT HISTORY. N. E. B. Zellner[1] [1]Department of Physics, Albion College, Albion, MI USA 49224 (nzellner@albion.edu)

Introduction: Lunar impact glasses are small samples that can lead to big science ideas about the timing of the lunar impact flux, which been the topic of many reports and reviews and debated at length [e.g., 1-14]. They can also provide important information about the Moon's surface, including areas not sampled by Apollo or Luna missions or lunar meteorites. A summary of past and current lunar impact glass investigations, using glasses from the Apollo 12, 14, 15, 16, and 17 regoliths, along with plans for future work, will be presented.

Background: Lunar impact glasses (Figure 1), formed in melted impact ejecta during ballistic flight, were an unexpected find in the Apollo samples. They are easily distinguishable from volcanic (i.e. "pristine") glasses, which have a high MgO/Al_2O_3 ratio, chemical homogeneity, and Mg-correlated abundances of Ni, among other criteria [e.g., 15]. In fact, while volcanic glasses are observed to cluster readily around certain chemical composition types, impact glasses have a range of chemical compositions, reflecting the variety of regolith sources [e.g., 15,16] and sizes of impact craters (< 1 km [e.g., 17, 18] to >100 km [e.g., 19,20,21,22]) in which they formed. The small sizes of lunar impact glasses (≤25μm – 6 mm in diameter [e.g., 23,24]) leave little room for contamination, and they are abundant in the regolith. In particular, impact glasses that are free of inclusions and chemically homogenous are ideal probes for investigating the compositions of their source regions and the timing of impact events because it is unlikely that they contain any contaminating material that would affect measurements of major and trace elements and argon.

Early Studies: The Apollo Soil Survey [25] and other studies [as listed in 26] reported only compositional groups of glasses, and though their sources (e.g., rock [27] vs. regolith [e.g., 26,28]) were debated, average compositions from clusters of similar glasses were thought to represent the composition of only the target materials. However, in a case study of Apollo 15 yellow impact glasses, Delano et al. [26,29] showed that their compositions could not be "duplicated by any combination of local components presently known to occur at the Apollo 15 landing site" [29] and were thus exotic to the landing (collection) site. This meant that these impact glasses were not formed in local impacts but rather were formed in impacts distal to the region. In another study, Delano [19] proposed that exotic glasses found in an Apollo 16 regolith resembled those found in two lunar highland meteorites, possibly representing "ancient regolith" in the Apollo 16 region. Both of these studies demonstrated that impact glasses formed in regolith and could be used to determine chemical constraints on indigenous and exogenous lithologies, including those not directly sampled by the Apollo or Luna missions [26].

Recent Studies: As analytical instruments and techniques evolved, studies of lunar impact glasses became more focused. Additionally, argon mass spectrometers capable of analzying small glasses with even smaller amounts of argon became available. Thus, it was inevitable that $^{40}Ar/^{39}Ar$ ages of lunar impact glasses would be determined; the ages of lunar impact glass spherules were used to interpret the lunar impact flux from ~4.5 Ga to the present [e.g., 30,31]. Ages derived from U-Pb and "chemical" U-Th-Pb [e.g., 18,32,33] have also been assigned to impact glass spherules, though in general, these ages do not agree with measured $^{40}Ar/^{39}Ar$ ages [33].

Not all lunar impact glasses are the same, however. In fact, impact glass spherules and shards (i.e., fragments) tell different stories. In a long-running study of lunar impact glasses from five different regoliths (Apollo 14, 15, 16, and 17), hundreds of lunar impact glass spherules and shards have been analysed to determine their size, shape, composition, and $^{40}Ar/^{39}Ar$ age. When compared to glasses with similar analyses [e.g., 31], it is observed that impact spherules are more likely to be young and thus reflect recent impact events, while shards reflect impact events over the age of the Moon (Figure 2). Using results from a model of impact flux scenarios, Huang et al. [34] suggest that the excess of young ages for lunar impact glass spherules is likely due to limitations of the regolith sampling strategy undertaken by the Apollo astronauts and does not reflect an actual increase in the recent lunar impact rate. Glass shards, on the other hand, because they have survived aeons of bombardment, may be the ideal samples to use to investigate the lunar impact flux [35].

An assessment of lunar impact glass compositions, $^{40}Ar/^{39}Ar$ ages, sizes, and shapes has been implemented to provide an interpretation of the lunar impact flux [e.g., 35-37] that has been more holistic than those previously reported [e.g., 30,31]. Additionally, quantitative constraints can be applied to-choosing appropriate samples for $^{40}Ar/^{39}Ar$ analyses [e.g., 38]. All of these considerations have been applied to create Figure 3, which shows our current understanding of the lunar impact flux as represented by lunar impact glasses. Similarities to ages of the lunar meteorites [e.g., 39] and to the dirth of lunar impact craters [e.g., 40] are evident, as well as an impact flux that appears to tail-off after ~3700 Ma [e.g., 8,37].

Future Work: In addition to the studies described herein, impact glasses can be used to improve our understanding of the lunar dynamo history [e.g., 41] and our understanding of specific proposed impact episodes [e.g, 36, 42]. Hundreds of lunar impact glasses suitable for compositional and $^{40}Ar/^{39}Ar$ analyses [e.g., 38] and other studies can be found in a 5-gram regolith sample, and more studies will only increase the value of the data gleaned from them.

Conclusions: In summary, not only do lunar impact glasses provide important information about the timing of the Moon's impact flux, but they also provide information about their provenance(s) of origin. Lunar impact glasses are abundant in the regolith and represent multiple regolith lithologies. Thus, they provide a data set with which we can investigate the Moon's geological characteristics and evolution over time, including that of areas not directly sampled by past, current, or future planned missions.

Acknowledgements: I thank Pham Nguyen for creating Figure 2.

References: [1] Baldwin, R. B. (1949) *The Face of the Moon*, Univ. of Chicago Press, Chicago. [2] Hartmann W. K. (1966) *Icarus*, **5**, 406–418. [3] Tera F. et al. (1974), *EPSL*, **22**, 1-21. [4] Turner G. et al. (1973) *Proc. 4th Lunar Sci. Conf.*, *GCA* Sup., 2, 1889-1914. [5] Ryder G. (1990) *Eos*, **71**, 313, 322, 323. [6] Bottke W. and Norman M. (2017) *Ann. Rev. Earth Plan. Sci.*, ***45***. [7] Michael G. et al. (2018) *Icarus*, **302**, 80-103. [8] Morbidelli A. et al. (2012) *EPSL* **355-356**, 144-151. [9] Norman M. and Nemchin A. (2014) *EPSL*, **388**, 387-398. [10] Fernandes V. et al. (2013) *MAPS*, **48**, 241-269. [11] Cohen B. et al. (2005) *MAPS*, **40**, 755. [12] Spudis P. et al. (2011) *JGR*, **116**, E00H03. [13] Frey H. (2011) *GSA Special Paper* **477**, 53-75. [14] Marchi S. et al. (2012) *EPSL*, **325-326**, 27-38. [15] Delano J.W. (1986) *JGR*, **91**, D201–D213. [16] Zellner et al. (2002) *JGR*, **107**(E11):5102–5115. [17] Hörz F. and Cintala M. (1997) *MAPS* **32**, 179-209. [18] Norman M. et al. (2012) *Aust. Journ. Earth Sci*. **59**, 291-306. [19] Delano J. W. (1991) *GCA*, **55**, 3019-3029 [20] Delano J. W. et al. (2007) *MAPS* **42**, 6, 993-1004. [21] Korotev et al. (2010) *GCA* **74**, 7362-7388. [22] Zeigler R. et al. (2006) *GCA* **70**, 6050-6067. [23] Keller L. and McKay D. (1992) *Proc. 22nd LPSC*, 137–141. [24] Ryder G. et al. (1996) *GCA* **60**, 693–710. [25] Apollo Soil Survey (1971) *EPSL*, **12**, 49-54. [26] Delano J.W. et al. (1981) *Proc. Lun. Plan. Sci.*, 12B, 339-370. [27] Reid et al. (1972) *Proc. 3rd Lun. Sci. Conf.*, 363-378. [28] Delano J. W. (1975) *Proc. 6th Lun. Sci. Conf.*, 15-47. [29] Delano J.W. et al. (1982) *Proc. 13th* LPSC, **87**, A159-A170. [30] Culler T. et al. (2000) *Science*, **287**, 1785-1788. [31] Levine J. et al. (2005) *GRL*, **32**, L15201. [32] Norman M. D. et al. (2013) *76th Met. Soc. Meeting*, Abstract 5163. [33] Zellner et al. (2013) *44th LPSC*, 2539.pdf. [34] Huang Y.-H. et al. (2018) *GRL*, **45**, 6805–6813. [35] Zellner N. E. B. and Delano J. W. (2015) *GCA*, **161**, 203-218. [36] Zellner et al. (2009) *GCA*, **73**, 4590-4597. [37] Zellner N. E. B. (2017) *OLEB*, **47**(3), 261-280. [38] Nguyen P. Q. and Zellner N. E. B. (2019) *Geosciences*, **9**(85). [39] Swindle T. D. et al. (2009) *MAPS*, **44**, 747-762. [40] Kirchoff M. et al. (2013) *Icarus*, **225**, 325-341. [41] Hess K. et al. (2019) *50th LPSC*, 3190.pdf. [42] Huang Y.-H. et al. (2019) *50th LPSC*, 3010.pdf.

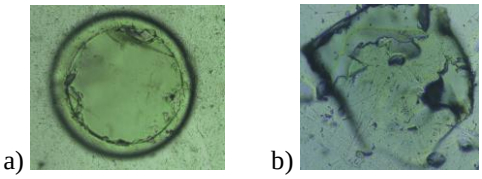

Figure 1. (a) Lunar impact glass spherule (#226, 174 µm in diameter) from Apollo 16 [20]. (b) Lunar impact glass shard (#137, ~300 µm across) from Apollo 14 [16].

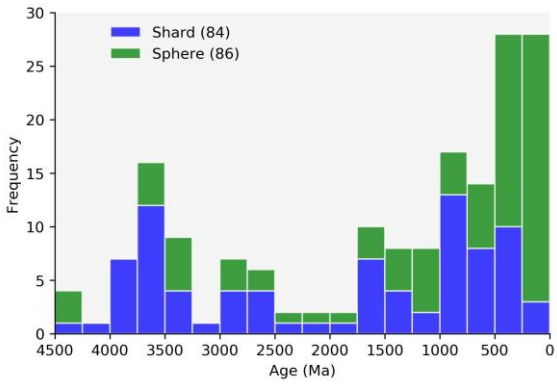

Figure 2. Lunar impact glasses spherules and shards whose $^{40}Ar/^{39}Ar$ ages were qualitatively assessed to be "good" or "fair". Data from [35,38].

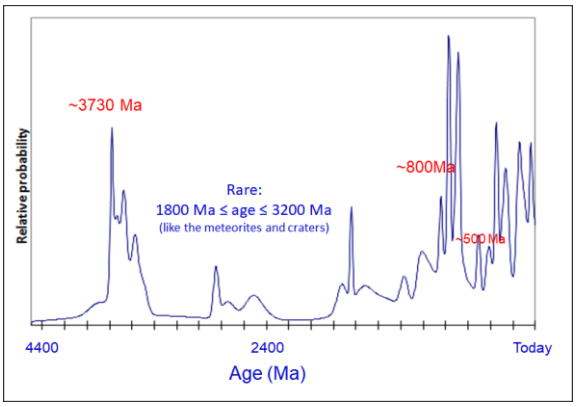

Figure 3. Lunar impact flux, as observed in lunar impact glasses with "good" or "fair" $^{40}Ar/^{39}Ar$ age assessements. Modified from [35,37].